Design and Study of Microwave Potentials for Interferometry with Thermal Atoms On a Chip

Mahdi Ammar

THÈSE DE DOCTORAT DE
l'UNIVERSITÉ PIERRE ET MARIE CURIE

Spécialité

Physique Quantique

Ecole Doctorale de Physique (Paris)

Présentée par

Mahdi AMMAR

Pour obtenir le grade de

DOCTEUR de l'UNIVERSITÉ PIERRE ET MARIE CURIE

Sujet de la thèse :

Design and Study of Microwave Potentials for Interferometry with Thermal Atoms On a Chip

soutenue le 17 juin 2014

devant le jury composé de :

Mme Hélène Perrin	Rapporteur
M. Pascal Szriftgiser	Rapporteur
M. Philipp Treutlein	Examinateur
Mme Catherine Schwob	Examinateur
M. Naceur Gaaloul	Examinateur
M. Olivier Patard	Membre invité
M. Jakob Reichel	Directeur de thèse
M. Sylvain Schwartz	Encadrant de thèse

DESIGN AND STUDY OF MICROWAVE POTENTIALS FOR INTERFEROMETRY WITH THERMAL ATOMS ON A CHIP

MAHDI AMMAR

Thales Research & Technology
Laboratoire Kastler Brossel

Dissertation submitted to the Faculty of Physics of the Université Pierre et Marie Curie, Paris

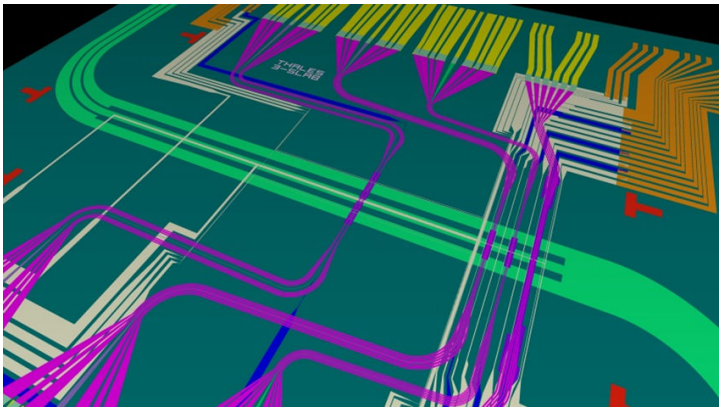

Paris, May 2014

ABSTRACT

In this thesis, we report the theoretical study of an atom interferometer using thermal (i.e. non condensed) atoms trapped on a chip, with reduced mean-field effects. To keep an adequate level of coherence, a high level of symmetry between the arms of such an interferometer is required. To achieve this goal, we describe an experimental protocol based on microwave near-fields created by two coplanar waveguides carrying currents oscillating at different frequencies. This method enables the creation of two symmetrical microwave potentials that depend on the atomic internal state, and allows a state-selective symmetrical splitting of the atoms. We mainly consider two symmetrical configurations to separate the atoms either along the longitudinal axis or along the transverse axis of the static magnetic trap.

In the case of a transverse splitting of the atoms, we discuss the advantages of using a custom microtrap that has the same field structure as a standard macroscopic Ioffe Pritchard trap, and we propose a practical design for such a microtrap.

In the case of an axial splitting of the atoms, we study some physical factors limiting the ultimate performances of this interferometer such as: the dissymmetry of the microwave potentials, the effect of the fluctuations of static and microwave fields and the stability of the interferometer gravitational signal. We derive a simplified one-dimensional harmonic model to describe the interferometer contrast decay. Finally, we consider the possibility of non-adiabatic atomic splitting and recombination without vibrational heating by designing appropriate trajectories of the trapping-potentials based on the theory of dynamical invariants.

Keywords: Ultracold atoms, Atom chip, Microtrap design, Atom interferometry, Microwave potentials, Shortcuts to adiabaticity

REMERCIEMENTS

J'ai effectué mon travail de thèse dans le laboratoire Micro et Nano-Physique (MNP) de Thales Research and Technology (TRT). Je remercie son responsable, Arnaud Brignon, pour son accueil, sa disponibilité et sa bonne humeur.

Je sais infiniment gré à Mme Hélène Perrin et M. Pascal Szriftgiser d'avoir accepté de rapporter cette thèse et de l'attention qu'ils ont portée à la lecture de ce manuscrit. Je suis également très honoré par la présence de M. Philippe Treutlein parmi le jury de ma thèse. Je remercie Mme Catherine Schwob et M. Naceur Gaaloul d'avoir accepté de faire partie du jury. Je les remercie tous pour leurs remarques constructives et pour l'intérêt qu'ils ont montré à mon travail de thèse.

Je tiens à remercier Jakob Reichel d'avoir accepté de diriger ma thèse et de m'avoir accueilli au sein de l'équipe Microcircuits à Atomes au LKB pour un stage de 4 mois avant le démarrage officiel de ma thèse CIFRE. Je remercie Jakob pour les échanges que nous avons eus tout au long de ces trois années de thèse, et pour le suivi administratif qu'il a toujours assumé. Je remercie également Romain Long qui m'a appris les moindres détails du refroidissement laser des atomes pendant mon stage au LKB.

J'ai eu la chance d'être encadré par Sylvain Schwartz tout au long de ma thèse à TRT. Sylvain a suivi de très près mon travail avec beaucoup d'optimisme. J'ai particulièrement apprécié son intelligence scientifique et ses qualités humaines. Je le remercie sincèrement pour la confiance et l'autonomie qu'il m'a accordées pour orienter mes recherches. Merci Sylvain pour ta relecture minutieuse de ce manuscrit, ta patience et tes nombreux conseils avant la soutenance.

Je remercie tous les autres membres de l'équipe Capteurs à Ondes de Matière à TRT. Merci à Christine Guerlin qui a connu le dur travail de la construction initial de la manip' d'atomes froids. Son travail a permis à l'équipe de partir sur une bonne base. Merci à Landry Huet, avec qui j'ai travaillé pendant deux années, pour son travail considérable sur la manip', sa rigueur, et son sens de l'humour. Je remercie également Matthieu Dupont-Nivet qui a rejoint notre l'équipe par la suite pour son implication dans le projet, son enthousiasme et sa persévérance. Son aide a été très précieuse non seulement sur la partie expérimentale mais aussi sur la partie théorique. Merci Matthieu pour ce travail et bon courage pour la suite. Je remercie Jean-Paul Pocholle qui a continué à suivre l'évolution du projet malgré son départ à la retraite.

Je remercie tous les membres du projet CATS qui ont participé aux travaux présentés dans ce manuscrit. Je remercie chaleureusement Chris Westbrook et Jérôme Estève qui m'ont beaucoup aidé à comprendre la physique de l'interférométrie atomique et à bien avancer sur les simulations numériques. Je remercie aussi mes collègues au 3-5 Lab pour leur implication dans le projet. Leur travail a permis de transformer en réalité le design de la puce 'atomique' malgré les nombreuses difficultés techniques.

Je remercie également mes collègues au groupe de physique qui ont partagé mon quotidien à TRT. Un grand merci à mes voisins de bureau : Pierre Colman, Sylvain Combrié, Alfredo Derossi, Christophe Wilhelm, Aude Martin, Perrine Berger, Jérôme Bourderionnet, Mayeul Chipaux et Thierry Debuisschert. Merci également à : Hamza Alami, Marie Antier, Ghaya Baili, Guillaume Bloom, Joachim Borner, Patrick Feneyrou, Eric Lallier, Christian Larat, Luc Leviandier, Jérémy Maxin, Loïc Ménager, Stéphanie Molin, Loïc Morvan, Pascale Noucchi, Grégoire Pillet, Dominique Papillon, Barbara Petit et Muriel Schwarz.

Je tiens à remercier Christopher Harrison de m'avoir accueilli au centre de recherche de Schlumberger (SDR) en 2009. Ce séjour à Boston a été un tournant décisif dans mon parcours. J'y ai grandement apprécié les personnes avec qui j'ai travaillé en particulier Mattiew Sullivian qui m'a résolu à poursuivre dans la voie de la recherche. Je profite aussi pour remercier mon ami Bogush pour les corrections d'anglais qu'il a apportées à ce manuscrit.

Enfin, je tiens évidemment à remercier mes parents, toute ma famille, et mes amis parisiens pour leur soutien et leurs encouragements. Un dernier merci à ma femme Hanen qui a toujours su être à mes côtés dans les meilleurs moments comme les plus durs et qui a toujours réussi à me rendre heureux.

Merci à tous.

CONTENTS

1 INTRODUCTION 1

2 ATOM CHIP THEORY 6

2.1 Magnetic trapping of neutral atoms 7

2.2 Quadrupole and Ioffe-Pritchard traps 9

2.2.1 Quadrupole traps 10

2.2.2 Standard Ioffe Pritchard trap 10

2.2.3 Magnetic chip traps 11

2.2.4 Topological constraints on Ioffe Pritchard traps 15

2.2.5 Custom design of an Ioffe Pritchard trap : Manhattan trap 17

2.3 Two-photon transition 21

2.4 Collisional shift 21

3 MICROWAVE ATOM CHIP 24

3.1 Microwave dressed potentials 25

3.2 Microwave chip design 31

3.2.1 Coplanar waveguide theory 31

3.2.2 Microwave field simulation 36

4 THERMAL TRAPPED-ATOM INTERFEROMETRY ON-CHIP 38

4.1 Introduction 38

4.2 Role of symmetry 39

4.3 Symmetrical interferometer in the quasi-resonant regime 40

4.3.1 Description of the interferometric sequence . . . 40

4.3.2 Coherent internal-state manipulation 41

4.3.3 Adiabatic Microwave potentials 42

4.3.4 Principle of a symmetrical microwave potentials 44

4.3.5 Potential-well and potential-barrier beam-splitter 45

4.3.6 Axial and transverse beam-splitter 46

5 AXIAL BEAM-SPLITTER : INTERFEROMETER ANALYSIS 50

5.1 Introduction 50

5.2 Effect of transition mixing 51

5.3 Trap depth of a potential-well beam-splitter 55

5.4 Axial beam-splitter analysis 56

5.4.1 Splitting distance and power requirement . . . 56

5.4.2 The eigen-frequencies of the microwave trapping potential 57

5.4.3 The role of the static field structure 57

5.5 Sensitivity to the static field fluctuations 60

5.5.1 Perfectly-symmetrical interferometer configuration 61

5.5.2 Perturbed-symmetrical interferometer configuration 62

5.6 Sensitivity to the microwave field fluctuations 68
5.6.1 Design of the microwave frequency chain 68
5.6.2 Static double-well 71
5.6.3 Microwave double-well 71
5.6.4 Proposal of symmetrical beam-splitter with one coplanar waveguide 77
5.7 Stability of the interferometer gravitational signal . . . 81
5.8 Conclusion : what is the best configuration ? 86
6 TRANSVERSE BEAM-SPLITTER : SPECIFIC CHIP DESIGN 88
6.1 Introduction 88
6.2 Transverse splitting with a typical static trap 89
6.2.1 Standard Ioffe-Pritchard 89
6.2.2 Typical microtraps : example of a Z-trap 89
6.2.3 Specific H*-trap 90
6.2.4 Custom microtrap design 91
6.2.5 Summary : comparison between different static traps 102
6.3 Full-simulation results 105
6.4 Magic field 107
6.5 Conclusion 109
7 BEAM-SPLITTER DYNAMICS AND CONTRAST ANALYSIS 110
7.1 Introduction 110
7.2 Adiabatic splitting and recombination 111
7.2.1 Cyclic and adiabatic transport 111
7.2.2 Interferometer contrast decay 112
7.2.3 Summary 119
7.3 Shortcut to adiabaticity for harmonic potentials 123
7.3.1 Properties of dynamical invariants 123
7.3.2 Forced harmonic oscillator with time-dependent frequency 124
7.3.3 Inverse engineering method 125
7.4 Conclusion 133
8 DESIGN AND FABRICATION OF THE ATOM CHIP 134
9 CONCLUSION 142

i APPENDICES 144
A FUNDAMENTAL CONSTANTS AND RUBIDIUM-87 DATA 145
B TENSORS OF THE MANHATTAN TRAP 146
C ANGULAR MOMENTUM MATRIX ELEMENTS 148
D AXIAL-SYMMETRY OF THE MICROWAVE BEAM-SPLITTER USING π-TRANSITIONS 150
E CLASSICAL TRANSPORT DYNAMICS 152
F TRANSITION PROBABILITY 154
F.1 Case of $\omega(t) = \omega_0$ 154
F.2 Case of $F(t) = 0$ 155
F.3 Case of $F(t) \neq 0$ and $\omega(t) \neq \omega_0$ 156

F.4 Symmetry of the transition probability $P_{n,k}$ 157

II PUBLICATIONS & BIBLIOGRAPHY 158
PUBLICATIONS 159
BIBLIOGRAPHY 163

1

INTRODUCTION

Quantum mechanics is one of the pillars of contemporary science. Yet, it is also probably the strangest theory ever proposed. More than a century since the formulation of the earliest versions of quantum mechanics, there is still no agreement on the deeper meaning of its foundations [1]. One of the most distinguished contributors to quantum theory, Richard Feynman, stated that problem clearly in 1965 [2] :

It is safe to say that nobody understands quantum mechanics

Today more than ever, quantum mechanics continues to be a source of mystery and astonishment.

Over the few decades, experimental access to quantum phenomena have been boosted by the tremendous development of the laser technologies [3, 4, 5, 6]. Hence, several fundamental problems have been investigated experimentally such as the measurement mechanism [7], decoherence and the interpretations of quantum mechanics [8, 9]. The most famous example is the experimental realization of the Bose-Einstein condensate (BEC) for the first time in 1995 [10, 11], which has opened up a new field lying between atomic physics and condensed-matter physics. In addition to the study of these fundamental questions, an impressive progress toward potential applications of coherent matter-waves has been made, including the development of atomic clocks [12, 13, 14], magnetometers [15, 16, 17], and to a lesser extent quantum information [18, 19]. Moreover, atom interferometry experiments have demonstrated promising capabilities for inertial sensing applications [20].

Atom interferometry

Since the early experiments of Young and Michelson [21, 22], interferometry has considerably transformed the field of precise measurements. In particular, we note the development in the 1960s of corner-cube gravimeters using a Michelson interferometer where one of the mirrors in freefall, and which offer an acceleration sensitivity of about 10^{-8} g/$\sqrt{\text{Hz}}$ [23, 24]. For rotation measurements, gyroscopes based-on Sagnac effect reach a rotation sensitivity on the order of

10^{-4} deg/$\sqrt{\text{hr}}$ with commercial Fiber-Optic Gyroscopes (FOG) and Ring-Laser Gyroscopes (RLG) [25, 26, 27, 28].

For the purpose of increasing the scale factor of a gyroscope (which increases its sensitivity), atoms present a promising alternative to optical devices [29, 30]. Moreover, the low velocity-speed of cold atoms helps to increase the interrogation time for free-falling gravimeters. In 1991, Mark Kasevich and Steven Chu group has made the first matter-waves gravimeter [31, 32]. In the same year, the first observation of the Sagnac effect in an atomic interferometer was made [33]. About twenty years later, many groups around the world use atom interferometers to achieve high-precision inertial measurements including gravimeters [34, 35, 36, 37] (which recently have reached performances comparable to corner-cube gravimeters [38, 39]), gyroscopes [38, 39] and gradiometer [40].

In the field of metrology, several applications are under investigation : the Watt balance experiment to redefine international unit of mass [41, 42], the measurement of the fine structure constant α to test the quantum electrodynamics [43], and the measurement of the Newtonian constant of gravity G [44, 45].

Moreover, several proposals to test the theory of General Relativity have been made such as : the weak equivalence principle [46], the gravitational redshift [47, 48], the Lense-Thirring effect [49], and for long-term perspective, the detection of gravitational waves [50, 51].

Inertial sensing applications

The measurement of the gravity acceleration and its gradients provides information about the Earth's mass distribution and potentially allows the detection of mass anomalies. This interests the geophysicists for several potential applications including the monitoring of seismic activity [52], tsunami detection [24] and oil exploration [53].

Furthermore, providing an inertial measurement of the accelerations and rotations along three different axes, the equations of motion can be integrated in order to deduce the accurate position of a moving vehicle such as an airplane or a submarine. This technique, called inertial navigation, has the advantage to be completely independent of external positioning system such as the Global Positioning System (GPS) and makes the navigation system of a vehicle autonomous. The applications mentioned above in geophysics and navigation raise the issues of portability of cold-atom instruments.

Atom chips

In the last decade, tremendous efforts have been made towards the realization of compact cold-atom systems. The group of Mark Kasevitch has developed a portable cold-atom gravimeter, gradiometer and gyroscope [54, 55]. Since then several groups in Europe have developed

compact atom interferometers for future space missions [56, 57, 58] and transportable cold-atom gravimeters [59, 60].

On the other hand, other thriving research activities aim to reduce the size and the cost of cold atom experiments. The *atom chip* [61, 62, 63, 64] is a crucial element in the miniaturization of cold-atom systems. Magnetic traps can be created by currents on wires which are microfabricated on a chip surface, often called *atom chip*. The progress on microfabrication techniques allows the design of versatile traps and lattice geometries. Furthermore, atom chips provide a strong atom confinement (compared to macroscopic coils using equivalent currents) which simplifies considerably the evaporative cooling. The first realization of BEC on a chip paved the way towards the realization of micro-scale fully integrated inertial matter-wave devices. The collaboration QUANTUS has developed a compact and mobile atom-chip experiment, which has been used in a droptower to create BEC in microgravity [65].

Yet, to achieve such results, the way to go is still long and difficult, but the interest for miniaturization is real [66]. Several key components are commercially available today[1], even though on the microchip scale, many integrated optoelectronic elements are still missing including optical shutter, acousto-optic modulator, and ultra-stable laser.

A major objective of the current experiments using atom chips is the realization of an integrated atom interferometer. One of the main difficulties in achieving such an interferometer is to obtain a coherent beam-splitter. The first coherent splitting of trapped atoms on an atom chip was achieved in 2005 [67]. Using adiabatic radiofrequency potentials, a single trapped BEC was split into two separate clouds in double well. This method overcomes the disadvantages of the full magnetostatic interferometers on chip [63, 68, 69] : high sensitivity to magnetic field fluctuations and low confinement during the splitting. Recently, a full Mach-Zehnder sequence including the development of beam splitter, phase shifter and recombiner [70], has been demonstrated.

On the other hand, for the first time in 2009, a trapped-atom interferometer using internal-state labeling in a BEC was demonstrated [71]. Microwave state-selective potentials were used to allow the internal states to entangle with the motional states. This method simplifies considerably the interferometer readout and improves its accuracy. In fact, the readout can be performed in this case by measuring the number of atoms in each state without the need for high spatial resolution of the interference fringes. Moreover, in contrast to state-insensitive beam splitters, the splitting and recombination can be controlled precisely, and the many-body effects can be (relatively) reduced, by using internal-state labeling [71].

1 http://coldquanta.com/ and http://www.vescent.com/

Nevertheless, interferometers based-on trapped BECs are not yet able to compete with thermal free falling ones in term of precision measurements [72]. In particular, the interactions are harmful for interferometry, as they cause phase diffusion and collisional shifts which eventually lead to decoherence and a loss of sensitivity [73, 74, 75].

This thesis

Current atomic instruments, using atoms in free fall, are already on the verge of surpassing the performances of conventional optical instruments. However, their sensitivity is proportional to the height of the instrument, and current performances are obtained for falls in the range meter. To reduce the size of the device, we chose to use an atomic cloud trapped in the vicinity of a chip. The project Chips for Atomic Sensors (CATS), initiated by Thales in partnership with the Charles-Fabry Laboratory (Institut d'Optique), the Kastler-Brossel Laboratory (Ecole Normale Supérieure), the SYRTE (Observatoire de Paris) and the III-V Lab, aims to combine atom chip technology [76] and the atomic gravimeters to improve the compactness of the device. The objective is to design a gravimeter prototype, using a trapped atom interferometer, with metrological performances as good as possible and with a reduced size compared to the free-fall gravimeters.

For a gravitational measurement, the phase difference accumulated in a trapped interferometer is : $\Delta\phi = mg\Delta z T_R/\hbar$ with m is the atomic mass, $\hbar$ is the reduced Plank constant, Δz is the height difference between the two traps, and T_R is the effective time during which the two traps are separated. Assuming that we can reach the shot noise limit, the sensitivity of the gravimeter would be : $\delta g = \hbar/(m\Delta z T_R N) \approx 10^{-6} \times g/\sqrt{\text{Hz}}$ for an interrogation time $T_R = 50$ ms, a separation distance $\Delta z = 50$ μm, and with $N = 1000$ atoms of Rubidium 87.

Moreover, in order to reduce the effect of atomic interactions, we propose in this thesis to use a thermal (i.e. non-condensed) ensemble of cold atoms trapped on chip. This can be seen as the equivalent of using white light in optics to reduce nonlinear effects. Yet, in this case, the coherence time will particularly depend on the symmetry of the interferometer arms.

We propose an experimental design for a symmetrical beam splitter using microwave potentials. This scheme is similar to the experimental demonstration in [71], using internal-state labeling and microwave potentials. Yet, we propose to preform a bilateral splitting of the atoms using two CPWs carrying different microwave frequencies (instead of a unilateral splitting using a single CPW in [71]) in order to improve the symmetry of the interferometer arms.

The thesis is organized as follows :

- The second chapter : we give an introduction to atom chips. We present the clock states and discuss magnetic trapping potentials on chip.
- The third chapter : we introduce the microwave atom chip with an integrated coplanar waveguide. We describe the state-selective microwave potentials. Then, we discuss the constraints on the design of waveguides and the simulation of their magnetic field distribution.
- The fourth chapter : we propose an experimental scheme to realize a thermal trapped-atom interferometer on chip. In particular, we discuss the symmetry constraints of the trapping-potentials that should be satisfied in this case.
- The fifth chapter : we focus on the interferometer analysis in the case of an axial beam-splitter.
- The sixth chapter : we discuss the possibility of a transverse beam splitter, and we propose an adequate design of the static trap on chip.
- The seventh chapter : we study the interferometer contrast in the case of an adiabatic (axial) splitting, and then we investigate the possibility of a fast (i.e. non-adiabatic) beam-splitter.
- The eight chapter : we discuss the design and fabrication of the atom chip.

2

ATOM CHIP THEORY

Magnetic traps have been proposed first for cold neutrons [77], and have been realized experimentally in 1978 [78]. The advance of laser cooling techniques in the eighties has allowed the trapping of neutral atoms [79]. Since then, magnetic trapping became the standard tool to manipulate ultra-cold atoms and to reach the Bose-Einstein condensation.

The magnetic field of these trapping potentials has been produced first using several type of macroscopic coils carrying static currents such as : QUIC[1] trap [80], Cloverleaf trap [81], Baseball trap [82] and Standard Ioffe Pritchard trap [83]. Although the created magnetic potentials using this method have large trapping volumes, the tailorability of their field structure is limited. Moreover, the gradient length-scale is comparable to the distance of the atoms from the macroscopic coils. In particular, creating steep traps with high angular frequencies (few kHz) demands the use of high currents (about 100 A) and cumbersome heat-dissipation devices.

On the other hand, magnetic trapping potentials can be produced by a micro-fabricated structure, called *atom chip*. On such a structure, the distance range r between the current-carrying structure and the trap can be reduced from centimeters to microns. As the steepness of a trap is related to the magnetic gradient (which scales as $1/r^2$), it is beneficial to reduce as much as possible to the distance r. This allows the production of stronger gradients with lower currents and lower heating [84]. Moreover, the wires arrangement on chip allow a considerable flexibility, such that non-trivial geometries can be implemented [85]. For example, by using micro-fabricated multilayer wire structures [71], custom potential configurations can be produced.

In the following, the basics of trapping neutral ^{87}Rb atoms on chip are presented. An overview of the trapping techniques can be found in these review articles [62, 64]. Moreover, the theoretical constraints on the topology of the magnetic traps are presented, and then the design prospects of tailorable magnetic traps on chip are discussed. The properties of the so-called "clock states" are presented, in particular the possibility to reduce their sensitivity to the magnetic field fluctuations. Finally, the effect of atom-atom collisions is briefly introduced.

1 Quadrupole-Ioffe configuration

2.1 MAGNETIC TRAPPING OF NEUTRAL ATOMS

The magnetic trapping of neutral atoms is based on the interaction of the magnetic moment $\boldsymbol{\mu}$ of a particle with an external magnetic field $\mathbf{B}$. In a classical description, the potential energy of the particle is given by :

$$E(\mathbf{r}) = -\boldsymbol{\mu}.\mathbf{B}(\mathbf{r}) \tag{1}$$

and the magnetic moment $\boldsymbol{\mu}$ is precessing at the Larmor frequency $\omega_L(r) = E(\mathbf{r})/\hbar$. In a classical approach, $\boldsymbol{\mu}$ can have any orientation relative to $\mathbf{B}$ [86].

In quantum mechanics, the projection of $\boldsymbol{\mu}$ onto $\mathbf{B}$ has discrete values given by the quantum number m_F of the z-component of the total angular momentum operator $\mathbf{F} = \mathbf{I} + \mathbf{J}$, where $\mathbf{I}$ is the nuclear-spin operator and $\mathbf{J}$ is the electron momentum operator. Therefore, in the limit of low magnetic field value ($\mu_B B \ll E_{\text{hfs}}$), atoms in a magnetic field $\mathbf{B}(\mathbf{r})$ have a potential energy :

$$E_{F,m_F} = \mu_B g_F m_F B(\mathbf{r}) \tag{2}$$

with μ_B the Bohr magneton, E_{hfs} the energy of the transition at $B = 0$ and g_F the Landé g-factor. The expression of g_F is given by [87] :

$$\begin{aligned} g_F =& g_J \frac{F(F+1) - I(I+1) + J(J+1)}{2F(F+1)} \\ &+ g_I \frac{F(F+1) + I(I+1) - J(J+1)}{2F(F+1)} \end{aligned} \tag{3}$$

The latter term related to the nuclear moment $\mathbf{I}$ can be neglected because it has a contribution in the order of 10^{-3}.

Since the Maxwell equations do not allow the existence of a local maximum of the magnetic field in empty space [88], only the states with $m_F g_F > 0$ can be trapped by a static magnetic field. Such states are called "low-field seekers".

Majorana spin flips

An atom in a magnetic trap is subject to change in the field direction and magnitude over an oscillation period. The atom remains trapped only if its spin follows adiabatically the magnetic field direction. In other terms, the change of the magnetic field direction relative to the magnetic moment, given by the angle θ, has to be slow compared to the Larmor precession frequency $\omega_L(B)$:

$$\frac{\mathrm{d}\theta}{\mathrm{d}t} \ll \omega_L(B) = \frac{\mu_B |g_F| B}{\hbar} \tag{4}$$

If this adiabaticity condition is fulfilled, m_F is a constant of the atom motion. For $g_F m_F < 0$ the potential becomes repulsive, and for

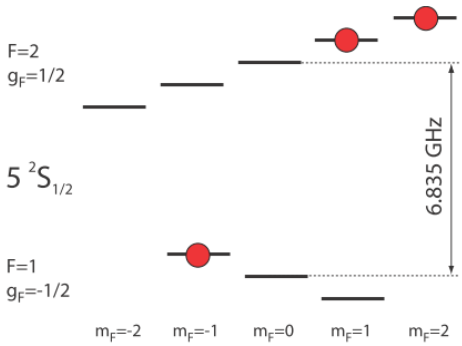

Figure 1: The structure of the hyperfine ground-state $5S_{1/2}$ of ^{87}Rb in a static magnetic field B. The magnetic sublevels $|F, m_F\rangle$ are shifted by a multiple of $\mu_B B/2$ due to the Zeeman effect. States that can be magnetically trapped are marked with a circle. Figure adapted From [69].

$g_F m_F = 0$ the atoms see no trapping potential (to the lowest order). Designing a magnetic trap with a region of vanishing field should be avoided. In these regions, transitions between m_F levels occur, taking the atom to states that cannot be trapped. The associated trap losses are known as Majorana spin flips [89].

Breit-Rabi formula

The potential energy, described above by the equation (2), indicates a linear variation of E_{F,m_F} as function of the magnetic field B. This is only an approximated model for weak fields. The analysis of the internal-state superposition in chapter 5 requires a higher precision on the description of the hyperfine energy levels by taking into account the coupling of the nuclear momentum $\mathbf{I}$. In this case, the energy levels are given by the Breit-Rabi formula [87] :

$$E_{F,m_F} = -\frac{E_{\text{hfs}}}{2(2I+1)} + \mu_B g_I m_F B \pm \frac{E_{\text{hfs}}}{2}\left(1 + \frac{4m_F\xi}{2I+1} + \xi^2\right)^{1/2} \tag{5}$$

where $\xi = \mu_B(g_J - g_I)B/E_{\text{hfs}}$, the $+(-)$ sign is for the $F = 2$ ($F = 1$), respectively.

The energies of these states in weak magnetic fields are plotted in Figure 1. The states $|1,-1\rangle$, $|2,1\rangle$ and $|2,2\rangle$ are magnetically trappable. The states with a magnetic moments $|m_F| = 1$ are particularly interesting, as they observe a similar energy shift in the magnetic field B. In Figure 2b, the energy difference $\Delta E = E_{2,1} - E_{1,-1} - E_{\text{hfs}}$ is shown as a function the magnetic field B. One can notice that the energy difference $\Delta E(B)$ have only a second-order dependence on the magnetic field around the spot $B_m \simeq 3.229$ G. Hence, the sensitivity of the transition frequency can be reduced by operating the magnetic field

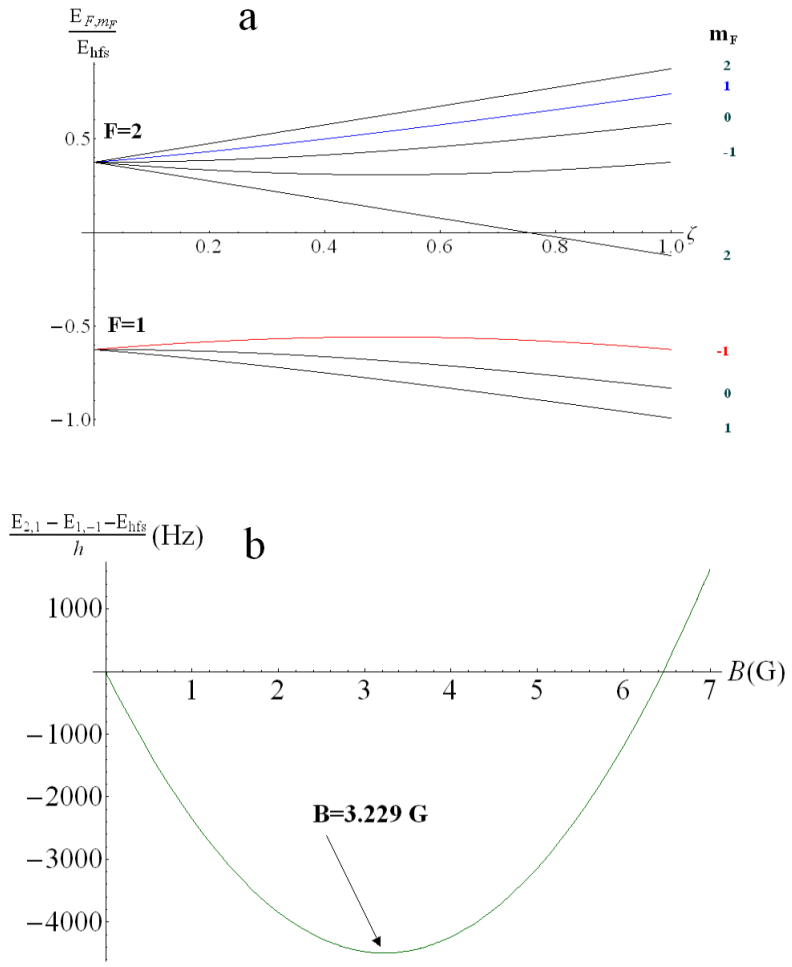

Figure 2: (a) Energy levels of the hyperfine states $|F, m_F\rangle$ of the ^{87}Rb computed using the Breit-Rabi formula. The clock states $|1,-1\rangle$ and $|2,1\rangle$ are colored in red and blue respectively. (b) Energy difference between the clock states as function of B (The offset energy E_{hfs} is subtracted). The *magic point* at $B = 3.229$ G is indicated.

around the latter spot B_m, usually called the "magic field" [90, 91]. The Zeeman frequency shift in the vicinity of the magic field B_m, can be written as :

$$\Delta E(B)/h = \Delta E(B_m)/h + \beta(B - B_m)^2 \tag{6}$$

where $\beta = 431.35957$ Hz/G^2 [92] and the frequency offset is given by $\Delta E(B_m)/h = -4.4974$ kHz with the energy reference defined at $B = 0$.

2.2 QUADRUPOLE AND IOFFE-PRITCHARD TRAPS

The magnetic traps usually used in cold-atom experiments can be classified into two types : Quadrupole traps, which have a zero mag-

netic field in the trap minimum, and Ioffe-Pritchard traps, which have a nonzero magnetic field at the trap center.

2.2.1 *Quadrupole traps*

In a quadrupole trap, the magnetic field vanishes at the trap minimum. The magnetic field around the minimum can be approximated by the following :

$$\mathbf{B} = \begin{pmatrix} B'_X X \\ B'_Y Y \\ B'_Z Z \end{pmatrix} \tag{7}$$

The following condition on the field gradients $\sum_i B'_i = 0$ should be fulfilled as required by the Maxwell's equations. The resulting trapping-potential is proportional to $\mathbf{B}$ modulus :

$$B = \sqrt{(B'_X X)^2 + \left(B'_Y Y\right)^2 + (B'_Z Z)^2} \tag{8}$$

Quadrupole traps suffer from trap loss due to Majorana spin flips near the trap center.

2.2.2 *Standard Ioffe Pritchard trap*

In order to avoid the Majorana losses[2], the trapping of cold atoms requires a field configuration with nonzero magnetic field at the trap center. Such a trap is called an Ioffe Pritchard trap (IP trap). The widely used *Standard*[3] Ioffe-Pritchard (SIP) trap [94], shown in Figure 3, fulfills this requirement by combining a 2D quadrupole field in the XY-plane with $B'_Y = -B'_Z = B'$, with a magnetic bottle field along the X-axis :

$$\mathbf{B} = B_0 \begin{pmatrix} 1 \\ 0 \\ 0 \end{pmatrix} + B' \begin{pmatrix} 0 \\ -Y \\ Z \end{pmatrix} + \frac{B''}{2} \begin{pmatrix} X^2 - (Y^2 + Z^2)/2 \\ -XY \\ -XZ \end{pmatrix} \tag{9}$$

The Taylor-expansion of the magnetic field modulus B, up to the second order, from the trap center is given by :

$$B(\mathbf{r}) = B_0 + \frac{B''}{2} X^2 + \frac{1}{2} \left(\frac{B'^2}{B_0} - \frac{B''}{2} \right) (Y^2 + Z^2) \tag{10}$$

2 In this case, the Majorana loss can be estimated [93], for $F = 1$ and $\omega_{\parallel} \ll \omega_{\perp}$, by : $\gamma_M = 4\pi\omega_{\perp} \exp(-2\omega_L/\omega_{\perp})$.

3 The word *Standard* is added here to avoid the ambiguity with the general Ioffe Pritchard case that will be discussed in section 2.2.4.

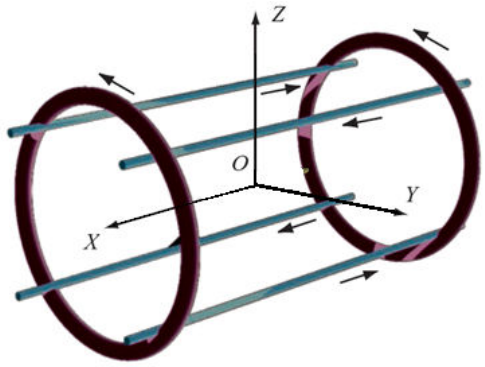

Figure 3: A Standard Ioffe-Pritchard (SIP) trap consists of a linear quadrupole created by four wires, and a 'bottle-field' along the X-axis (hexapole) created by two coils.

Therefore, one can deduce the trap angular frequencies :

$$\omega_X = \sqrt{\frac{\mu_B g_F m_F}{m} B''} \text{ and } \omega_\perp = \sqrt{\frac{\mu_B g_F m_F}{m}\left(\frac{B'^2}{B_0} - \frac{B''}{2}\right)} \tag{11}$$

along the longitudinal (ω_X) and transverse ($\omega_\perp$) direction, respectively.

As the gradient B' and the curvature B'' terms can be tuned independently (by controlling the currents in the wires and the coils, respectively), one can notice that the trap aspect ratio $\omega_X/\omega_\perp$ can be changed from prolate shape ($\omega_X \ll \omega_\perp$) to oblate shape ($\omega_X \gg \omega_\perp$). Moreover, the SIP trap has a distinguishable axial symmetry, which is not the case of (typical) chip-based traps.

2.2.3 *Magnetic chip traps*

The macroscopic traps such as Quadrupole and Standard Ioffe Pritchard traps described previously, are still commonly used in many cold-atom experiments [80, 95, 83]. On the other hand, the achievement of trapping potential using microwires on chip, proposed first in 1995 [96], has led to an active research field related to atom chips [76]. Several possibilities can be used to generate magnetic potentials on chip such as : current conducting wires [64], permanent magnets [97] and superconducting circuits [98]. Wire-based traps are widely used in the experiments due to the trap topological versatility, and the simplicity of fabrication process based-on lithography. In this section, we focus only on the wire-based traps. We describe the trapping principles using conducting wire structures on chip and we discuss some *typical* wire structures commonly used to create microtraps.

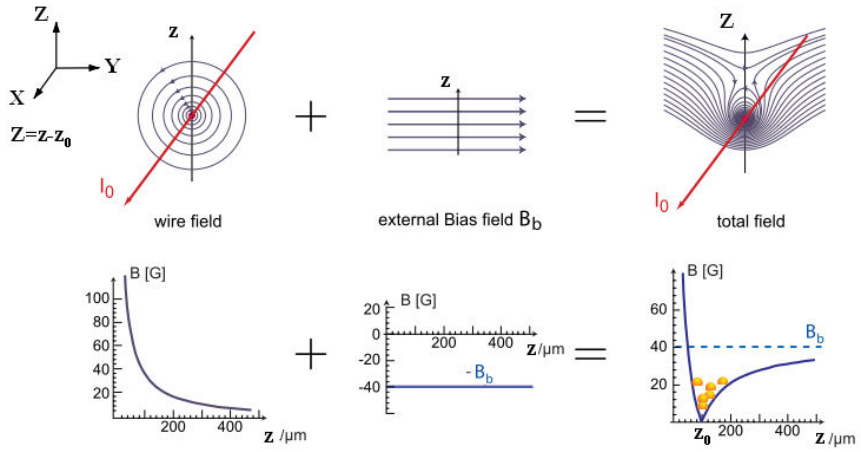

Figure 4: Wire guide trapping-potential. The trapping potential is a 2D quadrupole trap in the YZ-plane created by the superposition of the magnetic field from a single wire carrying a current I and an external homogeneous magnetic field B_b oriented perpendicular to the wire. In this case, atoms are trapped in YZ -plane, but are not trapped along the X-axis. The figure is adapted from [62].

Principle of wire traps

We consider a linear infinite wire, infinitely thin, carrying a current I. The latter creates a radial field as shown in Figure 4. This simple case can be used to derive few scaling laws of the magnetic field generated at a distance z_0 from the wire. For example, the field modulus, gradient and curvature are given respectively by :

$$B_w = \frac{\mu_0 I_0}{2\pi z_0}, B'_w = -\frac{\mu_0 I_0}{2\pi z_0^2} \text{ and } B''_w = \frac{\mu_0 I_0}{\pi z_0^3} \tag{12}$$

where μ_0 is the vacuum permeability. By adding external homogenous bias field B_b perpendicular to the current flow, the fields vanish at a distance $z_0 = \mu_0 I_0/(2\pi B_{b,Y})$ from the wire with a gradient B'. As shown in Figure 4, this wire structure allows a two dimensional confinement that can be used as an atom waveguide. From the scaling of B', one can notice that the trap becomes tighter as z_0 is decreased, for a given current I. The homogenous bias field is usually generated using external Helmholtz coils, but it can be created also with a suitable configuration of larger wires on the same chip [85]. Finally, 3D trapping fields can be generated by either bending the wire ends to form a Z-trap, or adding a second perpendicular wire to form a Dimple trap, as discussed in the following.

Dimple trap

By adding a second perpendicular wire, one can provide the required 3D Ioffe-Pritchard trap by closing the quadrupole guide in the longitudinal direction (see Figure 5(a-b)). In particular, the current I_1 along

the Y-axis together with a bias field $B_{b,X}$ along the X-axis allow longitudinal confinement and removes the field zero. For sufficiently small values of $|I_1/I_0|$, the transverse confinement is nearly unchanged and the dimple trap minimum is located at a distance $z_0 = \mu_0 I_0/(2\pi B_{b,Y})$ from the chip surface. The magnetic field in the trap minimum is given by :

$$B_0 \simeq |B_{b,X} + \mu_0 I_1/2\pi z_0| \tag{13}$$

The current I_1 provides also the curvature term :

$$B_d'' = \frac{\partial^2 B_x}{\partial x^2}\Big)_{x=0,z=z_0} = \mu_0 I_1/\pi z_0^3 \tag{14}$$

Hence, the trap angular frequencies can be approximated by :

$$\omega_X \simeq \sqrt{\frac{\mu_B g_F m_F}{m} B_d''} \text{ and } \omega_\perp \simeq \sqrt{\frac{\mu_B g_F m_F}{m} \frac{{B_w'}^2}{B_0}} \tag{15}$$

where the gradient term B_w' is given by equation (12).

As the wire-currents can be controlled independently, this configuration gives a versatile and simplified on chip Ioffe-Pritchard trap. In particular the trap position, frequencies and aspect ratio can be easily tuned [86].

One can show that the axial direction of the trap always lies in the XY-plane[4]. The azimuthal angle ψ_{IP} between the axial direction ($\boldsymbol{u}$) is given :

$$\tan \psi_{IP} = \frac{I_1}{I_0} \tag{16}$$

Further information about this configuration in the general case can be found in [86].

Ioffe Pritchard Z-trap

By bending the wire in the chip plane by 90°, the single wire 2D quadrupole trap can be transformed into a 3D trapping potential (see Figure 5c). In this case, the magnetic fields generated by the bent wires allow the axial confinement, while the central part of the wire enables the transverse confinement.

In atom chip experiments, this trapping technique is often used to create elongated IP traps (i.e. with a high aspect ratio). In this case, the length of the central wire is chosen such as : $L \gg 2z_0$ and the axial and transverse frequencies are approximately given by :

$$\omega_X \simeq \sqrt{6} t^2 \sqrt{\frac{\mu_B g_F m_F}{m} B_w''} \text{ and } \omega_\perp \simeq \sqrt{\frac{\mu_B g_F m_F}{m} \frac{B_w'^2}{B_0}} \tag{17}$$

with $t = z_0/2L$

4 For this purpose, one can use the gradient tensor (32) to determine the axial direction, as explained in section 2.2.4.

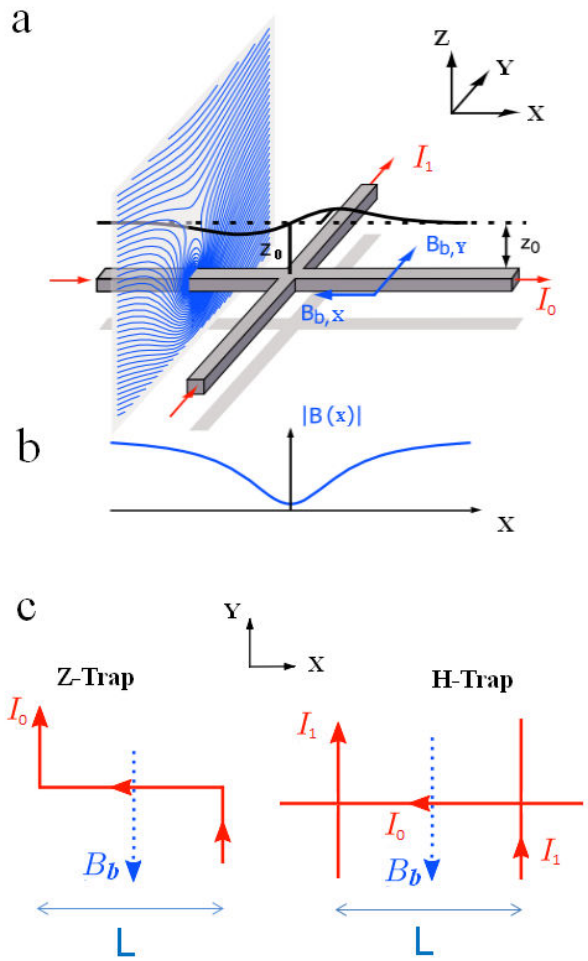

Figure 5: (a-b) Dimple trap formed by two perpendicular wires crossing and homogenous bias fields. The current I_0 together with the bias field $B_{b,Y}$ create a 2D quadrupole trap. The superposition of the magnetic field related to the current I_1 and the bias field $B_{b,X}$ provides the confinement along the X-axis. The Figure is adapted from [61]. (c) Sketches of the current and bias field configuration for Z and H shaped traps.

The gradient and curvature terms are given by equations (12) and $B_0 \approx B_{b,X}$.

The axial direction of the trap lies in the XY-plane. One can show that the azimuthal angle ψ_{IP} between the axial direction ($\mathcal{U}$) and the X-axis (i.e. the central wire direction) is given by [99] :

$$\tan\psi_{IP} = -\frac{\cos 2\theta}{\cos\theta(2+\cot^2\theta)} \text{ with } \tan\theta = t = z_0/2L \tag{18}$$

In particular, the axial direction is perfectly aligned with the central ($\psi_{IP} = 0$) if $t = 1$ (i.e. $\theta = \pi/4$).

Ioffe Pritchard H-trap

A similar confinement to the Z-trap can be created, by using in total three conductors to form an H-trap, instead of bending the wires (see Figure 5c). In this case, two independent wires ensure the axial confinement. This configuration is more flexible than the Z-trap since two currents can be used to adjust the trap parameters.

Similarly to the Z-wire configuration, an IP trap with a high aspect ratio can be created if the condition $t \ll 1$ is verified. In this case, one can show that the axial and radial frequencies are approximately given by :

$$\omega_X \simeq 2\sqrt{3}t^2\sqrt{\left|\frac{I_1}{I_0}\right|}\sqrt{\frac{\mu_B g_F m_F}{m}B''_H} \text{ and } \omega_\perp \simeq \sqrt{\frac{\mu_B g_F m_F}{m}\frac{{B'_H}^2}{B_0}} \tag{19}$$

$$\text{with } B_0 \approx B_{b,X}, B'_H = -\frac{\mu_0 I_0}{2\pi z_0^2} \text{ and } B''_H = \frac{\mu_0 I_1}{\pi z_0^3}$$

Moreover, the trap axis lies on the XY-plane, and the azimuthal angle is given by :

$$\tan\psi_{IP} = -2\frac{I_1}{I_0}\cos 2\theta \sin^2\theta \text{ with } \tan\theta = t = z_0/2L \tag{20}$$

In particular, $\psi_{IP} = 0$ if $t = 1$.

2.2.4 *Topological constraints on Ioffe Pritchard traps*

The ability to conceive non-trivial magnetic trapping potentials has been improved considerably by the development of atom chips [63]. Using the micro-fabrication techniques, a precise tailoring of the field sources is possible on a planar substrate, taking the form of either current-carrying wires or patterns in a permanent magnetic film [97, 100].

R. Gerritsma and R. J. C. Spreeuw [99] have investigated theoretically the properties of static magnetic traps controlled by externally applied homogenous fields. They have derived the required topological constraints that should be satisfied to design a custom Ioffe Pritchard trap. In this section, we summarize the principal results shown in this work.

The effective trapping potential, in equation (2), is proportional to the magnetic field modulus : $B(\mathbf{r})$. In the following, we are interested in the stationary points and the trapping frequencies of a trapping potential E_{F,m_F}. For this purpose, we can use $B^2(\mathbf{r})$ instead of E_{F,m_F} since a minimum or saddle point of B is also a minimum or saddle point of B^2. Stationary points of B^2 are defined by :

$$\partial B^2/\partial X_i = 0 \text{ for } i \in \{1,2,3\} \tag{21}$$

In order to determine the nature of a stationary point (i.e. a local minimum or a saddle point), at least the second derivatives of B^2 are required. Therefore, we expand $\mathbf{B}(\mathbf{r})$ up to the second order :

$$B_i = \sum_{j,k} \left(B_0 u_i + v_{ij} X_j + w_{ijk} X_j X_k \right) + \text{ (higher-order terms)} \quad (22)$$

where B_0 and u_i are the vector field value and direction at $X_i = 0$ (noted $\boldsymbol{\mathcal{U}}$), $v_{ij} = \partial B_i / \partial X_j$ is a tensor describing the field gradient (noted $\mathcal{V}$), and $w_{ijk} = \partial^2 B_i / \partial^2 X_j X_k$ is a curvature tensor (noted $\mathcal{W}$).

Moreover, we should consider the restriction imposed by Maxwell's equations for stationary fields in vacuum. From the conditions div $\mathbf{B} = 0$ and curl $\mathbf{B} = \mathbf{0}$ for stationary fields in free space, one can deduce that the gradient tensor $\mathcal{V}$ should be traceless and symmetric :

$$\sum_{i=1}^{3} v_{ii} = 0 \quad (23a)$$

$$v_{ij} = v_{ji} \text{ with } i \neq j \quad (23b)$$

This leaves 5 independent parameters for $\mathcal{V}$. Furthermore, the different partial tensors of the curvature tensor $\mathcal{W}$ must be also symmetric and traceless :

$$\sum_{i=1}^{3} w_{jii} = 0 \text{ for all } j \in \{1,2,3\} \quad (24a)$$

$$w_{ijk} = w_{ikj} = w_{kji} \quad (24b)$$

which leaves 7 independent parameters for $\mathcal{W}$.

In order to determine the stationary points, one can write the second-order Taylor-expansion of B^2 :

$$B^2 = \sum_{i,j,k} \left[B_0^2 u_i u_i + 2 u_i v_{ij} X_j + (u_i w_{ijk} + v_{ij} v_{ik}) X_j X_k \right] + \text{ (higher-order terms)} \quad (25)$$

Therefore, to have a stationary point in $X_i = 0$, the following condition should be verified :

$$\sum_{i=1}^{3} 2 u_i v_{ip} = 0 \text{ for all } p \in \{1,2,3\} \quad (26)$$

An Ioffe Pritchard (IP) trap has a nonzero field value in the minimum. In consequence, we must require that $\mathcal{V}$ has a (nonzero) eigenvector parallel to $\boldsymbol{\mathcal{U}}$ and its corresponding eigenvalue must be zero. In this thesis, we call this direction $\boldsymbol{\mathcal{U}}$ the IP trap axis. The latter conditions can be written :

$$\det \mathcal{V} = 0 \quad (27a)$$

$$\mathcal{V}.\boldsymbol{\mathcal{U}} = 0 \quad (27b)$$

If the previous condition is fulfilled, equation (25) can be simplified to :

$$B^2 = \sum_{i,j,k} \left(B_0^2 u_i u_i + g_{jk} X_j X_k \right) \tag{28}$$

where

$$g_{jk} = \partial^2 B^2 / \partial X_i \partial X_k = \sum_{i=1}^{3} \left(B_0 u_i w_{ijk} + v_{ij} v_{ik} \right) \tag{29}$$

defines the frequency tensor (noted $\mathcal{G}$) since the trapping eigenfrequencies in this potential are given by : $\omega_i = \sqrt{\mu_B g_F m_F G_i / m B_0}$ with G_i are the eigenvalues of $\mathcal{G}$. Hence, to verify the stationary point is a minimum, the eigenvalues G_i must be strictly positive.

It is worth noting that the sum of the squares of the trap eigenfrequencies is independent of the curvature $\mathcal{W}$ and depends only on the gradient $\mathcal{V}$ and the homogenous field B_0, because it can be shown, using equations (24) and (29), that :

$$\sum_i \omega_i^2 = \frac{\mu_B g_F m_F}{m B_0} \sum_{i,k} v_{ik} v_{ik} \tag{30}$$

In conclusion, the gradient tensor $\mathcal{V}$ has only 4 independent parameters, while the curvature tensor has at most 7 independent parameters, including 3 that can be used to tune the IP trap eigenfrequencies. Finally, for a given gradient tensor $\mathcal{V}$, only the modulus B_0 of the vector field in the trap minimum can be tuned, since its direction $\boldsymbol{\mathcal{U}}$ is determined by an eigenvector of the gradient tensor $\mathcal{V}$. Controlling B_0 is possible through the external bias fields that are given in this context by :

$$\mathbf{B_b} = B_0 \boldsymbol{\mathcal{U}} - \mathbf{B}_W(\mathbf{r}_0) \tag{31}$$

where $\mathbf{B}_W$ is the magnetic field created by the wires on chip.

2.2.5 *Custom design of an Ioffe Pritchard trap : Manhattan trap*

Magnetic microtraps offer a flexible platform to investigate diverse applications such as quantum simulation [101], quantum information processing [102] and atom interferometry [70, 71].

Schmied *et al.* developed a general procedure [85] for designing microtraps (and lattices) to achieve some desired properties and parameters, on the basis of patterned permanently magnetized films[5]. The algorithm for finding the optimal magnetization pattern satisfies

5 R. Schmied has developed a *Mathematica* package : *SurfacePattern*, for surface atom and ion traps. This package has been extensively used in this work to compute analytical expressions of magnetic fields.

the linear conditions (24) and (23) together with some additional linear conditions on the gradient or/and the curvature elements.

Here, we consider an alternative framework to design custom IP traps using an appropriate arrangement of current-carrying wires. In contrast to the algorithm of Schmied *et al.* that uses optimization methods, an exact resolution of any set of linear conditions in addition to Maxwell's equations is proposed.

In the following, we present some basic tools that can be used to design custom IP traps.

Star pattern

To create an IP trap centered at point $\mathbf{r_0} = \{x = 0, y = 0, z = h_0\}$, it is possible to use N wires intersecting at the chip origin $O = \{x = 0, y = 0, z = 0\}$, and we refer to it as the *star pattern*. The i-th wire (FL_i) has an orientation α_i relative to the x-axis, and carries a current I_i (see Figure 6a). The tensors $\mathcal{V}$, and $\mathcal{W}$ that characterize the trap are, respectively, a linear superposition of elementary tensors $\mathcal{V}_i$, $\mathcal{W}_i$ corresponding to the wire (FL_i). The latter elementary tensors are given by :

$$\mathcal{V}_i = \frac{\tilde{I}_i}{h_0^2} \begin{pmatrix} 0 & 0 & \sin\alpha_i \\ 0 & 0 & -\cos\alpha_i \\ \sin\alpha_i & -\cos\alpha_i & 0 \end{pmatrix} \tag{32}$$

$$\mathcal{W}_i = \frac{\tilde{I}_i}{h_0^3} \begin{pmatrix} W_1 \\ W_2 \\ W_3 \end{pmatrix} \tag{33a}$$

$$W_1 = 2 \begin{pmatrix} \sin^3\alpha_i & -\cos\alpha_i \sin^2\alpha_i & 0 \\ -\cos\alpha_i \sin^2\alpha_i & \cos^2\alpha_i \sin\alpha_i & 0 \\ 0 & 0 & -\sin\alpha_i \end{pmatrix} \tag{33b}$$

$$W_2 = 2 \begin{pmatrix} -\cos\alpha_i \sin^2\alpha_i & \cos^2\alpha_i \sin\alpha_i & 0 \\ \cos^2\alpha_i \sin\alpha_i & -\cos^3\alpha_i & 0 \\ 0 & 0 & \cos\alpha_i \end{pmatrix} \tag{33c}$$

$$W_3 = 2 \begin{pmatrix} 0 & 0 & -\sin\alpha_i \\ 0 & 0 & \cos\alpha_i \\ -\sin\alpha_i & \cos\alpha_i & 0 \end{pmatrix} \tag{33d}$$

where $\tilde{I}_i = (\mu_0/2\pi) \times I_i$. In the following, we will use the symbol ($\tilde{}$) to denote a multiplication of a current I by the constant : $\mu_0/2\pi$.

In this configuration, we can verify that the condition (27a), related to the existence of a stationary point at $\mathbf{r_0}$, is here verified systematically. This property is related to central symmetry (relative to O) of

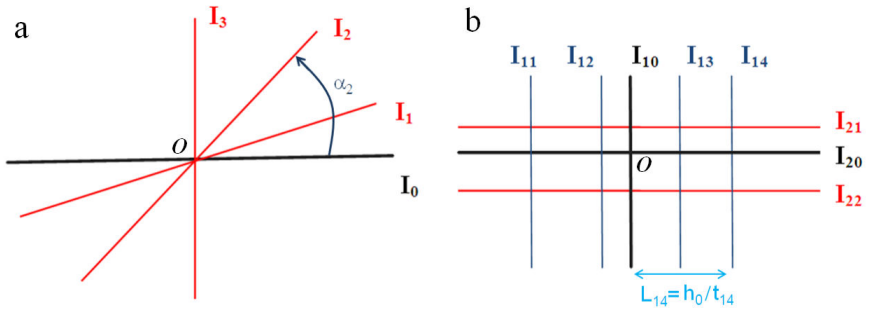

Figure 6: Custom design of Ioffe Pritchard traps. (a) Star pattern (b) Manhattan pattern, are a flexible wires architecture that allow the design of tailorable magnetic traps.

the wires (FL_j) and it remains valid using any elementary structure that has a central symmetry such a Z-shape wire for example.

One can use this method to engineer a custom IP trap by controlling the independent elements of the gradient and the curvature tensor. In principle, such a problem can be written as linear system of the currents $\tilde{I}_i$. The resolution of this system can be simplified if the number of wires N is chosen equal to the trap elements (v_{ij} and w_{ijk}) that we wish to control. Then, the IP trap frequencies (at least their positivity) should be controlled using the different angles α_i.

One can notice that the IP trap axis $: \boldsymbol{\mathcal{U}} \propto \sum_{i=1}^{N} \tilde{I}_i \{\cos\alpha_i, \sin\alpha_i, 0\}$ lies on the xy-plane, as it is the case for the typical microtraps discussed previously.

Despite its simplicity, this configuration can be used in practice only to control few elements as one can verify that the number of non-redundant elements[6] is only 4. Moreover, a particular care has to be taken to manage the high current density and the local heating at the origin O, especially if the number of wires $N \geq 3$.

Manhattan pattern

To create an IP trap at $\mathbf{r_0}$, it is also possible to use wires that do not pass through the origin O. However, in this case, the condition (27a) is not always verified contrary to the case of the *star* pattern. Here we introduce an alternative pattern, that we call *Manhattan*, using a set of perpendicular or parallel wires. In other words, N_1 wires are parallel to the x-axis and N_2 wires parallel to the y-axis (see Figure 6b). Each of the tensors $\mathcal{V}$, $\mathcal{W}$, that characterize the IP trap, is a linear superposition of elementary tensors $\mathcal{V}_{1,i}, \mathcal{V}_{2,i}$ and $\mathcal{W}_{1,i}, \mathcal{W}_{2,i}$, shown in Appendix B.

6 The non-redundant elements are : $v_{13}, v_{23}, w_{111}, w_{112}$.

One can impose additional conditions on the elements of the tensor $\mathcal{V}$ and $\mathcal{W}$ to design a custom IP trap. In this case, one can note that the tensor elements v_{ij} and w_{ijk} depend either on the currents $I_{1,i}$ or $I_{2,i}$ but never on both of them. Hence, controlling the trap parameters can be reduced to a simplified resolution of linear system of the currents, as explained previously. For example, one can control 4 elements[7] v_{ij} of the gradient tensor $\mathcal{V}$. Yet, in this case, one should pay attention to the resolution of the condition (27a), as it is not usually verified and may imply the resolution of a nonlinear equation.

Thereafter, one must ensure that the eigenvalues of the frequency tensor $\mathcal{G}$ are positive. This can be done using the reduced distances $t_{1i} = h_0/L_{1i}$ and $t_{2i} = h_0/L_{2i}$ of the wires or by controlling any currents that are not involved in the resolution of the previous linear system. Two practical resolutions (designs), will be discussed in section 6.2.4. In particular, we show that the number of required current-sources can be reduced to two, as it is often used to create a typical microtrap such as the Dimple trap. In the last step, one shall ensure that the designed IP trap has sufficient depth to capture laser-cooled atoms. This is the most difficult step as it is a non-local condition, and can only be verified retrospectively. In practice, in order to avoid the design of shallow traps, it is important to choose the elements of the tensor $\mathcal{V}$ such that the trap axis $\boldsymbol{\mathcal{U}}$ is almost parallel to the chip plane. Otherwise, the confinement would be weak or nonexistent [85].

Furthermore, one can analyze the evolution of the magnetic field zeros, with a simplified theory introduced by T.J. Davis [103] using complex numbers in order to investigate the 2D magnetic traps. In our case, the wires used to create the 2D quadrupole (i.e. transverse confinement) can be isolated, and the trap depth can be optimized using the remaining free parameters (h_0 and t_{1j} or t_{2j}) in order to eliminate or hold off the unwanted zeros from the local minimum.

Finally, it is important to note that the fabrication the Manhattan pattern requires[8] the use of a multilayer chip using an insulating layer [104]. If the reduced distances t_{1i} (or t_{2i}) are critical for the trap design, the corresponding wires $FL_{1,i}$ (or $FL_{2,i}$) should be placed in the lower layer, in order to avoid the uncertainty related to the planarity and the relative position of the upper layer. Yet, in some cases[9], the values of the reduced distances t_{1i} and t_{2i} are both critical for the IP trap. Thus, one should evaluate precisely the thickness d_T of the insulating layer (see Figure 17), and take it into account to set the wires $FL_{2,i}$ position on the second layer such as : $B_i = \{0, (h_0 - d_T)/t_{2i}, 0\}$. Furthermore, before starting the chip fabrication process, one may consider performing a full-simulation that takes account for the width of the

7 v_{11},v_{13},v_{22} and v_{23}
8 If $N_1 > 1$ and $N_2 > 1$
9 Such as the configuration $\mathcal{S}_1$ in section 6.2.4

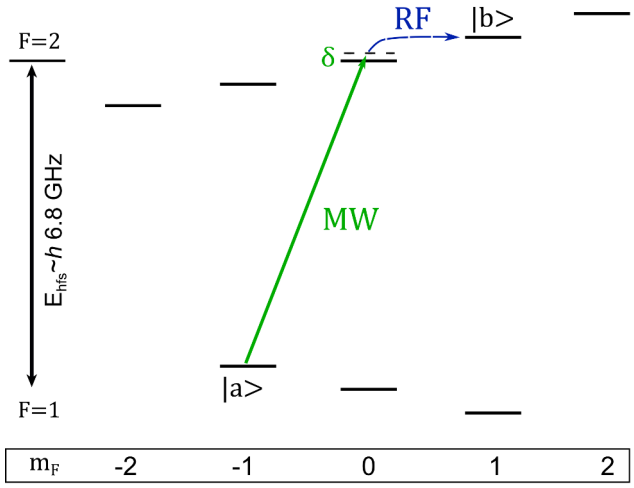

Figure 7: Coherent internal-state manipulation and generation of state-dependent microwave potentials. Hyperfine structure of the ^{87}Rb ground state in the static magnetic field of the microtrap. The clock states $|a\rangle$ and $|b\rangle$ are coherently coupled using a combination of microwave (MW) and radio-frequency (RF) fields ($\frac{\pi}{2}$-pulse).

wires in order to verify the stability of the conceived IP trap and its properties.

2.3 TWO-PHOTON TRANSITION

Coherent coupling between the clock states $|a\rangle$ and $|b\rangle$, shown in Figure 7, requires a two photon drive due to the selection rules of the angular momenta. This can be done using microwave at frequency ω_{mw}, blue detuned by Δ with respect to the transition $|1,-1\rangle \leftrightarrow |2,0\rangle$ and a radio-frequency ω_{rf} red detuned relative to the transition $|2,0\rangle \leftrightarrow |2,1\rangle$ such as : $\hbar(\omega_{mw}+\omega_{rf}) \approx E_{2,1} - E_{1,-1}$. If both single photon Rabi frequencies verify : $\Omega_{rf}, \Omega_{mw} \ll |\Delta|$, the population of the intermediate state $|2,0\rangle$ remains negligible and the three-level system behaves as a two-level system with an effective two photon Rabi frequency of [105] :

$$\Omega_{2P} = \frac{\Omega_{mw}\Omega_{rf}}{2\Delta} \tag{34}$$

2.4 COLLISIONAL SHIFT

Atomic collision has an essential role in explaining the properties of ultracold gases [106]. Interactions between trapped atoms ensure reaching the thermal equilibrium, which is necessary for the success of the evaporative cooling [107, 108]. However, once the atoms are cooled and trapped, the atomic density increase as the atoms are con-

fined in small volumes which leads to a change of the atomic energy and arises a particular difficulty for precision measurements.

A rigorous derivation of this effect can be done using the microscopic transport equation for the density matrix mapped onto a problem of precession of two coupled classical spins [109, 110, 111]. In this section, we introduce a simplified approach of the interaction effect as discussed in [90]. In a cloud of N atoms, the energy shift of one atom arises from the collisions with the other $N-1$ atoms. By neglecting collisions of more than two atoms, one atom immersed into a non-degenerate cloud of atoms experiences an energy shift of : $4\pi\hbar^2 an/m$, with n the atomic density and a the scattering length. For a two component gas, such as atoms in coherent superposition of the clock states $|a\rangle$ and $|b\rangle$, the energy shift is given by :

$$E_C^i = \frac{4\pi\hbar^2}{m}(n_i a_{ii} + n_j a_{ij}) \tag{35}$$

with $\{i,j\} = \{a,b\}$, and $i \neq j$. Therefore, the collisional frequency shift related to the transition between the clock states is given by :

$$\Delta E_C = E_C^b - E_C^a = \frac{2\hbar^2}{m} n \left[(a_{bb} - a_{aa}) + \frac{n_a - n_b}{n}(2a_{ab} - a_{aa} - a_{bb}) \right] \tag{36}$$

The ^{87}Rb atoms offers the great advantage of nearly equal scattering length with :

$$a_{aa} = 100.44 a_0 \tag{37a}$$
$$a_{bb} = 95.45 a_0 \tag{37b}$$
$$a_{ab} = 98.09 a_0 \tag{37c}$$

where $a_0 = 52.9 \times 10^{-12}$ m is the Bohr radius. The scattering lengths differ only by about 5%. Therefore, equation (36) leads to :

$$\Delta E_C = -\frac{2\hbar^2}{m} n a_0 (4.97 + 0.27 f) \tag{38}$$

with $f = (n_b - n_a)/n$ denotes the population imbalance between the clock states. It is important to note, that this shift is not uniform, because the atomic density is spatially inhomogeneous. Furthermore, using a pair of clock states trapped with a magnetic field set at the magic value ($B_0 = 3.23$ G), one can tune the magnetic field in order to balance, up to the second order, the spatial inhomogeneity due to the collisional shift. The compensation method is discussed in [112]. On the other hand, if the components of the gas are spatially separated (as it is the case, using a state-labelling beam splitter [71]), the interaction between different components are not possible. In this case, the collisional energy shift becomes :

$$\begin{aligned} \Delta E_C &= \frac{2\hbar^2}{m} n \left[(a_{bb} - a_{aa}) + \frac{n_b - n_a}{n}(a_{aa} + a_{bb}) \right] \\ &= \frac{2\hbar^2}{m} n a_0 (-4.97 + 195.91 f) \end{aligned} \tag{39}$$

In particular, the collisional energy shift can be reduced if the population unbalance f is about : $f_m \simeq 2.53\%$. Finally, the lifetime in the trap is limited by the inelastic and two body collisions which have been neglected in the previous model. A phenomenological analysis of these effects is given in [86].

3

MICROWAVE ATOM CHIP

Microwave radiation leads to an AC Zeeman shift of hyperfine states, which can be used to trap neutral atoms [113, 114]. In this case, the spontaneous emission is negligible which is a considerable advantage compared to optical potentials. However, in these pioneer references, an extremely high microwave power (on the order of megawatt) circulating inside a cavity were required and the field gradients were limited since the centimetric wavelength restricts the field focusing.

Furthermore, to make advantage of the clock states robustness discussed in section 2.1, the microwave is a suitable choice, for internal state-manipulation[1], because these states belong to different hyperfine levels (with $E_{\mathrm{hfs}}/h \simeq 6.8$ GHz).

Recently, a new technique to generate microwave potentials on chip using microwave near-fields has been demonstrated [71]. The microwave field is generated using a micrometer-sized transmission line, and so the near-field gradient has a weak dependence on the wavelength, and depends mainly on the transverse dimension of the transmission line. Hence, much higher gradients can be produced using only low microwave power ($100 - 500$ mW). Furthermore, this technique allows a flexible design and an accurate control of the potentials on the micrometer scale.

In a similar manner, radiofrequency potentials have been used to trap, cool and manipulate atoms on chip [67, 115]. For instance, several trapping topologies were proposed using radiofrequency dressing such as rings [116, 117] and lattices [118]. By comparison, microwave potentials are more selective since the different possible transitions can be isolated by tuning the microwave frequency [86]. State-dependent microwave potentials can be generated on chip [71], which paves the way to the study of various interesting effects including atom interferometry [119], spin squeezing [120], atom-surface interactions [121], collisions and entanglement [104, 122].

In this chapter, we introduce the theory of microwave dressed potentials. Then, we discuss the design constraints of the microwave guiding structures, in particular the coplanar waveguide (CPW).

1 By deriving the two-photon transition, cf. section 2.3

3.1 MICROWAVE DRESSED POTENTIALS

In this section, we introduce the dressed potentials using microwave fields, and we derive the dressed energies and states in the rotating wave approximation. A thorough theoretical derivation can be found in P. Treutlein's dissertation [104].

We consider the electronic ground state $5S_{1/2}$ of ^{87}Rb. The interaction of an atom with a static field $\mathbf{B}$ is described by the Breit-Rabi Hamiltonian [87] :

$$H_{BR} = (E_{\text{hfs}}/2)\mathbf{I}.\mathbf{J} + \mu_B(g_J\mathbf{J} + g_I\mathbf{I}).\mathbf{B} \tag{40}$$

The eigenenergies E_{F,m_F} and eigenstates $|F, m_F\rangle$ of this system are given in section 2.1.

We are also interested in the description of an atom in presence of both static field $\mathbf{B}$ and magnetic field $\mathbf{B_{mw}}$:

$$\mathbf{B}_{mw}(t) = B_{mw}(\boldsymbol{\epsilon} e^{-i\omega_{mw}t} + \boldsymbol{\epsilon}^\star e^{i\omega_{mw}t}) \tag{41}$$

$\boldsymbol{\epsilon}$ is a unit polarization vector and ω_{mw} is the microwave frequency. The first term of equation (40) describes the hyperfine coupling between the total electron spin $\mathbf{J}$ and the nuclear spin $\mathbf{I}$. The second term depicts the coupling of the static field to $\mathbf{I}$ and $\mathbf{J}$. The Hamiltonian that describes the coupled atom-field system is :

$$H = H_{BR} + H_{mw} \tag{42a}$$

$$H_{mw} = \mu_B(g_J\mathbf{J} + g_I\mathbf{I}).\hat{\mathbf{B}}_{mw} + \hbar\omega_{mw}(a^\dagger a + 1/2) \tag{42b}$$

with $\hat{\mathbf{B}}_{mw} = 2\sqrt{\hbar\omega_{mw}\mu_0/2V}(\boldsymbol{\epsilon} a + \boldsymbol{\epsilon}^\star a^\dagger)$ is the quantized microwave field operator, and $a^\dagger$ (a) is the creation (annihilation) operator in a quantization volume V. Due to the high number of photons, the microwave field can be described by a classical field. Yet, the quantized field gives a deeper understanding of the dressed state picture [123].

H_{mw} describes the interaction with the microwave field. The first term of equation (40) indicates the coupling of the atom to the microwave field and the second term describes the quantized microwave field. Moreover, one can write H in the rotating frame that moves around the quantization axis $\mathcal{Z}$ with the angular frequency ω_{mw} using the rotation operator : $\exp(i\omega_{mw}tF_{\mathcal{Z}})$, where the $\mathcal{Z}$-axis is given by the local direction of $\mathbf{B}$ and $F_{\mathcal{Z}}$ is the projection of the total magnetic moment $\mathbf{F}$ along the $\mathcal{Z}$-axis [84]. Furthermore, if the conditions : $\mu_B B, \mu_B B_{mw}, \hbar\Delta_{\text{hfs}} \ll \hbar\omega_{mw}$ with $\Delta_{\text{hfs}} = \omega_{mw} - \omega_{\text{hfs}}$ are fulfilled, we can make the rotating wave approximation (RWA).

In the classical picture[2], the RWA consists in neglecting the oscillating terms in the rotating frame, and considering only the constant terms [84].

2 An interpretation of the RWA in the dressed-state picture can be found in [86].

With these approximations, we can write H in the bare basis $|F, m_F\rangle$ such as :

$$\begin{aligned} H = &\sum_{m_2} \left(-\frac{1}{2}\hbar\Delta_{\text{hfs}} + E_{2,m_2} - E_{\text{hfs}} \right) |2, m_2\rangle\langle 2, m_2| \\ &+ \sum_{m_1} \left(\frac{1}{2}\hbar\Delta_{\text{hfs}} - E_{1,m_1} \right) |1, m_1\rangle\langle 1, m_1| \\ &+ \sum_{m_1,m_2} \left[\frac{1}{2}\hbar\Omega_{m_1}^{m_2} |2, m_2\rangle\langle 1, m_1| + c.c. \right] \end{aligned} \tag{43}$$

where E_{F,m_F} is the Breit-Rabi energy given by equation (5) and $\Omega_{m_1}^{m_2}$ is the Rabi frequency that couples between the transition $|1, m_1\rangle \leftrightarrow |2, m_2\rangle$ such that :

$$\Omega_{m_1}^{m_2} = \frac{\mu_B}{\hbar} B_{mw} \langle 2, m_2 | \boldsymbol{\epsilon}. (g_J \mathbf{J} + g_I \mathbf{I}) | 1, m_1 \rangle \tag{44}$$

Approximations

Furthermore, we can neglect the coupling of $\mathbf{I}$ to the magnetic fields because $|g_I/g_J| \ll 1$ and consider the static Zeeman effect in a perturbative manner (as we have supposed that $\mu_B B \ll \hbar\omega_{\text{hfs}}$). Hence, the bare energy E_{F,m_F} to the first order in B is given by :

$$E_{F,m_F} = \delta_{F,2} E_{\text{hfs}} + m_F g_F \mu_B B \tag{45}$$

where $\delta_{i,j}$ is the Kronecker delta and $g_F \simeq 1/2$. In addition, the expression of the coupling Rabi-frequency $\Omega_{m_1}^{m_2}$ can be written :

$$\Omega_{m_1}^{m_2} \simeq \frac{g_J \mu_B}{\hbar} B_{mw} \langle 2, m_2 | \boldsymbol{\epsilon}. \mathbf{J} | 1, m_1 \rangle \tag{46}$$

with $g_J \simeq 2$.

The first two terms of equation (43) describe the bare states which are identical to the eigenstates $|F, m_F\rangle$ (with an additional energy shift). The last term depicts the coupling of the atom to the field. The angular momentum matrix elements $\langle 2, m_2 | \boldsymbol{\epsilon}. \mathbf{J} | 1, m_1 \rangle$, where $\boldsymbol{\epsilon}$ is a the unit polarization vector of $\mathbf{B}_{mw}$, can be calculated using the Clebsch-Gordan coefficients (see Appendix C).

Dressed states

The full Hamiltonian H can be diagonalized numerically, in order to obtain the eigenstates $|K\rangle$, often called the dressed states. Figure 8 shows the energies $E(K)$ of the dressed states as a function of the microwave detuning Δ_{hfs} for a microwave field with equally strong polarization components. The dressed states $|K\rangle$ can be written as a linear superposition of the bare states $|F, m_F\rangle$. For a given detuning Δ_{hfs}, the color depicts the dominant bare state $|F, m_F\rangle$ in each dressed

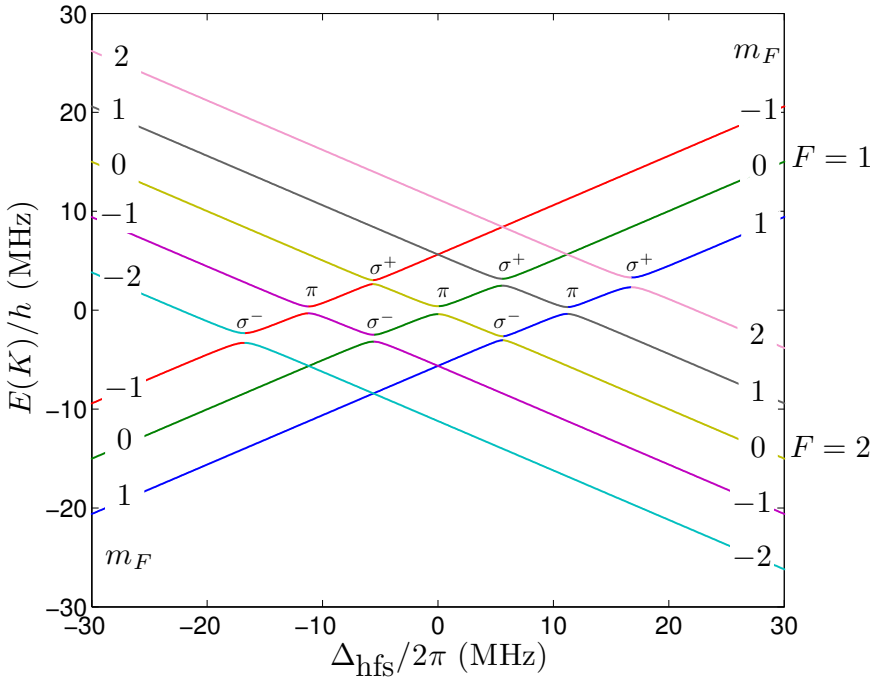

Figure 8: Energy levels of the dressed states $|K\rangle$ as function of the detuning $\Delta_{\rm hfs}$, for $B = 8$ G, $B_{mw} = 1$ G, and $\boldsymbol{\epsilon} = \frac{1}{\sqrt{3}}\{1, 1, 1\}$. Colors indicate the dominant bare state $|F, m_F\rangle$ in the dressed state $|K\rangle$. This Figure shows an agreement with the simulation results discussed in [86].

state $|K\rangle$. The bare states $|F, m_F\rangle$ and the dressed state $|K\rangle$ are approximately identical for high and large detuning $\Delta_{\rm hfs}$ values.

Furthermore, one can define the detuning :

$$\Delta_{m_1}^{m_2} = \Delta_{\rm hfs} - (m_2 + m_1)\mu_B B/2\hbar \tag{47}$$

An anticrossing between the bare states emerges if the detuning $\Delta_{m_1}^{m_2}$ vanishes but the corresponding $\Omega_{m_1}^{m_2}$ is non-vanishing. In the vicinity of an anticrossing, the dressed eigenstates are mainly a superposition of the anticrossing states. Therefore, near an anti-crossing, the energy difference between the dressed eigenstates can be given approximately by a two-level system [124, 125], and so it can be written as [86] :

$$E^{|+\rangle} - E^{|-\rangle} = \frac{\hbar}{2}\sqrt{|\Omega_{m_1}^{m_2}|^2 + |\Delta_{m_1}^{m_2}|^2} \tag{48}$$

where $|+\rangle(|-\rangle)$ denotes to the upper (lower) state.

In the case of two-level transition and supposing that an atom is initially prepared in the ground state $|g\rangle \equiv |1, m_1\rangle$ with a far detuned microwave such that $\Delta_{m_1}^{m_2}(t = 0) = \Delta_0 > 0$, one can completely transfer the system to the excited state $|e\rangle \equiv |2, m_2\rangle$, by tuning slowly the

microwave frequency over the resonance. This technique is called *adiabatic passage* and the adiabaticity criteria is given by [67, 123, 126] :

$$\frac{1}{2}|\dot{\Omega}_{m_1}^{m_2}\Delta_{m_1}^{m_2} - \Omega_{m_1}^{m_2}\dot{\Delta}_{m_1}^{m_2}| \ll \left[|\Omega_{m_1}^{m_2}|^2 + |\Delta_{m_1}^{m_2}|^2\right]^{3/2} \tag{49}$$

where the dot indicates the derivative with respect to time.

If the previous condition is verified, atoms initially prepared in the state $|g\rangle$ are transformed adiabatically into the dressed state $|+\rangle$, and observe the following dressed potential [124, 127] :

$$E^{|+\rangle} = \frac{E^{|g\rangle} + E^{|e\rangle}}{2} + \frac{\hbar}{2}\sqrt{|\Omega_{m_1}^{m_2}|^2 + |\Delta_{m_1}^{m_2}|^2} \tag{50}$$

where $E^{|g\rangle}(E^{|e\rangle})$ is the energy of the uncoupled level $|g\rangle$ ($|e\rangle$). The energy shift due to the microwave contribution can be defined as :

$$\begin{aligned} V_{mw}^{|+\rangle} &= E^{|+\rangle} - E^{|g\rangle} \\ &= \frac{\hbar}{2}\left[\sqrt{|\Omega_{m_1}^{m_2}|^2 + |\Delta_{m_1}^{m_2}|^2} - \Delta_{m_1}^{m_2}\right] + \frac{\hbar\omega_{mw}}{2} \end{aligned} \tag{51}$$

because : $\Delta_{m_1}^{m_2} = \omega_{mw} - (E^{|e\rangle} - E^{|g\rangle})/\hbar$.

In a similar manner, if the atoms are initially prepared in the state $|g\rangle$ and with $\Delta_0 = \Delta_{m_1}^{m_2}(t=0) < 0$, they are transformed adiabatically into the dressed state $|-\rangle$. In this case, one can deduce that the microwave shift is given by :

$$\begin{aligned} V_{mw}^{|-\rangle} &= E^{|-\rangle} - E^{|g\rangle} \\ &= \frac{\hbar}{2}\left[-\sqrt{|\Omega_{m_1}^{m_2}|^2 + |\Delta_{m_1}^{m_2}|^2} - \Delta_{m_1}^{m_2}\right] + \frac{\hbar\omega_{mw}}{2} \end{aligned} \tag{52}$$

In the previous equations of the microwave shifts V_{mw}, the term $\hbar\omega_{mw}/2$ is a constant energy shift. This term will be omitted in the following.

The transformation into the upper ($|+\rangle$) or lower ($|-\rangle$) dressed state depends on the sign of the initial detuning $\Delta_0 = \Delta_{m_1}^{m_2}(t=0)$, and so the microwave energy shift for an atom initially in $|g\rangle$ can be written as :

$$V_{mw}^{|g\rangle} = \frac{\hbar}{2}\left[\text{sign}(\Delta_0)\sqrt{|\Omega_{m_1}^{m_2}|^2 + |\Delta_{m_1}^{m_2}|^2} - \Delta_{m_1}^{m_2}\right] \tag{53}$$

The same approach can be used to derive the microwave energy shift for an atom initially in $|e\rangle$:

$$V_{mw}^{|e\rangle} = -\frac{\hbar}{2}\left[\text{sign}(\Delta_0)\sqrt{|\Omega_{m_1}^{m_2}|^2 + |\Delta_{m_1}^{m_2}|^2} - \Delta_{m_1}^{m_2}\right] \tag{54}$$

In the case of two-level transition, the system Hamiltonian can be simplified to [124, 127] :

$$H_{eg} = \frac{\hbar}{2}\begin{pmatrix} \Delta_{m_1}^{m_2} & \Omega_{m_1}^{m_2} \\ \Omega_{m_1}^{m_2} & -\Delta_{m_1}^{m_2} \end{pmatrix} + \frac{E^{|g\rangle} + E^{|e\rangle}}{2} \tag{55}$$

Thus, the dressed states (i.e. eigenstates of the system : {atom + photons}) can be written :

$$|+\rangle = \cos(\theta)|g\rangle + \sin(\theta)|e\rangle \tag{56a}$$
$$|-\rangle = \sin(\theta)|g\rangle - \cos(\theta)|e\rangle \tag{56b}$$

where θ is defined by :

$$\cos(2\theta) = \frac{\Delta_{m_1}^{m_2}}{\sqrt{|\Delta_{m_1}^{m_2}|^2 + |\Omega_{m_1}^{m_2}|^2}}\ ,\ \sin(2\theta) = \frac{\Omega_{m_1}^{m_2}}{\sqrt{|\Delta_{m_1}^{m_2}|^2 + |\Omega_{m_1}^{m_2}|^2}} \tag{57}$$

Atoms initially prepared in the state $|g\rangle$ with $\Delta_0 > 0$ are transformed adiabatically into the dressed state $|+\rangle$, which depends also on the state $|e\rangle$. The weight of the bare states, $|e\rangle$ relative to $|g\rangle$, in the dressed state is : $\mathcal{R}_{e/g} = \tan\theta$. In similar manner, atoms initially prepared in the state $|g\rangle$ with $\Delta_0 < 0$ are transformed into the dressed state $|-\rangle$, and the weight of the bare states, $|e\rangle$ relative to $|g\rangle$, in this dressed state is : $\mathcal{R}_{e/g} = -\cot\theta$. In both cases, assuming that the detuning $\Delta_{m_1}^{m_2}$ does not change its sign (i.e. $\Delta_{m_1}^{m_2}/\Delta_0 > 0$), one can show that :

$$|\mathcal{R}_{e/g}| = \left(-1 + \sqrt{1 + (\Omega_{m_1}^{m_2}/\Delta_{m_1}^{m_2})^2}\right) / (|\Omega_{m_1}^{m_2}|/|\Delta_{m_1}^{m_2}|) \tag{58}$$

Similar expression of the weight $|\mathcal{R}_{g/e}|$ can be derived for atoms initially prepared in the state $|e\rangle$.

Finally, we show in Figures 9 the energy levels $|K\rangle$ as a function of B_{mw} for the simulation parameters that will be used in the chapters 5 and 6, respectively. In particular, one can notice that the energy shift related to the state $|1,-1\rangle$ is much larger than the shift of the state $|2,1\rangle$ for low values of B_{mw}, because the latter state is off-resonance with the chosen parameters.

Far detuned microwave

In the case of a far-detuned microwave, the dressed energies $E(K)$ can be treated in a perturbative manner if the following condition is fulfilled :

$$|\Omega_{m_1}^{m_2}|^2 \ll |\Delta_{m_1}^{m_2}|^2 \tag{59}$$

The dressed states $|K\rangle$ are approximately identical to the bare states $|F, m_F\rangle$, and the admixture of the remaining states is on the order of $|\Omega_{m_1}^{m_2}/2\Delta_{m_1}^{m_2}|$. In this regime, the energy of an atom in the dressed state $|K\rangle \approx |F, m_F\rangle$ is given by :

$$\text{For the sublevels of } F = 1 : V_{mw}^{|1,m_1\rangle} = \frac{\hbar}{4}\sum_{m_1}\frac{|\Omega_{m_1}^{m_2}|^2}{\Delta_{m_1}^{m_2}} \tag{60a}$$

$$\text{For the sublevels of } F = 2 : V_{mw}^{|2,m_2\rangle} = -\frac{\hbar}{4}\sum_{m_2}\frac{|\Omega_{m_1}^{m_2}|^2}{\Delta_{m_1}^{m_2}} \tag{60b}$$

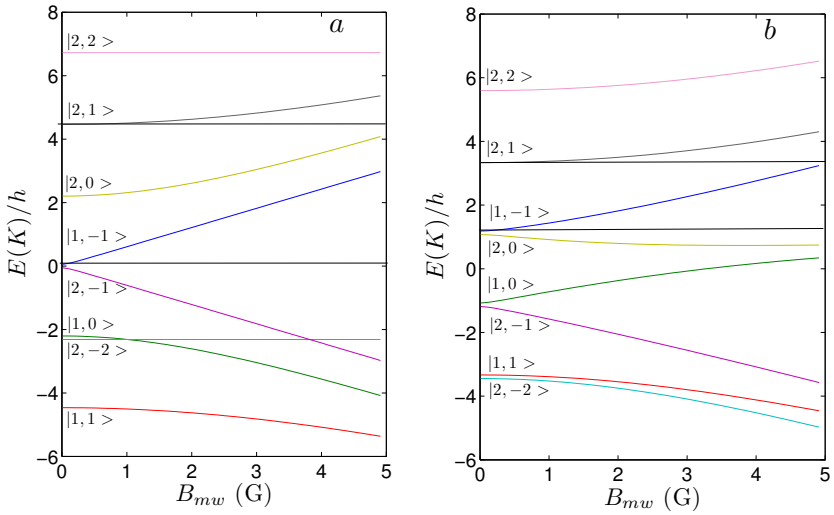

Figure 9: The energy levels $E(K)$ as function of B_{mw} for $B = 3.23$ G. (a) The frequency and the direction of the microwave field are chosen in order to couple the states $|1,-1\rangle$ and $|2,-1\rangle$ (π-transition) with $\boldsymbol{\epsilon} = \{0,0,1\}$ and $\Delta^1_{-1} = 0.05 \times \omega_L(B)$. (b) The frequency and the direction of the microwave field are chosen in order to couple the states $|1,-1\rangle$ and $|2,0\rangle$ (σ^+-transition) with $\boldsymbol{\epsilon} = \frac{1}{\sqrt{2}}\{1,1,0\}$ and $\Delta^0_{-1} = 0.05 \times \omega_L(B)$.

In the limit of large detuning, the microwave energy shift of $|F, m_F\rangle$ can be derived by considering all the possible transitions two-by-two. We will discuss, in section 5.2, how this approach can be extended to the general case (even if the condition (59) is not valid) by using equations (53) and (54).

3.2 MICROWAVE CHIP DESIGN

Microwave transmission lines are today increasingly widespread and used in several microwave devices including hybrid circuits, integrated circuits and antennas. They are partly responsible for the expansion of the microwave systems oriented to the mass market, such as GSM, GPS, and satellite television, in particular because of their compactness and their low fabrication cost. In modern microwave integrated circuits, the coplanar waveguide (CPW) is used as an element of transmission lines. The CPW was introduced first by C.P Wen [128] in 1969. However, the coplanar lines attracted high attention only in the 1990's with the push to high frequencies and monolithic technology and have experienced a growing demand since then due to their appealing properties [129, 130]. The microwave magnetic fields created in the near-field by the microwave currents have a similar length-scale dependence as the magnetic fields created by static currents [131]. This allows the realization of higher microwave gradients compared to the far-field gradients where the length scale is on the order of the wavelength ($\lambda_{mw} \approx 4.4$ cm in the vacuum).

The integration of a coplanar waveguide to an atom chip was proposed in [104] and experimentally demonstrated in [71]. In contrast to the historical interest to CPWs as transmission lines (in particular to their (low) propagation losses), we are more interested in the field distributions in the vicinity of the waveguide wires. The knowledge of their characteristic impedance is also important to avoid undesirable reflections.

In this section, we introduce some theoretical aspects of the CPWs including propagation, characteristic impedance and near-field distributions.

3.2.1 *Coplanar waveguide theory*

The coplanar waveguide consists ideally of a central conductor and two ground planes deposited on the same dielectric substrate, as shown in Figure 10a [128]. In practice, the CPW grounds usually have a finite width and the substrate has a finite thickness h, as shown in Figure 11(b-c).

The CPW can be seen as a multi-line guide with three wires : it has then two propagation modes [129] :

- the coplanar waveguide mode, a quasi-TEM mode often called the even mode, where the fields in the two slots are 180° out of phase as shown in Figure 10b.
- the slotline mode, a non-TEM mode often called the odd mode, where the fields are in phase as shown in Figure 10b.

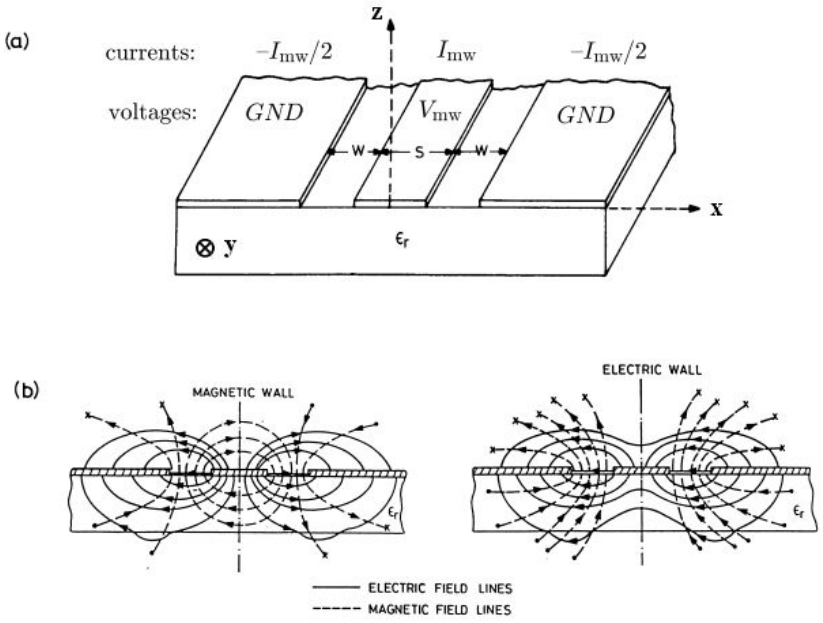

Figure 10: A schematic view of a coplanar waveguide (b) The field configurations of the coplanar mode (left) and the slotline mode (right). Figure adapted from [129].

In microwave circuits, the CPW mode is preferred due to its propagation and radiation properties [131]. The CPW mode can be excited by pulling both grounds to the same potential. However, parasitic effects and discontinuities in the CPW geometry can couple power from the CPW mode to the slotline mode, leading to unbalanced distribution of the microwave currents [17].

Full-wave analysis

The electric and magnetic field distributions **E** and **B** around the CPW can be computed using full-wave analysis, which also provides information regarding the frequency dependence of the phase velocity and the characteristic impedance. Several techniques has been developed including the spectral domain method [132, 133, 134, 135, 136], mode-matching technique [137], the integral equation approach [138], the method of moments [139], and the finite difference time domain technique [140]. These techniques are particularly important at higher frequencies ($\omega_{mw} > 10$ GHz).

Quasi-TEM fields

For the microwave field, only quasi-TEM mode can propagate since the transverse size of the CPW, $(S + 2W)$ in Figure 10a,is very small compared to the microwave length scale λ_{mw} [141]. In contrast to the (pure) transverse electromagnetic (TEM) wave, quasi-TEM waves

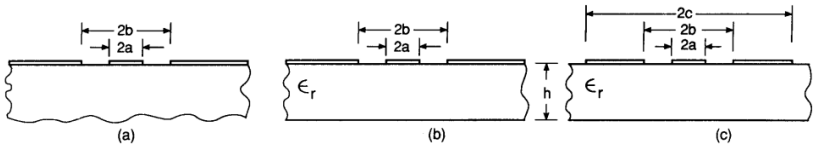

Figure 11: Different types of coplanar waveguides : (a) ideal CPW, (b) CPW with finite substrate thickness, and (c) CPW with finite ground planes and finite substrate thickness. Figure adapted from [129].

have small longitudinal components because the waves propagate within two different mediums (air and dielectric). Hence, the electromagnetic fields propagating on the transmission line are of the form :

$$\mathbf{E}(x,y,z,t) = \mathrm{Re}\left[\mathbf{E}(x,z)\exp(i\omega_{mw}t - \gamma y)\right] \tag{61a}$$

$$\mathbf{B}(x,y,z,t) = \mathrm{Re}\left[\mathbf{B}(x,z)\exp(i\omega_{mw}t - \gamma y)\right] \tag{61b}$$

where γ is the complex propagation constant.

If the quasi-TEM approximation is verified ($S + 2W \ll \lambda_{mw}$), the electromagnetic fields can be computed using a 2D quasi-static simulation that takes into account the effect of eddy currents and conductor loss, as discussed in [142, 143, 86]. This method considers also the skin effect[3] which changes the current-density distribution in the CPWs wires. This simulation can be performed using a finite element method with one of the following software programs : *Maxwell SV*[4] or *FEMM*[5].

Equivalent circuit model

The equivalent circuit shown in Figure 12 can be used to describe an infinitesimal piece of the transmission line. The circuit model includes the capacitance between the conductors C, the inductance L, the series resistance R of the conductors and the shunt resistance of the dielectric G. These parameters can be deduced using the fields $\mathbf{E}(x,z)$ and $\mathbf{B}(x,z)$ computed using a quasi-static simulation [86, 141]. Form this model, the propagation of the line can be deduced :

$$\gamma = \sqrt{(R + i\omega_{mw}L)(G + i\omega_{mw}C)},\ \mathrm{Re}[\gamma] > 0 \tag{62a}$$

$$Z_0 = \alpha + i\beta = \sqrt{\frac{R + i\omega_{mw}L}{G + i\omega_{mw}C}},\ \alpha > 0 \tag{62b}$$

where $Z_0 = V_{mw}/I_{mw}$ is the characteristic impedance and its argument indicates the phase shift between the electric and magnetic

3 Using a gold wires with the conductivity $\sigma_{Au} \simeq 4 \times 10^7$ S/m and a microwave frequency $\omega_{mw} = 2\pi \times 6.8$ GHz the skin depth $\delta_s = \sqrt{2/(\omega_{mw}\mu_0\sigma_{Au})} \simeq 0.9$ μm, is similar to the wire dimensions and so its effect has to be taken into account.

4 Now: Ansys Maxwell

5 http://www.femm.info/wiki/HomePage

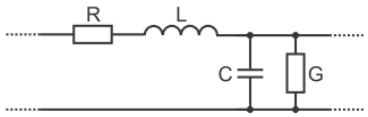

Figure 12: The equivalent circuit of a coplanar waveguide [142].

field[6]. An abrupt variation of Z_0 along the transmission line leads to undesirable reflection and should be avoided in the design stage. The estimation of the propagation constant γ is valid only for an infinitely long line, in contrast to the characteristic impedance Z_0 that gives a consistent local information related the line cross-section as it is approximately independent of the length of the line.

Conformal mapping

The basic approach in the conformal mapping method is to assume that the fields are quasi-TEM and all the dielectric interfaces in the structure can be modeled as magnetic walls[7]. Although the latter assumption is not always fully verified (especially for large slots), conformal mapping has proven to give good results for the most common transmission lines [144]. This gives rise to analytical expressions of the effective dielectric constant ϵ_{eff} and the characteristic impedance Z_0. The derivation of these expressions are beyond the scope of this discussion, but a complete overview can be found in [129]. In the following, we give the expression of Z_0 for the CPW structures shown in Figure 11 :

	CPW (a)	CPW (b)	CPW (c)
Z_0	$\frac{30\pi}{\sqrt{\epsilon_{\text{eff}}}}\frac{K'(k_1)}{K(k_1)}$	$\frac{30\pi}{\sqrt{\epsilon_{\text{eff}}}}\frac{K'(k_1)}{K(k_1)}$	$\frac{30\pi}{\sqrt{\epsilon_{\text{eff}}}}\frac{K'(k_1)}{K(k_1)}$
ϵ_{eff}	$\frac{\epsilon_r+1}{2}$	$1+\frac{\epsilon_r-1}{2}\frac{K(k_2)}{K'(k_2)}\frac{K'(k_1)}{K(k_1)}$	$1+\frac{\epsilon_r-1}{2}\frac{K(k_2)}{K'(k_2)}\frac{K'(k_1)}{K(k_1)}$
k_1	$\frac{a}{b}$	$\frac{a}{b}$	$\frac{a}{b}\sqrt{\frac{1-b^2/c^2}{1-a^2/c^2}}$
k_2	–	$\frac{\sinh(\pi a/2h)}{\sinh(\pi b/2h)}$	$\frac{\sinh(\pi a/2h)}{\sinh(\pi b/2h)}\sqrt{\frac{1-\sinh^2(\pi b/2h)/\sinh^2(\pi c/2h)}{1-\sinh^2(\pi a/2h)/\sinh^2(\pi c/2h)}}$

Table 1: Analytical expressions of Z_0 and ϵ_{eff} derived using conformal mapping [129], the CPW structures shown in Figure 11.

where ϵ_r is the dielectric constant of the substrate, and the functions K and K' are the complete elliptic integrals of the first kind and

6 The characteristic impedance Z_0 allows also the calibration of the electrostatic and magnetostatic simulations which are performed independently

7 By definition, there is no tangential magnetic field in the substrate interfaces, as shown in Figure 10b.

its complement, respectively[8]. The consistency between the 3 expressions of Z_0 related to the CPWs (a), (b) and (c) can be verified for $h \to \infty$ and $c \to \infty$.

For an ideal CPW, one can note that the characteristic impedance Z_0 is a function of the unique parameter : $k_1 = a/b = S/(S+2W)$. Therefore, the design of tapered ideal CPWs can be done without changing Z_0 by scaling the parameters S and W by the same factor. This rule remains approximately verified for the more realistic structures such as the CPWs shown in Figure 11(b-c) (as can be seen from the expressions of Z_0 shown in Table 1). In addition to modeling Z_0 and ϵ_{eff}, conformal mapping has also been used to examine the field distributions of CPWs [145, 146, 147].

Coupling between two adjacent coplanar waveguides

In the following chapters, we will be interested in estimating the coupling between two parallel CPWs spaced by a distance D, as shown in Figure 13. A rough estimation of this coupling can be derived using conformal mapping [144]. In this section, the effects due to the finite size of the substrate and transverse dimension of the CPW are neglected. The maximum possible coupling coefficient is given by [148] :

$$C = 20\log_{10}\left(\frac{Z^e - Z^o}{Z^e + Z^o}\right) \tag{63}$$

where Z^e and Z^o are the even and odd-mode impedances respectively. If the coupling is expected to be low, the latter expression can be simplified to :

$$C = 20\log_{10}\left(1 - Z^o/Z^\infty\right) \tag{64}$$

where Z_∞ is the CPW impedance when the distance D becomes infinite, and Z^o/Z^∞ is given by :

$$\frac{Z^o}{Z^\infty} = \frac{K'(k_3)}{K(k_3)}\frac{K(k_4)}{K'(k_4)} \tag{65a}$$

$$k_4 = \frac{2\sqrt{ab}}{a+b} \tag{65b}$$

$$k_3 = \frac{k_4}{\sqrt{1-(b-a)^2/D^2}} \tag{65c}$$

In our chip design, the two closest CPWs have the following scaling form :

$$a = u \tag{66a}$$

$$b = 2u \tag{66b}$$

$$D = 9u \tag{66c}$$

8 They are simply related to each other with the equation : $K'(k_1) = K(k_1')$ with $k_1' = (1-k_1^2)^{1/2}$. Simple and accurate analytical approximation of the ratio K/K' can be found in the literature [129].

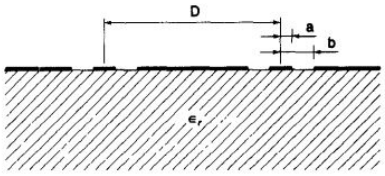

Figure 13: Two coupled parallel coplanar waveguides spaced by a distance D. Figure taken from [144].

with $u = 3$ μm (cf. Figure 52, Config. *II*). Hence, the coupling is about : $C \approx -30$ dB, which will be neglected in the following.

3.2.2 *Microwave field simulation*

An accurate simulation of the magnetic microwave field is essential to compute the microwave potentials, as discussed in section 3.1. We suppose that only the quasi-TEM mode of the CPW is excited by connecting the two outer wires to the ground. In this case, the microwave distribution of the currents is : $\{-I_{mw}/2, I_{mw}, -I_{mw}/2\}$, as shown in Figure 10a. The quasi-static simulation takes into account the effect of the eddy currents, and can be performed using 2D Finite Element Method (FEM).

In Figure 14, we compare the results of 2D quasi-static simulation and static simulation with infinitely thin wires. One can notice that the spatial distribution of the magnetic field is similar in both cases. In fact, the eddy currents reduce the effective power injected into the CPW (by about 14%, in the case of Figure 14) but do not change the shape of the field spatial distribution. The latter observation holds if the field is computed at a distance h_0 from the CPW that satisfy : $h_0 \gg W, S$. In the following chapters, we will use a simplified 2D static simulation (using Biot-Savart law) to model the microwave field distribution such that :

$$\begin{aligned} B_{mw}^{x,CPW} &= \frac{\mu_0 I_{mw}^{\text{eff}}}{2\pi h_0}\left[\frac{z}{x^2+z^2} - \frac{z}{2\left((-d_w+x)^2+z^2\right)} - \frac{z}{2\left((d_w+x)^2+z^2\right)}\right] \\ B_{mw}^{y,CPW} &= 0 \\ B_{mw}^{z,CPW} &= \frac{\mu_0 I_{mw}^{\text{eff}}}{2\pi h_0}\left[\frac{-x}{x^2+z^2} + \frac{-d_w+x}{2\left((-d_w+x)^2+z^2\right)} + \frac{d_w+x}{2\left((d_w+x)^2+z^2\right)}\right] \end{aligned} \tag{67}$$

where d_w is the distance between two adjacent wires of the CPW and I_{mw}^{eff} is the effective current injected in the CPW. The current I_{mw}^{eff} is related to the injected microwave power by : $P_{mw} = |Z_0||I_{mw}^{\text{eff}}|^2/2$ and we assume that $|Z_0| \approx 50$ Ohm. In practice, an experimental calibration of P_{mw} (I_{mw}^{eff}) is required to determine an accurate relationship between I_{mw}^{eff} and P_{mw}. This can be done by measuring the Rabi-frequency of an ultracold atomic cloud [71, 17]. In the following simulations, the microwave power P_{mw} will be always scaled relative

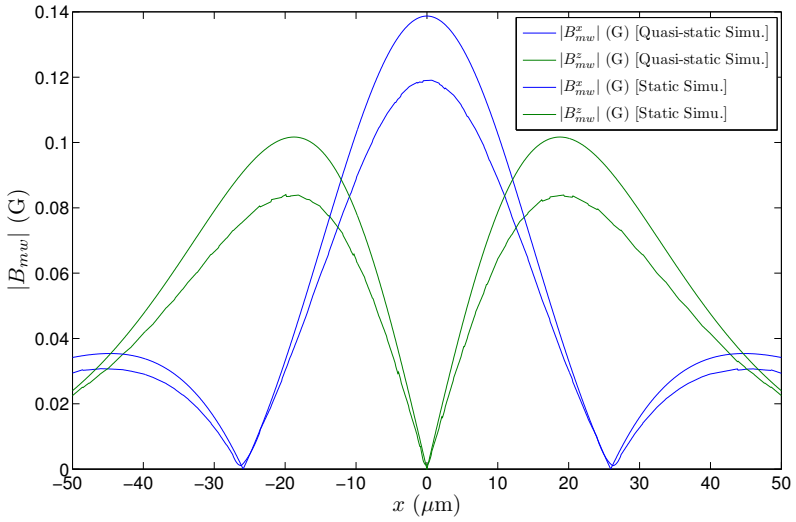

Figure 14: The microwave field components $\{B^x_{mw}, B^z_{mw}\}$ computed along the x-axis at a distance $h_0 = 44$ μm from the CPW, using 2D quasi-static simulation that takes into account the eddy currents (solid lines) and 2D static simulation with infinitely thin wires. The CPW parameters are : $a = u, b = 2u, c = 4u$ with $u = 3$ μm and $\epsilon_r = 11.9$ (cf. Figure 11c). The input microwave currents are given in Figure 10a with $I_{mw} = 76$ mA.

to $P_0 = |Z_0||I^0_{mw}|^2/2$ with $I^0_{mw} = 86$ mA. Of course, to make the experimental and numerical results match, an additional calibration of P_0 will be necessary.

4

THERMAL TRAPPED-ATOM INTERFEROMETRY ON-CHIP

4.1 INTRODUCTION

Bose-Einstein Condensate (BEC) has been widely studied as a promising coherent source for trapped interferometers, both in magnetic trap and in optical dipole trap. For example, atom chips have been used to split and recombine BECs by transforming an harmonic potential well into a double-well [67, 69]. Despite the BEC coherence properties, the interferometers based on trapped condensed atoms are not yet able to compete with the thermal free falling ones in term of precision measurements. It has been shown that interactions in a BEC are harmful for interferometry, causing phase diffusion and collisional shifts that eventually induce decoherence and a loss of sensitivity [73, 74, 75, 149]. One possible method to address these problems aims to reduce interactions by using Feshbach resonances [74]. Hence, several seconds of coherence time have been demonstrated in Bloch oscillation experiments with BECs [150, 151].

Recently, state-selective potentials have been used to allow the internal states to entangle with the motional states in BEC. However, residual interactions within each interferometer arm are still the limiting factor in attaining better sensitivity.

One possibility to reduce the effect of interactions, that we will study in this thesis, is to use a thermal (i.e. non-condensed) ensemble of ultracold atoms trapped on an atom chip. This can be seen as the equivalent of using white light in optics to reduce nonlinear effects [152]. In such a scheme, the coherence time will strongly depend on the symmetry of the interferometer arms.

4.2 ROLE OF SYMMETRY

We are interested in estimating the coherence time (related to the interferometer contrast) for thermal ensemble of atoms which are split and then evolve in two slightly different wells.

On the one hand, considering a semiclassical model, an atom can be assimilated by a point mass. Assuming that two point masses begin with the same position and velocity, they are separated after a certain time by a distance δx. One can estimate the coherence time τ_c as the time at which $\delta x = \lambda_{dB}$ with $\lambda_{dB} = \hbar\sqrt{2\pi/mk_BT}$ is the thermal de Broglie wavelength, T is the temperature of the atomic ensemble, and $\hbar$ and k_B are the reduced Plank and Boltzmann constants. Moreover, we assume that the potentials are harmonic such that : $V_a = m\omega_a^2 x^2/2$ and $V_b = m\omega_b^2 x^2/2$, with $\Delta\omega = |\omega_b - \omega_a| \ll \omega_a, \omega_b$. Thus, the motion of the atoms in the two wells can be easily determined, and so, one can deduce that : $\delta x \approx x_m \Delta\omega\tau_c$, where x_m is the amplitude of the oscillation in the wells, which can be approximated by the characteristic size σ of the thermal cloud : $x_m \approx \sigma = \sqrt{k_BT/m\omega_a^2}$. By combing the previous expressions, one can deduce that the coherence time is approximately given by :

$$\tau_c \approx \sqrt{2\pi}\hbar/(\eta k_B T) \tag{68}$$

where $\eta = \Delta\omega/\omega_a$ is the relative frequency difference.

On the other hand, considering a simplified quantum model where the atoms are trapped in harmonic potentials, it will be shown in section 7.2.2 by neglecting the splitting dynamics, that the coherence time is approximately given by equation (68).

For example, in order to limit the dissymmetry effect on the coherence time to 100 ms with $T = 100$ nK, the relative difference in frequency must not exceed 2×10^{-2}, which requires a careful design of the atomic splitter.

In the next section, we discuss an interferometer design[1] on chip intended to achieve a good level of symmetry and we investigate the principle of several possible configurations for a symmetrical beam splitter for thermal atoms trapped on an atom chip using near-field microwave dressing [71].

1 An alternative interferometer design using thermal trapped atoms is discussed in [153].

4.3 SYMMETRICAL INTERFEROMETER IN THE QUASI-RESONANT REGIME

The physical implementation of a symmetrical atomic beam splitter on chip poses tremendous challenges. Nevertheless, microwave internal-state labeling of the interferometer paths, as demonstrated in [71], offers an accurate control of the splitting and recombination process because it allows an almost a selective control of the desired hyperfine state by controlling the microwave frequency. Compared with optical potentials, microwave near-field potentials have the advantage of negligible spontaneous emission, modest power requirement, and potentially compactness. Moreover, the potential customization of this method is promising to design symmetrical state-selective potentials [85, 104].

4.3.1 *Description of the interferometric sequence*

In this section we describe the elementary principles of a trapped-atom interferometer on chip using the state-selective labeling method. The aim of this interferometer is to measure the phase shift induced by external perturbations (such as gravity) that affect the motional states of the atoms. The interferometer sequence that will be considered here is described by the following steps :

- Cooling and trapping of ultracold atoms to prepare a set of atoms in the first internal state $|a\rangle$, with an initial spatial position $\mathbf{r_0}$ close to the chip surface (*Cooling and Trapping*).
- Transfer of the atoms in a superposition with equal weight of the internal states $|a\rangle$ and $|b\rangle$, using a combination of the microwave and radio-frequency fields ($\frac{\pi}{2}$-Pulse). This derives each atom to an intermediate state : $(|a\rangle + |b\rangle)/\sqrt{2}$ (*Internal-State Manipulation*)
- Spatial separation of the atoms in two wavepackets using a microwave potential that depends on atom internal state (*Splitting*).
- Accumulation of the phase difference Φ related to the evolution of the atoms internal and external states. The atoms are then in the state : $(|a\rangle + \exp(-i\Phi)|b\rangle)/\sqrt{2}$ (*Holding*).
- Spatial recombination of the states $|a\rangle$ and $|b\rangle$, in a similar but reversed manner than the Splitting step (*Spatial Recombination*).
- Internal-states recombination by applying a second $\frac{\pi}{2}$-pulse (*Internal Recombination*).
- Measurement of the interferometer phase Φ. The measurement can be performed by counting the atoms in each state. If the

internal states evolution is well-controlled, one can have access to the external perturbation (*Phase Measurement*).

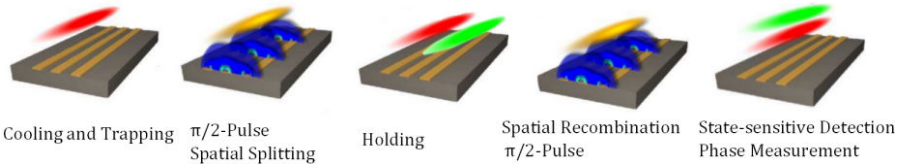

Figure 15: Trapped-atom interferometer on chip using the state-selective labeling method (concept) : Atoms are held in a magnetic microtrap and manipulated using a suitable combination of a microwave and a radio-frequency fields. The interferometer sequence is based on a Ramsey scheme [154]. The Figure is modified from [155].

4.3.2 *Coherent internal-state manipulation*

Atom-chip experiments are subject to ambient magnetic noise and to thermal magnetic near-field noise [156], which can ultimately limit their performance. This effect can be limited by choosing a pair of states whose energy difference is insensitive, at least in the first order, to magnetic-field fluctuations. This is the case for the so-called "clock" states : $|a\rangle \equiv |F = 1, m_F = -1\rangle$ and $|b\rangle \equiv |F = 2, m_F = 1\rangle$ hyperfine levels of the $5S_{1/2}$ ground state of ^{87}Rb atoms, under the appropriate static field. These states are known to be robust against decoherence [90]. Recently, a high-performance chip-based atomic clock with a long interrogation time has been shown experimentally [14].

The microwave state-dependent potentials discussed here can be performed by a combination of static magnetic field $\mathbf{B}(\mathbf{r})$ and microwave field $\mathbf{B_{mw}}(\mathbf{r}, t)$ created by the atom chip, as shown in [71]. Thanks to the advance in microfabrication techniques [86, 157], one can use a multilayer chip to create the static and microwave magnetic near-fields, and precisely control their relative positions, amplitudes and directions. However, unlike the static and radiofrequency currents, the microwave currents cannot be carried by simple wires on chip. Since the microwave wavelength is comparable to the atom chip dimensions, its transmission demands a careful design of the guiding structures [135, 142, 144, 158], in order to avoid undesirable couplings, losses and reflections.

For internal-state manipulation of the atoms, one can couple coherently both clock states by a two photon transition ($\frac{\pi}{2}$-pulse). The coupling can be accomplished using a suitable combination of a blue detuned microwave and red detuned radio-frequency fields (as can be seen in Figure 7) [71, 155].

4.3.3 *Adiabatic Microwave potentials*

The magnetic component of the microwave field couples the sublevels $|F = 1, m_1\rangle$ to the sublevels $|F = 2, m_2\rangle$ and leads to energy shifts that depend on m_1 and m_2. In a spatially varying microwave field, this results in a state-dependent potential landscape [71].

Microwave potentials in the regime of large detuning

The microwave coupling between two bare states $|1, m_1\rangle$ and $|2, m_2\rangle$ can be captured by a simple dressed-atom approach, that has been already applied to describe the atomic motion in laser light in the regime of large detuning [125].

In this regime, the microwave gives rise to the AC Zeeman shift V_{mw}, that can be approximated by the following dressed states model :

$$\text{For the sublevels of } F = 1 : V_{mw} = \hbar|\Omega_{m_1}^{m_2}|^2/4\Delta_{m_1}^{m_2} \tag{69a}$$
$$\text{For the sublevels of } F = 2 : V_{mw} = -\hbar|\Omega_{m_1}^{m_2}|^2/4\Delta_{m_1}^{m_2} \tag{69b}$$

where :

$\Omega_{m_1}^{m_2} = C_{m_1}^{m_2}\mu_B B_{mw}^{\text{eff}}/\hbar$	the Rabi frequency due to the coupling of the states $\|1, m_1\rangle$ and $\|2, m_2\rangle$
$C_{m_1}^{m_2}$	a coupling coefficient that depends only on the latter states (cf. Appendix C)
μ_B	the Bohr magneton
$\hbar$	the reduced Planck constant
B_{mw}^{eff}	the microwave field component along the parallel (normal) local direction of **B** in case of π-transition (σ-transition)
$\Delta_{m_1}^{m_2} = \Delta_{\text{hfs}} - (m_1 + m_2)\omega_L$	the microwave detuning between the coupled states
$\Delta_{\text{hfs}} = \omega_{mw} - E_{\text{hfs}}/\hbar$	the detuning from the transition at $B = 0$
ω_{mw}	the microwave frequency
$\omega_L = \mu_B B/2\hbar$	the Larmor frequency

This simple model, discussed in section 3.1, holds only if the microwave is far detuned from all transitions : $|\Omega_{m_1}^{m_2}| \ll \omega_L, |\Delta_{m_1}^{m_2}|$ and so, the bare states $|1, m_1\rangle$ and $|2, m_2\rangle$ are only weakly coupled.

The two-state description would be perfectly verified if only σ or π-transitions were involved, so that the state $|1, m_1\rangle$ would couple only to the state $|2, m_2\rangle$ due to selection rules as illustrated on Figure 16.

However, in practice both the static field and the microwave field polarizations are spatially varying, and transition mixing occurs.

Nevertheless, the two-state model is approximately valid in case of quasi-resonant coupling regime such as : $|\Delta_{m_1}^{m_2}| \ll \omega_L(B_0)$, because the other transitions are far off-resonance in this case, and where :

B_0	the static filed strength at $\mathbf{r} = \mathbf{r_0}$
$\mathbf{r_0}$	the static trap center

The value of B_0 is usually set to the magic field value $B_0 = B_m^0$, so one can define henceforth the reference frequency :

$\omega_L^0 = \mu_B B_m^0/2\hbar$	the Larmor reference frequency in $\mathbf{r_0}$
$\omega_L^0 \simeq 2\pi \times 6.26$ MHz	with $B_m^0 \simeq 3.23$ G.

Regarding the clock states, both are magnetically trappable and have nearly identical magnetic moments. Therefore, they can be trapped by nearly the same static potential : $V_{\text{dc}} = \mu_B B/2$ and the potential of the clock dressed states $|\bar{a}\rangle$ and $|\bar{b}\rangle$ is given by the following :

$$\begin{cases} V^{|\bar{a}\rangle} &= V_{\text{dc}} + V_{\text{mw}}^{|a\rangle} \\ V^{|\bar{b}\rangle} &= V_{\text{dc}} + V_{\text{mw}}^{|b\rangle} \end{cases} \tag{70}$$

where $V_{\text{mw}}^{|a\rangle}$ and $V_{\text{mw}}^{|b\rangle}$ are the microwave energy-shifts of the bare states $|a\rangle$ and $|b\rangle$ which are given by the equations (69a) and (69b), respectively.

A notable difference compared to the optical cases is that a quasi-resonant coupling (i.e. small detuning) is possible because the ground-state hyperfine levels have a negligible spontaneous emission.

Adiabatic microwave potentials in the quasi-resonant regime

We will consider here the spatial dependence of the magnetic fields : $B = B(\mathbf{r})$ and $B_{mw}(t) = B_{mw}(\mathbf{r}, t)$. These fields can be used to create a space-dependent microwave potential. If the motion of the atom in the resulting potential is sufficiently slow, its internal state follows adiabatically the potential spatial variation and the atom stays in the initial dressed state. The adiabaticity condition is on the form [84] :

$$|\dot{\Omega}_{m_1}^{m_2}\Delta_{m_1}^{m_2}| \ll \left(|\Delta_{m_1}^{m_2}|^2 + |\Omega_{m_1}^{m_2}|^2\right)^{3/2} \tag{71}$$

Once this condition is satisfied, one can write the microwave potential shift for the bare clocks states, as discussed in section 3.1, in the following form :

$$\begin{cases} V_{mw}^{|a\rangle} &= \frac{\hbar}{2}\left[S_{\Delta_a}\sqrt{|\Omega_a|^2 + |\Delta_a|^2} - \Delta_a\right] \\ V_{mw}^{|b\rangle} &= -\frac{\hbar}{2}\left[S_{\Delta_b}\sqrt{|\Omega_b|^2 + |\Delta_b|^2} - \Delta_b\right] \end{cases} \tag{72}$$

where S_{Δ_a} (S_{Δ_b}) gives the sign of $\Delta_a(\mathbf{r_0})$ ($\Delta_b(\mathbf{r_0})$).

One can show that these expressions are identical to equations (69) for large detunings. Moreover, these expressions are valid even in the vicinity of resonance ($\Delta_{m_1}^{m_2} \to 0$).

In the dressed-state picture, if the term S_{Δ_a} has a positive (negative) sign, the state $|a\rangle$ follows initially (at $t = 0^+$) the upper (lower) dressed state $|+\rangle(|-\rangle)$ which has the following energy :

$$E^{\pm} = \pm\frac{\hbar}{2}\sqrt{|\Omega_a|^2 + |\Delta_a|^2} \tag{73}$$

where $+(-)$ refers to the latter states. In the same reference, the energy of the bare state $|a\rangle$ is given by $\hbar\Delta_a/2$. Hence, the microwave energy shift given by equation (72) can be deduced, once S_{Δ_a} is known. A similar demonstration can be performed for the state $|b\rangle$. Yet, this analysis assumes that the atoms are at motional equilibrium in the static trap center $\mathbf{r_0}$ before the beginning of the interferometer sequence (for $t < 0$) and that the dressed energies variations are performed adiabatically.

In the next section, we will propose a design of a symmetrical beam-splitter based on the latter microwave shifts expressions since the static potential V_{dc} is (approximately) identical for the both clock states.

4.3.4 *Principle of a symmetrical microwave potentials*

To achieve the highest possible level of symmetry, we propose to use two microwaves frequencies on two independent coplanar waveguides (CPW). We place the two CPWs at the same distance δ from the static trap center (i.e. $\delta_1 = \delta_2$ in Figure 17) and we choose microwave frequencies to be in the quasi-resonant coupling regime. Hence, each waveguide interacts preferentially with only one of the two clock states since its microwave frequency is off resonance for the remaining states. This allows in principle a quasi-independent experimental control of the potentials in the two arms of the interferometer and makes this scheme a good candidate for implementing a symmetric configuration.

Figure 16 illustrates two possible ways to design a symmetrical beam splitter by either using the π or σ-transition. In the case of π-transition, the microwave frequencies are chosen such that the detunings $\Delta_a^{\pi} = \Delta_{-1}^{-1}$ and $\Delta_b^{\pi} = \Delta_1^1$ in the static trap minimum $\mathbf{r_0}$ have the same absolute value but opposite signs : $\Delta_a(\mathbf{r_0}) = -\Delta_b(\mathbf{r_0}) = \Delta_0$. In the same way, the Rabi frequencies $\Omega_a^{\pi} = \Omega_{-1}^{-1}$ and $\Omega_b^{\pi} = \Omega_1^1$ are equal at $\mathbf{r} = \mathbf{r_0}$: $|\Omega_a(\mathbf{r_0})| = |\Omega_b(\mathbf{r_0})|$, if we inject the same microwave power P_{mw} in the waveguides since the coupling coefficients C_{-1}^{-1} and C_1^1 are equal (i.e. $P_1 = P_2$ in Figure 17). Under these conditions, and considering a simple one-dimensional model, one can

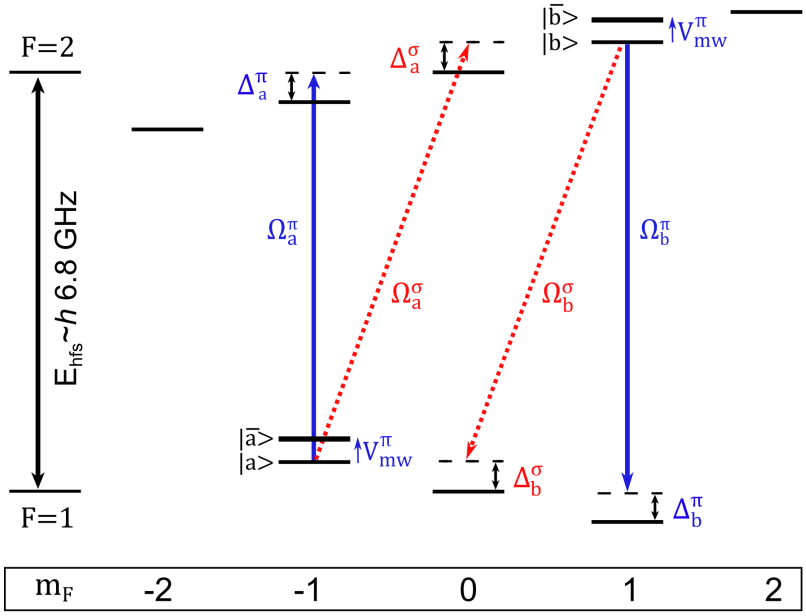

Figure 16: Energy levels of the ^{87}Rb ground states in combined static and microwave fields. To generate symmetrical state-dependent potentials, two microwave near-fields are used to couple the clock states $|a\rangle$ and $|b\rangle$ to two auxiliary states. Two combinations are possible by an adequate choice of the microwave frequencies using either π (solid line) or σ-transitions (dashed line). Ideally, in each case, the Rabi-frequency Ω and detuning Δ are the same (in absolute value) for both states. In this simple model, the resulting dressed states $|\bar{a}\rangle$ and $|\bar{b}\rangle$ are shifted in energy by nearly the same quantity V_{mw}.

show that both the detunings and the Rabi frequencies are symmetrical : $\Delta_a(-x) = -\Delta_b(x)$ and $|\Omega_a(-x)| = |\Omega_b(x)|$, which implies together with equations (72) and (70), the required symmetry of the potentials : $V_{mw}^{|a\rangle}(-x) = V_{mw}^{|b\rangle}(x)$ and $V^{|\bar{a}\rangle}(-x) = V^{|\bar{b}\rangle}(x)$. Similar demonstration can be performed to show the symmetry of the potentials using σ-transitions, if the injected microwave powers satisfy the following condition : $P_2/P_1 = \left(C_{-1}^0/C_0^1\right)^2 = 1/3$.

In practice, this symmetry is not perfect in particular because of the effect of non-resonant transitions. Sections 5.2 and 6.3 discuss this imperfect symmetry of the potentials in detail.

4.3.5 *Potential-well and potential-barrier beam-splitter*

Using the state-depend microwave potentials, one can create either a microwave potential-barrier or a microwave potential-well by choosing the detuning Δ_0. Figure 17 shows an example of two symmetrical potentials barriers : the detuning Δ_0 is positive and corresponds to blue (red) detuning of π-transition related the state $|a\rangle$ ($|b\rangle$). In this case, the dressed atoms in state $|a\rangle$ ($|b\rangle$) are trapped in the vicinity of

low Rabi frequency, and therefore, the microwave AC Zeeman shifts seen by the atoms can be approximated locally by equations (69). In the case of large detunings, it can be seen on the latter expressions that the attractive or repulsive nature of the microwave energy shift depends only on the sign of the detuning.

In general, using equations (72), one can show that the sign of the microwave energy shift initially at $\mathbf{r} = \mathbf{r_0}$ is given by S_{Δ_a} (S_{Δ_b}) for $V_{mw}^{|a\rangle}$ ($V_{mw}^{|b\rangle}$) respectively. The microwave beam-splitter can be performed by increasing adiabatically the Rabi frequencies $|\Omega_a|$ and $|\Omega_b|$ in a similar manner, by increasing the microwave power P_1 and P_2, while keeping the detunings constant. In such a case, each microwave energy shift increases during the splitting stage $|V_{mw}(t)| > |V_{mw}(t = 0^+)|$ and its sign remains unchanged. On the other hand, one has to pay attention to the adiabaticity condition especially in the beginning of the splitting : $t = 0^+$ since $\Omega_{m_1}^{m_2}(t = 0^+) \approx 0$ and so the right-hand term of equation (71) is minimum.

Using the same chip configuration, experimental implementation of both kinds of beam-splitter is possible by tuning the microwave frequencies. Nevertheless, their physical characteristics are different especially in term of the interferometer symmetry and the splitting distance. These aspects will be discussed and the pros and cons of each splitting method will be given in the following sections.

4.3.6 *Axial and transverse beam-splitter*

The orientation of the microwave field with respect to the static magnetic field is crucial for the topography of the effective microwave potentials (cf. equations (70) and (72)). In this section, we investigate the possibility of performing axial and transverse splitting with this technique. For the sake of simplicity, we assume that the static magnetic trap is performed by the combined fields of an infinite wire and a external homogeneous bias fields (cf. section 2.2.3). The field direction in the minimum of the trap is called the trap axis. It is given in this case by the trapping wire direction. Considering this simple one-wire trap model, one can examine two extreme cases : the trap axis is either parallel (y-axis) or perpendicular (x-axis) to the waveguides direction.

In the first case ($I_0 > 0, I_1 = 0$ in Figure 17), the trap and the waveguides are invariant under translation along y, reducing the system to the two-dimensional (2D) transverse plane. Therefore, the splitting occurs along the transverse (radial) directions : x and z, as can be seen in Figure 18a, which is similar to the case of splitting in a radio-frequency based double well [67]. We point out that the microwave field is perpendicular to the trap axis, which tends to select the σ-transitions in the vicinity of the trap minimum. Hence, the coupling

scheme in Figure 16 using σ-transitions[2] is more suited in this configuration.

In the second case ($I_0 = 0, I_1 > 0$ in Figure 17), the problem is not invariant under translation anymore, and the splitting is performed along the weak direction, as can be seen in Figure 18b, which is similar to the experimental demonstration in [71] using π-transition. For high aspect ratio of the static trap : $\omega_{y,z}/\omega_x \gg 1$, the splitting is well approximated by an axial one-dimensional problem.

This single infinite-wire trap model, despite its simplicity, shows that both transverse and axial splitting are conceptually possible using microwave potentials in the quasi-resonant regime, and their physical implementation can be made on the same chip.

Nevertheless, in the case of transverse splitting, numerical simulation using a more realistic trap model on chip, based on a Z-trap or Dimple trap, shows that axial splitting cannot be neglected. In this case, the splitting direction depends on the microwave power which could be a drawback for precision measurements. This drawback can be solved by a careful design of the static trap, which will be discussed in section 6.2.4.

2 Using the σ-transitions, it is worth noting that the state $|a\rangle$ can be coupled to two different sublevels : $|2,0\rangle$ and $|2,-2\rangle$, where the state $|b\rangle$ can be coupled to only one sublevel : $|1,0\rangle$. Yet, a coupling between $|a\rangle$ and $|2,-2\rangle$ cannot be used to design a symmetrical beam-splitter, since the dependence of the detunings on B are different, and so the symmetry condition $\Delta_a(-x) = -\Delta_b(x)$ can not be fulfilled.

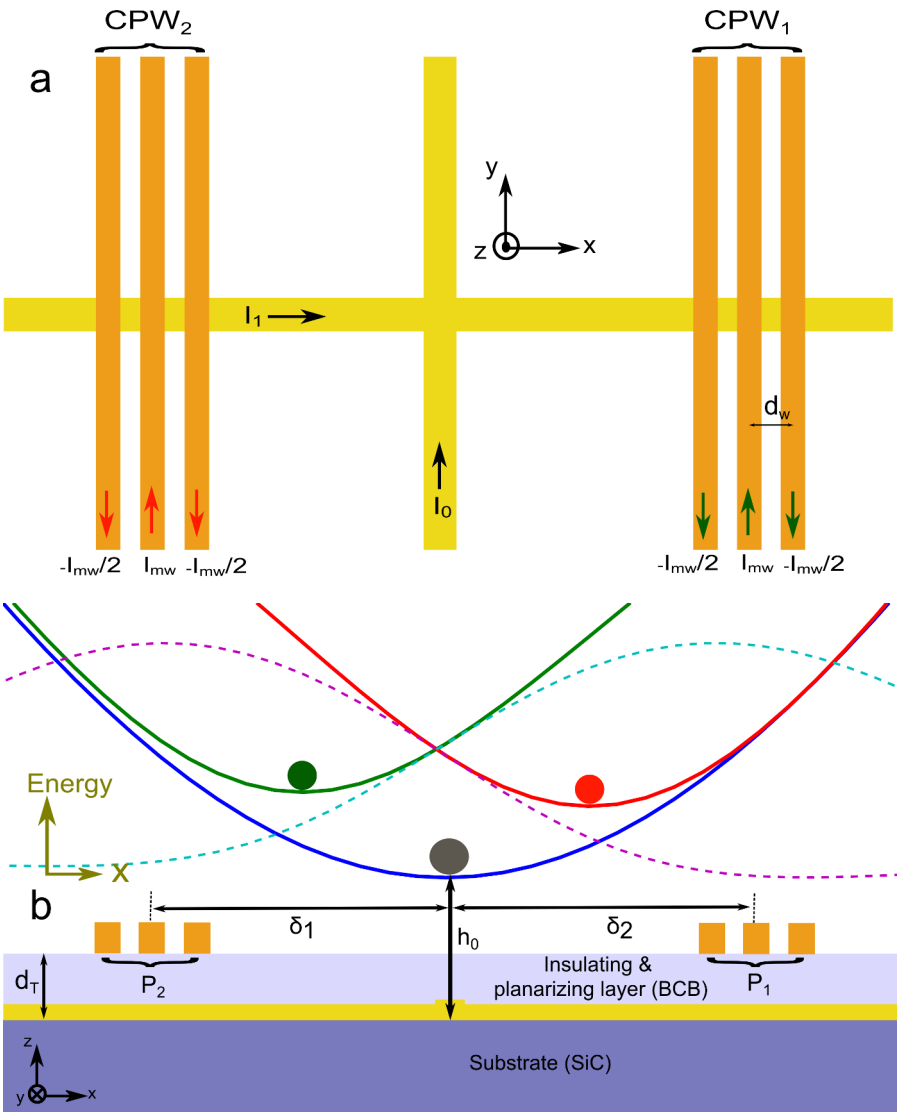

Figure 17: Schematic close-up of the experiment region on the atom chip. (a) Top view of wire layout. (b) Cut through substrate. The central wires (in yellow) that carry the static currents : I_0 and I_1 are used to create a static microtrap at a distance h_0 from the substrate surface ($\mathbf{r} = 0$ corresponds to these wires crossing). Two identical sets of three wires, separated by the same distance d_w, in the upper layer (in orange) form two microwave coplanar waveguides CPW_1 and CPW_2. An ideal CPW in even-mode has the following microwave-current amplitude distribution : $\{-I_{mw}/2, I_{mw}, -I_{mw}/2\}$ as indicated which corresponds to an injected microwave power : $P = |Z_0||I_{mw}|^2/2$. The CPWs are placed at the same distance $|\delta_1| = |\delta_2| = \delta$ from the center. An insulating layer separates the CPWs from the substrate surface by a distance d_T. The static potential (solid line, blue) is initially used to trap the atoms, then shifted by the (repulsive) microwave energies (dashed lines, cyan and magenta). The resulting potentials are state-dependent (solid lines, green and red) that can be used to split the clock states $|a\rangle$ and $|b\rangle$ in a symmetrical manner.

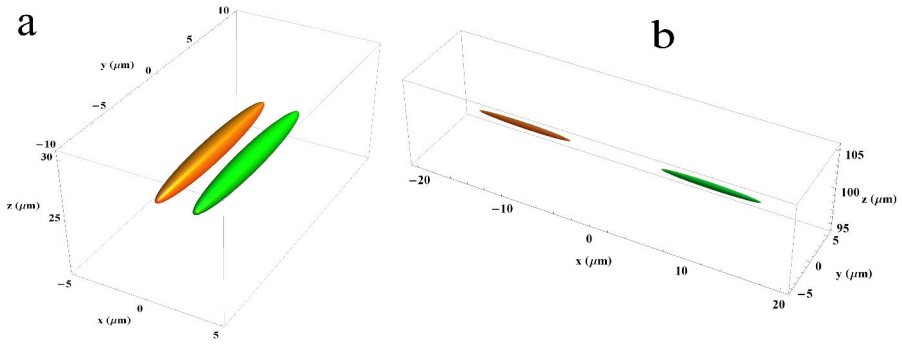

Figure 18: Schematic of the atoms splitting along (a) the longitudinal (axial) direction (b) the transverse directions of the static trap. 3D-equipotentials representation of the clock states : $|a\rangle$ (orange) and $|b\rangle$ (green), for the potential $k_B T$ with $T = 100$ nK (about $h \times 2$ kHz).

5

AXIAL BEAM-SPLITTER : INTERFEROMETER ANALYSIS

5.1 INTRODUCTION

Coherent manipulation of internal [14, 91] and motional [67, 75, 159, 160, 161] states on atom chips has been demonstrated first in separate experiments. The combined coherent manipulation of internal and motional states with a state-dependent potential on a chip was shown for the first time in the experiment reported in [71]. A state-dependent microwave potential has been used to implement a trapped-atom interferometer with internal-state labeling of the interferometer paths. The state-selective potential was generated by the on-chip microwave near-fields, to separate coherently the atoms along the axial direction of the static trap.

We study here the axial beam-splitter discussed in the previous chapter : a similar beam-splitter than [71] using ultracold non-condensed atoms, with an additional constraint on the symmetry of the microwave potentials.

In this chapter, we focus on the study of such an axial beam-splitter using π-transitions[1] (cf. Figure 16 and section 4.3.6). In particular, we discuss the effect of transition mixing, and we compare the possible splitting methods using either an attractive or a repulsive microwave potential.

Moreover, we discuss some physical factors limiting the ultimate performances of this interferometer such as : the microwave shift of the non-resonant transitions, and the effect of the fluctuations of both static and microwave fields on the interferometer coherence. Several solutions and practical designs will be discussed. Finally, we discuss the stability of the gravitational signal of the interferometer for the perspective of the development of a high performance gravimeter on a chip.

1 Using the σ-transitions, splitting often occurs along both axial and transverse directions, as will be discussed in section 6.2.

5.2 EFFECT OF TRANSITION MIXING

In this section, we shall discuss the validity of the two dressed states model used previously to design the symmetrical beam splitter. For this, one has to take into account the non-resonant transitions that can break the symmetry. Hence, in case of quasi-resonant π-transition, we include also the σ-transitions resulting from the same microwave field and all the transitions due to the second microwave signal.

This transition mixing is expected to disturb the symmetry of the potentials since the perturbations due to the non-resonant σ-transitions are not symmetrical. While the first clock state $|a\rangle$ is coupled (perturbatively) to two states : $|2,-2\rangle$ and $|2,0\rangle$, the second clock state $|b\rangle$ is coupled to only one state : $|1,0\rangle$. Here, we propose to quantify this dissymmetry effect.

A complete description of microwave potentials should consider the different coupling between the eight states : $|F,m_F\rangle$ which define a basis of the ^{87}Rb ground level. Using only one microwave frequency ω_{mw}, the Hamiltonian H is given by the following [86] :

$$\hat{H}_0 = \sum_{m_2}\left(-\frac{1}{2}\hbar\Delta_{\text{hfs}} + \hbar\omega_L m_2\right)|2,m_2\rangle|n\rangle\langle n|\langle 2,m_2| + \sum_{m_1}\left(\frac{1}{2}\hbar\Delta_{\text{hfs}} - \hbar\omega_L m_1\right)|1,m_1\rangle|n+1\rangle\langle n+1|\langle 1,m_1| \tag{74a}$$

$$\hat{H}_F(\omega_{mw}) = \hbar\omega_{mw}(a^\dagger a + 1/2) \tag{74b}$$

$$\hat{H}_{AF}(\omega_{mw}) = \sum_{m_1,m_2}\left[\frac{1}{2}\hbar\Omega_{m_1}^{m_2}|2,m_2\rangle|n\rangle\langle n+1|\langle 1,m_1| + c.c.\right] \tag{74c}$$

$$H = \hat{H}_0 + \hat{H}_F(\omega_{mw}) + \hat{H}_{AF}(\omega_{mw}) \tag{74d}$$

where $a^\dagger$ (a) is the creation (annihilation) operator, $\hat{H}_0$ is the Hamiltonian of the system in presence of the static field only, $\hat{H}_F$ is the Hamiltonian of the microwave field and $\hat{H}_{AF}$ describes the atom-microwave interaction. The eigenstates of $\hat{H}_F$ are the photon number states : $|n\rangle$ with $a^\dagger a|n\rangle = n|n\rangle$ and the eigenvalues of $\hat{H}_F$ are : $(n+1/2)\hbar\omega_{mw}$.

If the conditions : $\mu_B B, \mu_B B_{mw}, \hbar\Delta_{\text{hfs}} \ll \hbar\omega_{mw}$ with $\Delta_{\text{hfs}} = \omega_{mw} - \omega_{\text{hfs}}$ are satisfied, the rotating wave approximation can be made (cf. section 3.1). Thus, we consider only the set of 8 states :

$$\mathcal{S}(n) = \{|F=1,m_F=-1...1\rangle|n+1\rangle, |F=2,m_F=-2...2\rangle|n\rangle\} \tag{75}$$

and we neglect the coupling between different sets $\mathcal{S}(n)$. In the following, we suppress the reference to the field state, as H does not depend on the set of levels (i.e. the value of n). We also drop the con-

stant term $(n+1/2)\hbar\omega_{mw}$, which is a common energy offset for the states in $\mathcal{S}(n)$. Hence, the Hamiltonian H can be simplified to :

$$H_0 = \sum_{m_2}\left(-\frac{1}{2}\hbar\Delta_{\text{hfs}} + \hbar\omega_L m_2\right)|2,m_2\rangle\langle 2,m_2| + \sum_{m_1}\left(\frac{1}{2}\hbar\Delta_{\text{hfs}} - \hbar\omega_L m_1\right)|1,m_1\rangle\langle 1,m_1| \tag{76a}$$

$$H_{AF}(\omega_{mw}) = \sum_{m_1,m_2}\left[\frac{1}{2}\hbar\Omega_{m_1}^{m_2}|2,m_2\rangle\langle 1,m_1| + c.c.\right] \tag{76b}$$

$$H = H_0 + H_{AF}(\omega_{mw}) \tag{76c}$$

In our case, one has to consider the effect of both microwave frequencies. As discussed in sections 3.2.1 and 8, the coupling between the CPWs is very low, and will be neglected here.

Moreover, based on a second harmonic approximation [162], the role of the microwave frequencies interplay : $\omega_{mw,2} - \omega_{mw,1}$ can be neglected if :

$$\mu_B(B_{mw,1} + B_{mw,2}) \ll \hbar(\omega_{mw,2} - \omega_{mw,1}) \tag{77}$$

which is well satisfied in experiments.

The total Hamiltonian H_T is then given by the superposition of each CPW (i.e. microwave frequency) contribution with the Hamiltonian H_0 such as :

$$H_T = H_0 + H_{AF}(\omega_{mw,1}) + H_{AF}(\omega_{mw,2}) \tag{78}$$

The dressed states and corresponding energy levels can be obtained by the numerical diagonalization of the 8×8 matrix H_T. To calculate the potentials at $\mathbf{r}$, one needs to define carefully the microwave polarization with respect to the static field in order to calculate the matrix elements $\Omega_{m_1}^{m_2}$. The remaining terms are scalars and do not depend on the orientation of the quantization axis. This procedure has to be repeated in each point $\mathbf{r}$.

Figure 19 illustrates a numerical calculation of the potentials of the dressed clock states along the splitting axis x and the trap transverse axes y and z. The microwave energy shifts V_{mw} are calculated for the clock states : $|a\rangle$ (in cyan) and $|b\rangle$ (in magenta) using two different methods : (with plus-sign) a numerical diagonalization of the full Hamiltonian (cf. equation (78)) and (with dashed line) approximated analytical model (cf. equation (79)). A good agreement is observed between the two models since $|\Omega_{\max}/\omega_L^0| \ll 1$. (e.g. here, $|\Omega_{\max}/\omega_L^0| = \{0.097, 0.071\}$ in (a) and (b) respectively.)

Once the three-dimensional potentials are generated, one can search numerically for the new minimum positions then estimate the eigenfrequencies, which gives a first estimate of the overall dissymmetry.

In this case, as shown in Table 2, the highest frequency difference between the two wells is along x-axis and it is on the order of (7%, 2%) for a potential-well and a potential-barrier, respectively.

To make the potential dissymmetry smaller, one can make profit from the tunable experimental parameters (power and frequency in each waveguides) to balance out the frequencies of the two traps. This procedure can be done either experimentally or numerically.

For a time-efficient numerical optimization and to avoid iterative diagonalization of H_T, it is possible to generalize the quasi-resonant model of microwave potentials (cf. equation (72)) by considering all possible transitions two-by-two, if the condition : $|\Omega_{m_1}^{m_2}| \ll |\omega_L^0|$ is fulfilled, so that the anti-crossings [86] are well separated. Thus the microwave energy shifts, using only one microwave frequency ω_{mw}, can be written in the form :

$$V_{\mathrm{mw}}^{a/b}(\omega_{mw}) = \pm \sum_{m_1,m_2} \frac{\hbar}{2}\left[S_{\Delta_{m_1}^{m_2}}\sqrt{|\Omega_{m_1}^{m_2}|^2 + |\Delta_{m_1}^{m_2}|^2} - \Delta_{m_1}^{m_2}\right] \tag{79}$$

where $+(-)$ refers to the state $|a\rangle(|b\rangle)$ and $S_{\Delta_{m_1}^{m_2}}$ gives the sign of $\Delta_{m_1}^{m_2}(\mathbf{r_0})$. As described earlier, the contribution of both frequencies is given by :

$$V_{\mathrm{mw},T}^{a/b} = V_{\mathrm{mw}}^{a/b}(\omega_{mw,1}) + V_{\mathrm{mw}}^{a/b}(\omega_{mw,2}) \tag{80}$$

This model simplifies considerably the calculation of the potentials eigen-energies, and will be used in the chapter 7.2. The microwave beam-splitter design presented earlier rests upon the symmetry of the dressed states in the frame of the quasi-resonant coupling regime (i.e. $|\Delta_0| \ll \omega_L^0$). Since the spontaneous emission is negligible for microwave dressing, the detuning can be set arbitrarily low. However, this regime imposes supplementary constraints, related to the trap depth and the sensitivity to the static magnetic field fluctuations, which are discussed in the following sections.

	Potential-well			Potential-barrier		
	$\tilde{\mathbf{x}}$	$\tilde{\mathbf{y}}$	$\tilde{\mathbf{z}}$	$\tilde{\mathbf{x}}$	$\tilde{\mathbf{y}}$	$\tilde{\mathbf{z}}$
$\omega_a/2\pi$ (Hz)	186.6	1655.9	1636.1	127.9	1933.1	1907.5
$\omega_b/2\pi$ (Hz)	173.5	1654.4	1635.5	130.0	1937.3	1908.9
$\lvert\Delta\omega\rvert/2\pi$ (Hz)	13.1	1.47	0.685	2.12	4.19	1.46
$\lvert\frac{\Delta\omega}{\omega}\rvert \times 10^2$	7.03	0.089	0.041	1.66	0.216	0.076

Table 2: The eigenfrequencies $\{\omega_a, \omega_b\}$ and the dissymmetry $\Delta\omega = \omega_b - \omega_a$ of the microwave potentials $\{V^{|\bar{a}\rangle}, V^{|\bar{b}\rangle}\}$ related to the simulations in Figure 19. The eigen-directions : $\{\tilde{\mathbf{x}}, \tilde{\mathbf{y}}, \tilde{\mathbf{z}}\}$ are slightly rotated from the chip reference : $\{\mathbf{x}, \mathbf{y}, \mathbf{z}\}$.

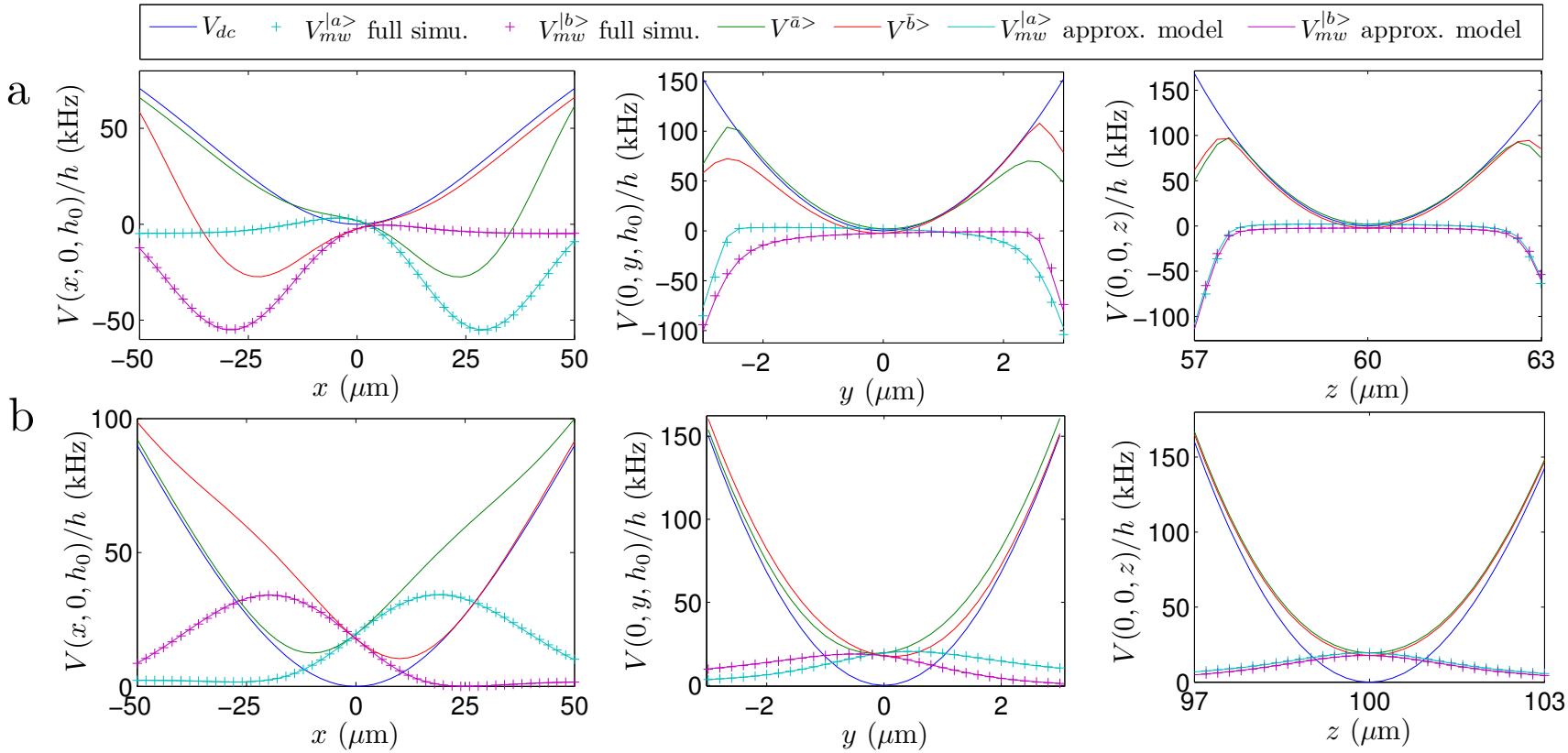

Figure 19: Simulated three-dimensional potentials of the dressed clock states : $|\bar{a}\rangle$ (in green) and $|\bar{b}\rangle$ (in red) shown along the axial direction x and the transverse directions y and z, for state-selective splitting using a potential-well (a) and a potential-barrier (b). The microwave energy shifts V_{mw} are calculated for the clock states : $|a\rangle$ (in cyan) and $|b\rangle$ (in magenta) using two different methods (cf. text). The static potential (in blue) is nearly identical for both states. The static currents on chip (shown in Figure 17) and the bias fields are chosen such that the static trap (in blue) is located at the distance h_0 from the chip surface ($h_0 = 60$ μm in (a) and $h_0 = 100$ μm in (b)), and has nearly the following axial and radial frequencies : $\omega_\perp/2\pi =$ 2000 Hz and $\omega_x/2\pi =$ 100 Hz. The microwave frequencies are chosen such as : $\Delta_a(\mathbf{r_0}) = -\Delta_b(\mathbf{r_0}) = \Delta_0$ ($\Delta_0/\omega_L^0 = -0.1$ in (a) and $\Delta_0/\omega_L^0 = 0.05$ in (b)). The injected microwave powers in the CPWs are equal : $P_1 = P_2 = P_{mw}$ ($P_{mw} = 3P_0/10$ in (a) and $P_{mw} = 4P_0$ in (b), $P_0 \approx 185$ mW) and the CPWs are placed at the same distance $\delta_1 = \delta_2 = \delta = 27$ μm with a distance between each CPW wires $d_w = 18$ μm. The insulating layer thickness is $d_T = 6.8$ μm. With a good approximation, both static and microwave magnetic fields are computed using one-dimensional Biot-Savart law, and the induced current has been neglected. The energy reference of the potentials corresponds to the energy in the center of the static trap ($\mu_0 B_0/2$).

5.3 TRAP DEPTH OF A POTENTIAL-WELL BEAM-SPLITTER

For a beam-splitter based on attractive microwave potentials, the detuning of the lower (upper) clock states must be negative (positive) at the static trap minimum $\mathbf{r_0}$ (i.e. $\Delta_0 < 0$). As illustrated in Figure 19a, an opening of the resulting adiabatic potential occurs in this case at two symmetrical positions from the trap center, corresponding to anticrossings of the energy levels under microwave coupling [86]. This occurs at the points where the detuning $\Delta_{m_1}^{m_2}$ changes sign, defined at $\mathbf{r} = \mathbf{r_d}$ with the resonance condition $\hbar\omega = \mu_B B(\mathbf{r_d})/2$. As a consequence, the trap depth is reduced considerably to the order of $\hbar|\Delta_0|$ in the case of low microwave coupling : $|\Omega_{m_1}^{m_2}| \ll |\Delta_0|$. In the general case, an energy splitting between the coupled states occurs at resonance, which reduce further the static trap-depth (TD) by approximately : $\hbar|\Omega_{m_1}^{m_2}(\mathbf{r_d})|/2$. As shown in Figure 19a, the trap depth along the transverse directions is about : $h \times 72$ kHz ($k_B \times 3.4$ μK), which is still sufficient to trap an atomic ensemble with a temperature of few hundred nano-Kelvin.

Such trap opening does not occur in the case of a splitting by repulsive microwave potentials (potential-barrier splitter), since the detuning does not vanish in this case. This effect is used in opportune manner for evaporative cooling using radio-frequency coupling [162]. The same idea has been used to perform a radio-frequency beam-splitter [84], where the second resonant potential is used to trap the atoms in the two local minimums around the resonances, by ramping up adiabatically the detuning from negatives to positives values.

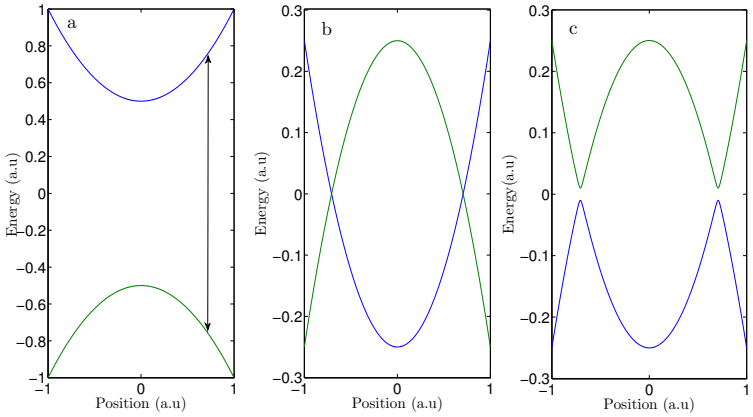

Figure 20: Schematic diagram of adiabatic dressed potentials. (a) Unperturbed bare states in a harmonic trap are coupled by the microwave field at resonance (arrows). (b) In the dressed basis, these levels are degenerated at resonance ($\mathbf{r} = \mathbf{r_d}$) for a vanishing microwave coupling. (c) For a finite coupling, the levels are split by nearly $\Omega_{m_1}^{m_2}(\mathbf{r_d})$ (cf. equation 69). Hence, at resonance, the lower potential opens which reduces the trap depth (solid line) and new potential minima are formed for the upper potential (dashed line) [84].

5.4 AXIAL BEAM-SPLITTER ANALYSIS

In this section, we study the characteristics of an axial beam-splitter, in particular the power efficiency and the splitting distance. Then, we discuss the dependence of the trap frequencies with the microwave power. and the role of the static field structure. Since the two interferometer arms are similar, we focus on the study of the splitting process of atoms initially in the state $|a\rangle$ due to the microwave field created by the waveguide : CPW_1 in Figure 17.

5.4.1 *Splitting distance and power requirement*

In the following, we propose to verify the one-dimensional approximation numerically and then to establish a simple one-dimensional model that predict the splitting distance for both splitting methods.

Using a full simulation of the resulting potentials $V^{|\bar{a}\rangle}(x,y,z)$, the coordinates of the potential minimum $\mathbf{r_m} = \{x_m, y_m, z_m\}$ along the 3 axis : $\{x,y,z\}$ can be estimated as explained previously. Figure 21 shows the variation of $\{x_m, y_m, z_m\}$ as a function of the microwave power P_{mw}. In order to compare the two splitting methods, we use the same static potential created using a Dimple trap and located at the distance $h_0 = 60$ μm from the chip surface. The remaining parameters are set as in Figure 19. In particular, the initial detunings $|\Delta_0|$ have different values : $|\Delta_0/\omega_L^0| = 0.1$ and $|\Delta_0/\omega_L^0| = 0.05$ for a potential-well and a potential-barrier beam-splitter, respectively. In the case of a potential-well, the detuning $|\Delta_0|$ cannot be set to a lower value[2] which reduces relatively, for a given Rabi frequency $|\Omega_{m_1}^{m_2}|$, the strength of the corresponding microwave shift (cf. equations (69)).

For low microwave power, the splitting using an attractive or repulsive potentials are similar. In a pinch, the repulsive potential has a slightly better power-efficiency since the initial detuning $|\Delta_0|$ can be set very low without compromising the trap depth (cf. equation (72)).

For a higher microwave power, despite the unfavorable choice of the detuning $|\Delta_0|$, the splitting is more efficient (in term of microwave power) in case of an attractive beam-splitter, because the static potential *relax* eventually around x_m^f and the atoms becomes mainly trapped due to the microwave energy shift V_{mw} (shown in cyan in Figure 19a), and so the position of the trap minimum x_m converges to the CPW position δ. The minima of the potentials along the transverse directions ($\mathbf{y}$ and $\mathbf{z}$) are weak (about $|x_m|/100$), which confirms the one-dimensional model assumed in section 4.3.4.

2 Otherwise the trap-depth would be very low as discussed in section 5.3

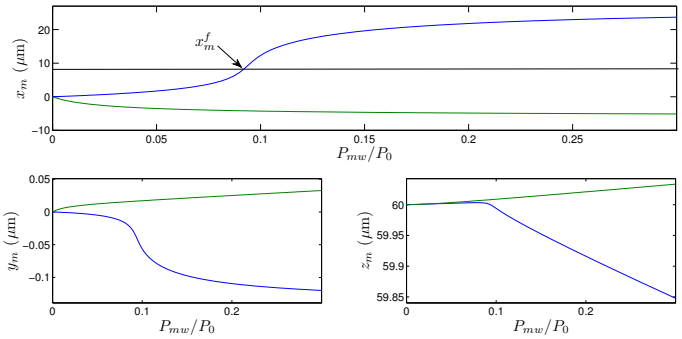

Figure 21: The coordinates $\mathbf{r_m} = \{x_m, y_m, z_m\}$ along the axis : {x, y, z} of the resulting potential $V^{|\bar{a}\rangle}$ as function of the microwave power P, for a potential-well (in blue) and a potential-barrier (in green) and the values of the detunings are respectively set to : $\Delta_0/\omega_L^0 = \{-0.1, 0.05\}$. The static trap is located at a distance $h_0 = 60$ μm from the chip surface and has the angular frequencies : $\omega_x/2\pi =$ 100 Hz and $\omega_\perp/2\pi = 2000$ Hz. The remaining parameters of the simulation are given Figure 19.

5.4.2 *The eigen-frequencies of the microwave trapping potential*

For the sake of completeness, we show the angular-frequencies evolution of the resulting potential in Figure 22 as function of the microwave power P_{mw}. Although the latter potential is not harmonic, the harmonic approximation is justified at very low temperatures, and can be used to describe the anisotropy of the atomic cloud. The effect of the potential anharmonicities and the variation of the angular frequency along the splitting direction **x** will be treated in chapter 7.

For a potential-well beam-splitter, we have discussed the curve inflections in Figure 21 (in blue). Similar inflection points can be seen on the profiles of the transverse eigenfrequencies $\{\omega_{\tilde{y}}, \omega_{\tilde{z}}\}$ shown in Figure 22.

In both case, the atomic cloud is compressed along the axial direction by a factor of (2, 3) for a potential-barrier and a potential-well respectively, which increases the atomic density. This variation of the trap aspect-ratio after splitting is an important feature of the axial splitting (by contrast to the transverse splitting where it remains nearly constant, as will be shown in section 7.2).

5.4.3 *The role of the static field structure*

Beyond the simplified one-wire trap model discussed in section 4.3.6, the structure of the static field components B_i, plays a crucial role on the design of symmetrical microwave potentials. Using a typical microtrap, such as Dimple trap or Z-trap, and considering only the

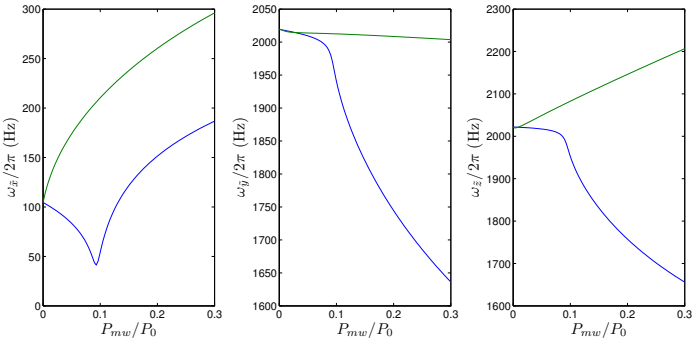

Figure 22: Eigen-frequencies of the resulting potential $V^{|\bar{a}\rangle}(x,y,z)$ as function of the microwave power P_{mw}, for a potential-well (in blue) and a potential-barrier (in green). The interferometer parameters are similar to Figure 21.

π-transitions, one can show that the microwave energy shifts have the following central symmetry :

$$V_{mw}^{|a\rangle}(-x,-y,z) = V_{mw}^{|b\rangle}(x,y,z) \tag{81}$$

For this purpose, one can note the following properties of the static and microwave fields : $B_x(-x,-y,z) = B_x(x,y,z)$, $B_y(-x,-y,z) = B_y(x,y,z)$ and $B_z(-x,-y,z) = -B_z(x,y,z)$ for a typical microtrap and $B_{mw}^x(-x,z) = B_{mw}^x(x,z)$, and $B_{mw}^z(-x,z) = -B_{mw}^z(x,z)$ for a CPW field. As $B_{mw}^y = 0$, the effective microwave field B_{mw}^{eff} is here given by :

$$B_{mw}^{\text{eff}} = (B_x B_{mw}^x + B_z B_{mw}^z)/B \tag{82}$$

considering only the π-transitions. Similar derivation will be given in detail in section 6.2.1 using the σ-transitions. As a consequence of equation (81), the minima of the potentials have also a central symmetry such as : $\{x_m^a = -x_m^b, y_m^a = -y_m^b, z_m^a = z_m^b\}$ and the eigen-frequencies of both potentials are equal, which is conceptually very important. Indeed, even if the one dimensional condition is not fully verified, the required symmetry of the eigen-frequencies remains valid if the effect of the non-resonant transitions can be neglected. The residual displacement $z_m - h_0$ along the z-axis is similar for both states and affects eigen-frequencies of both potentials in an identical manner. Moreover, the residual displacement y_m along the y-axis makes the splitting direction tilted from the x-axis with the small angle : $\theta_{ab} \simeq y_m/x_m$.

For a Standard Ioffe-Pritchard (SIP)[3], the coils can be placed relatively to the chip such that the trap-axis coincides with the x-axis, perpendicularly to the CPWs direction[4], in order to select the π-

3 Discussed in section 2.2.2.

4 Always given by the y-axis in this thesis, as shown in Figure 19.

transitions[5]. In this case, the symmetry properties of the static field **B** gives rise to a different beam-splitter behavior.

First, the microwave shift V_{mw} does not depend on[6] y, and so the splitting of both states occurs in the xz-plane. Hence, there is no residual displacement along the y-axis (i.e. $y_m^a = y_m^b = 0$). This symmetry property can be shown using equation (82) together with the magnetic field equations (9) and (67).

Second, the microwave shifts are not strictly symmetrical and, in particular, the variation along the z-axis is different for both states which affects the transverse frequencies symmetry[7]. In this case, the dissymmetry of the potentials can be reduced by increasing the transverse frequency $\omega_\perp$ of the static trap, in order to minimize the residual displacement along **z**.

Combing the advantages of the two previous beam-splitters would be possible, if the microwave shifts would had an axial symmetry :

$$V_{mw}^{|a\rangle}(-x, y, z) = V_{mw}^{|b\rangle}(x, y, z) \tag{83}$$

In this case, the splitting would be only along the x-axis (i.e. $\theta_{ab} = 0$), strictly symmetrical such that : $\{x_m^a = -x_m^b, y_m^a = y_m^b, z_m^a = z_m^b\}$, and so the eigen-frequencies of the microwave potentials would be equal. Using the π-transitions and the general form of an Ioffe Pritchard trap 2.2.4, we show in Appendix D that the previous condition can not be satisfied.

5 The π-transitions can be also selected if the SIP trap-axis is placed along the z-axis. Yet, this is not relevant for a comparison with typical microtraps, which always have a trap-axis on the xy-plane. Designing a microtrap with a trap-axis that has a large inclination from the chip surface is in theory possible, but the resulting trap would have a shallow depth [85].

6 As it is the case with the conceptual one-wire trap model discussed in section 4.3.6.

7 As the gradient seen by an atom is strongly dependent on its distance from the chip.

5.5 SENSITIVITY TO THE STATIC FIELD FLUCTUATIONS

The coherence properties of the clock states, described earlier, are critical for the interferometer design. Indeed, the differential Zeeman shift is quadratic in magnetic field around a *magic* value $B_m^0 = 3.229$ G [90], which makes the state pair insensitive, at the first order, to magnetic field fluctuations. The coherence properties of the clock states mentioned previously (in section 4.3) only hold for : $B_0 = B_m^0$.

In our case, the presence of the microwave dressing might affect this property, as will be discussed in the following. For this, let us consider the case of quasi-resonant π-transitions (neglecting all transition mixing effects described in section 5.2). Hence, the dressed microwave potentials are assumed to be perfectly symmetric. In this section, we consider the effect of both dressed potentials : $V^{|\bar{a}\rangle}$ and $V^{|\bar{b}\rangle}$, but for the sake of clarity, we refer to a clock state : $|a\rangle$ or $|b\rangle$ by $|S\rangle$.

A microwave adiabatic coupling with Rabi frequency Ω between two states $|S\rangle$ and $|P\rangle$ results in a dressed state $|\bar{S}\rangle$ which is a linear superposition of $|S\rangle$ and $|P\rangle$. Such mixture can spoil the good coherence properties of the clock states since $|S\rangle$ and $|P\rangle$ have an opposite magnetic moment. Far from resonance (i.e. $|\Delta| \gg |\Omega|$), the coupling effect can be treated in a perturbative manner such as : $|\bar{S}\rangle \approx |S\rangle \pm |\Omega/2\Delta||P\rangle$, where $+(-)$ refers to the case of potential-barrier (potential-well) respectively. Using the latter expression, one can define a *contamination* rate : $\kappa = |\Omega/\Delta|$. When $\kappa \ll 1$, the contamination of $|\bar{S}\rangle$ by $|P\rangle$ can be neglected. This low contamination hypothesis is reasonable especially in the case of a potential-barrier since the atoms are permanently repelled in the vicinity of $|\Omega|$ minimum, but would limit, in all the cases, the coherent splitting to small distances (few microns) [71].

In general, for a high contamination rate ($\kappa \geq 1$), the dressed states are given by equation (56). In particular, the weight of the bare states $|P\rangle$ relatively to $|S\rangle$ in the dressed state $|\bar{S}\rangle$ increases, and it is given by (equation (58)) :

$$|\mathcal{R}_{P/S}| = (-1 + \sqrt{1+\kappa^2})/\kappa \tag{84}$$

which is always lower than 1. One can also verify that $|\mathcal{R}_{P/S}| \simeq \kappa/2$, if $\kappa \ll 1$, as described previously.

Here, we present a quantitative study of the contamination effect in general case : low ($\kappa \ll 1$) and high contamination rate ($\kappa \geq 1$). First, in the case of a perfectly-symmetrical interferometer configuration, we discuss the critical contamination level allowed to preserve the magic field. Then, we introduce a new interferometer configuration in order to preserve the magic field even in the case of a high contamination rate.

5.5.1 *Perfectly-symmetrical interferometer configuration*

For this purpose, we use a rigorous description of the static Zeeman shift E_{F,m_F} given by the Breit-Rabi formula (5) of each hyperfine level $|F, m_F\rangle$ [87]. Therefore, an accurate estimation of detunings that take into account the nonlinear dependence of the static field B is given by :

$$\Delta_a(B) = \omega_{mw,1} - \left[E_{2,-1}(B) - E_{1,-1}(B)\right]/\hbar \tag{85a}$$
$$\Delta_b(B) = \omega_{mw,2} - \left[E_{2,1}(B) - E_{1,1}(B)\right]/\hbar \tag{85b}$$

The spatial dependence of the static field B can be neglected if the condition : $k_B T \ll \hbar\omega_L(B_0)$ is verified. For instance, the spatial variations seen by a thermal cloud is : $\delta B/B_0 \approx k_B T/\hbar\omega_L(B_0) \approx 10^{-3}$ with the following numerical values : $T = 100$ nK and $B_0 \approx B_0^m \simeq 3.23$ G.

Furthermore, we suppose that Ω is constant, and its value is calculated using the contamination rate κ that we wish to study. Indeed, we do not consider the spatial variations (i.e. gradient), and assume that Ω is also constant across the atomic cloud. In practice, one should only know Ω in the center of mass of the atoms in order to estimate the contamination rate κ.

The energy difference $\Delta\bar{E}(B)$ between the dressed clock states can be deduced using the following :

$$\Delta\bar{E}(B) = \bar{E}_b(B) - \bar{E}_a(B) \tag{86a}$$
$$\bar{E}_a(B) = E_{1,-1}(B) + V_{mw}^{|a\rangle}(B) \tag{86b}$$
$$\bar{E}_b(B) = E_{2,1}(B) + V_{mw}^{|b\rangle}(B) \tag{86c}$$

where $V_{mw}^{|a\rangle}$ and $V_{mw}^{|b\rangle}$ are the adiabatic microwave shifts (cf. equation 72), which assumes a slow variation of the static field B seen by the atoms. The microwave frequencies $(\omega_{mw,1}, \omega_{mw,2})$ in equations (85), are chosen as in Figure 19. The detuning Δ_0, which has been introduced in section 4.3.4, is here used to calculate the microwave frequencies with the following expressions :

$$\omega_{mw,1} = \omega_{\text{hfs}} - 2\omega_L^0 + \Delta_a^0 \tag{87a}$$
$$\omega_{mw,2} = \omega_{\text{hfs}} + 2\omega_L^0 + \Delta_b^0 \tag{87b}$$
$$\Delta_a^0 = -\Delta_b^0 = \Delta_0 \tag{87c}$$

where $\omega_L^0 = \omega_L(B_m^0)$ and B_m^0 is the static magic field in the absence of the microwave field (B_m^0 is set to 3.23 G in the following numerical simulations).

For low contamination ($\kappa \ll 1$) in the case of a splitting by a potential-well, Figure 23a shows that $\Delta\bar{E}$ has a minimum corresponding to a magic field B_m. As expected earlier, B_m is very close to the static value B_m^0. Yet, B_m exists only for contamination rates κ that are

lower compared to some critical value κ_c. Hence, κ has to be kept very low (typically less than a few percent) as shown in figure 23a.3. The shown results are relative to the case of a potential-well beam-splitter ($\Delta_0 < 0$), and similar results can be found for a potential-barrier beam-splitter ($\Delta_0 > 0$).

On the other hand, for a high contamination value ($\kappa \geq 1$), the magic point does not exist for both beam-splitter cases as shown in Figure 23b. This is due to the resonance behavior that occurs at $B = B_s$ (i.e. $\Delta(B_s) = 0$) where the local variation of $\Delta\bar{E}$ is very important. The proximity of B_s and $B_0 = B_m^0$ is due to the low initial value of the detuning Δ_0 since :

$$\omega_L(B_s) = \omega_L(B_0) - \Delta_0/2 \tag{88}$$

The resonance behavior, shown in Figure 23b, occurs at $B = B_s$ which does not depend on the applied microwave power (i.e. Ω). This property can be used to perform a precise calibration of the static field minimum B_0, since the energy variation $\Delta\bar{E}(B)$ around B_s in this case, depends only on the setting of the microwave frequencies[8,9].

Increasing $|\Delta_0|$ would allow a larger separation between B_s and B_m^0, and so a larger contamination κ could be used as shown in Figure 23a.3. In practice, $|\Delta_0/\omega_L^0|$ has to be kept low in order to preserve the symmetry of the potentials (cf. section 5.2).

One can also notice in Figure 23b.2 that $\Delta\bar{E}(B)$ has a new class of minima around 3 G. Yet, these points cannot be reached because the atoms would be lost around the resonance (cf. section 5.3). Unfortunately, by applying these results to the realistic beam-splitters proposed in Figure 19, one can show that the magic field B_m does not exist, since the contamination value seen by the atoms are estimated to $\{1.21, 0.45\}$ in (a) and (b) respectively.

In the following, we propose a solution to overcome the previous difficulty by modifying the perfectly-symmetrical interferometer configuration.

5.5.2 *Perturbed-symmetrical interferometer configuration*

The properties of the singular point B_s are closely related to the interferometer symmetrical design, proposed in section 4.3.4. In particular, the amplitude of the energy variation and the sign of its slope around

8 Which can be performed with a good accuracy.

9 This property can be also used to reach experimentally the *ideal* symmetrical configuration with : $\Delta_a^0 = -\Delta_b^0$ and $P_1 = P_2$ proposed in section 4.3.4. If the interferometer is not perfectly symmetrical, the latter property is no longer valid.

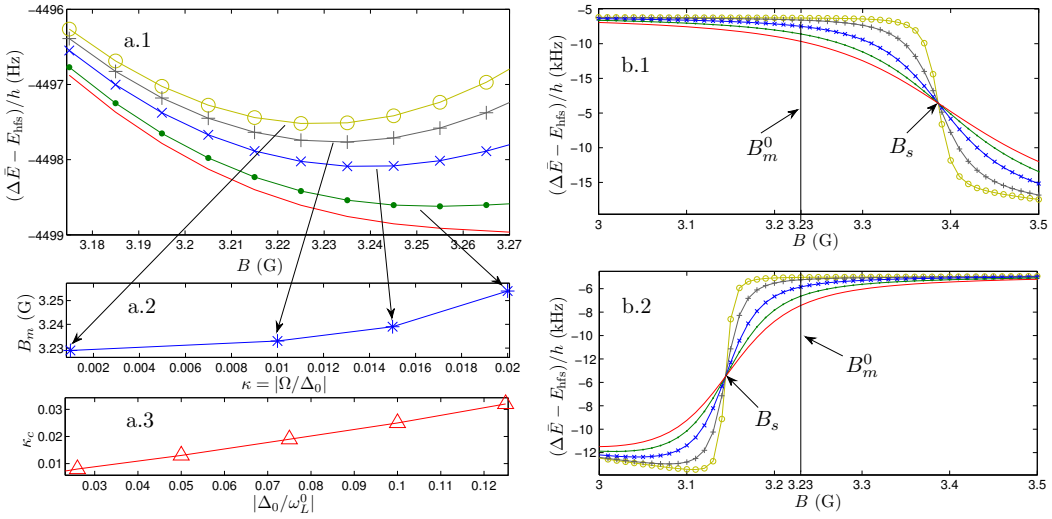

Figure 23: Contamination effect of the clock states for a perfectly-symmetrical interferometer configuration. (a) For low contamination (a.1) Energy difference $\Delta\bar{E}$ as a function of B in case of a potential-well for the detuning $|\Delta_0/\omega_L^0| = 0.1$. From top (circle-marked line) to bottom (solid line), colors correspond to the contamination : $\kappa = \{0.1, 1, 1.5, 2, 2.25\} \times 10^{-2}$. (a.2) Arrows indicate $\Delta\bar{E}(B)$ minima that correspond to the "magic" fields B_m. (a.3) B_m exists only if $\kappa < \kappa_c$: a critical contamination rate that depends on $|\Delta_0|$. (b) For high contamination, $\Delta\bar{E}$ as a function of B in the cases of a potential-well (b.1) and potential-barrier (b.2) for the detuning : $\Delta_0/\omega_L^0 = \{-0.1, 0.05\}$ respectively. From circle-marked line to solid line, colors correspond to the contamination : $\kappa = \{0.1, 0.25, 0.5, 0.75, 1\}$.

B_s can be changed by introducing a small perturbation to the interferometer parameters[10] such as :

$$\Delta_a^0 = (1+\epsilon)\Delta_0; \qquad \Delta_b^0 = -(1-\epsilon)\Delta_0 \tag{89a}$$

$$\Omega_a = (1+\frac{\epsilon}{2})\Omega; \qquad \Omega_b = (1-\frac{\epsilon}{2})\Omega \tag{89b}$$

where ϵ is a perturbation parameter such that : $|\epsilon| \ll 1$, and which has the same sign than Δ_0 (i.e. $\epsilon\Delta_0 > 0$).

The effect of this perturbation on the symmetry of the potentials is weak, especially for low contamination values ($\kappa \ll 1$) where the microwave shifts can be approximated by equations (69). In the latter case, using equations (72), the resulting relative dissymmetry is approximately given by :

$$\Delta V_{mw}/V_{mw} = (\kappa^2/2)\epsilon + \mathcal{O}(\epsilon^3) \tag{90}$$

10 which can be done experimentally by changing the parameters of the microwave fields.

More generally, for high values of contamination the microwave shifts can be approximated by equations (72), and so the relative dissymmetry as function of κ is about :

$$\Delta V_{mw}/V_{mw} = \left(1 - 1/\sqrt{1+\kappa^2}\right)\epsilon + \mathcal{O}(\epsilon^3) \tag{91}$$

where $(1 - 1/\sqrt{1+\kappa^2})$ is a bounded function of κ. The previous estimations are valid only in the limit of a small perturbation : $|\epsilon| \ll 1$.

The variation of the energy $\Delta\bar{E}(B)$ in the case of a potential-well are shown in Figure 25a where $\epsilon = -10^{-2}$. In this case, the magic points B_m reappears and remains even in the case of high contamination ($\kappa \geq 1$). Here, the slope sign of $\Delta\bar{E}(B)$ around the resonance (i.e. $B \approx B_s$) has changed compared to Figure 23b.1. Hence, this perturbation does not remove the static magic point B_m^0 but only shifts its value, as shown in 25b.

Similar results can be found for a potential-barrier by simply inverting the perturbation sign : $\epsilon = 10^{-2}$. Yet, in the latter case, the magic field B_m would be shifted to the lower values ($B_m < B_m^0$), since it is related to the resonance position $B_s < B_m^0$ (cf. Figure 23b).

The initial detuning value has been chosen relatively high ($|\Delta_0| = 0.31 \times \omega_L^0$), which plays an important role to preserve the existence of the magic point B_m up to high contamination values (cf. equation (88)). Moreover, by choosing a lower initial detuning $|\Delta_0|$, the perturbation would not play any significant role and the system would behave exactly like in the perfectly-symmetrical configuration.

As can be seen in Figure 26, the maximal allowed contamination κ_c remains very low[11], if $|\Delta_0|$ is chosen lower than some threshold-value : $|\Delta_0^{T_1}| \simeq 0.255 \times \omega_L^0$, for a potential-well ($\Delta_0 < 0$) and $|\epsilon| = 10^{-2}$. Whereas, for $|\Delta_0| > |\Delta_0^{T_1}|$, κ_c increases in exponential manner.

This threshold-value $|\Delta_0^{T_1}|$ indicates the existence of a second minimum[12] $B_m^{(2)}$ close to the singular point B_s in addition to the first minimum $B_m^{(1)}$ which is close to the original minimum B_m^0, as can been seen in Figure 24. For a potential-well beam-splitter, as shown in Figure 26, the second minimum $B_m^{(2)}$ remains even for very high contamination value ($\kappa \to \infty$).

Both minima eventually collapse forming a single minimum if $|\Delta_0| > |\Delta_0^{T_2}|$, where $|\Delta_0^{T_2}| \simeq 0.283 \times \omega_L^0$, for a potential-well, is a second threshold-value. In the latter case, the variation of B_m as a function of κ is continuous, as can be seen in Figure 25b. Therefore, it is possible to follow adiabatically the evolution of the magic field B_m, in contrast to the intermediate case : $|\Delta_0^{T_1}| < |\Delta_0| < |\Delta_0^{T_2}|$ where an abrupt variation (i.e. discontinuity) of B_m occurs, as shown in Figure 24.

11 In order of few percent as shown in Figure 23a.3.

12 The detuning $\Delta(B_m^{(2)})$ is very low in this case, so we have verified that its sign does not change by increasing κ. It is worth noticing that $B_m^{(2)}$ do not exist if the microwave power is off ($\kappa = 0$).

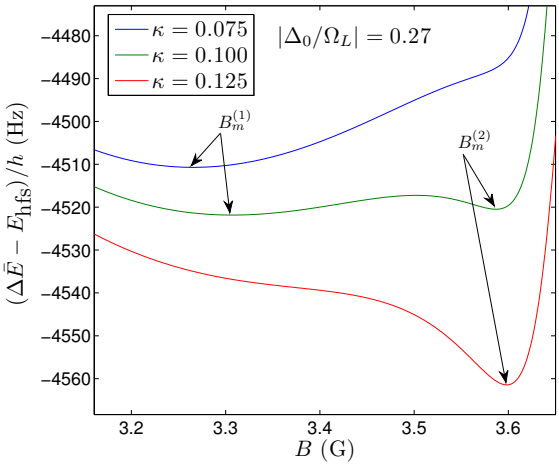

Figure 24: Energy difference $\Delta\bar{E}$ as a function of B, in case of a potential-well, with the initial detuning $|\Delta_0/\omega_L^0| = 0.27$ and the perturbation parameter $\epsilon = -10^{-2}$. From top to bottom, color lines correspond to the ratio : $\kappa = |\Omega/\Delta_0| = \{0.075, 0.100, 0.125\}$. In this case, for $\kappa = 0.1$, there exists two magic fields $B_m^{(1)}$ and $B_m^{(2)}$.

As expected, the threshold-value $|\Delta_0^{T_2}|$ depends on the perturbation value $|\epsilon|$; in particular, it can be made lower by choosing a lager perturbation value $|\epsilon|$ as shown in Figure 27.

In Figure 25, the initial value of $|\Delta_0|$ is relatively high. Nevertheless, this does not compromise the validity of the two-level model used in this section because the static field $\mathbf{B_0}$, initially seen by the atoms, allows the selection of only π-transitions (i.e. $\mathbf{B_0}.\mathbf{z} = 0$). In addition, the interferometer symmetry is also not affected since $|\Delta(B_m)|$ decreases during the splitting to reach eventually $0.1 \times \omega_L$, as shown in Figure 25c, where the quasi-resonant coupling regime is valid.

Experimentally, the internal state superposition of the clock states can be prepared initially in the magic static field B_m^0, then the evolution of the magic field B_m can be followed adiabatically while splitting by increasing the value of magnetic field in the trap center $\mathbf{r_0}$. This can be done by changing the bias field values and without affecting the position and angular frequencies of the static trap [85, 99]. Nevertheless, as B_m is now varying, one should pay attention to the variation of the detuning value $|\Delta|$ (cf. equation (85)) to estimate the contamination such as : $\kappa_a = |\Omega/\Delta(B_m)|$ where $|\Delta|$ is here defined as the mean value of $|\Delta_a|$ and $|\Delta_b|$; and κ_a is called adiabatic contamination in the following.

The second derivative of the energy $\Delta\bar{E}(B)$ at $B = B_m$ is computed in Figure 25d. Even though this variation shows an increase by a factor of 10 compared to the initial variation, it is still important to follow the magic point B_m variation in order to reduce the effect of the static field fluctuations [112].

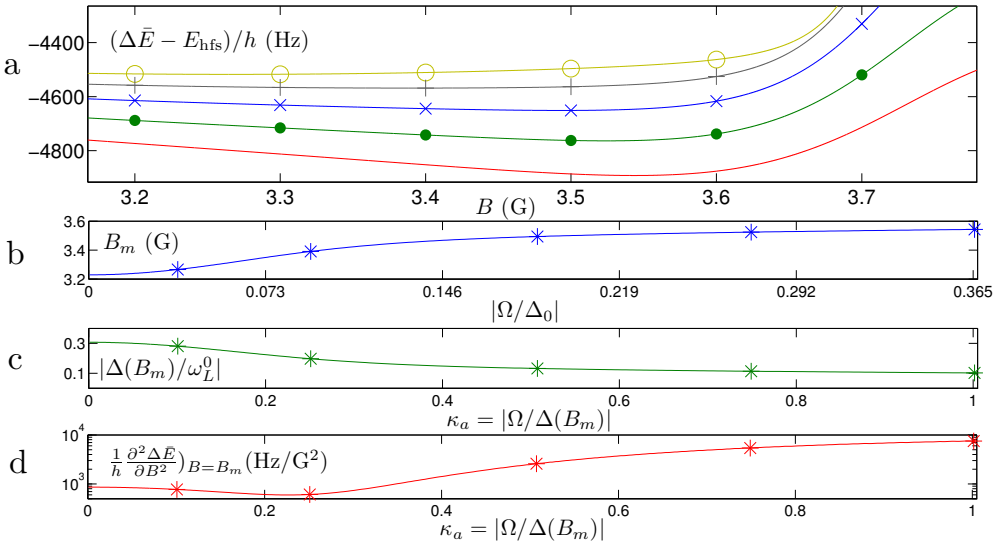

Figure 25: Contamination effect of the clock states for a perturbed symmetrical interferometer, in case of potential-well, with the initial detuning $|\Delta_0/\omega_L^0| = 0.31$ and the perturbation parameter $\epsilon = -10^{-2}$. (a) Energy difference $\Delta\bar{E}$ as a function of B. From top (circle-marked line) to bottom (solid line), colors correspond to the ratio : $|\Omega/\Delta_0| = \{0.093, 0.168, 0.235, 0.301, 0.365\}$. (b) The magic field B_m as function of the contamination $\kappa = |\Omega/\Delta_0|$. (c) Assuming that the system follows adiabatically the evolution of the magic B_m, the detuning evolution is given by : $|\Delta(B_m)|$. The star markers correspond to the minima of the energy curves shown up here and with the adiabatic contamination $\kappa_a = |\Omega/\Delta(B_m)| = \{0.1, 0.25, 0.5, 0.75, 1\}$. (d) The sensitivity to the magnetic field fluctuations around the magic field B_m is given by the quadratic term : $\partial^2\Delta\bar{E}/\partial B^2)_{B=B_m}$.

Finally, it is worth noting that the spatial variations of the trapping static field B seen by the atoms during the splitting, are in the order of few percents[13], and should be also taken into account. This is another advantage of the (perturbed-) symmetrical beam-splitter design since the static magnetic field can be set at the magic value B_m for both clock states at the same time, which is not possible using a unilateral beam-splitter with only one CPW [71].

13 On the order of $\{3\%, 1\%\}$ in Figure 19a and 19b, respectively.

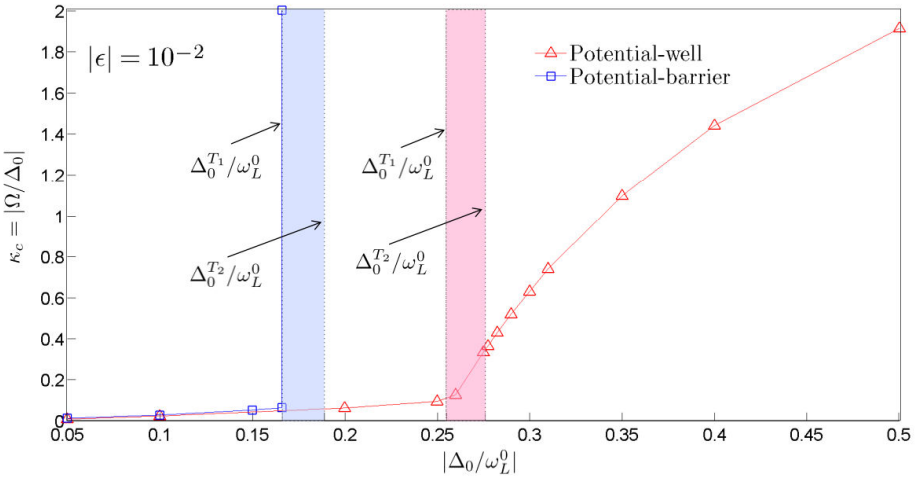

Figure 26: The maximum allowed contamination rate $\kappa_c = |\Omega/\Delta_0|$ as a function of the initial detuning $|\Delta_0|$, for a potential-barrier (in blue) and a potential-well (in red), and with the perturbation parameter $|\epsilon| = 10^{-2}$. For $\kappa > \kappa_c$ the magic point B_m does not exist. The parameters $\Delta_0^{T_1}$ and $\Delta_0^{T_2}$ indicate the region where two minima of $\Delta\tilde{E}(B)$ exists. It is colored in blue (red) for a potential-barrier (well).

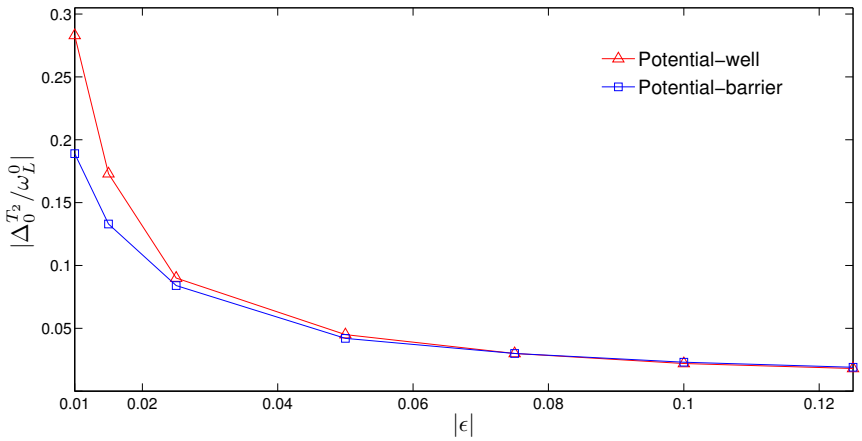

Figure 27: The variation of $|\Delta_0^{T_2}|$ as a function the perturbative parameter $|\epsilon|$ for a potential-barrier (in blue) and a potential-well (red). Following adiabatically the variation of the magic field B_m is possible if : $|\Delta_0| > |\Delta_0^{T_2}|$.

5.6 SENSITIVITY TO THE MICROWAVE FIELD FLUCTUATIONS

A variation of the Rabi frequency due to power fluctuations of microwave (or radio-frequency) field will degrade the interferometer signal by two mechanisms :

- A noisy preparation of the population of the internal states after the first $\pi/2$ pulse will directly propagate onto the measured transition probability after the second $\pi/2$ pulse, which is similar to a detection noise. This effect is fully treated and measured in the atomic clock on chip experiment (TACC) [111].
- A change of the microwave energy-shifts due to the dressing field seen by the clock states $|a\rangle$ and $|b\rangle$. Hence, the energy difference between the dressed states $|\bar{a}\rangle$ and $|\bar{b}\rangle$ is sensitive to the microwave power fluctuations. In case of this interferometer design, this effect is expected to be the main source of technical noise. The state-of-art microwave-power stabilization is relatively about : $\Delta P_{mw}/P_{mw} = 10^{-4} - 10^{-5}$ [163] and so the precision of the phase measurement would be limited by the same amount.

In the following, by making profit of the interferometer symmetrical design, we propose several solutions to overcome the previous limitation.

5.6.1 *Design of the microwave frequency chain*

The interferometer design described in section 4.3 requires the use of two microwave frequencies : $\omega_{mw,1}$ and $\omega_{mw,2}$ with the average value : $\bar{\omega}_{mw} \simeq E_{\text{hfs}}/\hbar \approx 6.834$ GHz and difference : $\Delta\omega_{mw} = |\omega_{mw,2} - \omega_{mw,1}| \approx 4\omega_L^0 \approx 2\pi \times 9$ MHz.

A technical solution to reduce the effect of the microwave power fluctuation can be performed by using the same microwave source in order to generate both microwave signals, and make the power fluctuations of the source common mode for the two microwave dressing potentials. This frequency conversion, shown in Figure 28a, is usually performed using a double balanced mixer (based on amplitude modulation). In this case, the local-oscillator (LO) frequency and the radio-frequency (RF) have to be set as the following : $\omega_a = \bar{\omega}_{mw}$ and $\omega_b = \Delta\omega_{mw}/2$, respectively. The mixer is able to generate two side bands with the required frequencies. Nevertheless, this solution is not suitable for two main reasons :

- The mixer will generate the frequencies $\omega_{mw,1}$ and $\omega_{mw,2}$ but both come out of the intermediate frequency (IF) port. There will be also leakage of the LO frequency and some harmonic

intermodulation products. In order to be left with only ω_a in one channel and ω_b in the other, very sharp filter are needed with a quality factor in the order of $4\omega_L/\omega_{\text{hfs}} \approx 7.5 \times 10^5$. Such a filter does not exist in the market and it is challenging to build one.

- Even if filters with the required rejection can be build, they need also to be extremely-well amplitude-matched, which is very difficult to realize in practice.

Here, we propose a design of a microwave-frequency chain that does not require the use of rejection filters. Instead, single-sideband modulation (SSBM) can be used in order to avoid the bandwidth doubling (RF signal), and the power wasted on a carrier (LO signal). Single-sideband has the mathematical form of quadrature amplitude modulation (QAM, IQ modulation) in the special case where one of the baseband waveforms is derived from the other, instead of being independent signals:

$$s_{ssbm}(t) = s(t)\cos(\omega_a t) - \hat{s}(t)\sin(\omega_a t) \tag{92}$$

where $s(t)$ is the RF signal, $\hat{s}(t)$ is its Hilbert transform. Figure 28b shows a schematic of the microwave frequency chain and its power stabilization circuits. The SSMB component requires both I and Q signals which are two RF signals in quadrature. These signals have an identical frequency and are generated using the same function generator (FG), so they are expected to have a common-mode power fluctuation. The quality of the undesired sideband rejection rests upon the precision of the quadrature phase between the RF I and Q signals (estimated about 25 dB) [164]. The output signals are expected to share the same amplitude fluctuations caused by the RF and MW generators. However, a small difference of the power fluctuations might occur, due to the difference between the two modulator components (which should be limited since these components are passive). Moreover, amplification of the output signal is usually required because the LO generator and SSBM components have a limited output power (about 15 mW) [163]. Therefore, a microwave stabilization circuit is recommended in order to reduce power fluctuations caused by the amplifier. A relative power-precision of about : 10^{-4} has been shown in [163].

Proposal to transfer to a stable double-well after splitting

After splitting the clock states, one can transfer them to a stable double well. Here, we discuss two proposals to transfer the clock states to :

- a static double-well after splitting using a potential-well
- a microwave double-well after splitting using a potential-barrier

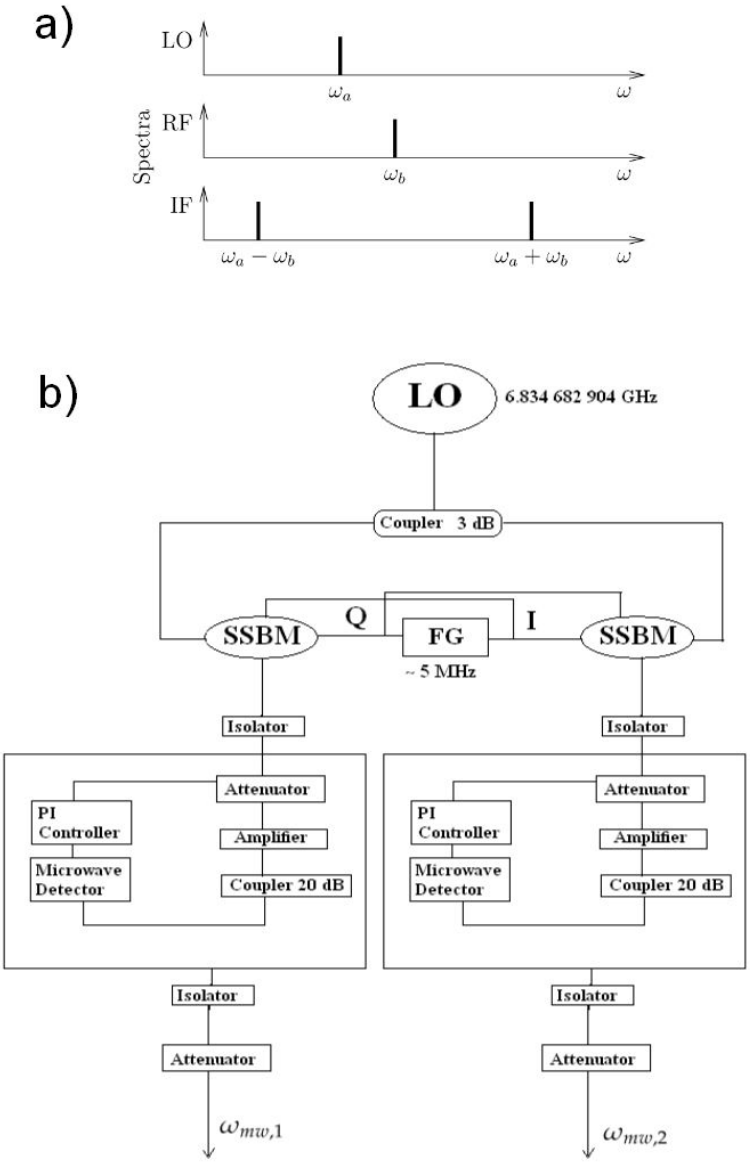

Figure 28: (a) Frequency conversion scheme (b) The microwave frequency chain.

LO : Microwave Generator	R&S SMF100A-B22-B32
GF : Generator Function	TEKTRONIX AFG3102
SSBM : Modulator	MITEQ SSM0208 C2MDQ | SDM0208LC1CDQ
Amplifier	MC ZVA-183-S+
Coupler 20 dB	PULSAR CS20-10-435/1
Coupler 3 dB	AAM CS-PWD-2W-4G-8G-10W-Sf
Isolator	AEROTEK H14-1LFF
Attenuator	AAT-24-479/2S
Microwave Detector	AGILENT NRP-Z11

5.6.2 *Static double-well*

After splitting using an attractive potential, the atoms become eventually trapped (mainly) by the microwave energy V_{mw}, in the vicinity of the CPWs positions ($|x_m| \simeq \delta$, cf. section 5.4.1). In this case, the wires of each CPW can be used to create a static potential similar to V_{mw}, by injecting static currents in the same proportion than its corresponding microwave currents : $\{-I_{dc}/2, I_{dc}, -I_{dc}/2\}$. Hence, the sensitivity of the clock states potentials to the microwave field fluctuations is suppressed during the holding time [165].

Moreover, it is possible to transfer adiabatically the atoms from the microwave potential to the static potential. This can be done by rumping up the static currents while switching off the microwave power in each waveguide, which is technically possible using on-chip bias-tee [163]. The created potentials are similar for both states, and so called double-well (DC-DW) [69]. However, one has to verify that dressed potentials of the clock states have a large trap-depth compared to the atomic-cloud temperature, in order to reduce the mixing of the clock states between the wells (due to the thermal motion of the atoms and the tunnelling effect).

On the other hand, this proposal can be seen as a solution to reduce the effect of the transition mixing during the holding time, treated in section 5.2, since the potentials are conceptually perfectly-symmetrical. In practice, small dissymmetry of the potentials is expected due to the experimental uncertainties about the static trap positon $\mathbf{r_0}$ (due to the fabrication uncertainties or the width of the wires). This type of dissymmetry is potentially low and can be minimized experimentally by adjusting slightly the bias field values.

Further discussion about this proposal is given in section 5.7, where the effect of fluctuations of the currents will be treated.

5.6.3 *Microwave double-well*

In this section, we discuss the possibility of creating perfectly symmetrical potentials using only microwave dressing, in order to avoid the additional technical complexity required by the previous method (additional static-currents sources, bias-tee on chip).

In general, to design perfectly-symmetrical potentials, one should take into account, for each clock state, the potential spatial-dependencies related to :

- The type of transition $\{\pi, \sigma\}$ which depends respectively on $B_{mw}^{\text{eff}} = \{B_{mw}^{\parallel}, B_{mw}^{\perp}\}$, (cf. equation (69)).
- The coplanar waveguides positions.

The symmetry conditions, using a one-dimensional model, can be written :

$$\text{Direct} - \text{Potentials} : \quad V_{mw,\,\pi}^{|a\rangle,\,CPW_1}(-x) = V_{mw,\,\pi}^{|b\rangle,\,CPW_2}(x) \tag{93a}$$

$$V_{mw,\,\sigma}^{|a\rangle,\,CPW_1}(-x) = V_{mw,\,\sigma}^{|b\rangle,\,CPW_2}(x) \tag{93b}$$

$$\text{Crossed} - \text{Potentials} : \quad V_{mw,\,\pi}^{|a\rangle,\,CPW_2}(-x) = V_{mw,\,\pi}^{|b\rangle,\,CPW_1}(x) \tag{93c}$$

$$V_{mw,\,\sigma}^{|a\rangle,\,CPW_2}(-x) = V_{mw,\,\sigma}^{|b\rangle,\,CPW_1}(x) \tag{93d}$$

For the sake of simplicity, we assume that the large detuning condition is fulfilled, therefore, the microwave energy shift V_{mw} is given by equations (69) and the spatial variation of the detunings $\Delta_{m_1}^{m_2}$ can be neglected (i.e. $\Delta_{m_1}^{m_2}(\mathbf{r}) \approx \Delta_{m_1}^{m_2}(\mathbf{r_0})$). Using a symmetrical disposition of the CPWs as shown in Figure 17, the latter equations can be simplified to the following :

$$\frac{P_1}{\Delta_a^\pi} = -\frac{P_2}{\Delta_b^\pi} \tag{94a}$$

$$\frac{P_1}{\omega_L^0 + \Delta_a^\pi} + \frac{1}{6}\frac{P_1}{-\omega_L^0 + \Delta_a^\pi} = -\frac{1}{2}\frac{P_2}{\omega_L^0 + \Delta_b^\pi} \tag{94b}$$

$$\frac{P_1}{-4\omega_L^0 + \Delta_a^\pi} = -\frac{P_2}{4\omega_L^0 + \Delta_b^\pi} \tag{94c}$$

$$\frac{P_1}{-3\omega_L^0 + \Delta_a^\pi} = -\frac{P_2}{5\omega_L^0 + \Delta_b^\pi} - \frac{1}{6}\frac{P_2}{3\omega_L^0 + \Delta_b^\pi} \tag{94d}$$

One can show that this system of equations has a unique solution[14] : $\Delta_a^\pi = -\Delta_b^\pi = 2\omega_L^0$ and $P_1 = P_2$. This corresponds to the case where only one microwave signal, with the frequency $\omega_{mw} = E_{\text{hfs}}/\hbar$, injected in both coplanar waveguides.

This proposal can be done experimentally using the microwave frequency chain introduced in section 5.6.1, where the local oscillator (LO) frequency is set equal to ω_{hfs} and the radio-frequency (i.e. frequency-generator (FG)) power is progressively set to zero after the splitting stage. This proposal simplifies considerably the microwave frequency chain, at least during the holding stage, by using only one microwave generator. As a consequence, the fluctuations of the microwave powers seen by each clock state are expected to be highly correlated and the common-mode noise rejection would be better using this interrogation method.

On the other hand, one can notice that the detuning sign Δ_a^π (Δ_b^π) is positive (negative). Hence, the splitting should be done using a

14 Combining these equations implies the resolution of the following polynomial equation : $(R_a - 2)(9 - 21R_a + 24R_a^2 - 14R_a^3 + 4R_a^4) = 0$, where $R_a = \Delta_a^\pi/\omega_L^0$. This equation has a unique real solution : $R_a = 2$.

potential-barrier beam-splitter[15], because these detunings should not change signs while splitting (adiabatically), as discussed in section 5.3.

Figure 29a shows an example of the dressed potentials simulated using a full-simulation (equation (79)). It turns out that the potentials are not only symmetrical $V^{|\bar{a}\rangle}(-x) = V^{|\bar{b}\rangle}(x)$ but are also identical $V^{|\bar{a}\rangle}(x) = V^{|\bar{b}\rangle}(x)$. Hence, each potential is self-symmetrical which makes this proposal similar to the static double-well proposal and justifies its naming as : microwave double-well (MW-DW).

The spatial variation of the direct and crossed potentials, described by equations (93), are shown in Figure 29b. These potentials have been generated using equation (72) and the spatial variation of the detunings has been taken into account. In particular, one can notice that the symmetry conditions of these potentials are satisfied. Since all the detunings $|\Delta_{m_1}^{m_2}|$ are larger than ω_L^0, the approximation of a large detuning regime is verified ($\Omega^{max} \approx 0.4\omega_L^0$ with $\omega_L^0 = \omega_L(B_0)$ and $B_0 = B_0^m$). Moreover, the spatial variation of the detunings, neglected earlier, has no-significant effect on the symmetry of the clock state potentials. Indeed, the relative dissymmetry of the eigen-frequencies, corresponding to the trapping potentials, is : $\{3.9 \times 10^{-4}, 2.2 \times 10^{-6}, 2.2 \times 10^{-6}\}$ along the eigen-directions $\{\tilde{\mathbf{x}}, \tilde{\mathbf{y}}, \tilde{\mathbf{z}}\}$, which is a considerable improvement compared to the potentials shown in Figure 19 (cf. Table 2).

Nevertheless, this proposal has a major drawback : due to the high detuning values $|\Delta_{m_1}^{m_2}|$, a high microwave coupling $\Omega_{m_1}^{m_2}$ is required to produce a significant energy-shift ($|V_{mw}| \approx |\Omega_{m_1}^{m_2}|^2/4|\Delta_{m_1}^{m_2}|$) in the trap center, in order to reduce the mixing of the clock states between the wells, as can be seen in Figure 29a. This can be done using two different methods :

- Increasing the injected microwave power P_{mw} in the CPWs. In practice, this is limited by the size of the CPW wires which has been chosen intentionally small to create high field gradient. In our chip design, the maximum allowed power is about : $P_{\max} = 4P_0 \approx 740$ mW.

- Decreasing the static trap distance from the chip surface h_0 in order to increase the Rabi frequency $\Omega_{m_1}^{m_2}$. This is the case of Figure 29 ($h_0/\delta = 2.59$, where $h_0/\delta = 3.70$ in Figure 19b). Yet, the transfer after splitting to this configuration remains challenging, since the chosen ratio h_0/δ does not allow a state-selective splitting[16] using a microwave potential-barrier beam-splitter[17].

  A possible solution would be to reduce further the CPWs distance from the center δ, either by reducing the size of the CPW

15 The initial detunings should be chosen such that : $\Delta_a^\pi = -\Delta_b^\pi > 0$.

16 As a proof of principle, this method can be used to split only one state in a double-well, by ramping up a barrier, in the static-trap center, in similar way to the well-established RF-splitting method [67].

17 In this case, with $h_0/\delta = 2.59$, the microwave gradient in trap center would be weak since it corresponds to the side lobe of the component B_{mw}^x, shown in Figure 14

wires or by using two adjacent striplines[18] instead of CPWs, as described in section 8 and Figures 52 & 54b [Config. *IV*].

An alternative solution that does not require to change the chip design, would be to reduce the ratio : h_0/δ form 4 to 2.5 by reducing h_0 while splitting, which would demand a careful calibration of all the experimental parameters (DC and MW currents, bias fields).

- Decreasing the Larmor frequency $\omega_L(B_0)$, by reducing the static field value $B_0 < B_m^0 = 3.23$ G, in order to reduce the detunings : $|\Delta_{m_1}^{m_2}| \approx 2\omega_L(B_0)$. B_0 is usually set equal to the magic field value B_m that can be reduced, in case of a potential-barrier, up to about 20% from the common value B_m^0 as discussed in section 5.5.2 (cf. Figure 25). Higher reduction of B_0 value is possible, at least in principle, by setting $B_0 < B_m$. Yet, the magic field condition is not fulfilled in this case.

This (MW-DW) proposal can be seen as an efficient tool to reduce the dissymmetry of the potentials and their sensitivity to the microwave field fluctuations. However, with the current chip design (cf. section 8), the transfer of clock states to the configuration shown in Figure 29 requires a supplementary experimental and modelling efforts.

Hereafter, we present a transfer-solution to the microwave double-well configuration shown in Figure 29a, by setting the static field in the trap center B_0 lower than the magic value B_m^0 during the splitting stage ($B_0 = B_m^0/10$).

As shown in Table 3, initially the ratio h_0/δ is set to 4.4 to allow a state-selective splitting using a potential-barrier, and the detunings are set to : $|\Delta_\pi^a| = |\Delta_\pi^b| = 0.05 \times \omega_L^0$ to allow a quasi-symmetrical splitting using π-transitions. The static trap is created using a Z-trap[19]. The length of the central wire is $L = 600$ μm. The static-trap angular frequencies can be adjusted by changing the static current flowing through the Z-wire and the trap distance from the chip surface h_0 by changing the bias-fields values. As shown in Figure 30 and Table 3, the splitting is performed by increasing the microwave power P injected in the CPWs [step (a-b)], then the detunings are increased progressively to reach eventually the required value $\Delta_\pi^a = -\Delta_\pi^b = 2\omega_L(B_0)$ [Step (c-e)]. Once the splitting is performed, the distance h_0 can be reduced to allow a high microwave shift $|V_{mw}|$ without exceeding the maximal allowed microwave power $P_{\max}$ [step (d-f)]. Finally, the static field value B_0 is increased, by changing the bias fields, to reach the magic value B_m^0 [step (f)]. This transfer solution is experimentally realistic using the current chip design, yet the effect of the

18 A stripline (CPS) [166, 167] has only two wires, so the distance between the microwave signals 2δ can be reduced in principle to (almost) zero, but in practice, one has to take into account the coupling effect.

19 Which has a better trap-depth than a Dimple trap in the case of low axial frequency.

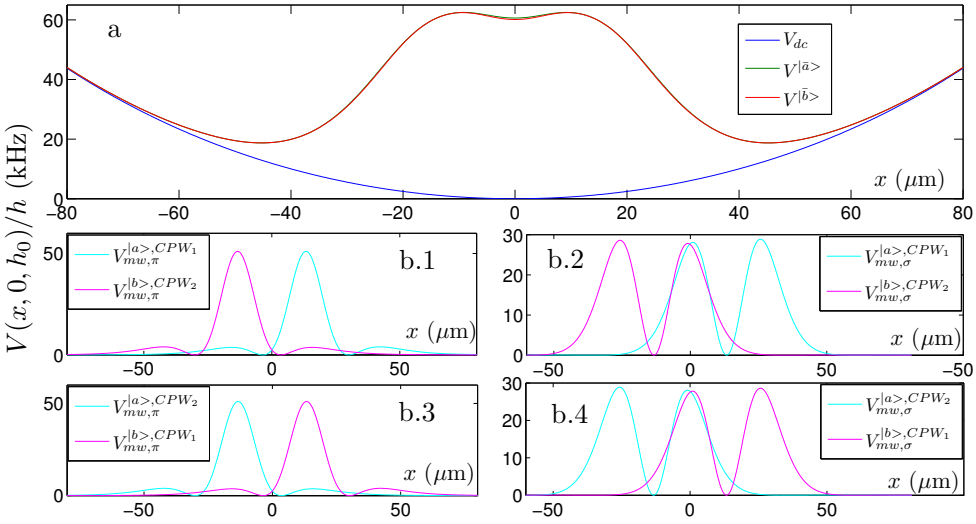

Figure 29: The microwave double-well proposal (MW-DW). (a) The clock-state potentials shown along the axial direction x. The static field parameters are chosen such the static trap V_{dc} has the following characteristics : $\omega_\perp/2\pi = 1800$ Hz, $\omega_x/2\pi = 38$ Hz and $h_0 = 35$ μm and created using a Z-wire pattern on-chip where the length of its central wire is : $L = 600$ μm. The microwave field parameters are : $\omega_{mw,1} = \omega_{mw,2} = E_{\text{hfs}}/\hbar$, $P_1 = P_2 = 2P_0$ and the CPWs positions are : $\delta_1 = \delta_2 = 13.5$ μm (cf. Figure 52 [Config. *III*]). (b) The microwave energy shifts V_{mw}, classified as direct (b.1, b.2) and crossed (b.3, b.4) potentials, are shown as a function of x.

static field B fluctuations during this stage has to be analyzed experimentally since $B_0 < B_0^m$.

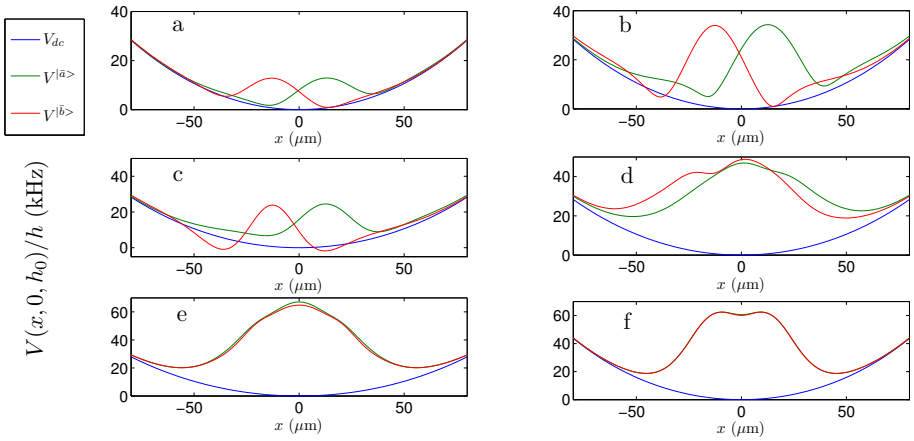

Figure 30: The potentials of the clock states during the splitting and transfer to the microwave double-well configuration (MW-DW). The parameters of the static and microwave fields, for each step (a-f), are described in Table 3.

Step	h_0 [μ m]	B_0 [G]	$\omega_x/2\pi$ [Hz]	$\omega_\perp/2\pi$ [Hz]	$\Delta_a^\pi/\omega_L(B_0)$	$\Delta_b^\pi/\omega_L(B_0)$	P_{mw}/P_0
a	60	0.323	30	650	0.05	-0.05	0.1
b	60	0.323	30	650	0.05	-0.05	$\downarrow$ 0.5
c	60	0.323	30	650	$\downarrow$ 0.5	$\downarrow$ -0.5	$\downarrow$ 2
d	60	0.323	30	650	$\downarrow$ 1.5	$\downarrow$ -1.5	$\downarrow$ 4
e	$\downarrow$ 50	0.323	30	$\downarrow$ 930	$\downarrow$ 2	$\downarrow$ -2	$\downarrow$ 2
f	$\downarrow$ 35	$\downarrow$ 3.23	$\downarrow$ 38	$\downarrow$ 1800	$\downarrow$ 2	-2	2

Table 3: Sequence of the static and microwave fields parameters for splitting and transferring the clock states to the microwave double well proposal (MW-DW) shown in Figure 29 using the Config. *III* on our chip (cf. Figure 52). The microwave powers injected in the CPWs are set such that : $P_1 = P_2 = P_{mw}$. The static trap is created using a Z-trap where the length of the central wire is : $L = 600$ μm.

5.6.4 *Proposal of symmetrical beam-splitter with one coplanar waveguide*

The sensitivity of the clock states to the microwave field fluctuation is expected to be high due to the complexity of interferometer design where the generation of two microwave frequencies is required. Using the proposed frequency chain in section 5.6.1, the microwave fluctuations seen by the clock states can be put in common, but a careful calibration of the microwave components in Figure 28b is necessary. In the previous proposal (MW-DW), a unique microwave frequency (i.e microwave source) is required to create a microwave double-well, which is interesting during the holding stage, but the generation of two microwave frequencies remains necessary during the splitting stage.

Here, we present a proposal of a new beam-splitter using only one microwave frequency injected in a unique coplanar waveguide (CPW) during the whole interferometer sequence, as demonstrated in [71] but with an additional constraint on the symmetry of the potentials.

First, we suppose that the CPW and the Dimple wires are both located at $\mathbf{r} = \mathbf{0}$, as shown in Figure 31a. Then, let's suppose that the microwave shift is proportional to the microwave field such as : $V_{mw} \propto B_{mw}$. In the case of one-dimensional problem, one can imagine a symmetrical beam-splitter using the z-component of the microwave field B^z_{mw}, shown in Figure 31b, since the microwave shifts V_{mw} of the clock states have an opposite sign and B^z_{mw} is anti-symmetrical along the x-axis, such as :

$$V^{|a\rangle}_{mw}(-x) \propto B^z_{mw}(-x) = -B^z_{mw}(x) \propto V^{|b\rangle}_{mw}(x) \tag{95}$$

In practice, the microwave shift V_{mw} is proportional to the *square* of the effective microwave field : $V_{mw} \propto |B^{\text{eff}}_{mw}|^2$ (cf. equation (69)). Yet, the previous assumption can be approximately verified if one can add, to the CPW field B^z_{mw}, an additional homogenous *microwave* field along the z-axis : $B^z_{b,mw}$ created by the same microwave source. If the role of the terms : $|B^z_{b,mw}|^2$ and $|B^z_{mw}|^2$ can be neglected, one can write the microwave shift as :$V_{mw}(x) \propto (B^z_{b,mw})B^z_{mw}(x)$.

Furthermore, the effective field B^{eff}_{mw} can be assimilated to B^z_{mw} if the σ-transitions are dominant and only in the vicinity of the static trap center, where the trap axis is along the x-axis. Therefore, equation (95) can be satisfied : $V^{|a\rangle}_{mw,\sigma}(-x) = V^{|b\rangle}_{mw,\sigma}(x)$ by adjusting the microwave frequency ω_{mw} (i.e. the detuning Δ^{π}_{a}) in order to compensate the dissymmetry induced by the coupling coefficients $C^{m_2}_{m_1}$ (cf. Appendix C). Using equation (94b) with $P_1 = P_2 = P$ and $\Delta^{\pi}_{a} = \Delta^{\pi}_{b} + 4\omega^0_L$, one can show that two solutions of ω_{mw} are possible : $\Delta^{\pi}_{a} \simeq 5.71 \times \omega^0_L$ and $\Delta^{\pi}_{a} \simeq 0.78 \times \omega^0_L$. For the first solution, the microwave frequency ω_{mw} is far detuned from all transitions as shown in Figure 32. The second solution is not interesting since the π-transitions would break the

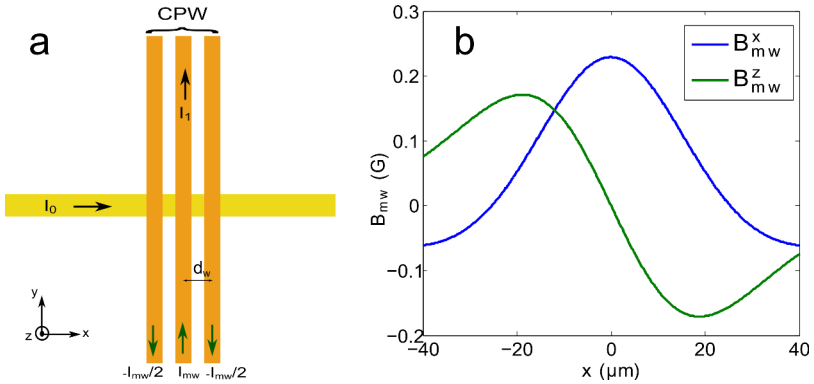

Figure 31: (a) Schematic of the chip wires configuration. The static currents I_0 and I_1 are used to create a Dimple trap. Here, the reference $\mathbf{r} = \mathbf{0}$ corresponds to the wires crossing and to the CPW position. (b) The spatial variation along the x-axis of the microwave field components B^x_{mw}, and B^z_{mw} along the x-axis and z-axis respectively. $B^x_{mw}(x)$ and $B^z_{mw}(x)$ have respectively a symmetrical and anti-symmetrical spatial profiles.

symmetry of the resulting potentials. Hence, only the first solution will be considered in the following.

Figure 33a(1-2) shows the microwave shifts V_{mw} related to the σ and π-transitions along the x-axis, using the first solution $\Delta^{\pi}_{a} \simeq 5.71 \times \omega^0_L$, and where $B^z_{b,mw} = 0$. As expected, the clock states splitting is not possible in this case, since the gradient of $V_{mw,\sigma}$ around $x = 0$ vanishes due to the second-order dependence of $B^z_{mw}(x)$.

By applying an additional *microwave* bias-field along the z-axis : $B^z_{b,mw} = 1$ G, we show in Figure 33b.3 that a symmetrical splitting of 14.7 μm using only one microwave frequency is possible in principle. This is due to the linear dependence of V_{mw} to B^z_{mw} as explained previously. The remaining terms that have been neglected in the previous discussion, have either a second-order dependence on B^z_{mw} (σ-transitions) or on B^x_{mw} (π-transitions), do not affect the symmetry of the potentials, but imply an additional energy shift[20] of about $h \times 20$ kHz, of each clock state, as can be seen in Figure 33b.3.

Nevertheless, the symmetry of the potentials are altered compared to the ideal case due to the static field dependence of the detunings $\Delta^{m_2}_{m_1}(B)$. In particular, the detunings Δ_b related to the clock state $|b\rangle$, are positive in the trap center : $\Delta_b(\mathbf{r_0}) > 0$ and their signs can be changed spatially due to the spatial variations of the static field B across the trap, as explained in section 5.3. This effect does not concern the detunings Δ_a related to the state $|a\rangle$, which affects the symmetry of the potentials especially along the transverse directions. This problem can be solved, as shown in Figure 33b, by increasing further the detuning value such as : $\Delta^{\pi}_{a}(\mathbf{r_0}) = 9\omega^0_L$. In addition, the choice of $B^z_{b,mw}$ should be moderate (here 1 G) in order to minimize

20 This energy shift can be calibrated experimentally.

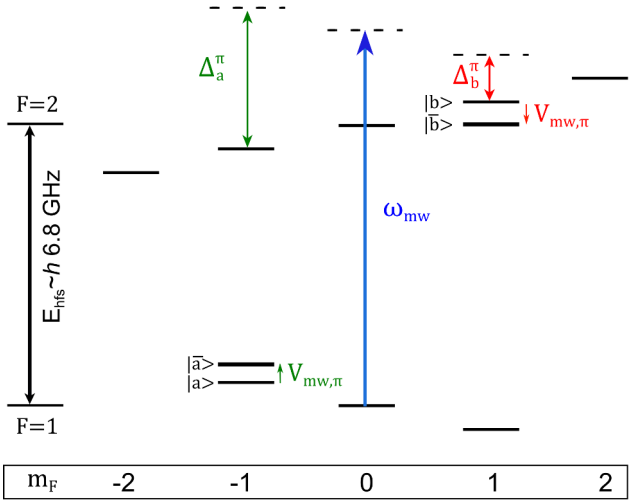

Figure 32: Energy levels of the ^{87}Rb ground states in combined static and microwave fields. A unique microwave frequency is used to couple the clock states with the auxiliary states. The microwave frequency is far detuned from all transitions : $|\Delta_{m_1}^{m_2}| \gg |\Omega_{m_1}^{m_2}|$.

the trap opening of the state $|b\rangle$ along the z-axis (cf. section 5.3). Hence, the overall relative dissymmetry of the resulting potentials in Figure 33b.3 along the eigen-directions : $\{\tilde{\mathbf{x}}, \tilde{\mathbf{y}}, \tilde{\mathbf{z}}\}$ are respectively : $\{0.45, 0.91, 0.088\} \times 10^{-2}$.

Furthermore, it should be pointed out that the static field structure, in this proposal, is of great importance. Indeed, using a Dimple trap as shown in Figure 33a.(1-2), the microwave shifts $V_{mw,\pi}$ are symmetrical along the x-axis : $V_{mw,\pi}(-x) = V_{mw,\pi}(x)$. This property is not verified, for example, if a Z-trap had been used instead, which would affect further the symmetry of the potentials.

Finally, this beam-splitter proposal allows a considerable simplification of the symmetrical interferometer design by using only one CPW and one microwave source, which makes the fluctuations of the microwave field in common, during the different interferometer stages. Nevertheless, the generation of a homogenous microwave field along the z-axis might be difficult to realize experimentally. One can use a microwave horn for this purpose but controlling the polarization and creating a magnitude in the order of 1 G in the far-field are experimentally challenging. An alternative solution that can be implemented in the future versions of our atom-chip, would be to use a on-chip circular resonator or a combination of several parallel CPWs to create a homogenous field up to the second order (or higher order) along the z-axis.

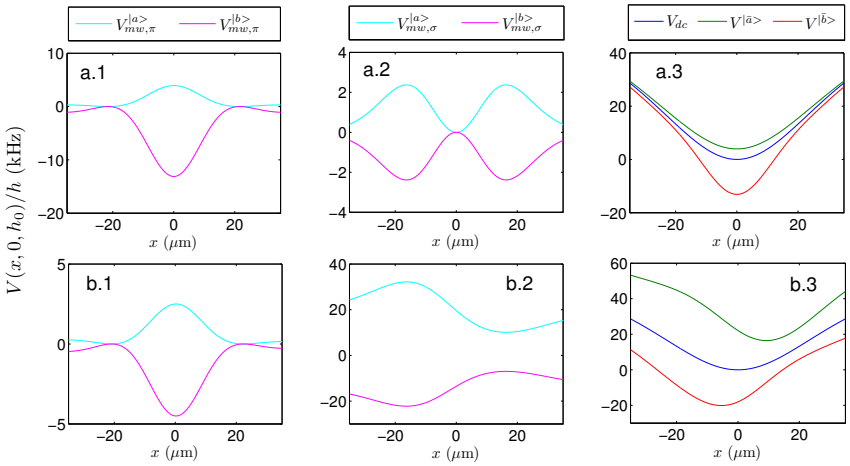

Figure 33: Proposal of symmetrical beam-splitter with one coplanar waveguide (CPW). (a) In the absence of a homogeneous microwave field : $B^z_{b,mw} = 0$, no splitting of the clock states occurs. (b) In the presence of an additional microwave bias-field : $B^z_{b,mw} = 1$ G, the clock states are spilt by : 14.7 μm. The microwave energy shifts V_{mw} are classified with respect to the π-transitions (a.1, b.1) and σ-transitions (a.2, b.2), respectively. The microwave frequency ω_{mw} is chosen such as : (a) $\Delta^{\pi}_{a} = 5.71\omega^0_L$ and (b) $\Delta^{\pi}_{a} = 9\omega^0_L$ (cf. text). The injected microwave power is here : $P_{mw}/P_0 = 0.1$. The static trap is created using on-chip Dimple structure in order to have the following trap parameters : $h_0 = 40$ μm and $\{\omega_x/2\pi, \omega_\perp/2\pi\} = \{100, 2350\}$ Hz. The CPW parameters correspond to the Config. *III* (CPW_1) on our chip (cf. Figure 52).

5.7 STABILITY OF THE INTERFEROMETER GRAVITATIONAL SIGNAL

The stability of the interferometer signal : the phase difference between the separated states, is a major concern for precision measurement based on atom interferometry.

The phase difference due to the gravitational acceleration g is given by[21] is given by :

$$\Phi = \frac{mgs}{\hbar} T_R \tag{96}$$

where s is the splitting distance and T_R is the holding time (i.e. the interrogation time). In this case, the stability of the interferometer signal, is mainly[22] related to the stability of the splitting distance s, which relies, in the case of an atom-chip interferometer, in particular on the stability of the current sources.

In our case, the fluctuations of these currents impact directly the internal clock-states evolution, and so reduce the coherence time [104]. These effects have been discussed previously, and several solutions have been proposed to minimize the effects of both static (section 5.5) and microwave (section 5.6) field fluctuations. Moreover, these fluctuations affect also the external states via the splitting distance s fluctuations, which eventually reduces the precision of the interferometry measurement.

The stability of the distance s can be improved experimentally by using an ultra-stable bipolar current sources, for the critical chip wires used to create the static trap. These current sources have a maximum output current $I_{max} = 5$ A and exhibit a root-mean-square (RMS) current noise on the order of $|\Delta I / I_{max}| = 10^{-5}$ [163]. As discussed previously in section 5.6.1, the microwave current sources can reach a similar level of stability (on the order of 10^{-4} [163]) provided a careful design of the microwave frequency chain.

Hence, the precision of the phase measurement would be limited[23] by the stability of the current sources, and so the uncertainty of the gravity measurement is expected to be about : $\Delta g / g \approx 10^{-5}$.

Here, we propose a solution that improves the stability of the interferometer gravitational signal by reducing the dependence of the distance s, during the holding stage, to the current fluctuations.

21 The contribution of the energy difference : $E_{2,1} - E_{1,-1}$ is omitted here.
22 Since the holding time T_R can be controlled very precisely.
23 In case of an optimistic estimation that neglects the decoherence effect.

Transfer to a stable static double-well after splitting

Form the proposals discussed earlier to reduce the effects of current fluctuations on the internal states during the holding stage, the static double-well (DC-DW, section 5.6.2) is an excellent candidate mainly because of its simplicity. In this case, the fluctuations of the internal energy difference is reduced by setting the magnetic field to the standard magic field B_m^0, and so there is no need for a further calibration of the new magic field B_m in the presence of the microwave field (cf. section 5.5). Furthermore, the static-current sources are easier to control than the microwave currents, and ultra-stable sources are commercially available[24].

To create a static double-well, at least 4 different current-sources are needed :

I_Z	associated to initial static field B_Z created using a Z-wire
I_{CPW}	injected in the two CPWs to create a static field B_{CPW} similar to the microwave field B_{mw}
$I_{b,x}$	used to create the bias-field $B_{b,x}$ along the x-axis
$I_{b,y}$	used to create the bias-field $B_{b,y}$ along the y-axis

Here, we use a Z-trap to create the initial static trap which requires only one current flowing on-chip to create the initial static trap[25]. We also assume that the currents flowing in the 6 wires associated to the two CPWs are created using only one current source. Finally, we suppose that the currents $I_{b,x}$ and $I_{b,x}$ are proportional to the bias-fields : $B_{b,x}$ and $B_{b,y}$.

In the following, we analyze the fluctuation of the distance s under the variation of a static current I_k by computing numerically the nondimensional quantity : $\frac{I_k}{s}\frac{\partial s}{\partial I_k}$. For a precise example, we consider the following numerical parameters : $L = 1000\ \mu$m and $2\delta = 2 \times 22.5\ \mu$m, which corresponds respectively to the length of the central Z-wire and the distance between the CPWs along the splitting axis x. The remaining parameters (that do not depend on the chip design) are here considered as tunable, but the static field B_0 in the trap center $\mathbf{r_0}$ has to be fixed to magic value B_m^0. In practice, only the following parameters : $\mathcal{P} = \{I_Z, I_{CPW}, h_0\}$ are tunable.

These parameters $\mathcal{P}$ can be used to minimize the RMS of the distance s variation, defined as: $\mathcal{S}^2(\mathcal{P}) = \sum_k |\frac{I_k}{s}\frac{\partial s}{\partial I_k}|^2/n$, with n is the number of the static currents I_k. For a set of parameters $\mathcal{P}$, we compute numerically s and the 4 derivatives $\frac{\partial s}{\partial I_k}$ then deduce an estimation of $\mathcal{S}^2(\mathcal{P})$. The optimization of $\min_{\mathcal{P}}(\mathcal{S}^2)$ is done here numerically[26].

24 http://www.kepcopower.com/ and http://www.highfinesse.com/

25 Compared to a Dimple trap which requires two currents.

26 A simple analytical model of the distance s as a function of the parameters : $\mathcal{P}$, and $\{h_0, \delta\}$ can be derived : the coordinates of (right) minimum of the double-well

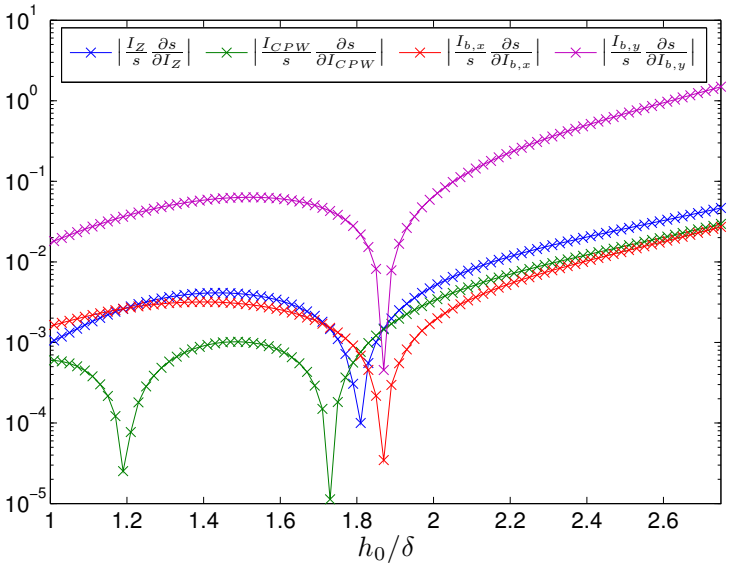

Figure 34: The (nondimensional) derivatives $|\frac{I_k}{s}\frac{\partial s}{\partial I_k}|$ as function of h_0/δ.

The variation of the distance s derivatives as function of the parameter h_0 are shown in Figure 34. One can notice the existence of an optimal parameter h_0^k where the derivative $\frac{\partial s}{\partial I_k})_{h=h_0^k}$ vanishes. Moreover, the bias-field $B_{b,y}$ causes the highest fluctuation (of about $10^{-1} - 10^{0}$). This strong dependence arises because fluctuations in $B_{b,y}$ change the position of the trapped atoms h_0 in the inhomogeneous fields created by the CPWs. Such a high sensitivity has been also observed experimentally [163]. Hence, the overall optimization of $\mathcal{S}^2$ depends mainly on the minimization of the term : $|\frac{\partial s}{\partial I_{b,y}}|$. Figure 35 corresponds to the optimal tunable parameters $\mathcal{P}_m = \{I_Z = 0.2 \text{ A}, I_{CPW} = -73.1 \text{ mA}, h_0 = 1.87 \times \delta \simeq 42 \ \mu\text{m}\}$ that minimize the RMS fluctuation of s : $\mathcal{S}_m = 1.11 \times 10^{-3}$ and reduce the fluctuation of s by 3 order of magnitude, compared to the mean of the fluctuations of s caused by the $B_{b,y}$, which can be seen in Figure 34. As the RMS current noise is about 10^{-5}, the (relative) precision of the measured gravitational signal can reach the accuracy range of 10^{-8}. The value of $\mathcal{S}_m$ can be reduced further by increasing the length of the Z-wire : $\mathcal{S}_m = 3.37 \times 10^{-4}$ for $L = 1700 \ \mu\text{m}$[27].

Nevertheless, the transfer to the static double-well in Figure 35 arises a supplementary difficulty since the ratio $h_0/\delta < 2$. Yet, this ratio can be tuned during the splitting, by adjusting the position of the

potential V are approximately given by : $\mathbf{r_m} = \{\delta, 0, h_0\}$. An analytical first order correction $\epsilon_i, (i \in \{x_1, x_2, x_3\} = \{x, y, z\})$ can be found by inversing the following 3×3 matrix : $\{(\partial B_i(\mathbf{r})/\partial x_j)_{r=r_m}\}$, which allows an analytical estimation of s and its derivatives as : $s^2/4 = (\delta + \epsilon_1)^2 + (\epsilon_2)^2$. This model can be simplified further by assuming that $\epsilon_2 = 0$. Nevertheless, a direct numerical estimation of s (and its derivatives) is more accurate but requires a larger computation time.

27 The axial trap frequency would be in this case very low : $\omega_x/2\pi \approx 4$ Hz for $\mathcal{P} = \mathcal{P}_m$, which requires a large splitting time.

trapped atoms h_0, as proposed previously in section 5.6.3. Here, we propose an alternative solution. To perform the state-selective splitting of the clock states, we design two intermediate coplanar waveguides : CPW_1^0 and CPW_2^0 located at $\delta_0 = \pm 13.5$ μm along the x-axis, as shown in Figure 36. Hence, the splitting can be performed using a potential-well beam-splitter since $h_0/\delta_0 > 3$ (cf. Figure 19b). Then, to ensure the transfer to the static double-well, the current I_{dc} can be injected in the coplanar waveguides : CPW_1 and CPW_2 while the microwave currents I_{mw} in CPW_1^0 and CPW_2^0 are switched-off progressively.

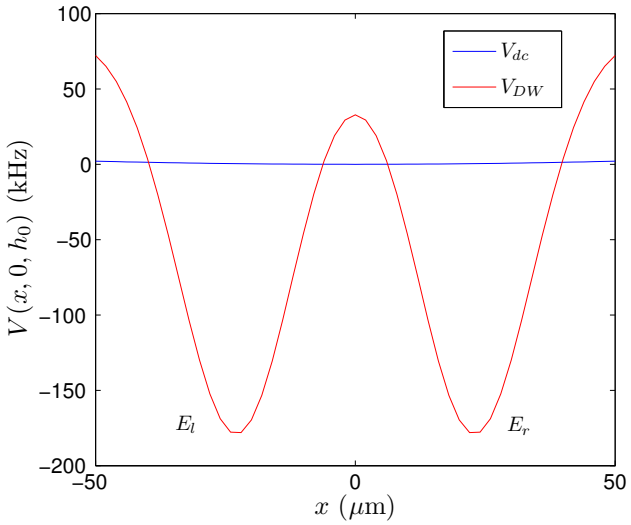

Figure 35: The double-well potential V_{DW} (in red) as function of x, for the optimal parameters $\mathcal{P}_m$ which minimize the RMS variation of s under the current fluctuations. The static trap V_{dc} (in blue) has the following angular frequncies :$\{\omega_x/2\pi, \omega_\perp/2\pi\} = \{14, 1140\}$ Hz.

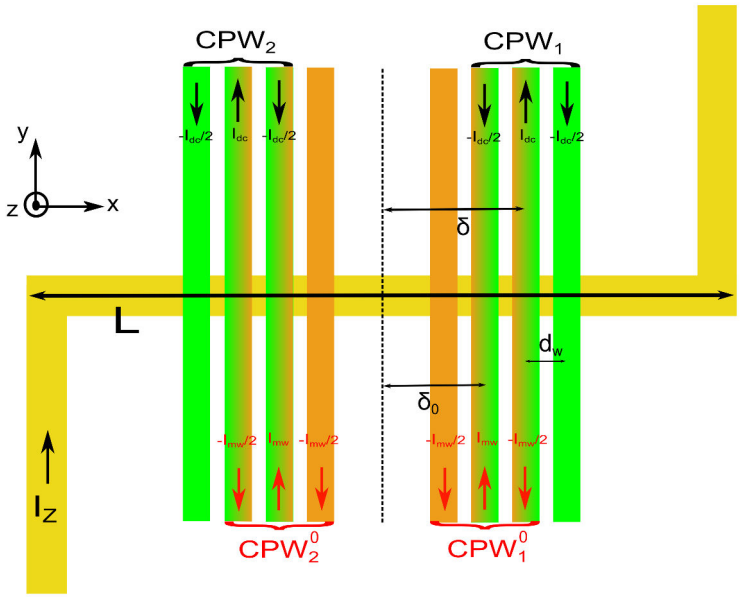

Figure 36: Chip design to split and transfer the atoms into the static double-well (DC-DW). The initial static trap is created using on-chip Z-wire ($L = 1000$ μm). Two coplanar waveguides : CPW$_1$ and CPW$_2$ located along the x-axis ($\delta = 22.5$ μm and $d_w = 9$ μm) are used to create the static double-well, by injecting a static current I_{dc}. Two additional intermediate waveguides : CPW$_1^0$ and CPW$_2^0$ ($\delta_0 = 13.5$ μm) are required to perform a state-selective splitting of the atoms (cf. text). This configuration corresponds to the Config. *III* on our chip (cf. Figure 52)

5.8 CONCLUSION : WHAT IS THE BEST CONFIGURATION ?

To summarize, we have proposed an experimental design for a symmetrical splitting of trapped thermal atoms, along the axial direction of the magnetic trap, using micro-wave dressing for the ^{87}Rb clock states on an atom chip. In particular, we have compared two splitting schemes : potential-well and potential-barrier, that can be implemented using the same chip design, but have different features. We have simulated the microwave splitting potentials and analyzed the inherent sources of dissymmetry. We have developed an analytical model of the microwave potential that can be of great interest to optimize the symmetry of the potentials.

The potential-well beam-splitter allows a power-efficient splitting : higher splitting distance are possible with less microwave power. However, it suffers from a reduced trap-depth in the limit of the quasi-resonant coupling regime. Therefore, a compromise has to be taken between the trap-depth and the interferometer symmetry (cf. Figure 19 and Table 2).

In the case of a perfectly symmetrical interferometer, the magic fields are available only for low contamination values which is not suitable for splitting with a potential-well since the atoms are always attracted in the vicinity of the highest (in space) microwave coupling values. In contrast, the potential-barrier beam-splitter repels atoms into the vicinity of the lowest (in space) microwave coupling values. However in practice, the existence of the magic field is limited to small splitting distances (few microns).

The perturbed symmetrical interferometer is a promising solution to reach high contamination values, for both splitting methods, but it would be more difficult to implement experimentally since two parameters (the microwave power and the bias fields) have to be changed simultaneously during the splitting.

In order to reduce the fluctuation effect of the magnetic fields, the atoms can be transferred after splitting into a stable double well where the technical noise in the interferometer arms can be common-mode. The potential-well method can be used to transfer the atoms to a stable static double well (DC-DW, cf. section 5.6.2) since the static and microwave potentials can be intrinsically matched in this case. On the other hand, the potential-barrier method can be used to transfer the atoms to a stable microwave double-well (MW-DW, cf. section 5.6.3). Yet, the static double-well has several advantages. In addition to the uniqueness of its magic field value ($B_m = B_m^0 \approx 3.23$ G), this configuration can be used to stabilize the interferometer gravitational signal (cf. section 5.7), in particular the fluctuations of s (the distance between the separated wavepackets) due to the noise of the required current sources.

During the splitting stage, where the microwave fields are necessary for internal state labelling, we propose a microwave chain design in section 5.6.1 that attempts to put in common, as much as possible, the fluctuations of the field amplitudes even using two different microwave frequencies.

In the next chapter, we discuss the possibility of a transverse splitting using the σ-transitions as proposed in section 4.3.6.

6

TRANSVERSE BEAM-SPLITTER : SPECIFIC CHIP DESIGN

6.1 INTRODUCTION

In the case of an adiabatic separation of the atoms, the required splitting time depends mainly on the trap angular frequency along the splitting axis (here $2\pi/\omega_x$, (cf. chapter 7)), so it can be reduced significantly in the case of transverse splitting, compared to axial splitting, discussed in the previous chapter.

As discussed in section 4.3.6, σ-transitions are more suited for transverse splitting. Hence, in this section, we focus on the study of a beam-splitter using σ-transitions (dashed lines in Figure 16).

Furthermore, the choice of the static trap and its orientation relative to the coplanar waveguides (CPWs) has a great importance. We present here the characteristics of a transverse beam-splitter in some typical static traps, well-known in the literature and described previously in section 2.2.3. We show the necessity to design a specific microtrap. Thereafter, we describe the required symmetry of the static field and we provide several custom microtrap designs, for this purpose.

In this study, we suppose that the condition of the quasi-resonant regime is fulfilled, so we can neglect the effects of non-resonant transitions (i.e. we neglect the effect of the transitions $\sigma^{(-)}$ and π). Moreover, in this section, we choose a potential-barrier beam-splitter in order to avoid the trap-opening constraint (cf. section 5.3).

We assume also that the CPWs are placed parallel to the y-axis, as shown in Figure 17. In order to power the σ-transitions, we choose the orientation of the static trap along y-axis in order to favor the atoms splitting along the x-axis.

6.2 TRANSVERSE SPLITTING WITH A TYPICAL STATIC TRAP

In the following, we study the behavior of the transverse beam-splitter in some typical static traps such : Standard Ioffe-Pritchard (macroscopic trap) and Z-trap (microtrap).

6.2.1 *Standard Ioffe-Pritchard*

For a Standard Ioffe-Pritchard (SIP) (cf. section 2.2.2), the coils can be placed relatively to the chip such that the trap-axis coincides with the y-axis. We will show in the following that the symmetry properties of the static field $\mathbf{B}$ are favorable in this case[1]. The numerical simulation shows that the splitting is perfectly symmetrical relative to the x-axis, since the coordinates of resulting potentials minima verify : $\{x_m^a = -x_m^b, y_m^a = y_m^b, z_m^a = z_m^b\}$. Thus, the splitting direction is parallel to the transverse axis $\mathbf{x}$, as shown in Figure 37a. The displacements of atoms along the directions $\mathbf{y}$ and $\mathbf{z}$, shown in Figure 37b, are identical for both clock states, and so, they do not change the splitting direction.

These results are a consequence of the axial-symmetry of the microwave shifts V_{mw}. In this case, using a second order expansion of the static field B components (equation (9)) and if the microwave frequencies and powers are chosen as explained in section 4.3.6, one can show[2] that :

$$V_{mw}^{|a\rangle}(-x, y, z) = V_{mw}^{|b\rangle}(x, y, z) \tag{97}$$

Moreover, one can also show that the eigenfrequencies of the trapping potentials are equal, as expected previously. As can be seen in Figure 37c, the relative variation of the trapping-potential eigenfrequencies, as function of the microwave power during the splitting, is low. In particular, the potential aspect ratio remains nearly constant which is an important characteristics and advantage of the transverse splitting (unlike the axial splitting, cf. Figure 22).

6.2.2 *Typical microtraps : example of a Z-trap*

For a typical microtrap such as Z-trap or Dimple trap , we place the principle wire, that ensures the transverse confinement, along the y-axis, so the trap-axis is close to it. Usually, this axis is on the chip plane ($\mathbf{x}$,$\mathbf{y}$) but it is not necessarily parallel to the y-axis[3].

The numerical simulations show that the potentials minima have a central symmetry such as : $\{x_m^a = -x_m^b, y_m^a = -y_m^b, z_m^a = z_m^b\}$. This

1 Especially because the non-diagonal terms of the gradient tensor $\mathcal{V}$ are zero.
2 Similar derivation will be given in 6.2.4.
3 The inclination angle from the y-axis is given by : $\psi_{IP} = \arctan(-v_{13}/v_{23})$, where v_{ij} are the elements of the gradient tensor $\mathcal{V}$.

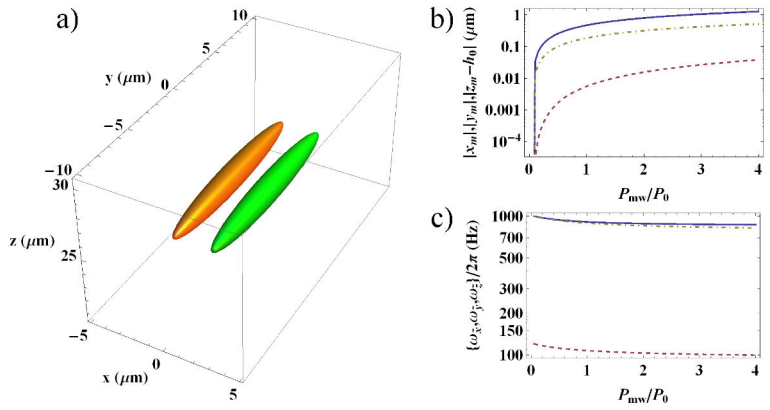

Figure 37: Standard Ioffe-Pritchard (SIP) : (a) 3D-equipotentials representation of the clock states : $|a\rangle$ (orange) and $|b\rangle$ (green), for the potential $k_B T$ with $T = 100$ nK (about $h \times 2$ kHz). (b-c) The variations of the minimum coordinates $\mathbf{r_m} = \{x_m, y_m, z_m\}$ and the eigenfrequencies $\{\omega_{\tilde{x}}, \omega_{\tilde{y}}, \omega_{\tilde{z}}\}/2\pi$ of the resulting potential $V^{|\bar{a}\rangle}(r)$, shown respectively in straight, dashed, and dot-dashed lines, as function of the microwave power P_{mw}. (cf. section 6.2.5 for the simulation parameters.)

result is a consequence of the microwave shifts symmetry, as one can show that :

$$V_{mw}^{|a\rangle}(-x,-y,z) = V_{mw}^{|b\rangle}(x,y,z) \tag{98}$$

Nevertheless, the atoms splitting along the longitudinal direction $\mathbf{y}$ can not be neglected, as shown in Figure 38.a, using a Z-Trap. Since the displacement along the z-axis is similar for both states, the splitting direction is on the xy-plane and forms an angle θ_{ab} with the x-axis defined as :

$$\theta_{ab} = \arctan\left(\frac{y_m^b - y_m^a}{x_m^b - x_m^a}\right) \tag{99}$$

The control of the splitting direction and its stability due to the currents fluctuations is important, in the perspective of precision measurements application (such as gravimetry). Figure 38.b shows the evolution of θ_{ab} during the splitting stage. Here, the splitting along $\mathbf{y}$ is larger than along $\mathbf{x}$, as $\theta_b \approx 75°$; yet the splitting is still considered as transverse since the potential aspect ratio remains nearly constant.

The splitting direction can be calibrated, but its stability will depend on the current sources. This problem can be avoided by using a specific microtrap, where the evolution θ_{ab} is minimized (ideally zero).

6.2.3 *Specific H*-trap*

A first intuitive approach to solve the problem would be to align perfectly the trap-axis along the y-axis. The H-trap allows such alignment

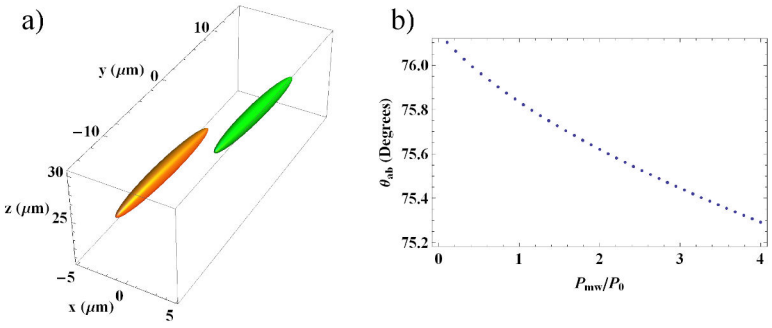

Figure 38: Z-Trap : (a) 3D-equipotentials representation of the clock states : $|a\rangle$ (orange) and $|b\rangle$ (green), for the potential $k_B T$ with $T = 100$ nK. (b) The variation of the splitting direction θ_{ab} as function of the microwave power P_{mw}. (cf. section 6.2.5 for the simulation parameters.)

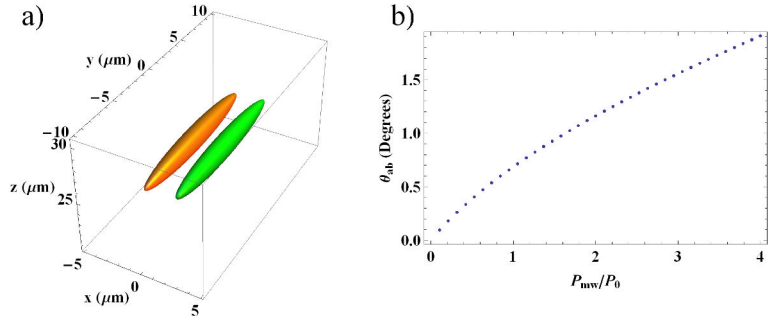

Figure 39: H*-Trap : same legend than Figure 38.

by an appropriate choice of the distance L between the lateral wires[4] : $L = 2h_0$ (i.e. $t_{21} = t_{22} = 1$). We refer to this configuration as : H*-Trap. Such an alignment is also possible using a Z-trap [99], however the H*-trap has the advantages of a symmetrical wires structure with respect to the x-axis, which reduces considerably the splitting along the axial direction y, as can be seen in Figure 39. Nevertheless, the trap-depth of this trap is considerably reduced as the two lateral wires are very close, as we will discuss in section 6.2.4. In this case, a tradeoff has to be made between the trap-depth and the axial frequency.

In the next section, we describe in detail the approach we have followed to design a custom microtrap, with significant trap depth, to control the splitting direction.

6.2.4 *Custom microtrap design*

In the following, we use the method described in section 2.2.5, to design a custom microtrap that allows a symmetrical splitting along the

4 As $v_{13} = 0$ and so $\psi_{IP} = 0$.

transverse direction (x-axis) with a minimal separation along the axial direction (y-axis). As discussed previously, such a beam-splitter is possible using a Standard Ioffe-Pritchard trap, because the microwave shifts have an axial-symmetry (equation (97)).

Using a typical microtrap, the microwave shifts V_{mw} have a central symmetry (equation (98)) even in the case of the H*-Trap. In the following, we derive the necessary constraints on the Ioffe-Pritchard microtrap to create a microwave shifts that satisfy the axial-symmetry condition (equation (97)).

Ioffe-Pritchard trap and constraints on the symmetry of the potentials

The condition (97) is sufficient (but not necessary) to realize the required separation along the x-axis. Using only the σ-transitions, the microwave shifts V_{mw} are given by the equations (72) in the limit of the quasi-resonant regime. The previous condition is verified if the Rabi frequencies and the detunings verify the following :

$$|\Omega_a^\sigma(-x,y,z)| = |\Omega_b^\sigma(x,y,z)| \tag{100a}$$
$$|\Delta_a^\sigma(-x,y,z)| = |\Delta_b^\sigma(x,y,z)| \tag{100b}$$

Equation (100b) is verified if $|\Delta_a^\sigma(\mathbf{r_0})| = |\Delta_b^\sigma(\mathbf{r_0})|$ (as required[5] in section 4.3.4) and B is an even function of x (i.e. $B(-x,y,z) = B(x,y,z)$). Hence, each component B_i of the static field has to verify :

$$B_i^2(-x,y,z) = B_i^2(x,y,z),\ i \in \{x,y,z\} \tag{101}$$

Moreover, assuming that the field created by the waveguide CPW$_1$ (CPW$_2$) interacts only with the state $|a\rangle$ ($|b\rangle$), equations (100a) and (101) give the following condition :

$$\left|B_{mw}^{\perp,CPW_1}(-x,y,z)\right|^2 = \left|B_{mw}^{\perp,CPW_2}(x,y,z)\right|^2 \tag{102}$$

where $B_{mw}^{\perp,CPW_k}$ is the microwave field component along the normal local direction of $\mathbf{B}$, created by the waveguide CPW$_k$ ($k \in \{1,2\}$) and its expression is given by the following :

$$\begin{aligned}&\left|B_{mw}^{\perp,CPW_k}(x,y,z)\right|^2 = \\ &\frac{B_y^2(x,y,z)}{B^2(x,y,z)}\left[\left|B_{mw}^{x,CPW_k}(x-\delta_k,z)\right|^2 + \left|B_{mw}^{z,CPW_k}(x-\delta_k,z)\right|^2\right] + \\ &\left[\frac{B_x(x,y,z)}{B(x,y,z)}B_{mw}^{z,CPW_k}(x-\delta_k,z) - \frac{B_z(x,y,z)}{B(x,y,z)}B_{mw}^{x,CPW_k}(x-\delta_k,z)\right]^2\end{aligned} \tag{103}$$

with $\delta_k = (-1)^{k+1}\delta$ is the position of the CPW$_k$ along the x-axis, and $\{B_{mw}^{x,CPW_k}, B_{mw}^{z,CPW_k}\}$ are the components of microwave field $\mathbf{B}_{mw}$ created by the CPW$_k$, and given by equations (67).

5 Which can be satisfied by a convenient choice of the microwave frequencies.

As $\{B_{mw}^{x,CPW_k}, B_{mw}^{z,CPW_k}\}$ are $\{\text{even}, \text{odd}\}$-functions of x respectively and by applying the same microwave power P_{mw} in the CPWs, equations (101) and (102) are verified only if :

$$\begin{aligned} &\{B_x, B_z\} \text{ are } \{\text{even}, \text{odd}\}\text{-functions of } x \text{ respectively} \\ &\text{or } \{B_x, B_z\} \text{ are } \{\text{odd}, \text{even}\}\text{-functions of } x \text{ respectively} \quad (104a) \\ &B_y^2 \text{ is an even-function of } x \quad (104b) \end{aligned}$$

In addition, to allow the selection of the σ-transitions, at least the following condition should be satisfied at the trap center :

$$B_y(\mathbf{r_0}) \neq 0 \quad (105)$$

As a consequence, B_y can not be an odd-function and, in order to verify equation (104b), we should have :

$$B_y \text{ is an even-function of } x \quad (106)$$

On the other hand, as discussed in section 2.2.4, the gradient tensor $\mathcal{V}$ of $\mathbf{B}$ at $\mathbf{r_0}$, is defined as : $(\mathcal{V})_{i,j} = v_{ij} = \frac{\partial B_i}{\partial x_j}\Big)_{\mathbf{r}=\mathbf{r_0}}$ and has the following form :

$$\mathcal{V} = \begin{pmatrix} v_{11} & v_{12} & v_{13} \\ v_{12} & v_{22} & v_{23} \\ v_{13} & v_{23} & -v_{11} - v_{22} \end{pmatrix} \quad (107)$$

and B has a nonzero minimum at $\mathbf{r_0}$ only if :

$$\begin{aligned} \text{Det}(\mathcal{V}) &= 0 \quad (108a) \\ \mathcal{V}.\boldsymbol{\mathcal{U}} &= 0 \quad (108b) \end{aligned}$$

with $\boldsymbol{\mathcal{U}}$ defined as : $\boldsymbol{\mathcal{U}} = \mathbf{B_0}/B_0$.

Furthermore, using a first order Taylor expansion of B_y, equation (106) gives : $v_{12} = 0$. Hence, using equation (108a), one can derive the following equation :

$$v_{11}^2 v_{22} + v_{13}^2 v_{22} + v_{11} v_{22}^2 + v_{11} v_{23}^2 = 0 \quad (109)$$

Now assuming from equation (104a) that $\{B_x, B_z\}$ are $\{\text{even}, \text{odd}\}$-functions respectively, one can show[6] using equations (104) and (109),

6 In this case, $v_{11} = 0$ (as B_x is an even-function). Equation (109a) requires that : $v_{22} = 0$ or $v_{13} = 0$. Yet, as $B_y(\mathbf{r_0}) \neq 0$ and using (108b), we deduce that $v_{13} \neq 0$. Then, we have $v_{22} = 0$ and, as B_x is an even-function, we can show using equation (108b) that : $v_{23} = 0$. Therefore, one can deduce that all elements of the gradient tensor $\mathcal{V}$ expect v_{13} have to be zero. In the same manner, using the assumed B_i symmetry, one can show that all elements of the curvature tensor $\mathcal{W}$ expect w_{111} are zero. Finally, one can deduce that $\text{Det}(\mathcal{G}) = 0$, where $\mathcal{G}$ is a tensor that gives the trap angular frequencies, and defined in section 2.2.4.

that B has a saddle point (not a minimum) at $\mathbf{r_0}$. Hence, $\{B_x, B_z\}$ have to be $\{\text{odd}, \text{even}\}$-functions respectively, and so the conditions (104) can be simplified to the following conditions :

$$B_x \text{ is an odd-function of } x \tag{110a}$$
$$B_y \text{ is an even-function of } x \tag{110b}$$
$$B_z \text{ is an even-function of } x \tag{110c}$$

Moreover, using equation (109) together with the previous conditions (110) and equation (105), one can derive[7] the following equations :

$$v_{12} = 0 \tag{111a}$$
$$v_{13} = 0 \tag{111b}$$
$$v_{11} \neq 0 \tag{111c}$$
$$v_{22}^2 + v_{11}v_{22} + v_{23}^2 = 0 \tag{111d}$$

The stationary point conditions (111(c-d)) have two different solutions :

$$\text{Solution } (\mathcal{S}_I) : v_{22} = 0, v_{23} = 0, \text{ and } v_{11} \neq 0 \tag{112a}$$
$$\text{Solution } (\mathcal{S}_{II}) : v_{11} = -(v_{22}^2 + v_{23}^2)/v_{22}, \text{ and } v_{22} \neq 0 \tag{112b}$$

Therefore, using equation (108b), one can show that the trap-axis $\boldsymbol{\mathcal{U}}$ is given in each case by :

$$\text{Solution } (\mathcal{S}_I) : \boldsymbol{\mathcal{U}} = \{0, 1, 0\} \tag{113a}$$
$$\text{Solution } (\mathcal{S}_{II}) : \boldsymbol{\mathcal{U}} = \{0, \frac{-v_{23}}{\sqrt{v_{22}^2 + v_{23}^2}}, \frac{v_{22}}{\sqrt{v_{22}^2 + v_{23}^2}}\} \tag{113b}$$

For the solution $(\mathcal{S}_I)$, one can recognize that the gradient tensor $\mathcal{V}$ and the trap-axis $\boldsymbol{\mathcal{U}}$ are similar to those of the Standard Ioffe-Pritchard (cf. section 2.2.2).

Moreover, for the solution $(\mathcal{S}_{II})$, one can notice that the trap-axis $\boldsymbol{\mathcal{U}}$ is in the yz-plane, and has an inclination angle ϕ_{IP} from the chip surface, defined as : $\phi_{IP} = \arctan(-v_{22}/v_{23})$. As discussed in [85], $|\phi_{IP}|$ should be minimized in order to avoid the conception of a shallow trap. In this case, the following condition has to be verified :

$$|v_{23}| \gg |v_{22}| \tag{114}$$

7 Equations (111(a-b)) are derived using conditions (110(b-c)) respectively. For equation (111c), assuming that $v_{11} = 0$, one can deduce from equations (108) and (111(a-b)) that $\boldsymbol{\mathcal{U}} = \{1, 0, 0\}$, so equation (105) can not be verified. Finally, equation (111d) is derived using equation (109) and equations (111(b-c)).

The curvature tensor $\mathcal{W}$ of the field $\mathbf{B}$ at $\mathbf{r_0}$, is given by :

$$\mathcal{W} = \begin{pmatrix} W_1 \\ W_2 \\ W_3 \end{pmatrix} \tag{115}$$

where the tensors W_i are defined in section 2.2.4 as $(W_i)_{j,k} = w_{ijk} = \left(\frac{\partial B_i}{\partial x_j x_k}\right)_{\mathbf{r}=\mathbf{r_0}}$, and have the following form :

$$W_1 = \begin{pmatrix} w_{111} & w_{112} & w_{113} \\ w_{112} & w_{122} & w_{123} \\ w_{113} & w_{123} & -w_{111} - w_{122} \end{pmatrix} \tag{116a}$$

$$W_2 = \begin{pmatrix} w_{112} & w_{122} & w_{123} \\ w_{122} & w_{222} & w_{223} \\ w_{123} & w_{223} & -w_{112} - w_{222} \end{pmatrix} \tag{116b}$$

$$W_3 = \begin{pmatrix} w_{113} & w_{123} & -w_{111} - w_{122} \\ w_{123} & w_{223} & -w_{112} - w_{222} \\ -w_{111} - w_{122} & -w_{112} - w_{222} & -w_{113} - w_{223} \end{pmatrix} \tag{116c}$$

By applying the conditions (110) to the second order expansion of B_i, one can deduce the following equations :

$$w_{111} = 0 \tag{117a}$$
$$w_{122} = 0 \tag{117b}$$
$$w_{123} = 0 \tag{117c}$$

In particular, the curvature tensor $\mathcal{W}$ becomes identical to a Standard Ioffe-Pritchard, if the following additional conditions are verified :

$$w_{113} = 0 \tag{118a}$$
$$w_{223} = 0 \tag{118b}$$

Finally, one should verify that B has a minimum (and not a saddle point) at $\mathbf{r_0}$, which can be done by deriving the eigenvalues of the tensor $\mathcal{G} = \mathcal{V}.\mathcal{V} + (B_0\boldsymbol{\mathcal{U}}).\mathcal{W}$

Let's assume that the transverse confinement is much larger than the axial one : $\left|(\mathcal{V}.\mathcal{V})_{i,j}\right| \gg \left|((B_0\boldsymbol{\mathcal{U}}).\mathcal{G})_{i,j}\right|$. In this case, the eigenvalues of the tensor $\mathcal{G}$, for both solutions $(\mathcal{S}_I)$ and $(\mathcal{S}_{II})$, are approximately given by :

$$\tilde{G} = \{v_{11}^2, B_0 w_{222}, v_{11}^2\} \tag{119}$$

corresponding to the eigenvectors $\{\tilde{\mathbf{x}}, \tilde{\mathbf{y}}, \tilde{\mathbf{z}}\}$ respectively. Hence, the three-dimensional confinement is possible in this case, if the sign of w_{222} can be controlled such as : $w_{222} > 0$.

In conclusion, we have found two possible trap structures : $(\mathcal{S}_I)$ and $(\mathcal{S}_{II})$ that verify both the symmetry of the potentials constraints and the Ioffe-Pritchard (IP) topological constraints.

Custom microtrap : Manhattan trap

To design a custom IP trap on chip that satisfies the previous conditions (111) and (117), the *Manhattan* architecture, discussed in section 2.2.5, is a good candidate as the elements[8] : v_{12}, w_{122}, w_{123}, and w_{112} are zero by construction.

Moreover, in this architecture the elements v_{11}, v_{13} and w_{111} are tunable and depend only on the parameters $\{\tilde{I}_{1,j}, t_{1j}\}$ related to the wires $(FL_{1,j})$ (parallels to y-axis). Hence, these wires can be used to verify the conditions : (111(b-c)) and (117a).

Since the elements v_{13} and w_{111} are a linear combinations of the currents $\tilde{I}_{1,j}$, solving the remaining symmetry conditions : (111b) and (117a) can be written as a linear problem. By choosing the number of wires $(FL_{1,j})$: $N_1 = 3$, these equations are verified if the currents $\tilde{I}_{1,j}$ satisfy the following matrix equation :

$$\begin{pmatrix} \frac{t_{11}^2\left(-1+t_{11}^2\right)}{\left(1+t_{11}^2\right)^2} & \frac{t_{12}^2\left(-1+t_{12}^2\right)}{\left(1+t_{12}^2\right)^2} \\ \frac{t_{11}^4\left(-3+t_{11}^2\right)}{\left(1+t_{11}^2\right)^3} & \frac{t_{12}^4\left(-3+t_{12}^2\right)}{\left(1+t_{12}^2\right)^3} \end{pmatrix} \begin{pmatrix} \tilde{I}_{1,1} \\ \tilde{I}_{1,2} \end{pmatrix} = \begin{pmatrix} -\tilde{I}_{1,0} \\ -\tilde{I}_{1,0} \end{pmatrix} \tag{120}$$

which gives the following solutions :

$$\begin{pmatrix} \tilde{I}^{\mathrm{s}}_{1,1} \\ \tilde{I}^{\mathrm{s}}_{1,2} \end{pmatrix} = \begin{pmatrix} \frac{\left(1+t_{11}^2\right)^3\left(-1+3t_{12}^2\right)}{t_{11}^2(t_{11}^2-t_{12}^2)\left(3-t_{11}^2-t_{12}^2+3t_{11}^2t_{12}^2\right)}\tilde{I}_{1,0} \\ \frac{\left(1+t_{12}^2\right)^3\left(-1+3t_{11}^2\right)}{t_{12}^2(t_{12}^2-t_{11}^2)\left(3-t_{12}^2-t_{11}^2+3t_{12}^2t_{11}^2\right)}\tilde{I}_{1,0} \end{pmatrix} \tag{121}$$

One can reduce the required number of current sources by imposing additional conditions. For example, one can impose here the currents equality (in absolute value) in the wires $(FL_{1,j})$: $|\tilde{I}^{\mathrm{s}}_{1,1}| = |\tilde{I}^{\mathrm{s}}_{1,2}| = |\tilde{I}_{1,0}|$, by adjusting the wire positions t_{1j}. The numerical resolution gives the following solutions :

$$\{|t^{\mathrm{s}}_{11}|, |t^{\mathrm{s}}_{12}|\} \simeq \{0.7427, 5.2463\} \tag{122}$$

which corresponds to the currents setting : $\tilde{I}_{1,1} = -\tilde{I}_{1,2} = \tilde{I}_{1,0}$. We choose the solution that places the wires $(F_{1,1})$ and $(F_{1,2})$ on two different sides of the y-axis (i.e. $(t_{11}t_{12}) < 0$), in order to optimize the value of the gradient $|v_{11}|$.

In addition, the elements v_{22}, v_{23} and w_{222} depend only on the parameters of the wires $(FL_{2,j})$: $\{\tilde{I}_{2,j}, t_{2j}\}$. Hence, these wires can be

8 Here, the condition $w_{112} = 0$ is not required.

used to satisfy the conditions (111d) and verify that the angular frequencies of B are well-defined by adjusting the sign of w_{222} (cf. equations (119)). In the following, we choose the number of wires $(FL_{2,j})$: $N_2 = 3$ and we distinguish between the two possible solutions $(\mathcal{S}_I)$ and $(\mathcal{S}_{II})$.

- Case I : $(\mathcal{S}_I)$-Manhattan trap :

The condition (112a) can be written as a linear problem of the currents $\tilde{I}_{2,j}$, that can be solved, as shown in equations (120). Hence, one can derive the following solutions :

$$\begin{pmatrix} \tilde{I}^{s}_{2,1} \\ \tilde{I}^{s}_{2,2} \end{pmatrix} = \begin{pmatrix} \frac{t_{21}\left(1+t_{22}^2\right)^2}{t_{22}^2(t_{21}-t_{22})(1+t_{21}t_{22})}\tilde{I}_{2,0} \\ -\frac{t_{22}\left(1+t_{21}^2\right)^2}{t_{21}^2(t_{21}-t_{22})(1+t_{21}t_{22})}\tilde{I}_{2,0} \end{pmatrix} \tag{123}$$

Then, we choose the positions of these wires such as :

$$|\tilde{I}^{s}_{2,1}| = |\tilde{I}^{s}_{2,2}| = |\tilde{I}_{2,0}| \tag{124}$$

Two sets of solutions are possible[9]. We choose the symmetrical solution[10] :

$$t_{21} = -t_{22} = t \tag{125a}$$

$$t = \sqrt{\sqrt{5}+2} \simeq 2.0581 \tag{125b}$$

which corresponds to the currents setting : $\tilde{I}^{s}_{2,1} = \tilde{I}^{s}_{2,2} = -\tilde{I}_{2,0}$. In this case, one has $w_{223} = 0$ (equation (118b)), so the trap frequency tensor is given by :

$$\mathcal{G} = \begin{pmatrix} v_{11}^2 & 0 & 0 \\ 0 & B_0 w_{222} & 0 \\ 0 & 0 & v_{11}^2 - B_0 w_{222} \end{pmatrix} \tag{126}$$

where $w_{222} = (5-\sqrt{5})\tilde{I}_{2,0}/2h_0^3 \simeq 1.3819 \times \tilde{I}_{2,0}/h_0^3$ and $v_{11} \simeq 0.6953 \times \tilde{I}_{1,0}/h_0^2$. Therefore, we confirme that only two current sources are required for this trap (as it is usually the case for a Dimple trap). The longitudinal and transverse angular frequencies can be controlled independently by tuning the currents $\tilde{I}_{2,0}$ and $\tilde{I}_{1,0}$ respectively.

The eigenvectors of the frequency tensor $\mathcal{G}$ are identical to the eigenvectors[11] of the gradient tensor $\mathcal{V}$, which is a particular property of a Standard Ioffe-Pritchard. Moreover, the curvature w_{222} and the gradient v_{11} elements are completely uncoupled, as they can be tuned

9 The second solution is :$\{t_{21}, t_{22}\} \simeq \{-0.7554, 5.3411\}$.

10 That minimize the splitting force (which is identical here for both states) along the axial direction $\mathbf{y}$.

11 In this case the eigenvectors are given by the axes : $\{\mathbf{x}, \mathbf{y}, \mathbf{z}\}$.

using two independent currents : $I_{2,0}$ and $I_{1,0}$ respectively, which is another distinguished property of a Standard Ioffe-Pritchard. Hence, by controlling the value of w_{222} compared to v_{11}^2/B_0, the trap aspect ratio $\omega_\parallel/\omega_\perp$ can be tuned from prolate (cigar-shaped, $\omega_\parallel \ll \omega_\perp$) to oblate (pancake-shaped, $\omega_\parallel \gg \omega_\perp$) [86], as demonstrated in [83].

For the sake of completeness, we mention that the curvature tensors $\mathcal{W}$ of both IP traps do not have exactly the same form. One can note the following differences :

$$w_{113} \neq 0 \text{ and } w_{112} = 0 \text{ for } (\mathcal{S}_I)\text{-Manhattan trap}$$
$$w_{113} = 0 \text{ and } w_{112} = -w_{222}/2 \text{ for Standard Ioffe-Pritchard}$$

The value of w_{113} can be set to zero if desired[12].

- Case II : $(\mathcal{S}_{II})$-Manhattan trap :

The condition (112b) can be satisfied by an appropriate choice of the current $\tilde{I}_{1,0}$, since the elements v_{22} and v_{23} do not depend on the currents $\tilde{I}_{1j}$ and $v_{11} \propto \tilde{I}_{1,0}$.

In this case, there is no constraint on the choice of the parameters of wires $(FL_{2,j})$ $\{t_{2j}, \tilde{I}_{2,j}\}$, only that $v_{22} \neq 0$. In the following, we choose a symmetrical arrangement of these wires : $t_{21} = -t_{22} = t$ and, to reduce the number of the current sources, we set : $\tilde{I}_{2,1} = -\tilde{I}_{2,2} = \tilde{I}_{2,0}$ so that $v_{22} = -4\tilde{I}_{2,0}t^3/h_0^2(1+t^2)^2 \neq 0$. Therefore, the value of $\tilde{I}_{1,0}$ is given by :

$$\tilde{I}^{\mathrm{s}}_{1,0} = 0.3595 \times \tilde{I}_{2,0}\frac{(1+t^2)^2}{t^3}\left(1+\frac{16t^6}{(1+t^2)^4}\right) \tag{128}$$

Moreover, the inclination angle ϕ_{IP} of the trap axis $\boldsymbol{\mathcal{U}}$ is given by :

$$\phi_{IP} = \arctan(-v_{22}/v_{23}) = \arctan\left(4t^3/\left(1+t^2\right)^2\right) \tag{129}$$

As $|\phi_{IP}|$ should be minimized, one should place the wires $(FL_{2,j})$ such as : $|t| \ll 1$.

In this case, the eigenvectors of the frequency tensor $\mathcal{G}$ are slightly tilted from the chip axes, as it is usually the case for a microtrap. They are approximately given by equation (119) with : $v_{11} \approx \tilde{I}_{2,0}/(4h_0^2t^3)$ and $w_{222} = 2\tilde{I}_{2,0}/h_0^3$. Then, once the parameter t is fixed, only the current value $\tilde{I}_{2,0}$ can be tuned to adjust both the axial and transverse frequencies.

12 The element w_{113} depends only on the wires $(FL_{1,j})$. Once the symmetry conditions are satisfied (equation 121), its expression is given by : $w_{113} = -2\tilde{I}_{1,0}(-1+3t_{11}^2)(-1+3t_{12}^2)/(h_0^3(t_{11}-t_{12})(-3+t_{11}^2+t_{12}^2-3t_{11}^2t_{12}^2))$. If desired, its value can be set to zero by choosing : $t_{11} = 1/\sqrt{3}$, and the currents $\{\tilde{I}^{\mathrm{s}}_{1,1}, \tilde{I}^{\mathrm{s}}_{1,2}\} = \{8\tilde{I}_{1,0}, 0\}$. In this case, we obtain the simplest possible IP trap where only two elements of the gradient $\mathcal{V}$ and curvature $\mathcal{W}$ tensors (equations (107) and (115)) are not zero : $v_{11} = \sqrt{3}\tilde{I}_{1,0}/h_0^2$ and $w_{222} = (5-\sqrt{5})\tilde{I}_{2,0}/2h_0^3$ (the trap structure here is even simpler than a Standard Ioffe-Pritchard). Yet, in this case an additional current source is required (3 sources in total). Another solution can be found, by choosing $N_1 = 4$ and adding the condition $w_{113} = 0$ to the linear system (120).

Beyond the second order approximation

A second order expansion of the static field components B_i is sufficient if the typical length $\xi = B_0/B'$ is very large compared to both the transverse splitting s and the size χ of the atomic cloud along the transversal axis (i.e. $\xi \ll s, \chi$). With the following parameters : $T = 100$ nK, $\omega_\perp/2\pi = 1$ kHz and $B_0 = 3.23$ G, we have $\xi \approx 16$ μm and $\chi \approx 1$ μm, and to separate the atomic clouds completely[13], the numerical simulation shows that the second-order expansion of the static field is not sufficient.

In the following, we propose to take into account higher order terms to design a custom trap. Up to the fourth order, this can be performed by deriving the following tensors :

$$(\mathcal{W}^{(3)})_{ijkl} = \frac{\partial^3 B_i}{\partial x_j \partial x_k \partial x_l}\Big)_{\mathbf{r}=\mathbf{r_0}} \tag{130a}$$

$$(\mathcal{W}^{(4)})_{ijklm} = \frac{\partial^4 B_i}{\partial x_j \partial x_k \partial x_l \partial x_m}\Big)_{\mathbf{r}=\mathbf{r_0}} \tag{130b}$$

In order to satisfy the symmetry conditions (110) up to the fourth order, we found that only two additional conditions : $w^{(3)}_{1113} = 0$ and $w^{(4)}_{11111} = 0$, are required if we use the Manhattan architecture, as most of the required conditions are redundant or fulfilled by construction. Moreover, these conditions depend only on the wires ($FL_{1,j}$)

Thus, we choose $N_1 = 5$ in order to satisfy the four conditions of symmetry : $v_{13} = 0$, $w_{111} = 0$, $w^{(3)}_{1113} = 0$ and $w^{(4)}_{11111} = 0$, which can be written as a linear system (similar to equation (120)) :

$$M \begin{pmatrix} \tilde{I}_{1,1} \\ \tilde{I}_{1,2} \\ \tilde{I}_{1,3} \\ \tilde{I}_{1,4} \end{pmatrix} = \begin{pmatrix} -\tilde{I}_{1,0} \\ -\tilde{I}_{1,0} \\ -\tilde{I}_{1,0} \\ -\tilde{I}_{1,0} \end{pmatrix} \text{ with} \tag{131}$$

$$M = \begin{pmatrix} \frac{t_{11}^2\left(-1+t_{11}^2\right)}{\left(1+t_{11}^2\right)^2} & \frac{t_{12}^2\left(-1+t_{12}^2\right)}{\left(1+t_{12}^2\right)^2} & \frac{t_{13}^2\left(-1+t_{13}^2\right)}{\left(1+t_{13}^2\right)^2} & \frac{t_{14}^2\left(-1+t_{14}^2\right)}{\left(1+t_{14}^2\right)^2} \\ \frac{t_{11}^4\left(-3+t_{11}^2\right)}{\left(1+t_{11}^2\right)^3} & \frac{t_{12}^4\left(-3+t_{12}^2\right)}{\left(1+t_{12}^2\right)^3} & \frac{t_{13}^4\left(-3+t_{13}^2\right)}{\left(1+t_{13}^2\right)^3} & \frac{t_{14}^4\left(-3+t_{14}^2\right)}{\left(1+t_{14}^2\right)^3} \\ \frac{t_{11}^4-6t_{11}^6+t_{11}^8}{\left(1+t_{11}^2\right)^4} & \frac{t_{12}^4-6t_{12}^6+t_{12}^8}{\left(1+t_{12}^2\right)^4} & \frac{t_{13}^4-6t_{13}^6+t_{13}^8}{\left(1+t_{13}^2\right)^4} & \frac{t_{14}^4-6t_{14}^6+t_{14}^8}{\left(1+t_{14}^2\right)^4} \\ \frac{t_{11}^6\left(5-10t_{11}^2+t_{11}^4\right)}{\left(1+t_{11}^2\right)^5} & \frac{t_{12}^6\left(5-10t_{12}^2+t_{12}^4\right)}{\left(1+t_{12}^2\right)^5} & \frac{t_{13}^6\left(5-10t_{13}^2+t_{13}^4\right)}{\left(1+t_{13}^2\right)^5} & \frac{t_{14}^6\left(5-10t_{14}^2+t_{14}^4\right)}{\left(1+t_{14}^2\right)^5} \end{pmatrix}$$

Once the currents $\tilde{I}^s_{1_j}$ (i.e. the solutions) are computed, we can reduce the number of required currents by imposing that : $|\tilde{I}_{1,j}| = |\tilde{I}_{1,0}|$ and adjusting the wire positions : t_{1j}.

The numerical resolution gives the following solutions :

$$\{|t_{11}|, |t_{12}|, |t_{13}|, |t_{14}|\} \simeq \{1.0173, 12.0972, 0.4455, 1.1868\} \tag{132}$$

13 In this case, the clock states should be separated by a distance $s \approx 3$ μm.

However, this solution may be difficult to realize in practice. For example, if we set the trap center at a distance $h_0 = 25$ μm from the chip surface, the smallest separation (distance) between the wires $(F_{1,0})$ and $(F_{1,2})$ would be : $L_{12} = h_0/|t_{12}| \approx 2$ μm, which may be difficult to reach in practice because of the non-negligible width of the wires (about 1 μm at least).

Yet, the previous technical difficulty can be avoided if we use an additional source of current. For this purpose, we solve the following equations :

$$|\tilde{I}_{1,1}| = |\tilde{I}_{1,2}| = 5|\tilde{I}_{1,0}|/4 \tag{133a}$$
$$|\tilde{I}_{1,3}| = |\tilde{I}_{1,4}| = |\tilde{I}_{1,0}| \tag{133b}$$

A similar set of solution than equations (132) can be found, but with a lower value of $|t_{12}|$. In order to maximize the gradient $|v_{11}|$, we choose the following solution :

$$\{t_{11}, t_{12}, t_{13}, t_{14}\} \simeq \{1.0196, 5.9525, -0.6561, -1.5298\} \tag{134}$$

which corresponds to the currents setting :

$$\tilde{I}_{1,0} = -4\tilde{I}_{1,1}/5 = -4\tilde{I}_{1,2}/5 = \tilde{I}_{1,3} = \tilde{I}_{1,4} \tag{135}$$

and the gradient value : $v_{11} = -1.9521 \times \tilde{I}_{1,0}/h_0^2$. The stationary point conditions (111(c-d)) can be satisfied using the wires $(FL_{2,j})$ as explained previously. Thus, this higher order improvement can be applied to both Manhattan solutions $(\mathcal{S}_I)$ and $(\mathcal{S}_{II})$. We refer to them by : $(\mathcal{S}_I^\star)$ and $(\mathcal{S}_{II}^\star)$, respectively.

Two practical wire-settings for the Manhattan solutions are given for $h_0 = 25$ μm, in Figure 40. In the following, we discuss the performance of these custom traps and compare it to the typical traps.

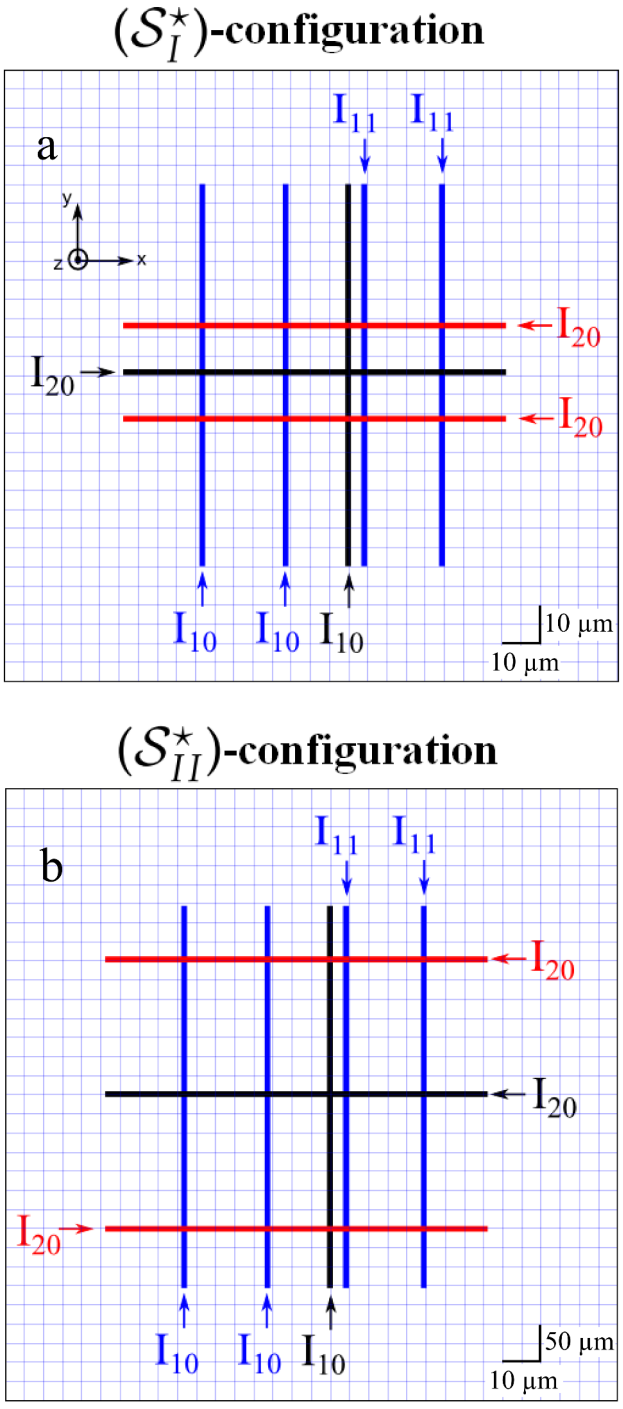

Figure 40: Wire layout of the custom Manhattan traps for $h_0 = 25$ μm. (a) $(\mathcal{S}_I^\star)$-Manhattan trap (b) $(\mathcal{S}_{II}^\star)$-Manhattan trap for $|t_{21}| = |t_{22}| = 0.14$ (the x-axis scale and the y-axis scale are different). The cross-section of the wires is here : $1\mu\text{m} \times 1.5\mu\text{m}$. So, the wires in the lower (upper) layer can carry a current up to about 82 mA (42 mA), respectively [163].

6.2.5 *Summary : comparison between different static traps*

In Table 4, we summarize the results of a transverse microwave splitting using different static traps. The simulations have been done with the same microwave field parameters and, as much as possible, the same static field parameters.

For the static fields, the currents and bias fields, shown in Table 4, are chosen such as :

- The trap distance from the chip surface is $h_0 = 25\ \mu$m[14].
- The transverse and axial angular frequencies are $\{\omega_x, \omega_y\}/2\pi = \{1000, 120\}$ Hz[15].
- The field value in the trap center is $B_0 = 3.23$ G.

The microwave field parameters are chosen such as :

- The detunings verify : $\Delta_a^\sigma(\mathbf{r_0}) = -\Delta_b^\sigma(\mathbf{r_0}) = 0.05 \times \omega_L^0$, which corresponds to a potential-barrier beam-splitter.
- The microwave power is $P_{mw} = P_1 = 3P_2 = 4P_0$.
- The coplanar waveguides (symmetrical) position along the x-axis is $\delta = 54\ \mu$m[16].

In particular, one can note that the Manhattan traps require a nonzero bias field along the z-axis (normal to the chip surface), compared to the typical microtraps where the z-component of the bias field is equal to zero.

The Manhattan traps are designed to allow the creation of a microwave shift V_{mw} that has an axial symmetry, as is possible with a Standard Ioffe-Pritchard (SIP). In this case, the splitting direction θ_{ab} is independent of the values of the currents and coincides with the transverse axis, as can be seen in Figure 41b and Table 4.

Nevertheless, the trap-depth (TD) of the ($\mathcal{S}_I^\star$)-Manhattan trap is very low because of the proximity of the wires ($FL_{2,j}$) to the x-axis. This is also the case of the H*-trap. In both case, the trap-depth is approximately given by : $TD \simeq \frac{1}{2}m\omega_y^2(h_0/t)^2$ where $t = |t_{21}| = |t_{22}|$. As the parameter t is constant for both traps, only the remaining parameters can be modified to improve the trap-depth. For the ($\mathcal{S}_I^\star$)-Manhattan trap , this problem can be avoided by setting the value of t

14 h_0 is relatively low here, since the splitting along the transverse axe requires much higher splitting force than the axial splitting. Reducing the distance of the atoms from the CPWs allows a significant increase of the microwave shift V_{mw} value.

15 The axial frequency value can be chosen lower, but some traps ($H^\star$ and $\mathcal{S}_I^\star$) will not have a sufficient trap-depth in this case.

16 Here, $\delta \approx 2h_0$. Thus, the displacement along x is more important than along z as the microwave gradient is similar along both directions. Reducing δ would increase the microwave shift V_{mw} and the splitting distance s at the cost of a higher residual displacement along z.

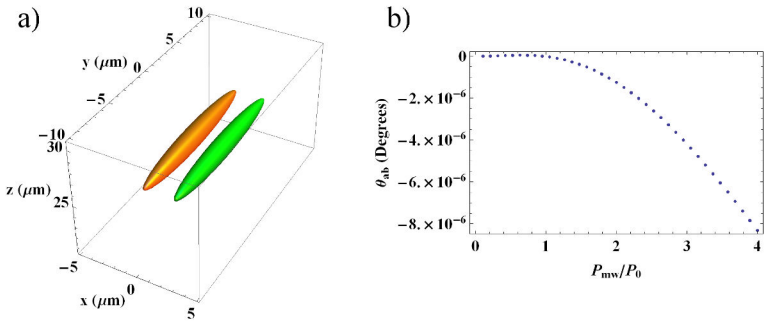

Figure 41: $(\mathcal{S}^{\star}_{II})$-Manhattan trap : (a) 3D-equipotentials representation of the clock states : $|a\rangle$ (orange) and $|b\rangle$ (green), for the potential $k_B T$ with $T = 100$ nK. (b) The variation of the splitting direction θ_{ab} as function of the microwave power P_{mw}. (cf. section 6.2.5 for the simulation parameters.)

in equation (125a) to a lower value[17], but an additional current-source will be required since the equation (124) will be no longer verified.

Finally, one can notice that the splitting distance $|x_m|$ along $\mathbf{x}$ and the residual variation $|z_m - h_0|$ along $\mathbf{z}$ are similar for all the static traps. However, the residual variation $|y_m|$ along $\mathbf{y}$ is particularly low for the SIP, H* and $(\mathcal{S}^{\star}_{I})$-Manhattan traps, which is mainly related to the field gradient structure : since the element v_{22} is zero, the splitting force along $\mathbf{y}$ is nearly zero at $\mathbf{r_0}$.

17 Which corresponds to a larger distance of the wires $(FL_{2,j})$ from the center $\mathbf{r} = \mathbf{0}$. For example, the trap-depth can be increased by a factor of 4 (from $h \times 5.4$ to $h \times 86.4$ kHz) by decreasing the parameter t by a factor of 2.

Trap	Static Potential						Microwave Potential						
	Trap-depth [kHz]	I_{10} [mA]	I_{20}	$B_{b,x}$	$B_{b,y}$ [G]	$B_{b,z}$	$\lvert x_m \rvert$	$\lvert y_m \rvert$	$\lvert z_m - h_0 \rvert$ $[\mu m]$	$\lvert \theta_{ab} \rvert$	$\omega_{\tilde{x}}/2\pi$	$\omega_{\tilde{y}}/2\pi$ $[Hz]$	$\omega_{\tilde{z}}/2\pi$
SIP	-	-	-	-	-	-	1.28	0.03	0.52	0°	867.45	99.40	822.42
Z	1680	62.58	-	-4.70	2.94	0.00	1.59	6.08	0.37	75.27°	862.63	90.13	804.57
Dimple	38.4	62.73	0.69	-4.98	3.29	0.00	1.26	0.94	0.52	36.65°	853.91	96.24	748.73
$H^\star$	16.5	-62.30	-1.40	4.98	3.12	0.00	1.25	0.04	0.55	1.94°	852.19	96.62	734.51
$(\mathcal{S}_I^\star)$-Manhattan	5.4	31.90	1.00	-0.38	3.18	4.45	1.32	0.02	0.58	10^{-6°	852.91	93.09	786.97
$(\mathcal{S}_{II}^\star)$-Manhattan	33.1	32.05	-0.69	-0.38	-3.28	4.43	1.31	0.44	0.57	10^{-5°	852.82	95.71	793.70

Table 4: Simulation of the Transverse beam-splitters. A comparison between the (resulting) microwave potentials generated using several static traps : SIP, Z-trap (with $t = 0.248$), Dimple trap, $H^\star$-trap and the custom Manhattan traps (cf. text). In each case, the trap-depth and the following experimental parameters are given (for the microtraps) : the currents $\{I_{10}, I_{20}\}$ along the axes $\{\mathbf{x}, \mathbf{y}\}$ respectively, and the homogenous bias field along the axes $\{\mathbf{x}, \mathbf{y}, \mathbf{z}\}$ (cf. text). For the microwave trapping-potentials, the coordinates of the minimum $\mathbf{r_m} = \{x_m, y_m, z_m\}$, the splitting direction θ_{ab}, and the eigenfrequencies $\{\omega_{\tilde{x}}, \omega_{\tilde{y}}, \omega_{\tilde{z}}\}$ are computed.

6.3 FULL-SIMULATION RESULTS

In this section, we present the results of a complete simulation taking into account the effect of the non-resonant transitions. We focus on the study of the transverse beams-splitter, using the H*-trap[18], with the field parameters used previously in section 6.2.5. This configuration corresponds to the Config. *I* on our chip (cf. Figure 52).

Figure 42 shows the resulting potentials, computed using the full numerical model (equation (78)) and the approximated analytical model (equation (79)). Form the last simulation, the dissymmetry of the potentials can be estimated, as shown in Table 5. The highest frequency difference between the two wells is along the axial direction $\mathbf{x}$: about 2%. These dissymmetries can be reduced to the order of 0.1% by fine-tuning the microwave powers $\{P_1, P_2\}$ and the microwave frequencies $\{\omega_{mw,1}, \omega_{mw,2}\}$.

Moreover, one can notice a discrepancy between the numerical (78) and analytical (79) models, unlike the case of an axial beam-splitter where an excellent agreement has been shown (cf. Figure 19). This is due to the fact that, the condition of well-separated anti-crossing : $|\Omega_{m_1}^{m_2}| \ll |\omega_L^0|$ is not fully satisfied here. In particular, the Rabi frequencies $\Omega_{m_1}^{m_2}$ should be relatively important in order to compensate the high transverse confinement ($\omega_\perp/2\pi = 1$ kHz). For instance in Figure 42, the Rabi frequencies related to the σ-transitions are estimated in the trap center $\mathbf{r_0}$ by : $\left|\Omega_a^{\sigma^{(-)}}\right| = 0.32 \times \omega_L^0$ and $\left|\Omega_a^{\sigma^{(+)}}\right| = \left|\Omega_b^{\sigma^{(-)}}\right| = 0.19 \times \omega_L^0$. Yet, the approximated model still can be used for a quick screening of the tunable microwave parameters, as the accuracy of the frequencies estimation is about 1%.

Finally, we point out that similar results can be found using a potential-well beam-splitter. As expected, the dissymmetry of the potentials are higher due to the reduction of the trap-depth discussed in section 5.3. Moreover, as the splitting distances in both cases are similar (≈ 2 μm), there is no advantage in using an attractive microwave potential for a transverse splitting.

	$\tilde{\mathbf{x}}$	$\tilde{\mathbf{y}}$	$\tilde{\mathbf{z}}$
$\lvert\Delta\omega\rvert/2\pi$ (Hz)	15.82	1.21	11.16
$\lvert\frac{\Delta\omega}{\omega}\rvert \times 10^{-2}$	1.81	1.29	1.55

Table 5: The dissymmetry of the potentials $\Delta\omega = \omega_b - \omega_a$, related to the simulations shown in Figure 42, along the eigendirections : $\{\tilde{\mathbf{x}}, \tilde{\mathbf{y}}, \tilde{\mathbf{z}}\}$. The latter are slightly rotated from the chip reference : $\{\mathbf{x}, \mathbf{y}, \mathbf{z}\}$.

18 As the Manhattan-trap configurations are not implemented in the current chip version.

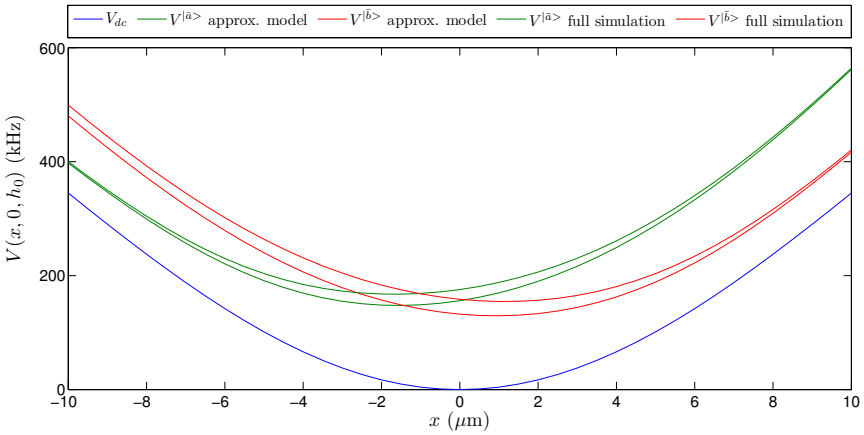

Figure 42: The H*-trap configuration. Numerical simulation of the dressed clock states $|\bar{a}\rangle$ (in green) and $|\bar{b}\rangle$ (in red) potentials and the static potential (in blue), shown here along the transverse direction **x**, using two different models (cf. text). This configuration corresponds to the Config. *I* on our chip (cf. Figure 52).

6.4 MAGIC FIELD

The effect of the microwave dressing on the magic field using π-transitions has been studied in section 5.5. In a similar manner, we propose to analyze the effect of the microwave dressing using σ-transitions.

For this purpose, we use the same formalism than section 5.5 where the detunings and the microwave frequencies are given by :

$$\Delta_a(B) = \omega_{mw,1} - \left[E_{2,0}(B) - E_{1,-1}(B)\right]/\hbar \tag{136a}$$
$$\Delta_b(B) = \omega_{mw,2} - \left[E_{2,1}(B) - E_{1,0}(B)\right]/\hbar \tag{136b}$$
$$\omega_{mw,1} = \omega_{\text{hfs}} - \omega_L^0 + \Delta_a^0 \tag{136c}$$
$$\omega_{mw,2} = \omega_{\text{hfs}} + \omega_L^0 + \Delta_b^0 \tag{136d}$$
$$\Delta_a^0 = -\Delta_b^0 = \Delta_0 \tag{136e}$$

Figure 43 shows the maximal allowed contamination κ_c as function of the initial detuning $|\Delta_0|$ in the case of a potential-barrier ($\Delta_0 > 0$). One can notice a significant improvement of the κ_c values compared to the case of microwave dressing using π-transitions. For instance, κ_c is higher by a factor of 5.3 if $|\Delta_0| = 0.05 \times \omega_L^0$.

This can be explained simply by the weak dependance to the magnetic field B of the energies $\{E_{2,0}, E_{1,0}\}$ corresponding to the states $\{|2,0\rangle, |1,0\rangle\}$, which are coupled to the clock states $\{|a\rangle, |b\rangle\}$, respectively. In case of the σ-transitions, the variation of the coupling-energies $\{E_{2,0}, E_{1,0}\}$ as function of B is (nearly) of a second order as $m_F = 0$, unlike the case of the π-transitions, where the variation of the coupling-energies $\{E_{2,-1}, E_{1,1}\}$ have (approximately) a linear dependence of B as $|m_F| = 1$.

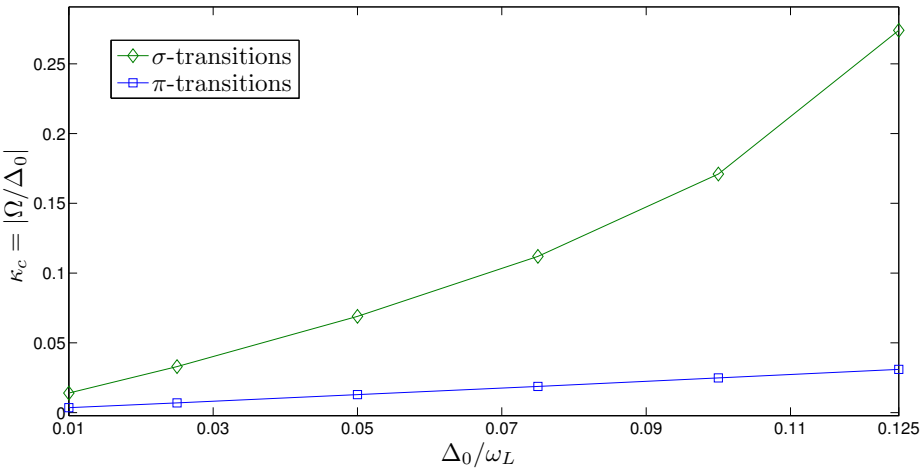

Figure 43: The maximum allowed contamination rate $\kappa_c = |\Omega/\Delta_0|$ as a function of the initial detuning $|\Delta_0|$, using π-transition (in blue) and σ-transitions (in green), in the case of a potential-barrier.

Nevertheless, the values obtained of κ_c are not sufficient to perform a transverse splitting, with the parameters discussed earlier. For example, in section 6.3, the contamination value at $\mathbf{r_0}$ is about : $\kappa = |\Omega/\Delta_0| \approx 4$. Hence, the perturbed-symmetrical configuration discussed in section 5.5.2 can be also a useful solution here to increase the value of κ_c. As shown in Figure 26, in the case of π-transitions and a potential-barrier, the maximal contamination value is no longer limited ($\kappa_c \to \infty$) if $|\Delta_0| > |\Delta_0^{T_1}|$, where $\Delta_0^{T_1}$ is the first-threshold value. Similar results can be found here with σ-transition. Moreover, by choosing $|\Delta_0| > |\Delta_0^{T_2}|$ where $\Delta_0^{T_2}$ is the second-threshold value and $|\Delta_0^{T_1}| < |\Delta_0^{T_2}|$, it is possible to follow adiabatically the evolution of the magic field $B_m(\kappa)$. Figure 44 shows the second-threshold value $\Delta_0^{T_2}$ as a function of the perturbation parameter ϵ. For instance, in order to set the initial detuning[19] to $|\Delta_0| = 0.05 \times \omega_L^0$, and to avoid the limitation on the contamination value κ, the perturbation parameter $|\epsilon|$ has to be set (at least) to : $\{4 \times 10^{-2}, 0.6 \times 10^{-2}\}$ using π, σ-transitions respectively. Here also, using σ-transitions is more advantageous as the perturbative parameter can be set to a lower value, so the dissymmetry of the potentials given by equation (91) can be reduced further.

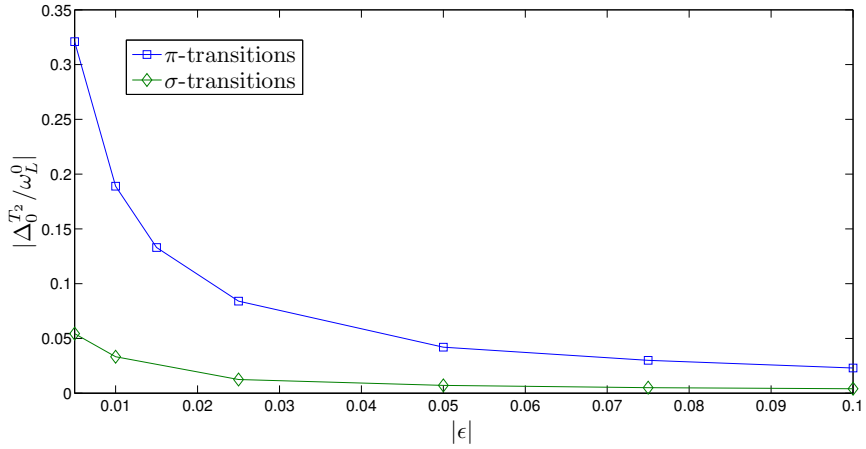

Figure 44: The variation of $|\Delta_0^{T_2}|$ as a function the perturbative parameter $|\epsilon|$ using π-transitions (in blue) and σ-transitions (green), for a potential-barrier. Following adiabatically the variation of the magic field B_m is possible if : $|\Delta_0| > |\Delta_0^{T_2}|$. The contamination value κ is not limited in this case.

19 As it is the case in Figures 42 and 19b.

6.5 CONCLUSION

The transverse splitting has two principle advantages compared to the axial one : it allows a short splitting time and keeps the trap-aspect ratio (nearly) unchanged after splitting. Nevertheless, it requires a larger Rabi frequency (with a larger microwave power or/and shorter distance from the chip surface) and allows only a relatively small splitting distance (few microns). Moreover, using a typical microtrap, the splitting direction would be dependent on the experimental splitting parameters (e.g. static and microwave currents) which may be a drawback for precision measurements. In order to overcome this disadvantage, we have designed specific static traps on chip such as the H*-trap and the Manhattan trap, but these solutions further complicate the experimental realization.

However, this framework allowed the design of a custom microtrap, the ($\mathcal{S}_l$)-Manhattan trap, that has a field structure similar than a Standard Ioffe-Pritchard, and so, can be used to tune widely the trap aspect-ratio on chip (which can not be done with typical microtraps).

In the next section, we will focus on the study of the dynamical behavior of our interferometer. For the sake of clarity, only the axial beam-splitter is analyzed.

7

BEAM-SPLITTER DYNAMICS AND CONTRAST ANALYSIS

7.1 INTRODUCTION

For a trapped (thermal) interferometer, studying the beam-splitter dynamics is of great importance. Uncontrolled fast splitting would induce motional excitation, giving rise to heating, atom losses and a reduction of the interferometer coherence time. In the case of a state-selective beam-splitter considered in this work, the interferometer dynamics is considerably simplified compared to a double-well scheme [168], since the evolutions in the two interferometer arms are not coupled for the most part and can be treated independently. Hence, this subject can be treated as an atomic transition-less transport, which has been extensively studied in the literature [169], and is still a major goal for many applications such as quantum information processing in trap arrays [170], loading atoms in optical lattices [171], or placing atoms in a high-Q optical cavity [172, 173, 174]. Recently, interest to perform fast atomic transport has led to a surge of theoretical [175] and experimental activity [176, 177].

An obvious solution at least in principle, to avoid vibrational excitations, is to perform a sufficiently slow transport such that the atoms follow adiabatically the changes in the trapping potential. This requires that the duration of the transport is long with respect to the typical oscillation period of the trapped atoms along the splitting direction [178].

In this chapter, we focus on the axial beam splitter and we study the interferometer contrast in the case of an adiabatic transport (splitting), and then we investigate the possibility of fast transitionless transport (i.e. faster than adiabatic transport).

7.2 ADIABATIC SPLITTING AND RECOMBINATION

The adiabaticity condition required here is related to external states of the atoms. This condition is more restrictive for the external states, than for the internal states discussed earlier in section 4.3.3. Indeed, the *internal* time scale is governed by the Larmor frequency (about 6 MHz) while the *external* time scale is related to the microtrap frequencies (about $0.1 - 2$ kHz). In the case of a compression of an harmonic potential, this condition can be written [178]: $|\dot{\omega}_x|/\omega_x^2 \ll 1$, where ω_x is the angular frequency of the harmonic oscillator.

A typical trapped interferometer scheme is formed from three stages : Splitting-Holding-Recombination as shown in Figure 7. In the interferometer envisioned here, by switching off the microwave signal, we can recombine the two interferometer arms in the static trap center. In principle, splitting and recombination can be implemented in an identical manner, which we call "temporal-symmetry" of the interferometer, in contrast with spatial symmetry discussed previously (cf. Figure 49a). Since splitting and recombination occur at the same spatial location, this interferometer fulfills the so called "cyclic" transport condition [179].

7.2.1 *Cyclic and adiabatic transport*

In a seminal paper, Berry has provided a general solution for such a cyclic and adiabatic transport problem [179], for a system that evolves under an Hamiltonian H that can be changed by varying the parameters $\mathbf{R}$ on which it depends.

For instance, in our case, $\mathbf{R}$ can be associated to the experimental parameters $\{\omega_{mw,1}, P_1, \omega_{mw,2}, P_2\}$: the microwave parameters of the signals injected into the CPWs. The evolution of the system between $t = 0$ and $t = t_f$ can be seen as transport around a closed path (called here $\mathcal{C}$) of $\mathbf{R}(\mathbf{t})$ in parameter space if $\mathbf{R}(\mathbf{t_0}) = \mathbf{R}(\mathbf{t_f})$. Moreover, if the system is prepared initially in an eigenstate $|n_0\rangle \equiv |n(t_0)\rangle$ of $H(t_0)$ and the parameters $\mathbf{R}(\mathbf{t})$ are slowly changed, it follows from the adiabatic theorem [178] that the system will be at any instant in an eigenstate $|n(t)\rangle$ of $H(t)$. After this slow and cyclic transport, the wavefunction $|n(\mathbf{R}(t))\rangle$ can be written :

$$|n\left(\mathbf{R}(t)\right))\rangle = \exp[i\theta_n(t)] \times \exp[i\beta_n(t)]|n_0\rangle \tag{137}$$

where θ_n is the classical dynamical phase and β_n is the geometrical Berry phase.

The dynamical term (θ_n) is given by :

$$\theta_n(t_{r.o}) = \int_0^{t_{r.o}} \mathrm{d}t(E_n(t)/\hbar) \tag{138}$$

where $E_n(t)$ are the eigenvalues of H.

The geometrical term (β_n) satisfy the following relation :

$$\dot{\beta}_n(t) = i\langle n(\mathbf{R}(t))\frac{d}{dt}|n(\mathbf{R}(t))\rangle \tag{139a}$$

$$= i\langle n(\mathbf{R})\nabla_{\mathbf{R}}|n(\mathbf{R})\rangle \times \dot{\mathbf{R}} \tag{139b}$$

since $n(\mathbf{R}(t))$ evolves under the Schrödinger equation [179].

The total phase $\beta_n(t_{r.o})$ after a transport along the closed path $\mathcal{C}$ can be transformed to a circuit integral $\beta_n(\mathcal{C})$ as :

$$\beta_n(\mathcal{C}) = i\oint_{\mathcal{C}} \mathrm{d}\mathbf{R}\langle n(\mathbf{R})\nabla_{\mathbf{R}}|n(\mathbf{R})\rangle \tag{140}$$

which is a time independent expression.

The latter phase is a purely geometrical (topological) phase. It can be seen, from classical-mechanics viewpoint, as a parallel (tangential) transport of a vector along a loop [180, 181]. After completing the closed path, the vector goes back to the original point but rotated by an angle with respect to the initial direction. For example, after a parallel transport of a vector along the closed path shown in Figure 45, the rotation angle is $\pi/2$. Such rotation angle is of a geometrical origin, and known for quantum systems as the *Berry phase*. This term ($\beta_n(\mathcal{C})$) vanishes in case of a time-symmetrical interferometer (assuming that the parameters $\mathbf{R}(t)$ are reversed in time, cf. Figure 49a), since the surface in the interferometer parameters space encloses no area [179].

Moreover, it is also null if the space parameter $\mathbf{R}$ forms a flat surface such as a plane [181]. In our case, each interferometer arm is controlled mostly by two experimental parameters (e.g. $\mathbf{R}_1 = \{\omega_{mw,1}, P_1\}$ for the for right-hand arm) as described in chapter 4. This is an additional argument to ensure that the geometrical phase vanishes even if the interferometer is not perfectly symmetrical on time.

Finally, the remaining dynamical phases (θ_n) can be seen as the system internal clocks that record the passage of time [179].

7.2.2 *Interferometer contrast decay*

For a statistical thermal ensemble prepared at a temperature T, the interferometer evolution should be described using the density operator for each clock state [182]. Let's suppose that the system is initially prepared in the internal state $|a\rangle$. Hence, it can be described by the density matrix :

$$\varrho(t < t_0) = \sum_n p_n |n, a\rangle\langle n, a| \tag{141}$$

where p_n is the occupation probability of n^{th} level in the static potential and is given by the Boltzmann factors : $e^{-E_n^0/k_BT}/Z$ with E_n^0 is the n^{th} eigenenergy of the static potential and $Z = \sum_n e^{-E_n^0/k_BT}$ is the partition function.

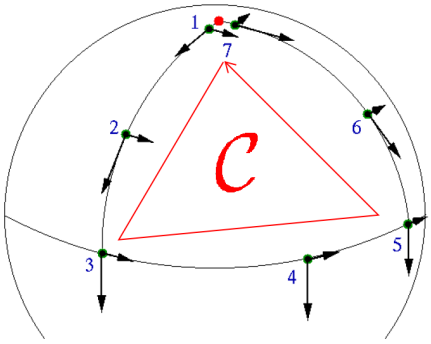

Figure 45: Schematic of the geometrical Berry phase. In classical mechanics, parallel transport of a vector along a closed path ($\mathcal{C}$) : a loop on a sphere induces a rotation compared to the original orientation. Here, the loop surrounds one eighth of the sphere and the rotation angle amounts to $\pi/2$. Such a rotation angle is of a topological origin and is known as the Berry phase in quantum mechanics.

For a Ramsey-type interferometer, the sequence starts with a $\pi/2$ pulse in order to put the atoms in a coherent superposition of the clock states. After splitting and recombination, the phase read-out is performed by applying a second $\pi/2$ pulse to close the interferometer. At the read out time $t = t_{r.o}$, the total population of the internal state $|a\rangle$ reads $p_a = \mathrm{Tr}(\varrho|a\rangle\langle a|) = 1/2[1 - \mathrm{Re}(A)]$, where A is given by:

$$A = \sum_n p_n \exp\left[i \int_0^{t_{r.o}} \mathrm{d}t \left(E_n^a(t) - E_n^b(t)\right)/\hbar\right] \tag{142}$$

in the case of an adiabatic transformation and $E_n^a(t)$ ($E_n^b(t)$) is the n^{th} eigenenergy of the microwave trapping-potential associated to the state $|a\rangle$ ($|b\rangle$), respectively. The occupation probability p_n remains unchanged since the transitions between the different levels vanish exponentially in this case [178].

The modulus of A describes the interferometer contrast decay which can be written :

$$C = \left|\sum_n p_n \exp\left[i \int_0^{t_{r.o}} \mathrm{d}t \left(E_n^a(t) - E_n^b(t)\right)/\hbar\right]\right| \tag{143}$$

In case of a quasi-symmetrical beam splitter, the energy difference $\Delta E_n(t) = E_n^b(t) - E_n^a(t)$ is small compared to the average energy $(E_n^b(t) + E_n^a(t))/2$. Furthermore, $\Delta E_n(t_0) \simeq 0$ since both states share the same static potential initially.

To simplify the problem, we assume that $\Delta E_n(t)$ increases linearly with time during the splitting stage, from zero to the constant value

$\Delta E_n^1 = \Delta E_n(\tau)$, where τ is the splitting time[1]. This leads to the following contrast expression :

$$C \simeq \left| \sum_n p_n \exp\left(i T_R' \Delta E_n^1 / \hbar \right) \right| \tag{144}$$

where $T_R' = T_R + \tau$, the parameter T_R being the holding time (also called Ramsey time).

In the case where the splitting time τ is very small compared to the holding time T_R (i.e. $\tau \ll T_R$ and $T_R' \approx T_R$), the system can be seen as a conservative system (i.e. H does not depend explicitly on time) and its dynamics can be captured by the stationary evolution of the energy levels during the holding stage.

In probability theory, the contrast expression can be written in term of the first moment (expectation) related to the Boltzmann distribution as :

$$C = \left| \mathcal{E}\left[e^{i\Theta} \right] \right| \tag{145}$$

where Θ is a discrete random variable defined as the ensemble of the dynamical phases $\Delta\theta_n = \int_0^{t_{r.o}} \mathrm{d}t (\Delta E_n(t)/\hbar) \simeq T_R' \Delta E_n^1 / \hbar$, associated with the probability distribution p_n. From equation 145, the contrast can be rewritten as a function of the second moment (variance) of the centered variable $\bar{\Theta} = \Theta - \mathcal{E}[\Theta]$ such as :

$$1 - C^2 = \mathrm{Var}\left[\cos(\bar{\Theta})\right] + \mathrm{Var}\left[\sin(\bar{\Theta})\right] \tag{146}$$

Case of 1D harmonic potentials

In this section, we suppose that the resulting potential of each clock state can be described by an harmonic trap. In addition, if the 1D harmonic approximation holds (i.e. $\hbar\omega_x, k_B T \ll \hbar\omega_\perp$), the contrast (144) leads to :

$$C_{\mathrm{H.O}} = \frac{1}{\sqrt{1 + \left(\frac{\sin(\Delta\omega_1 T_R'/2)}{\sinh(\hbar\omega_0 / 2k_B T)} \right)^2}} \tag{147}$$

where $\Delta\omega_1 = 2\Delta E_0^1/\hbar$ is the difference between the traps frequencies during the holding period, $\omega_0 = \omega_x(t_0)$ is the trap frequency at equilibrium ($t < t_0$). Equation (147) has the same form as the transfer function of a Fabry-Perot cavity in optics. One can define a coherence time as the shortest possible time to reduce the initial contrast by half (i.e. $C(\tau_c) = 1/2$).

For high temperature ($k_B T \gg \hbar\omega_0$), the coherence time is given by :

$$\begin{aligned} \tau_c &= \frac{2}{\Delta\omega_1} \arcsin\left(\sqrt{3} \sinh(\hbar\omega_0 / 2k_B T) \right) \\ &\approx \sqrt{3}\hbar / (\eta k_B T) \end{aligned} \tag{148}$$

1 τ is also recombination time in case of time-symmetrical interferometer, cf. Figure 49a.

with $\eta = \Delta\omega_1/\omega_0$, which gives a similar estimation of the coherence time than expression (68). Moreover, one can notice that the contrast expression (147) is periodic. This periodicity of the contrast is a signature of the harmonicity of the potentials, and results from the following rephasing condition :

$$\text{There is an integer } k \text{ such as : } \Delta E_n^1/\Delta E_0^1 = k \tag{149}$$

In the case of 1D harmonic potential, it can be shown that : $k = 2n+1$.

Case of 1D anharmonic potentials

We can improve the latter 1D harmonic model by considering the anharmonicity effects. However, the Schrödinger equation obtained can no longer be solved analytically. We must then resort to solving it numerically. There exists, however, an approximated method to obtain analytically approximate solution, known as "stationary perturbation theory" in case of conservative quantum system [183].

Perturbation theory is applicable when the Hamiltonian of the system being studied can be put in the from :

$$H = H_0 + W \tag{150}$$

where the eigenstates and eigenvalues of H_0 are known and where W is much "smaller" than H_0 (i.e. the matrix elements of W are much smaller than H_0). To make this more explicit, we assume that W is proportional to a real parameter Λ which is dimensionless :

$$W = \Lambda\hat{W} \tag{151}$$

and where $\hat{W}$ is an operator whose matrix elements are comparable to those of H_0 and $|\Lambda| \ll 1$. Perturbation theory consists of expanding the eigenvalues and eigenstates of H in power of Λ, keeping only a finite number of terms of these expansions.

In our case, H_0 is the Hamiltonian of an harmonic oscillator (H.O) with an angular frequency ω_1, and its corresponding eigenstates and eigenvalues (eigenenergies) are respectively given by the following :

$$\phi_n(x) = \frac{1}{\sqrt{2^n n!}}\left(\frac{m\omega_1}{\pi\hbar}\right)^{1/4} e^{-\frac{m\omega_1 x^2}{2\hbar}} H_n\left(\sqrt{\frac{m\omega_1}{\hbar}}x\right) \tag{152}$$

$$E_n^{H.O} = \hbar\omega_1(n+1/2) \tag{153}$$

where H_n are the Hermite polynomials. The eigenvalues form a discrete and non-degenerate spectrum of energy (i.e. n is an integer).

The second-order energy correction for the state $|\phi_n\rangle$ can be calculated using the perturbation theory [183] :

$$E_n(\Lambda) = E_n^{(0)} + E_n^{(1)} + E_n^{(2)} + O(\Lambda^3) \tag{154a}$$

$$E_n^{(0)} = \langle\phi_n|H_0|\phi_n\rangle \tag{154b}$$

$$E_n^{(1)} = \langle\phi_n|W|\phi_n\rangle \tag{154c}$$

$$E_n^{(2)} = \sum_{k\neq n} \frac{|\langle\phi_k|W|\phi_n\rangle|^2}{E_n^{(0)} - E_k^{(0)}} \tag{154d}$$

The correction of the state $|\phi_n\rangle$ can be also calculated but is not necessary here since only the energy level E_n is required for the contrast estimation (cf. equation (144)). In practice, the second order correction is enough (at least in our case, as will be shown in the next section).

In the case of a one dimensional model, the anharmonicity is a superposition of perturbative terms in the form of : $W_k = \hbar\omega_1\sigma_k X^k$ where $X = x/a_{\text{H.O}}$ with $a_{\text{H.O}} = \sqrt{\hbar/m\omega_1}$ and k is an integer. The particular cases where $k = \{0,1,2\}$ correspond to a perturbation of the potential minimum value, position and frequency, which are not relevant here.

On the other hand, one can show that the first correction term of the energy : $\langle\phi_n|W|\phi_n\rangle$ vanishes for $k > 3$, which minimizes the effect of the anharmonic perturbations. Moreover, the non-dimensional coefficients of the perturbative terms σ_k relative to each clock state have (approximately) similar absolute values along the x-axis[2]. Generally, this property can be verified for higher order terms, if the symmetry condition $V^{|\bar{a}\rangle}(-x) = V^{|\bar{b}\rangle}(x)$ is nearly verified.

These correction terms can be calculated analytically [24, 183], by writing the operator : $X = \frac{1}{\sqrt{2}}(a + a^\dagger)$ where a and $a^\dagger$ are annihilation and the creation operators respectively. Using the properties of the quantum harmonic oscillator, we can deduce that the matrix elements of W_k.

For W_3 ($k = 3$), using a second-order perturbation theory, the calculation yields to the energy shift :

$$E_n - E_n^{(0)} = -\sigma_3^2\left[\frac{15}{4}\left(n + 1/2\right)^2 + \frac{7}{16}\right]\hbar\omega_1 \tag{155}$$

The difference between two adjacent levels is no longer independent of n as it is the case for the quantum harmonic oscillator.

Applying this anharmonicity consideration to the previous contrast formula (144), makes in principle the rephasing condition (149) no more valid. In practice, the harmonic approximation holds if the temperature T is chosen such as :

$$\left|\left(\left(\sigma_3^b\right)^2 - \left(\sigma_3^a\right)^2\right)\mathcal{E}\left[\frac{15}{4}\left(n + 1/2\right)^2 + \frac{7}{16}\right]\right| \ll 1 \tag{156}$$

2 As shown in Table 6 (the term X^3), which corresponds to σ_3 in this case.

where $\mathcal{E}$ is the first moment in term of the Boltzmann distribution[3], and σ_3^a and σ_3^b are given in Table 6.

Case of simulated full 3D potentials

We present here a study of the contrast decay using a full 3D numerical simulation. The microwave potentials correspond to the potential-barrier and potential-well beam-splitter, shown in Figure 19, and are calculated using equation (79). As explained in the previous section, the energy level must be computed numerically.

In this section, we investigate the solutions given by the stationary perturbation theory, described in previously (cf. equation (154)), but applied here to the full 3D potentials with a numerical approach to evaluate the correction terms.

First, for each trapping-potential, we estimate numerically the coordinates of the minimum $\mathbf{r_m} = \{x_m, y_m, z_m\}$, and we define the chip reference as :

$$\{X, Y, Z\} = \{x - x_m, y - y_m, z - z_m\} \tag{157}$$

Then, we evaluate the eigenvectors $\{\tilde{\mathbf{X}}, \tilde{\mathbf{Y}}, \tilde{\mathbf{Z}}\}$ (as function of $\{\mathbf{X}, \mathbf{Y}, \mathbf{Z}\}$) and the eigenfrequencies $\{\omega_{\tilde{X}}, \omega_{\tilde{Y}}, \omega_{\tilde{Z}}\}$ in the minimum, during the holding stage. The quantum harmonic oscillator (H.O) gives a first estimation of the energy levels ($E_n^{a/b}$). The latter evaluation is then improved using the stationary perturbation theory [183] to take into account the effect of anharmonicity. For each clock state, we define the perturbation potential W as :

$$\begin{cases} W = V' - \tilde{V} \\ V' = V(X, Y, Z) - V(0, 0, 0) \\ \tilde{V} = \frac{1}{2} m(\omega_{\tilde{X}}^2 \tilde{X}^2 + \omega_{\tilde{Y}}^2 \tilde{Y}^2 + \omega_{\tilde{Z}}^2 \tilde{Z}^2) \end{cases} \tag{158}$$

where V and $\tilde{V}$ are the full 3D potential and the approximated 3D harmonic potential respectively. Both potentials are centered around zero.

Expression of W is deduced using equation (79) to generate the microwave potential V. Then, it is used together with the expression (153) of the eigenstate $\phi_n(x)$ to compute the diagonal $\langle \phi_n | W | \phi_n \rangle$ and off-diagonal $\langle \phi_k | W | \phi_n \rangle$ matrix elements in equation (154). The latter elements are related to the first order and second-order energy corrections, respectively. The diagonal elements $\langle \phi_n | W | \phi_n \rangle$ are no longer zero due to the anharmonic terms. For instance, the contribution of anharmonic potential of the form $X^i Y^j Z^k$ is not zero, where i, j, k are nonzero integers.

The numerical computation is performed using *Mathematica*, that allows a precise and time-efficient numerical evaluation of integrals[4].

3 Further derivation of this moment is given in [24].

4 It allows also parallel computation using up to 16 cores, which reduces the computation time of the energy levels to only few hours.

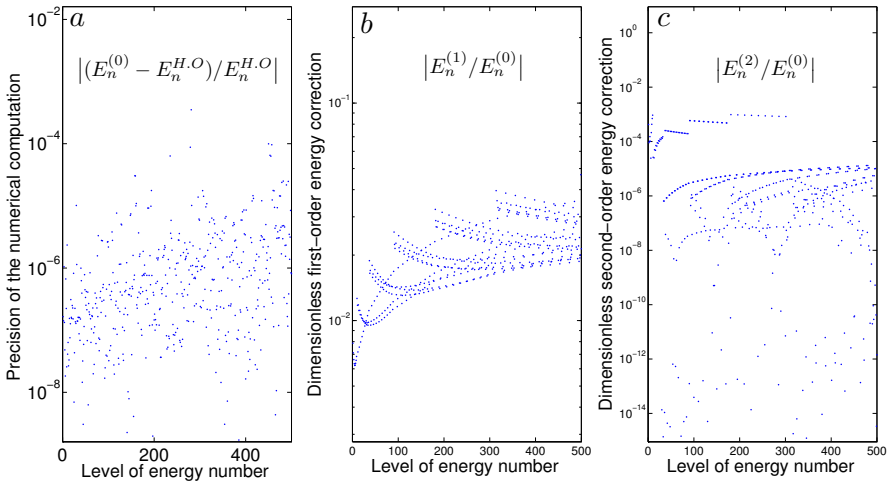

Figure 46: Energy-levels computation using the stationary perturbation theory, for the potential $V^{|\bar{a}\rangle}$ shown in Figure 19b. (a) The zero-order energy-levels $E_n^{(0)}$ given by the perturbative calculation : $\langle\phi_n|V|\phi_n\rangle$, are compared to the energy-levels of an harmonic oscillator $E_n^{H.O}$ (related to the trapping-potential eigenfrequencies). This allows an estimation of the (integrals) numerical-computation accuracy. (b) The first-order energy corrections $E_n^{(1)}$ are in the order of $10^{-2}E_n^{(0)}$. (c) The second-order energy corrections $E_n^{(2)}$ are in the order of $10^{-4}E_n^{(0)}$

The accuracy of the numerical computation is verified, as shown in Figure 46a, by comparing the energy level $E_n^{H.O}$ (related to an harmonic oscillator) and the integral $E_n^{(0)} = \langle\phi_n|V'|\phi_n\rangle$ (zero-order of perturbative calculation, cf. equations (154)). The first 500 energy levels (about $h \times 12$ kHz) are calculated with a relative numerical accuracy[5] better than 10^{-5}, using a second order correction as shown in Figure 46c. Moreover, Figure 46(b-c) shows that the first and second order corrections are on the order of $\{10^{-2}E_n^{(0)}, 10^{-4}E_n^{(0)}\}$, respectively.

Figure 47 illustrates the contrast decay for different values of the parameter $N = k_B T/\hbar\omega_{0,x}$, which gives an estimation of the number of populated energy levels, for $k_B T \gg \hbar\omega_{0,x}$.

For short time scale, there is no significant difference for both harmonic and anharmonic models, for low N values. This shows that harmonicity is not a necessary condition to maintain coherence in our case. As a matter of fact, in the ideal 1D case where the symmetry condition : $V^{|\bar{a}\rangle}(-x) = V^{|\bar{b}\rangle}(x)$ is fulfilled[6], the latter potentials have the same eigenenergies (even though they are not harmonic), which preserves the contrast (i.e. $\Delta E_n^1 = 0$ in equation (144)). In prac-

5 Due to the analytical expressions of the potentials V and W, the numerical computation of the integrals can be performed with high precision and accuracy goals (here, with a relative precision goal of 10^{-5}).

6 cf. section 4.3.4

tice, the dissymmetry of the potentials is not negligible, but its effect can be described by the 3D harmonic model.

Nevertheless, in the case of a potential-barrier beam-splitter, a notable difference between the 3D harmonic and 3D anharmonic models can be seen for high $N \approx \omega_\perp/\omega_x$ (e.g. $N = 10$) in Figure 47a.2, where ω_x and $\omega_\perp$ are the axial and transverse angular frequencies of the static trap, respectively. In the latter case, the harmonic approximation is no longer valid. The anharmonicity effect accelerates the contrast decay and so must be considered to estimate the coherence time τ_c, at short time scale. On the other hand, in the case of a potential-well, the 3D harmonic approximation remains valid even for high N values, since the anharmonicity is relatively low especially along the transverse directions, as can be seen in Table 6.

For large time scale, the revivals expected from the 1D harmonic model (cf. equation (144)) are observed for : $N \lesssim \omega_\perp/\omega_x$. For larger $N \gg \omega_\perp/\omega_x$, many transverse levels are populated, and the rephasing condition (equation (149)) is no longer verified. The first revival occurs nearly at $T'_R \sim 2\pi/\Delta\omega_{1,x}$, a time related to the axial dissymmetry $\Delta\omega_{1,x}$ which is more important than the transverse ones (cf. Table 2). The amplitude of this revival is always optimum (equal to 1) for the 1D harmonic model contrary to the full 3D model where the length of the revival peak decreases as function of the number N (i.e. the temperature T). This loss of contrast can be understood using the 3D harmonic model. Indeed, if $N \approx \omega_\perp/\omega_x$ the system becomes sensitive also to transverse energy levels, which usually do not fulfill the rephasing condition (149). Thus, the amplitude of the first revival can be used to evaluate the overall dissymmetry of the potentials.

This is consistent with the fact that the 1D harmonic approximation is valid only if : $N \ll \omega_\perp/\omega_x$, and can also explain the disagreement between the 1D and 3D harmonic models at short time scale. This disagreement is in particular notable in Figure 47a.2, as the potential aspect-ratio is : $\omega_\perp/\omega_x \approx \{5.75, 14.6\}$ for the potential-well and potential-barrier analyzed here, respectively.

7.2.3 *Summary*

This three dimensional study confirms the existence of the contrast revivals expected from the one dimensional model (equation 147) and their robustness against the potentials anharmonicity, at least in our interferometer design. An experimental observation of these revivals would open up the possibility of large interrogation time using trapped thermal atoms. However, this is expected to happen only in the one dimensional regime, which sets an upper bound on the temperature :

$$T_{max} \approx \hbar\omega_\perp/k_B \tag{159}$$

On the other hand, the temperature has also a lower bound given by the condensation temperature T_c, if we want to stay in the thermal regime. For a uniform three-dimensional gas with non-interacting $\mathcal{N}$ particles, T_c is given by [184, 185] :

$$T_{min} = T_c \approx 0.94 \times \mathcal{N}^{1/3}(\omega_\perp/\omega_x)^{-1/3}(\hbar\omega_\perp/k_B) \tag{160}$$

Then one can deduce, approximately, a maximum allowed number of atoms in order to respect the constraints above :

$$\mathcal{N}_{max} \approx \omega_\perp/\omega_x \tag{161}$$

Numerical estimation, in the case studied above, shows that the atoms number $\mathcal{N}$ is relatively small and should be limited to the range : $10 - 100$ atoms. The number of atoms can be increased by $1 - 2$ order of magnitude in case of transverse splitting since the trap axial frequency ω_x can be set very low (about few Hz), yet only small splitting distance (about few microns) are allowed.

		Potential-barrier		Potential-well	
		$V^{\|\bar{a}\rangle}/\hbar\omega_x^a$	$V^{\|\bar{b}\rangle}/\hbar\omega_x^b$	$V^{\|\bar{a}\rangle}/\hbar\omega_x^a$	$V^{\|\bar{b}\rangle}/\hbar\omega_x^b$
Harmonic Terms $(\alpha_{i,j,k})$	X^2	0.50	0.50	0.50	0.50
	XY	1.18	1.18	0.74	0.71
	Y^2	7.17	7.06	4.27	4.61
	XZ	-0.020	0.012	0.18	-0.20
	YZ	-0.006	0.005	0.080	-0.082
	Z^2	7.08	6.96	4.24	4.58
Anharmonic Terms $(\beta_{i,j,k})$	X^3	-0.0019	0.0017	0.0070	-0.0079
	X^2Y	-0.014	0.013	0.0086	-0.0087
	XY^2	-0.11	0.11	-0.052	0.063
	Y^3	-0.094	0.093	-0.033	0.037
	X^2Z	-0.0064	-0.0064	-0.015	-0.015
	XYZ	-0.017	-0.017	-0.022	-0.020
	Y^2Z	-0.038	-0.038	0.036	0.039
	XZ^2	-0.10	0.099	-0.059	0.070
	YZ^2	-0.096	0.095	-0.036	0.040
	Z^3	-0.033	-0.033	0.037	0.040

Table 6: The three-dimensional Harmonic and Anharmonic Taylor expansion of the microwave potentials shown in Figure 19. The potential $\tilde{V}$ expansion is here given by : $\tilde{V}/\hbar\omega_x = \sum_{(i+j+k=2)} \alpha_{i,j,k} X^i Y^j Z^k + \sum_{(i+j+k=3)} \beta_{i,j,k} X^i Y^j Z^k$ where $(\alpha_{i,j,k})$ and $(\beta_{i,j,k})$ are respectively the second-order and third-order terms respectively, $\{X, Y, Z\} = \{x/a^x_{\text{H.O}}, y/a^y_{\text{H.O}}, z/a^z_{\text{H.O}}\}$ and $\{a^x_{\text{H.O}}, a^y_{\text{H.O}}, a^z_{\text{H.O}}\} = \{\sqrt{\hbar/m\omega_{1,x}}, \sqrt{\hbar/m\omega_{1,y}}, \sqrt{\hbar/m\omega_{1,z}}\}$.

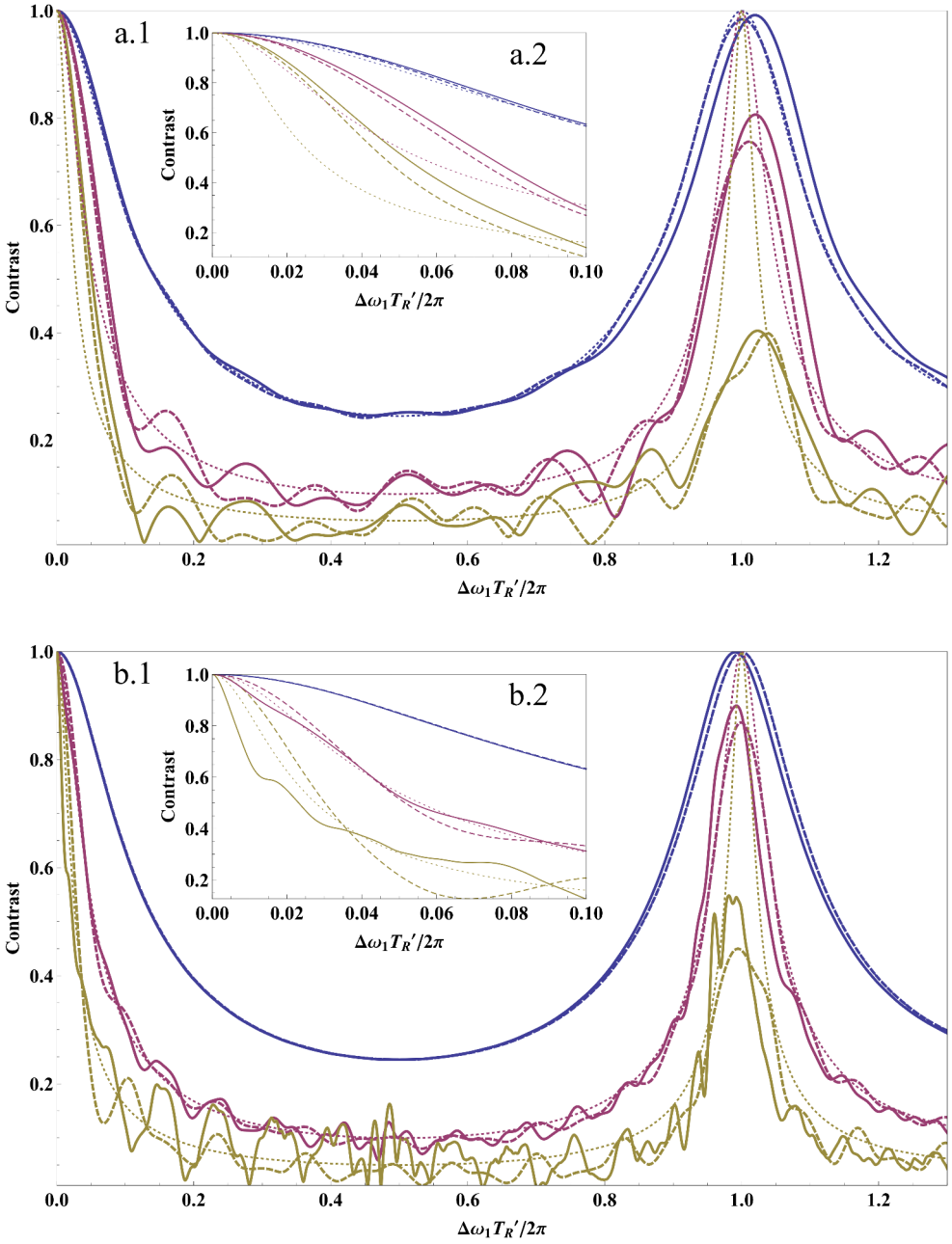

Figure 47: Interferometer contrast as a function of the (reduced) dissymmetry of the potentials : $\Delta\omega_1 T_R'/2\pi$, in case of the potential-well (a) and the potential-barrier (b) shown in Figure 19, and calculated using three different methods : simple 1D harmonic model along the axial direction (dotted line), 3D harmonic model (dashed line) and 3D anharmonic model that takes into account the potentials anharmonicity (solid line). From top to bottom, colors correspond to : $N = \{2, 5, 10\}$. A zoom of the contrast evolution at short time scale is inserted in each case.

7.3 SHORTCUT TO ADIABATICITY FOR HARMONIC POTENTIALS

The adiabatic condition discussed previously is very restrictive, especially in the case where splitting is performed along the weak direction. Here we propose a non-adiabatic splitting scheme that takes profit from the development of an emergent field : "Shortcuts To Adiabaticity" (STA) for cold atoms [175, 186] by keeping the same populations of energy levels in the initial and final traps, but in a much shorter time. In this literature, some methods use optimal control theory to optimize the transition to a target state [187], whereas others use Invariant-based inverse engineering method that yields the same state that would have been reached after an adiabatic transformation. However, this usually comes at the cost of imposing simple and tailorabale trap such as : box trap [188] or harmonic trap [189]. For instance, the harmonic oscillator is particularly interesting because an arbitrary trapping-potential can be approximated by an harmonic potential at the vicinity of the minimum. Following the conclusions of section 7.2, we neglect the effect of anharmonicity and we consider a 1D time-dependent forced harmonic oscillator to describe the dynamics during the splitting stage. We also neglect the effect of the dissymmetry of potentials, and we do not distinguish between the clock states $|a\rangle$ and $|b\rangle$ because their motions are decoupled due the internal states labeling.

We will provide the main concepts and formulas related to the transport problem in a time dependent harmonic oscillator and describe the invariant-based inverse engineering method that we will use to design a beam-splitter sequence [182, 190].

7.3.1 *Properties of dynamical invariants*

The concept of the invariant of motion, generalized to the case of explicitly time-dependent Hamiltonians by Lewis and Riesenfeld [191], can be used to derive the general solution of the Schrödinger equation :

$$i\hbar\frac{\partial|\psi(t)\rangle}{\partial t} = H(t)|\psi(t)\rangle \tag{162}$$

A time-dependent Hermitian operator $I(t)$ is a dynamical invariant of the system described by $H(t)$ if :

$$\frac{\mathrm{d}I}{\mathrm{d}t} \equiv \frac{\partial I}{\partial t} + \frac{1}{i\hbar}[I, H] = 0 \tag{163}$$

As discussed in [189], one can show that the following properties are satisfied [191] :

- $I|\psi(t)\rangle$ is a solution of (162), if $|\psi(t)\rangle$ is a solution of equation (162).

- Assuming that the eigenvalues $\lambda_n(t)$ and the corresponding eigenstates $|\psi_n(t)\rangle$ of $I(t)$ form a complete set, the eigenvalues are real (because I is Hermitian) and time-independent : $\lambda_n(t) = \lambda_n$.
- $|\psi(t)\rangle$ can be expanded in terms of constant coefficients c_n and eigenvectors $|\psi_n(t)\rangle$ of I :

$$|\psi(t)\rangle = \sum_n c_n e^{i\alpha_n(t)} |\psi_n(t)\rangle \tag{164}$$

If the invariant I does not include the operator $(\partial/\partial t)$, and the phases $\alpha_n(t)$ are chosen to solve the equation :

$$\hbar \frac{d\alpha_n}{dt} = \left\langle \psi_n \left| i\hbar \frac{\partial}{\partial t} - H \right| \psi_n \right\rangle \tag{165}$$

7.3.2 *Forced harmonic oscillator with time-dependent frequency*

We consider the following time-dependent harmonic potential, described by the one-particle Hamiltonian :

$$H(t) = \frac{p^2}{2m} + \frac{1}{2m}\omega(t)^2 \left[q - q_0(t)\right]^2 \tag{166}$$

where $\omega(t)$ is the time-dependent angular trap frequency, $q_0(t)$ is the position of its minimum, and p and q are the usual quantum operators corresponding to position and momentum respectively.

For an harmonic oscillator, the classical formalism [192] has been used first to derive the invariant I [191, 193], which is also an invariant of the corresponding quantum system :

$$I = \frac{1}{2m}\left[\rho\left(p - m\dot{q}_c\right) - m\dot{\rho}\left(q - q_c\right)\right]^2 + \frac{1}{2}m\omega_0^2\left(\frac{q - q_c}{\rho}\right)^2 \tag{167}$$

where the dot denotes the derivation with respect to time t, ω_0 is an arbitrary constant that we set here to : $\omega_0 = \omega(t_0)$, ρ and q_c, are functions of time that satisfy the equations :

$$\ddot{\rho} + \omega^2(t)\rho = \frac{\omega_0^2}{\rho^3} \tag{168}$$

$$\ddot{q}_c + \omega^2(t)\left[q_c - q_0(t)\right] = 0 \tag{169}$$

Their physical interpretation in the context of transport is detailed in Appendix E.

Once an invariant has been found, the general solution $|\psi(t)\rangle$ of the Schrödinger equation is a superposition of eigenvectors $|\psi_n\rangle$ of I, as written in equation (164), where the c_n are time-independent amplitudes and α_n is the phase term that satisfies equation (165) and is given by [193] :

$$\alpha_n(t) = -\frac{1}{\hbar}\int_0^t \mathrm{d}t' \left(\frac{(n + 1/2)\omega_0}{\rho^2} + \frac{m(\dot{q}_c\rho - q_c\dot{\rho})}{2\rho^2}\right) \tag{170}$$

The wavefunction ψ_n, associated to the state $|\psi_n\rangle$, can be written as [193] :

$$\psi_n(q,t) = e^{\frac{im}{\hbar}\left[\dot{\rho}q^2/2\rho + (\dot{q}_c\rho - q_c\dot{\rho})q/\rho\right]} \frac{1}{\rho^{1/2}} \phi_n\left(\frac{q-q_c}{\rho}\right) \tag{171}$$

in terms of the well-known eigenfunctions ϕ_n of a quantum harmonic oscillator with the angular frequency ω_0 (cf. equation (152)).

The average position and the standard deviation of ψ_0 are respectively : q_c and $\rho a_{\text{H.O}}$ where $a_{\text{H.O}} = \sqrt{\hbar/m\omega_0}$ is the harmonic oscillator length at $t = t_0$. From these expressions, the physical interpretation of q_c and ρ are clarified as the center of mass and the (scaled) width of the atomic cloud, respectively [194].

We point out that the dynamical phase $\theta_n(t)$ for an harmonic oscillator that controls the contrast decay, as discussed previously in case of an adiabatic splitting, is given here by the n-dependent part of $\alpha_n(t)$ in equation (170) such as :

$$\left|\theta_n(t_{r.o})\right| = \frac{(n+1/2)\omega_0}{\hbar} \int_{t_0}^{t_{r.o}} \frac{\mathrm{d}t'}{\rho(t')^2} \tag{172}$$

The Taylor expansion of $\rho(t)$ from equation (168), in case of adiabatic transformation [169] with $\omega/\dot{\omega} \gg \omega_0^{-1}$, is given at the zero-order, by : $\rho(t) \approx \sqrt{\omega_0/\omega(t)}$. Hence, the expression (172) is in agreement with equation (138) applied to an harmonic oscillator.

We notice that only the angular frequency $\omega(t)$ is involved in the contrast decay (i.e. in the phase $\theta_n(t)$) for an adiabatic transport. As will be discussed next, both $\omega(t)$ and $q_0(t)$ play an important role in case of fast transport.

7.3.3 *Inverse engineering method*

The invariant I has been used in a direct way by setting the transport function $q_0(t)$ and analyzing the final heating in quasi-adiabatic regime [169]. Here, we will use an inverse engineering approach. This method has been first introduced to realize fast atomic expansion in harmonic trap $\left(\omega(t_f) < \omega(t_0)\right)$ [194]. Indeed, the invariant $I(t)$ can be engineered to commute with the Hamiltonian $H(t)$ at initial and final times :

$$[I(t), H(t)] = 0 \text{ at } t = t_0 \text{ and } t = t_f \tag{173}$$

In general, these boundary conditions (BC) are sufficient to perform a shortcut to adiabaticity (STA). In case of atomic expansion, this can be achieved by setting the following conditions :

$$\rho(t_0) = 1; \dot{\rho}(t_0) = 0; \ddot{\rho}(t_0) = 0 \tag{174a}$$

$$\rho(t_f) = \sqrt{\omega(t_0)/\omega(t_f)}; \dot{\rho}(t_f) = 0; \ddot{\rho}(t_f) = 0 \tag{174b}$$

Hence, the eigenvectors of the invariant $I(t)$ (called "expanding" modes in this case) coincide with the eigenvectors of the Hamiltonian $H(t)$ at initial and final times. In practice, this can be achieved by setting an appropriate function $\omega(t)$ such as the scaling factor $\rho(t)$ satisfies both : the Ermakov equation (168) and the boundary conditions (174).

In addition, the inverse engineering method has been applied for fast atomic transport in a "rigid" harmonic trap (i.e. $\omega(t) = \omega_0$) [190], to ensure that the transport modes (eigenvectors of $I(t)$) coincide with the eigenvectors of $H(t)$ at initial and final times. This can be done by first designing the classical trajectory $q_c(t)$ to satisfy the following conditions :

$$q_c(t_0) = q_0(t_0) = 0; \dot{q}_c(t_0) = 0; \ddot{q}_c(t_0) = 0 \tag{175a}$$
$$q_c(t_f) = q_0(t_f) = s; \dot{q}_c(t_f) = 0; \ddot{q}_c(t_f) = 0 \tag{175b}$$

Then, the trap-center trajectory $q_0(t)$ has to be set by inversing the classical equation of motion (169).

Application to atom interferometry on-chip

The interferometer sequence using thermal atoms (cf. Figure 49a) can be seen as a cyclic transport problem. Yet, we cannot apply directly the STA methods studied in the literature in the case of a rigid transport [176, 190], because $\omega(t)$ is intrinsically coupled to $q_0(t)$ for an atom chip as shown in Figure 48a.

Indeed, keeping $\omega(t)$ constant to perform a rigid transport (i.e. $\omega(t) = \omega_0$) [190], might be possible on chip at least in principle by updating the static trap frequency while splitting. In practice, this would demand to vary almost all the controllable parameters at the same time (microwave and static currents, and bias fields) which would be an additional source of noise and complexity. Otherwise, the interferometer beam-splitter can be seen as a combination of the two previous problems : compression $(\omega(t_0 + \tau) > \omega(t_0))$ (or expansion), and transport $(q_0(t_0 + \tau) \neq q_0(t_0))$.

In this section, we shall describe a solution to perform a STA in this interferometer taking into account the additional constraint $\omega/\omega_1 = f(q_0/s)$, where f is a function that can be computed numerically for a given situation. Indeed, our main concern is to avoid vibrational transitions, especially at the read-out time $t_{r.o}$. This can be done if the boundary condition (173) is verified at least for $t_f = t_{r.o}$. This would allow a *fast* and *transitionless* cyclic transport compared to the *adiabatic* cyclic transport discussed earlier.

Furthermore, the STA problem can be considerably simplified by taking advantage of the temporal symmetry of our interferometer, in

particular the trap trajectory $q_0(t)$ and the angular frequency $\omega(t)$ can be set such as :

$$q_0(t-t_0) = q_0\left(-(t-t_{r.o})\right) \tag{176a}$$
$$\omega(t-t_0) = \omega(-(t-t_{r.o})) \tag{176b}$$

One can also define a new time reference : $t' = t - t'_0$, centered at $t'_0 = (t_{r.o} - t_0)/2 = \tau + T_R/2$. Then, the latter time-symmetry equations can be written : $\omega(-t') = \omega(t')$ and $q_0(-t') = q_0(t')$, and so : $H(-t') = H(t')$.

The desired fast and transitionless cyclic transport, can be seen also as an atomic transport where transitions between energy levels are allowed after splitting, but the interferometer parameters can be designed such as the probability transition between the energy levels $P_{n,m}$ are time-symmetrical : $P_{n,m}(-t') = P_{m,n}(t')$. A general discussion about the transition probability and its symmetry can be found in Appendix F.

The classical equations (168) and (169) are also time-symmetrical and their corresponding solutions $\rho(t)$ and $q_c(t)$ can be reversed in time : $t' \leftrightarrow -t'$ (i.e. $(t-t_0) \leftrightarrow -(t-t_{r.o})$) if the following (initial) conditions are fulfilled :

$$\rho(t_0+\tau+T_R) = \rho(t_0+\tau);\ q_c(t_0+\tau+T_R) = q_c(t_0+\tau) \tag{177a}$$
$$\dot{\rho}(t_0+\tau+T_R) = -\dot{\rho}(t_0+\tau) \tag{177b}$$
$$\dot{q}_c(t_0+\tau+T_R) = -\dot{q}_c(t_0+\tau) \tag{177c}$$

During the holding stage, analytical solutions of equations (168) and (169) are known. Indeed, $q_c(t)$ and $\rho(t)$ are both oscillating at the following frequencies respectively : $\omega_1 = \omega(t_0+\tau)$ and $2\omega_1$ (cf. Appendix E). Therefore, equations (177) can be simplified to the corresponding constraints :

$$T_R = 2\pi k/\omega_1 \tag{178a}$$
$$\dot{\rho}(t_0+\tau) = 0 \tag{178b}$$
$$\dot{q}_c(t_0+\tau) = 0 \tag{178c}$$

where k is an integer.

The first condition (178a) can be satisfied by a convenient choice of the holding time T_R. Then, to satisfy equation (178c), one can design $q_0(t)$ by imposing the boundary conditions (175) with $t_f = t_0 + \tau$. In this case, the center of mass of the atomic cloud does not oscillate during the holding stage, which is expected to reduce the sensitivity to the potential anharmonicity [153] and to the interferometer spatial-dissymmetry.

For this purpose, we choose the simplest polynomial ansatz P as a solution to the 6 boundary conditions (175), such as :

$$q_c(t-t_0)/s = P\left((t-t_0)/\tau\right) \tag{179}$$

for $t_0 \leqslant t \leqslant t_0 + \tau$. So, P is here chosen as [190] :

$$P(X) = 10X^3 - 15X^4 + 6X^5 \tag{180}$$

Then, we deduce q_0 by numerically solving equation (169), that can be written here as :

$$f^2(q_0/s)\,[q_0/s - P(X)] = \frac{1}{\omega_1^2\tau^2}\frac{\mathrm{d}^2P(X)}{\mathrm{d}X^2} \tag{181}$$

and $0 \leqslant X \leqslant 1$.

Finally, the last condition (178b) remains to be satisfied in order to perform an STA at the read-out time $t_{r.o}$ (i.e. to perform a transtionless transport at $t = t_{r.o}$). Obviously, once $q_0(t)$ is fixed, the angular frequency $\omega(t)$ can not be designed freely to fulfill the last condition (178b). However, since $\omega(t)$ is known, we shall analyze the corresponding profile of $\rho(t)$.

In Figure 48b, $\rho_1 = \rho_\tau(t_0 + \tau)$ is computed by solving numerically equation (168) (to determine $\rho_\tau(t)$) in iterative manner for different splitting time τ with $\omega = \omega_1 f(q_0/s)$ and q_0 is the function designed previously (and that satisfies equation (181)), for a potential-barrier beam-splitter. The atoms are assumed to be at (motional) equilibrium initially, so the initial conditions used are : $\rho(t_0) = 1$ and $\dot\rho(t_0) = 0$. Figure 48b shows that $\dot\rho_\tau(t_0 + \tau)$ has several zeros τ_e where the condition (178b) can be verified. Figure 48c shows q_0 and q_c that correspond to the τ_e times. For short splitting time τ, the corresponding trajectories could exceed the interval $[0, s]$ and require very fast variation of the splitting parameter (i.e. P_{mw} here) which may be difficult to implement experimentally [189]. Similar results were found in case of rigid transport in [190].

In Figure 49, the parameters $\rho(t)$ and $q_c(t)$ are computed numerically for the second $\dot\rho_\tau(t_0 + \tau)$-zero time τ_e. As expected, $\rho(t)$ oscillates while $q_c(t)$ remains constant during the holding time. Moreover, $q_0(t)$ and $\omega(t)$ are designed so that $\rho(t)$ and $q_c(t)$ at final time ($t = t_{r.o}$) return to their initial values, which is well verified.

Nevertheless, the STA boundary conditions are not fully satisfied after the splitting because the condition $\rho(t_0 + \tau) = \sqrt{\omega_0/\omega_1}$ (cf. equations (174b) with $t_f = t_0 + \tau$) is not necessarily satisfied. Hence, we expect vibrational excitations to occur during the holding stage, which can potentially reduce the coherence time (cf. Figure 47). This can be quantified in terms of the average adiabatic energy-transfer $\Delta E_n^{(\mathrm{ad})}(t)$ (i.e. energy difference between the fast and adiabatic transformations) which is given in general by :

$$\Delta E_n^{(\mathrm{ad})}(t) = \hbar\omega_1(\mathrm{Y}_F(t) + \mathrm{Y}_\omega^n(t)) \tag{182}$$

where $\mathrm{Y}_F(t)$ and $\mathrm{Y}_\omega(t)$ describe the energy-transfer, in unit of $\hbar\omega_1$, due to perturbation with the driving force $F(t) = m\omega(t)^2 q_0(t)$ and

the harmonic perturbation $\omega(t)$ respectively (cf. Appendix F, equation (234a)). These energy expressions, derived in Appendix F (equations (223) and (233)), are given by :

$$\begin{aligned} \mathrm{Y}_F(t) &= \mathcal{W}(t)/\hbar\omega_1 \\ &= \frac{1}{2m\hbar\omega_1}\left|\int_{t_0}^{t} F(t')\xi(t')\mathrm{d}t'\right|^2 \end{aligned} \tag{183}$$

$$\begin{aligned} \mathrm{Y}^n_\omega(t) &= \Delta E^{(\mathrm{ad})}_\omega(t)/\hbar\omega_1 \\ &= \frac{(2n+1)}{4\omega_0\omega_1}\left[\dot\rho^2 + \omega(t)^2\rho^2 + \omega_0^2/\rho^2 - 2\omega_0\omega_1\right] \end{aligned} \tag{184}$$

where $\xi(t)$ is a solution of the classical equation :

$$\ddot\xi(t) \; + \; \omega^2(t)\xi(t) = 0 \tag{185}$$

discussed in Appendix E. For instance, in case of rigid transport ($\omega(t) = \omega_0$), and $\mathrm{Y}_F(t \to \infty)$ can be seen as a Fourier transform of the driving force $F(t)$ [176]. In our case, $q_0(t)$ is designed in order to respect the boundary conditions (175) during the splitting stage ($t_f = t_0 + \tau$), so we make sure that $\mathrm{Y}_F(t)$ vanishes during the holding time ($t > t_0 + \tau$).

In addition, the time-average energy $\bar{\mathrm{Y}}^n_\omega$ during the holding time can be calculated as follows : the solution of the Ermakov equation (168) for $t > t_0 + \tau$ assuming a constant intermediate angular frequency ω_1 with the boundary conditions $\rho(t_0 + \tau) = \rho_1$ and $\dot\rho(t_0 + \tau) = 0$ is :

$$\rho(t) = \sqrt{[(\omega_0^2 - \omega_1^2\rho_1^4)/\omega_0^2\rho_1^2]\sin^2\left(\omega_1(t - t_0 - \tau)\right) + \rho_1^2} \tag{186}$$

Then, the time-average of the quantities : $\dot\rho(t)^2$, $\rho(t)^2$, and $1/\rho(t)^2$ can be easily calculated. If condition (178a) holds, the derivation of $\bar{\mathrm{Y}}^n_\omega$ can be simplified to :

$$\bar{\mathrm{Y}}^n_\omega = -(2n+1)\frac{(\rho_1^2 - \gamma)(\rho_1^4 + \gamma\rho_1^2 - 2)}{4\gamma} \tag{187}$$

where $\gamma = \omega_0/\omega_1$. For the numerical values of $\dot\rho_\tau(t_0 + \tau)$-zeros shown in Figure 48b, $\rho_1 = \{1.16, 0.11, 0.75\}$ and $\bar{\mathrm{Y}}^0_\omega = \{-0.20, -0.48, 0.01\}$ respectively. In this case, the transition effect is weak in average, especially for the third $\dot\rho_\tau(t_0 + \tau)$-zero. For the first and second zeros, this effect can be seen (an average) as a reduction of the number N of populated energy-levels[7]. Moreover, such effect can be neglected if N is chosen such as : $(2N+1)|\mathrm{Y}^0_\omega| < 1$, because the perturbation of the higher populated energy level would be lower than an energy quanta $\hbar\omega_1$.

7 In contrast to the case of an adiabatic transformation where the number of populated energy-levels remains constant.

Furthermore, one can adjust slightly ω_0 and ω_1 values, starting from the first $\dot{\rho}_\tau(t_0+\tau)$-zero time τ_e, such as :

$$\rho_1 = \sqrt{\left(\sqrt{8+\gamma^2}-\gamma\right)/2} \tag{188}$$

in order to minimize the time-average energy-transfer[8] $|\bar{Y}^0_\omega|$, during the holding time T_R. Even better, one can fulfill the last remaining boundary condition (174) : $\rho_1 = \sqrt{\gamma}$, starting from the third $\dot{\rho}_\tau(t_0+\tau)$-zero time, so all transitions during holding time would be completely canceled.

We point out that the coherence of our interferometer is robust to perturbations thanks to its symmetrical design. In fact, imperfect experimental control usually allows small transition effect at the readout time; however this is not harmful for the phase contrast as long as these imperfections are similar for both interferometer arms. This is possible, if the two microwave signals are created using the same frequency chain in order to suppress common-mode perturbations.

8 In different context, satisfying the equations (188) and (178b) might be used to perform a frictionless cooling as in [194, 186], with a cooling times shorter than those obtained using optimal-control bang-bang methods and without using a negative angular frequency as proposed in [194]. In this case, the energy levels of $< H(t) >$ are on average identical to the initial energy levels even though the system is not at equilibrium.

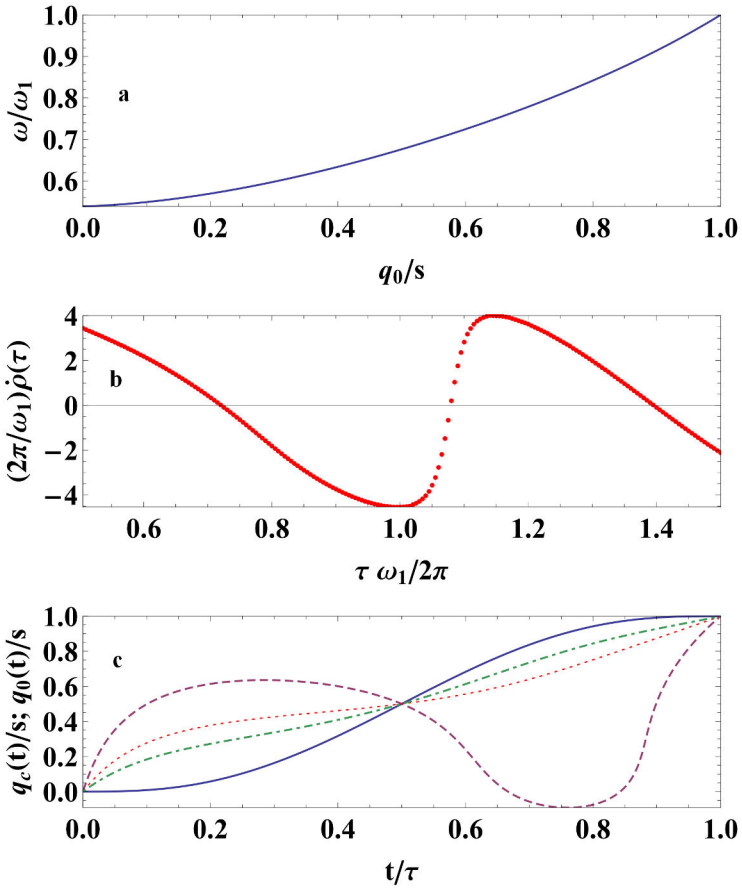

Figure 48: Shortcut to adiabaticity applied to the potential-barrier beam-splitter. (a) The trap angular-frequency ω/ω_1 as function of the trap position q_0/s during the splitting stage (i.e. $\omega/\omega_1 = f(q_0/s)$). The times functions $q_0(t)$ and $\omega(t)$ are estimated here for a potential-barrier using the same parameters in Figure 19b and by varying the microwave power P_{mw}. (b) $\dot{\rho}_\tau(t_0+\tau)$ as a function of the splitting time τ with $t_0 = 0$. The second "cyclic" condition (178b) is verified in 3 points : $\tau_e = \{0.72, 1.08, 1.40\} \times 2\pi/\omega_1$ which corresponds to $\dot{\rho}_\tau(t_0+\tau)$-zeros. (c) Engineered $q_0(t)/s$ as function of time t/τ. Color lines correspond to the latter $\dot{\rho}_\tau(t_0+\tau)$-zero points τ_e, plotted in dashed, dotted and dot-dashed lines respectively. In solid line, the resulting cloud center of mass $q_c(t-t_0)/s$ is given by the polynomial $P\left((t-t_0)/\tau\right)$ (cf. text), which is the same of all three cases.

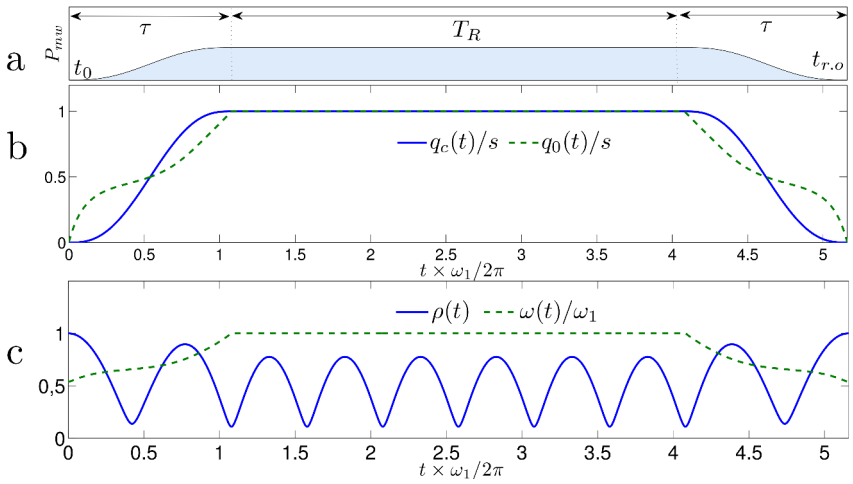

Figure 49: (a) Schematic of the interferometer sequence formed from three stages : Splitting-Holding-Recombination, that last $\{\tau, T_R, \tau\}$ respectively. t_0 and $t_{r.0}$ indicate the interferometer initial and final times. (b, c) The interferometer parameters as a function of time t where the STA conditions at $t_f = t_{r.o}$ are fulfilled (cf. equation 178) by making profit of the interferometer temporal-symmetry. Here $T_R = 3 \times 2\pi/\omega_1$ and $\tau = 1.08 \times 2\pi/\omega_1$ which corresponds to the second $\dot{\rho}_\tau(t_0 + \tau)$-zero in Figure 48b. (b) q_{cm} and q_0 are designed to respect the STA conditions (175) at $t_f = t_0 + \tau$. (c) ρ does not respect the STA condition (174) at $t = t_0 + \tau$, and so, ρ is oscillating at the angular frequency $2\omega_1$ during the holding time.

7.4 CONCLUSION

We have discussed the effects of the beam-splitter dynamics on the interferometer contrast. We have shown, in case of adiabatic splitting, that the potentials anharmonicity in our case, have a negligible role on the contrast decay if the 1D condition is fulfilled. In most cases, the 3D harmonic model is sufficient to predict the interferometer contrast evolution.

We believe that the limited coherence time due to the potential dissymmetry may be overcome by a careful choice of the microwave potential parameters and setting the interferometer read-out time equal to the first revival time of the interferometer contrast.

Then, we have shown that fast splitting time : $\tau \simeq \frac{1}{2}(2\pi/\omega_0)$ is possible with low vibrational heating, using the invariant-based techniques. The transfer is achieved by engineering specific trajectories of the external trapping positions. Theoretically, the design of the transfer process turned out to be possible thanks to the harmonic shape of the external potentials. Yet, the effects of the anharmonic terms (shown in Table 6) remain to be characterized experimentally. This scheme is flexible enough to be adapted to both beam-splitter methods : potential-well and potential-barrier. In particular, we have shown that the potential-barrier method allows the design of straight ramps that has been demonstrated experimentally [189].

Finally, the shortcut-to-adiabaticity (STA) schemes are not restricted to the field of ultracold atoms and could be applied in many different physical problems. For instance, a similar method was proposed for the fast cooling of a mechanical resonator to its ground state [195]. Recently, several optimization methods such as Optimal Control Theory (OCT) has been used for a better control of the quantum systems [196, 197, 198, 199, 200]. These techniques, which could be combined to the STA exact solutions, will play a important role in the future in particular to overcome the decoherence that represents a challenge for the practical realization of quantum devices.

8

DESIGN AND FABRICATION OF THE ATOM CHIP

The design and fabrication of our atom chip is greatly inspired by the work of P. Treutlein and P. Böhi [86, 163]. In particular, they have succeeded to overcome the following technical challenges :

- Implementing two layers of wires separated by a thin insulating layer (few microns). This would allow the implementation of complex trap design with several crossing wires, such as the *Manhattan* Trap discussed in section 2.2.5.
- Integrating a coplanar waveguide on an atom chip. This allows the state-selective manipulation of atoms using near-field microwave gradients.
- Implementing a bias-tee on an atom chip so that static and microwave currents can be superimposed in the CPW ground-wires [163]. External bias-tee can be used to superimpose microwave and static currents in the CPW signal-wire.

In addition to the previous challenges, we have implemented in our atom chip for the first time, the following features :

- Silicon carbide (SiC) atom chip. An SiC substrate is an optically transparent dielectric which has an outstanding thermal conductivity[1]. In particular, we demonstrated a magneto-optical trap with several beams passing through the chip [201].
- Adjacent waveguides with low coupling, in order to create multi-frequency potentials (which lead to better symmetry of the interferometer).
- Up to eight waveguides are implemented and connected on the same (27×26 mm^2) chip. This paves the way for the implementation of multiple sensors on the same chip.

Photograph and wire layout of the chip assembly are shown in Figure 50. The atom chip is an assembly of three elementary chips shown in Figure 51 :

1 Over 390 $m^{-1}K^{-1}$ for SiC dielectric compared to 148 $m^{-1}K^{-1}$ for Si dielectric.

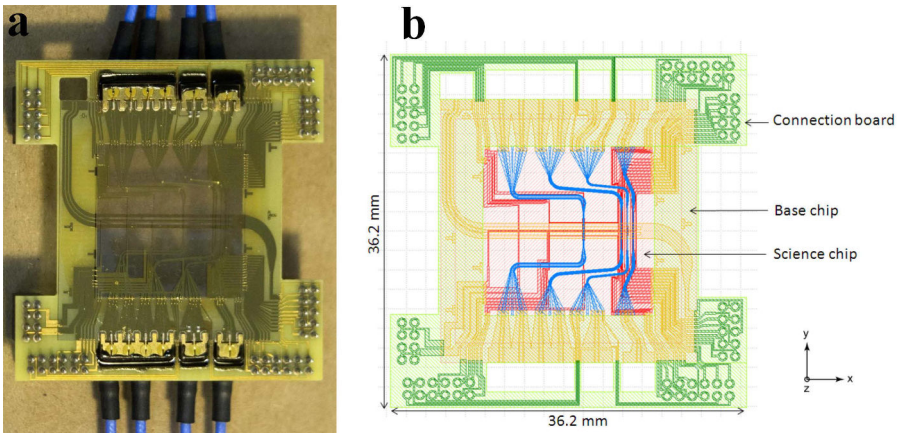

Figure 50: (a) Photograph of the atom chip assembly connected to the microwave cables. Photo courtesy of Jean-François Dars. (b) Wire layout of the atom chip.

- *Connection board* : it is a standard Printed Circuit Board (PCB) that provides connection to the static sources. Seven standard sockets are soldered onto the PCB back.

- *Base chip* : SiC chip that ensures the mechanical stability of the assembly, is glued on the top of the vacuum cell. The CPWs are connected to the microwave[2] sources through miniature custom-made connectors[3]. These connectors are designed to be surface-mounted on the SiC base chip, in order to avoid the necessity of a second series of bonding wires form the waveguide wires on the base chip to the connection board. Moreover, a large CPW is designed to create an homogenous magnetic microwave field in order to perform a controlled two-photons transition, as discussed in [155]. This CPW has also a Z-shape, so the central wire might be used[4] to create a static field that can be used to lift up the atoms to the vicinity of the chip surface, instead of using an external Z-wire [203].

- *Science chip* : SiC chip glued to the base chip and acting as a spacer chip that allows easy access of the imaging laser of the atoms. This chip holds two metallization layers which are separated by a BCB[5] insulating layer of about 7 μm thick. The BCB ensures also the planarization of the upper gold layer, which has a thickness of 1 μm. The lower gold layer has a thickness of 3 μm and designed to carry static currents. The large central wire can carry current pulses of up to 4 A and the other wires

2 The static connectors (pins) cannot be soldered to the base chip because drilling holes into an SiC substrate is extremely difficult [202].

3 G4PO engineered at Corning Gilbert : www.corning.com [SK-4782-FD & SK-4768-FD].

4 Using an external bias-tee

5 Benzocyclobutene C_8H_8

can carry currents of up to 1 A. The upper layer is designed to propagate microwave currents, but can also carry static currents of up to 150 mA.

The atom chip was designed to be glued to a glass cell provided by *ColdQuanta*, as can be seen in Figure 53, which will be later related to a single chamber vacuum system [204]. The three elementary chips are connected to each other's through gold (edge) bonded wires. The fabrication of the SiC chips has been done by Olivier Patard form *III-V Lab*[6]. An overview of the fabrication recipe of microwave atom chip can be found in [86]. The connection board has been made by *Cibel*[7] and the bond wires by *Systrel*[8].

The science chip is designed to allow an experimental investigation of 4 configurations, shown in Figure 52, that are discussed in detail in the following chapters :

- Config. I : Transverse beam-splitter using the $H^{\star}$-trap [section 6.3, Figure 42, Table 4]
- Config. II : Axial beam-splitter [section 5.2, Figure 19]
- Config. III : Static double-well (DC-DW) [section 5.7, Figure 36]. Microwave double-well (MW-DW) [section 5.6.3, Figure 30, Table 3]
- Config. IV : Microwave double-well (MW-DW) [section 5.6.3]

The configurations I, II and III are formed by two adjacent CPWs, while the configuration IV is composed by two adjacent coplanar striplines (CPS) [144, 166]. The configuration IV would allow a higher splitting distance[9] but coupling between the striplines is very likely in this case since the signal wires are very close[10]. In the following section, we analyze the transmission parameters of these structures.

S-parameters: simulation and measurement

To design the waveguide structures, as discussed previously, we have used the simplified quasi-static simulations and its related conformal mapping method. Yet, we have verified the characteristics of these tapered waveguides before associating the chip to the glass cell. For this purpose, we have considered two different approaches.

On the one hand, we have estimated the scattering matrix (S_{ij}) [141] using a 3D planar simulation with *Ansoft Designer*. The reflection (S_{11}), the transmission (S_{12}), and the coupling parameters (S_{13}) and (S_{14}) of

6 www.3-5lab.fr
7 www.cibel.com
8 www.hcm-systrel.com
9 A larger gradient of the microwave field can be created in the vicinity of the static trap center, cf. section 5.6.3
10 This configuration can be used to design directional couplers [205].

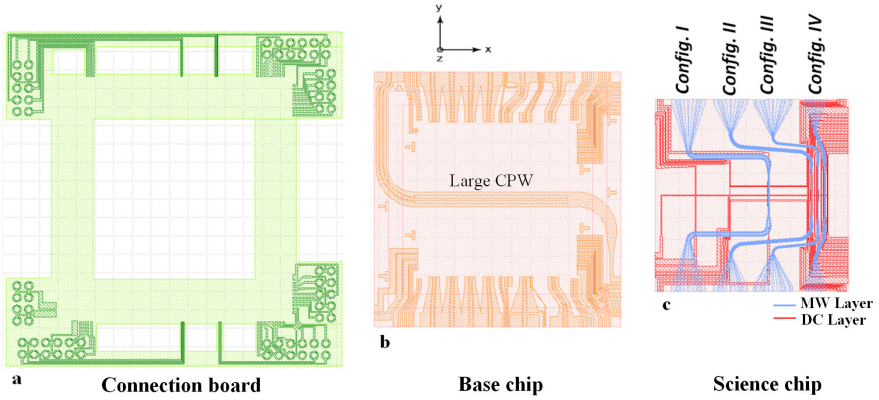

Figure 51: Atom chip layout. Wire layout on : (a) the connection board [in green, size : 36.2×36.2 mm^2] (b) the base chip [in orange, size : 27×26 mm^2] (c) the science chip : [size : 17.4×17.4 mm^2] lower layer (in red) for the static wires and the upper layer (in blue) for the microwave waveguides. There are several waveguide structures on the science chip. Each pair of CPWs corresponds to a configuration discussed earlier in this thesis.

the adjacent waveguide structures, in each configuration of Figure 52, have been computed. In contrast to 3D full-wave simulation[11], the thickness of each layer, is assumed to be constant with this method. A cross section of the simulated structure is shown in Figure 54c. The setting of the 4 ports in the configurations II and IV are shown in Figure 54(a-b). We take into account the presence of the DC wires on the lower layer (which affects the characteristic impedance of the structure). These simulations have been done with the help of Stéphane Piotrowicz from III-V Lab.

On the other hand, we have measured the S-parameters of the microwave structures on the science chip using a network analyzer connected to a microwave probe station. The reflection (S_{11}) and the transmission (S_{12}) parameters have been measured for the configurations I, II and III. These measurements have been done with the help of Didier Lancereau from III-V Lab.

The results of both methods are compared in Figure 55 for the configuration I, II and III. The transmission coefficient S_{12} is flat over a large range of frequency. However, for high microwave frequencies, the simulations underestimate the transmission loss. For example, around 6.8 GHz, the transmission loss are estimated approximately by -3 dB, while the measurements give a transmission loss of about -6 to -8 dB.

Moreover, the measurements of the reflection coefficient S_{11} show a resonance behavior around $6 - 7$ GHz, and to lesser extent a second resonance around 4 GHz for the configurations I and II. These resonances can be seen in the simulation results but their amplitudes

11 Which can be done using the software *ANSYS HFSS*

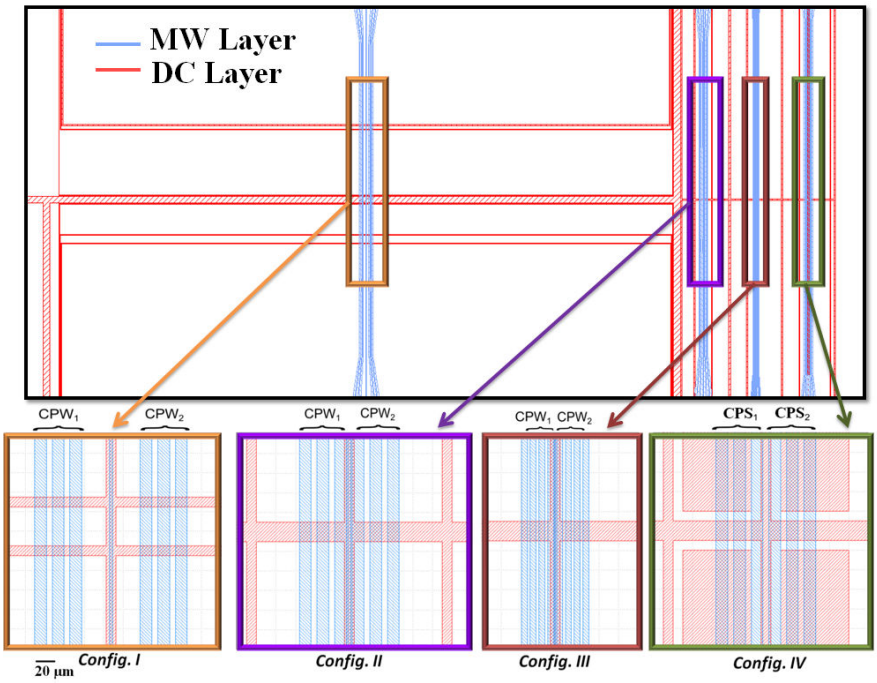

Figure 52: Wire layout on the science chip. A zoom of the waveguide structures on the experiment regions.

are not accurate. This is mostly due to the simplified structures of the MW and DC layers used in the simulation, as can be seen in Figure 54a. The meshing grid might also affect the accuracy of the simulation around the resonance points. For the configuration *III*, the resonance occurs near 5.8 GHz which is in agreement with the simulation.

Furthermore, Figure 56 shows the simulation of the coupling parameters (S_{13}) and (S_{14}). As expected from the rough estimation in section 3.2.1, the coupling between two adjacent CPWs is about -30 dB around 6.8 GHz.

Finally, the *S*-parameters of the configuration *IV*, are shown in Figure 57. The transmission and reflection parameters are similar to the CPWs discussed previously but the resonance behavior of S_{12} is shifted to around 8 GHz. This is probably due to the large wires in the lower layer (DC Layer), as shown in Figure 54b. In fact, these structures can be considered as a conductor-backed waveguides [147, 206]. Nevertheless, the coupling is approximately about -11 dB around 7 GHz, which is relatively high[12]. This coupling effect can be minimized, in the future, by adjusting the distance between the signal wires in order to shift the resonance of the coupling coefficients from 7.5 GHz to 6.8 GHz.

12 This result is also consistent with an estimation using the quasi-static simulation.

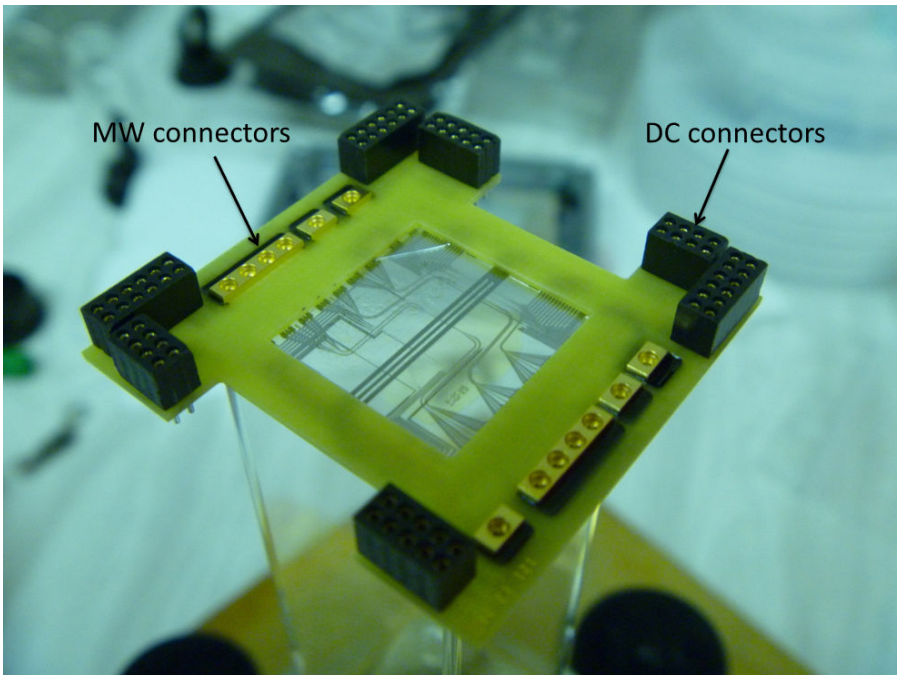

Figure 53: The atom chip is glued to a glass cell (provided by *ColdQuanta*). The base chip creates a wall of the vacuum system. The connection board provides electrical power (DC and MW currents) through to the vacuum for the science chip. Photo courtesy of Jean-François Dars.

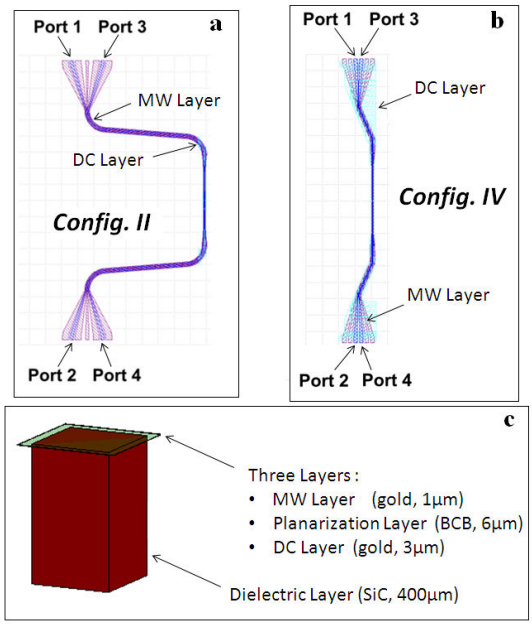

Figure 54: 3D planar simulations using *Ansoft Designer*. Layout of the tapered CPWs(a) CPSs(b) (MW Layer) corresponding to the Config. *II* (a) and *IV* (b) in Figure 52. The signal wires are indicated in blue. The effect of the static wires in the lower layer (DC Layer in cyan) is taken into account. (c) Schematic of the science chip cross-section used in the simulation.

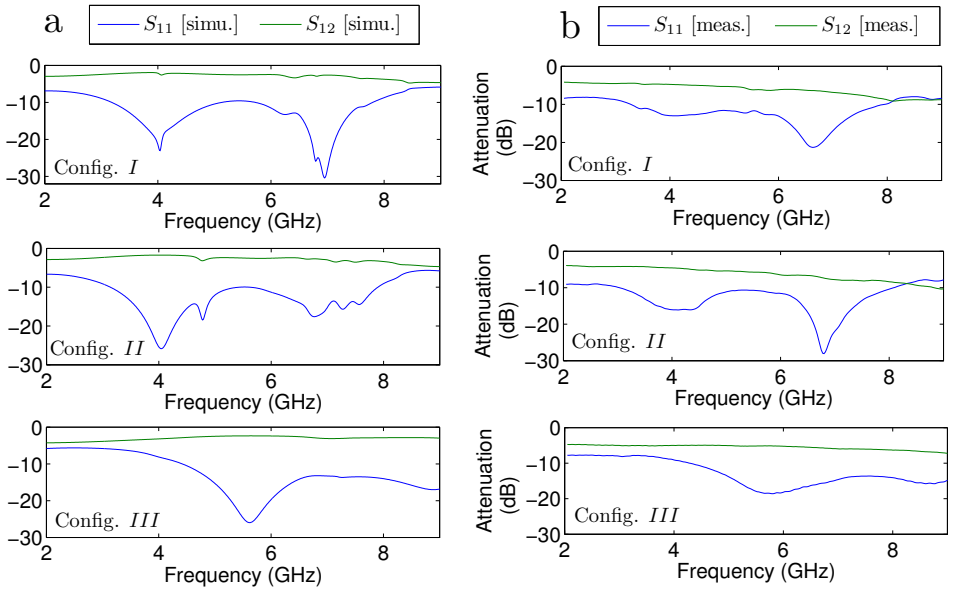

Figure 55: Microwave transmission (S_{12}) and refection (S_{11}) parameters of the microwave structures of the configurations I, II and III using (a) 3D planar simulation and (b) experimental measurements. These data are related to the (CPW_2) in each configuration shown in Figure 51c).

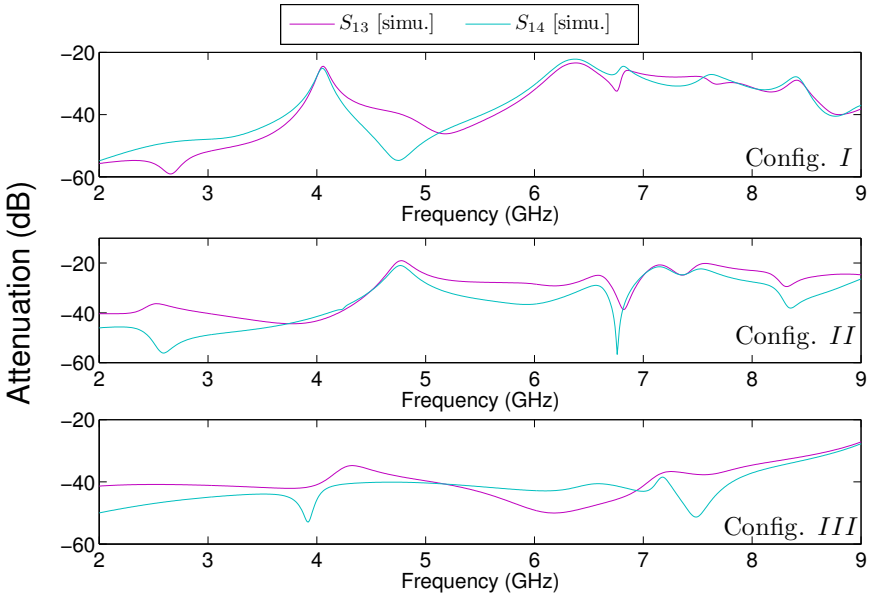

Figure 56: Simulation of the coupling parameters S_{13} and S_{14} between the two adjacent CPWs related to the configurations I, II and III.

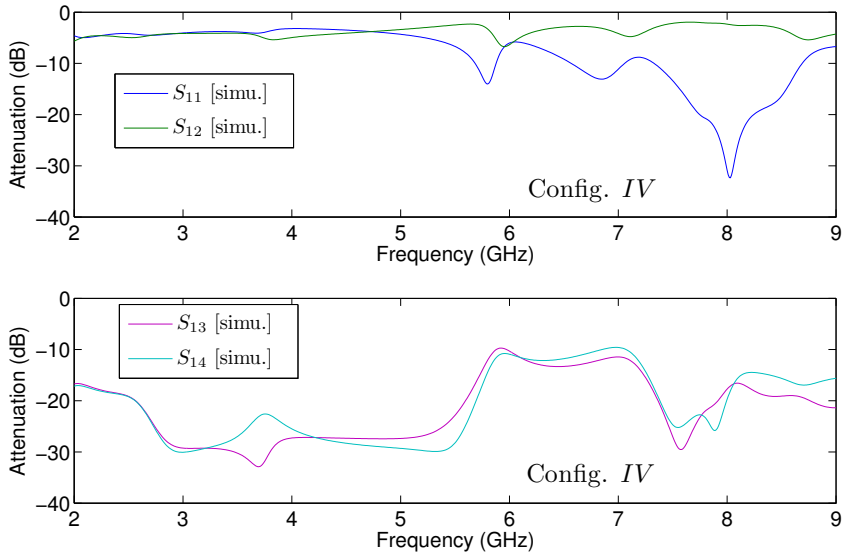

Figure 57: Simulation of the transmission, reflection and coupling parameters of the coplanar strips in the configuration IV.

9

CONCLUSION

In this thesis, we have proposed an experimental design for a symmetrical beam splitter with thermal atoms trapped on chip using microwave induced potentials.

First, we have considered an axial beam-splitter, similar to the experimental demonstration in [71] but using two CPWs carrying different microwave frequencies, and we have compared two splitting schemes : potential-well and potential-barrier. These methods have different features in term of microwave power requirements, splitting distances and resulting trap-depths, but they can be both tested experimentally on the same configuration by tuning the microwave frequencies. We have simulated the microwave splitting potentials and analyzed the inherent sources of dissymmetry. Moreover, we have developed an analytical model of the microwave potentials that can be used to minimize the asymmetry of the potentials. We have investigated the fluctuation effects of the static trapping field on the clock states in the presence of a dressing microwave field, and we have shown the existence of a new class of magic fields.

Second, we have considered a transverse beam-splitter, with a splitting of the trapped atoms similar to the experimental demonstration in [67]. This method allows a short splitting time and keeps the trap-aspect ratio approximately unchanged during splitting. Yet, we have shown in this case that the axial separation is not negligeable compared to the transverse separation. To overcome the latter disadvantage, we have developed a new scheme to design a tailorable trap on chip, and we have proposed a custom microtrap : The Manhattan Trap.

Third, we have discussed the dynamics of an axial beam-splitter. We have shown, in the case of adiabatic splitting, that the potential anharmonicities have a negligible role in the decay of the interferometer contrast, and their effects can be understood using a simplified 1D harmonic model. Then, by using the invariant-based techniques, we have shown that fast splitting time, in the order of one oscillating period along the longitudinal direction, can be reached without vibrational heating.

Finally, we believe that the limited coherence time due to the dissymmetry of the potentials may be overcome by a careful choice of the

microwave parameters and setting the interferometer read-out time to the first revival time of contrast.

This thesis suggests that building an interferometer on chip with thermal trapped atoms is a promising alternative to BEC interferometers, mainly because it allows a considerable reduction of the interaction effects. This could eventually lead to a new class of compact and integrated inertial sensors. In that sense, we have discussed the main physical factors that would limit the ultimate performances of these sensors such as : the fluctuation effects of both static and microwave fields. Several solutions have been proposed and practical designs have been made on the same chip. It is our hope that these configurations will be soon tested experimentally. The clock state transition has been also used to demonstrate a chip-based atomic clock with long interrogation times [112, 111]. I hope that this work contributes, even in a modest way, to create a high-performance Inertial Measurement Unit (IMU) integrated on chip.

Part I

APPENDICES

A

FUNDAMENTAL CONSTANTS AND RUBIDIUM-87 DATA

Planck's constant	h	$6.62606896(33) \times 10^{-34}$ J s
Bohr magneton	μ_B	$9.27400915(23) \times 10^{-24}$ J/T
Permeability of vacuum	μ_0	$4\pi \times 10^{-7}$ N/A^2
Permittivity of vacuum	ϵ_0	$8.854187817 \times 10^{-12}$ F/m
Bohr radius	a_0	$0.52917720859(36) \times 10^{-10}$ m

Table 7: Fundamental constants [87].

Atomic mass	m	$1.443160648(72) \times 10^{-25}$ kg
Nuclear spin	I	3/2

Table 8: Rubidium-87 data [87].

Zero-field hyperfine splitting	E_{hfs}	$h \times 6.834682610904290(90)$ GHz
Electron spin g-factor	g_J	2.00233113(20)
Nuclear spin g-factor	g_I	$-0.0009951414(10)$

Table 9: 5 $^2S_{1/2}$ ground state properties [87].

B

TENSORS OF THE MANHATTAN TRAP

For the Manhattan trap, introduced in section 2.2.5, the gradient tensor $\mathcal{V}$ is a linear superposition of the following elementary tensors :

$$\mathcal{V}_{1,i} = \frac{\tilde{I}_{1,i}}{h_0^2} \frac{t_{1i}^2}{1+t_{1i}^2} \begin{pmatrix} \frac{2t_{1i}}{1+t_{1i}^2} & 0 & \frac{1-t_{1i}^2}{1+t_{1i}^2} \\ 0 & 0 & 0 \\ \frac{1-t_{1i}^2}{1+t_{1i}^2} & 0 & \frac{-2t_{1i}}{1+t_{1i}^2} \end{pmatrix} \tag{189}$$

$$\mathcal{V}_{2,i} = \frac{\tilde{I}_{2,i}}{h_0^2} \frac{t_{2i}^2}{1+t_{2i}^2} \begin{pmatrix} 0 & 0 & 0 \\ 0 & \frac{-2t_{2i}}{1+t_{2i}^2} & \frac{-1+t_{2i}^2}{1+t_{2i}^2} \\ 0 & \frac{\left(-1+t_{2i}^2\right)}{1+t_{2i}^2} & \frac{2t_{2i}}{1+t_{2i}^2} \end{pmatrix} \tag{190}$$

The curvature tensor $\mathcal{W}$ is a linear superposition of the following elementary tensors :

$$\mathcal{W}_{1,i} = \frac{\tilde{I}_{1,i}}{h_0^3} \begin{pmatrix} W_1^{(y)} \\ W_2^{(y)} \\ W_3^{(y)} \end{pmatrix} \tag{191a}$$

$$W_1^{(y)} = \frac{2t_{1i}^3}{\left(1+t_{1i}^2\right)^{3/2}} \begin{pmatrix} \frac{t_{1i}\left(3-t_{1i}^2\right)}{(1+t_{1i}^2)^{3/2}} & 0 & \frac{\left(1-3t_{1i}^2\right)}{(1+t_{1i}^2)^{3/2}} \\ 0 & 0 & 0 \\ \frac{\left(1-3t_{1i}^2\right)}{(1+t_{1i}^2)^{3/2}} & 0 & \frac{-t_{1i}\left(3-t_{1i}^2\right)}{(1+t_{1i}^2)^{3/2}} \end{pmatrix} \tag{191b}$$

$$W_2^{(y)} = \begin{pmatrix} 0 & 0 & 0 \\ 0 & 0 & 0 \\ 0 & 0 & 0 \end{pmatrix} \tag{191c}$$

$$W_3^{(y)} = \frac{2t_{1i}^3}{\left(1+t_{1i}^2\right)^{3/2}} \begin{pmatrix} \frac{\left(1-3t_{1i}^2\right)}{(1+t_{1i}^2)^{3/2}} & 0 & \frac{-t_{1i}\left(3-t_{1i}^2\right)}{(1+t_{1i}^2)^{3/2}} \\ 0 & 0 & 0 \\ \frac{-t_{1i}\left(3-t_{1i}^2\right)}{(1+t_{1i}^2)^{3/2}} & 0 & \frac{-\left(1-3t_{1i}^2\right)}{(1+t_{1i}^2)^{3/2}} \end{pmatrix} \tag{191d}$$

$$\mathcal{W}_{2,i} = \frac{\tilde{I}_{2,i}}{h_0^3} \begin{pmatrix} W_1^{(x)} \\ W_2^{(x)} \\ W_3^{(x)} \end{pmatrix} \tag{192a}$$

$$W_1^{(x)} = \begin{pmatrix} 0 & 0 & 0 \\ 0 & 0 & 0 \\ 0 & 0 & 0 \end{pmatrix} \tag{192b}$$

$$W_2^{(x)} = \frac{2t_{2i}^3}{\left(1+t_{2i}^2\right)^{3/2}} \begin{pmatrix} 0 & 0 & 0 \\ 0 & \frac{-t_{2i}\left(3-t_{2i}^2\right)}{(1+t_{2i}^2)^{3/2}} & \frac{-\left(1-3t_{2i}^2\right)}{(1+t_{2i}^2)^{3/2}} \\ 0 & \frac{-\left(1-3t_{2i}^2\right)}{(1+t_{2i}^2)^{3/2}} & \frac{t_{2i}\left(3-t_{2i}^2\right)}{(1+t_{2i}^2)^{3/2}} \end{pmatrix} \tag{192c}$$

$$W_3^{(x)} = \frac{2t_{2i}^3}{\left(1+t_{2i}^2\right)^{3/2}} \begin{pmatrix} 0 & 0 & 0 \\ 0 & \frac{-\left(1-3t_{2i}^2\right)}{(1+t_{2i}^2)^{3/2}} & \frac{t_{2i}\left(3-t_{2i}^2\right)}{(1+t_{2i}^2)^{3/2}} \\ 0 & \frac{t_{2i}\left(3-t_{2i}^2\right)}{(1+t_{2i}^2)^{3/2}} & \frac{\left(1-3t_{2i}^2\right)}{(1+t_{2i}^2)^{3/2}} \end{pmatrix} \tag{192d}$$

The parameters used in this Appendix were introduced in section 2.2.5.

The tensors $\mathcal{V}_{1,i}, \mathcal{W}_{1,i}$ correspond to the i-th wire ($FL_{1,i}$), in Figure 6b, perpendicular to the x-axis at the point $A_i = (L_{1i} = h_0/t_{1i}, 0, 0)$, while the tensors $\mathcal{V}_{2,i}, \mathcal{W}_{2,i}$ correspond to the i-th wire ($FL_{2,i}$) perpendicular to the y-axis in the point $B_i = (0, L_{2i} = h_0/t_{2i}, 0)$. The first points A_0 and B_0 point coincide with the origin O.

C

ANGULAR MOMENTUM MATRIX ELEMENTS

To diagonalize the Hamiltonian describing the coupling of the atom to a microwave field (section 3.1), one should compute the following matrix elements : $\langle 2, m_2 | \boldsymbol{\epsilon}.\mathbf{J} | 1, m_1 \rangle$, where $\boldsymbol{\epsilon} = \{\epsilon_x, \epsilon_y, \epsilon_z\}$ is a unit polarization (complex) vector. One can write $\boldsymbol{\epsilon}.\mathbf{J}$ using $J_x = (J_+ + J_-)/2$ and $J_y = -i(J_+ - J_-)/2$ such as :

$$\begin{aligned} \boldsymbol{\epsilon}.\mathbf{J} &= \epsilon_x J_x + \epsilon_y J_y + \epsilon_z J_z \\ &= \frac{1}{2}(\epsilon_x - i\epsilon_y)J_+ + \frac{1}{2}(\epsilon_x + i\epsilon_y)J_- + \epsilon_z J_z \end{aligned} \tag{193}$$

Here, we give the matrix elements $\langle 2, m_2 | J_q | 1, m_1 \rangle$, with $q = \{+, -, z\}$ (only the non-zero elements are listed). The reader is referred to [86] for more details.

$$\langle 2, 2 | J_+ | 1, 1 \rangle = \sqrt{3/4} \tag{194a}$$
$$\langle 2, 1 | J_+ | 1, 0 \rangle = \sqrt{3/8} \tag{194b}$$
$$\langle 2, 0 | J_+ | 1, -1 \rangle = \sqrt{1/8} \tag{194c}$$

$$\langle 2, 0 | J_- | 1, 1 \rangle = -\sqrt{1/8} \tag{195a}$$
$$\langle 2, -1 | J_- | 1, 0 \rangle = -\sqrt{3/8} \tag{195b}$$
$$\langle 2, -2 | J_- | 1, -1 \rangle = -\sqrt{3/4} \tag{195c}$$

$$\langle 2, 1 | J_z | 1, 1 \rangle = -\sqrt{3/16} \tag{196a}$$
$$\langle 2, 0 | J_z | 1, 0 \rangle = -\sqrt{1/4} \tag{196b}$$
$$\langle 2, -1 | J_z | 1, -1 \rangle = -\sqrt{3/16} \tag{196c}$$

In section 4, we have described the Rabi frequency, in the case of a linearly polarized microwave field $\mathbf{B}_{mw}$, by the following expression :

$$\Omega_{m_1}^{m_2} = C_{m_1}^{m_2} \mu_B B_{mw}^{\text{eff}} / \hbar \tag{197}$$

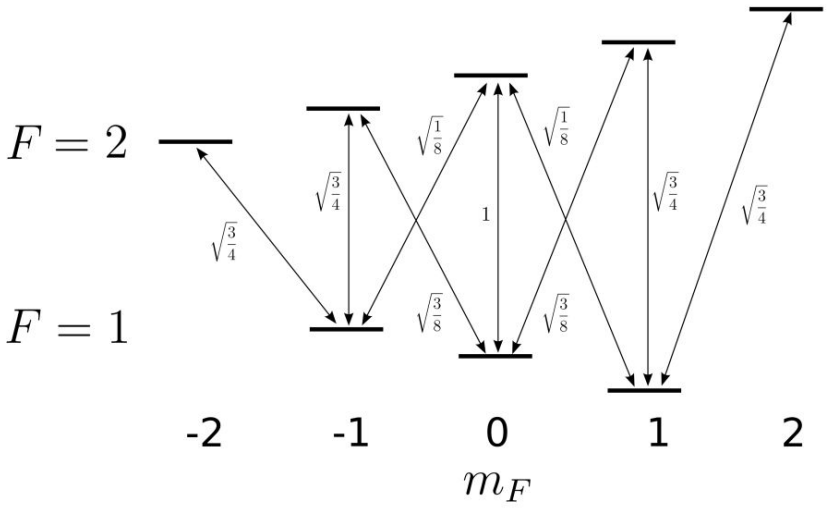

Figure 58: The coupling coefficients $|C_{m_1}^{m_2}|$.

where B_{mw}^{eff} is the microwave effective filed[1] and $C_{m_1}^{m_2}$ is the coupling coefficient between the states $|1, m_1\rangle$ and $|2, m_2\rangle$. The absolute value of the nonzero coefficients $C_{m_1}^{m_2}$ are summarized in Figure 58.

1 The microwave field component a long the parallel (normal) local direction of **B** in case of π-transition (σ-transition)

D

AXIAL-SYMMETRY OF THE MICROWAVE BEAM-SPLITTER USING π-TRANSITIONS

In this appendix, we discuss the possibility to design a custom microtrap, which combined with two CPWs placed along the x-axis as shown in Figure 17, allows the creation of a microwave energy-shifts using the π-transitions that have the following axial symmetry:

$$V_{m\,w}^{|\,a\,\rangle}(-x,y,z) = V_{m\,w}^{|\,b\,\rangle}(x,y,z) \tag{198}$$

The microwave shifts are given by equation (72), and the effective microwave field $B_{m\,w}^{\text{eff}}$, in the case of the π-transitions, are given by :

$$B_{m\,w}^{\text{eff}} = (B_x B_{m\,w}^{x} + B_z B_{m\,w}^{z}) / B \tag{199}$$

As the microwave field is on the xz-plane, the trap-axis $\boldsymbol{\mathcal{U}}$ should have its larger component also in the xz-plane (i.e. $u_y^2 \ll u_x^2 + u_z^2$), in order to select only the π-transitions. Here, we exclude the particular case where $\nu = \{0,0,1\}$ as it gives rise usually to a microtrap with a low trap-depth [85]. Thus, the following condition should be verified :

$$B_x(\mathbf{r_0}) \neq 0 \tag{200}$$

Using the previous condition and the symmetry properties of the components of the microwave field, one can easily show[1] that the following conditions :

$$B_x \text{ is an even-function of } x \tag{201a}$$
$$B_y^2 \text{ is an even-function of } x \tag{201b}$$
$$B_z \text{ is an odd-function of } x \tag{201c}$$

should be verified to satisfy equation (198). Using a first order expansion, equations (201a) and (201c) give respectively the following conditions on the elements of the gradient tensor $\mathcal{V}$:

$$v_{11} = 0 \tag{202a}$$
$$v_{22} = 0, v_{23} = 0 \tag{202b}$$

1 Similar derivation is given in section 6.2.4 for the σ-transitions.

Hence, as the trap-axis should verify : $\mathcal{V}.\boldsymbol{\mathcal{U}} = 0$, one can deduce that :

$$\boldsymbol{\mathcal{U}} = \{0, \frac{-v_{13}}{v_{13}^2 + v_{12}^2}, \frac{v_{12}}{v_{13}^2 + v_{12}^2}\} \tag{203}$$

which is in contradiction with the condition (200). Therefore, using the π-transitions and on-chip Ioffe Pritchard trap, we conclude that the axial-symmetry condition (198) can not be satisfied.

E

CLASSICAL TRANSPORT DYNAMICS

The time-dependent invariants approach described earlier has been successful in the quantization of time dependent harmonic oscillators. Here, we establish the general classical solution following Ermakov approach [192, 169] and show the classical nature of equation (168). In this section, we summarize the results shown in [169].

The motion of the atoms in a trapping-potential, if we neglect the anharmonic terms, follows the classical equation (169). We can find the homogeneous solution by setting $q_0(t) = 0$ in equation (169) and solve the remaining equation :

$$\ddot{\xi} + \omega^2(t)\xi = 0 \tag{204}$$

Then we set $\xi = \rho(t)e^{i\mu(t)}$ where $\rho(t)$ and $\mu(t)$ are the modulus and the phase respectively, and are both real. By considering real and imaginary parts in equation (204b), we get the two equations :

$$\ddot{\rho} - \rho\dot{\mu}^2 + \omega^2(t)\rho = 0 \tag{205}$$

$$2\dot{\rho}\dot{\mu} + \rho\ddot{\mu} = 0 \tag{206}$$

The second equation can be integrated, and so can simplified to :

$$\rho(t)^2\dot{\mu}(t) = k_0 \tag{207}$$

where k_0 is an integrating function. By inserting this to equation (205), we obtain the Ermakov equation (168) where we set $k_0 = \omega(t_0)$. Thus we establish the classical nature of equation (168). Obviously, the second equation (169) that governs the quantum solution (152), is also classical.

For periods of constant frequency $\omega = \omega_1$, such as the holding period in our interferometer, analytical solution can be found :

$$\rho(t) = \sqrt{\cosh(a) + \sinh(a)\sin(2\omega_1 t + b)} \tag{208}$$

where a and b are time-independent constants that depend on the system evolution in the past.

Once $\rho(t)$ is known, $\mu(t)$ can be easily deduced, thus the general homogeneous solution :

$$q_h(t) = a_0 \mathrm{Re}[\xi(t)] = a_0\rho(t)\cos(\mu(t) + \varphi_0) \tag{209}$$

with the amplitude a_0 and initial phase φ_0 are fixed by the initial conditions.

The particular solution can be determined in the framework of the green function $G(t,t')$ such as :

$$q_p(t) = \int_{t_0}^{t} \mathrm{d}t' G(t,t') F(t')/m \tag{210}$$

where $F(t) = m\omega(t)^2 q_0(t)$ is the driving force, and $G(t,t')$ is related to the homogeneous solution $\xi(t)$ by the following :

$$G(t,t') = \Theta_E(t-t')\rho(t)\rho(t')\sin\left(\mu(t)-\mu(t')\right)/\omega_0 \tag{211}$$

where Θ_E is the step function.

Thus, we obtain the general solution of equation (169) as sum of the general homogeneous solution and a particular solution :

$$\begin{aligned} q_c(t) &= q_h(t) + q_p(t) \\ &= \frac{1}{2}\left[a_0\rho(t)e^{i(\mu(t)+\varphi_0)} + \xi^\star(t)\zeta(t)\right] + c.c \end{aligned} \tag{212}$$

where

$$\zeta(t) = i\int_{t_0}^{t} \mathrm{d}t' e^{i\mu(t')}\rho(t')F(t')/m\omega_0 \tag{213}$$

If the atoms are initially at equilibrium (i.e. $a_0 = 0$), the classical solution depends only on the particular solution q_p :

$$q_c(t) \equiv q_p(t) = \xi^\star(t)\zeta(t)/2 + c.c \tag{214}$$

Then, we define the quantity $\Xi(t) = \dot{q}_p(t) + i\omega(t)q_p(t)$ that can be used to derive the energy transferred to the oscillator giving by [207, 208] :

$$\mathcal{W}(t) = m\left|\Xi(t)\right|^2/2 \tag{215}$$

$$= \frac{1}{2m}\left|\int_{t_0}^{t} F(t')\xi(t')\mathrm{d}t'\right|^2 \tag{216}$$

at instant t where $F(t) = 0$ (e.g. during the holding period in our case).

F

TRANSITION PROBABILITY

An alternative formulation of the quantum mechanics (i.e. Schrödinger description), can be given by the unitary operator $U(t)$:

$$\psi(q,t) = U(t)\psi(x,0) \tag{217}$$

where the operator $U(t)$ is given by :

$$U(t) = e^{-iH(t)t/\hbar} \tag{218}$$

where $H(t)$ is the system Hamiltonian. Let consider $U(t)_{n,k}$ the matrix elements of U with respect to a set of orthogonal functions Φ_n that evolve under H. The transition probability from Φ_k to Φ_n can be introduced as :

$$P_{n,k}(t) = \left|U(t)_{n,k}\right|^2 \tag{219}$$

In the case of the Hamiltonian (166), the functions Φ_n can be set using the eigenstates ψ_n of the invariant I (equation (167)) such as : $\Phi_n(q,t) = e^{i\alpha_n(t)}\psi_n(q,t)$, so one can derive an explicit expression of the probability transition :

$$\begin{aligned} P_{n,k}(t) &= \left| \int_{-\infty}^{\infty} \mathrm{d}q \; e^{i(\alpha_n(t)-\alpha_k(0))}\psi_n(q,t)\psi_k^\star(q,0)\right|^2 \\ &= \left| \int_{-\infty}^{\infty} \mathrm{d}q \; \psi_n(q,t)\phi_k^\star(q)\right|^2 \end{aligned} \tag{220}$$

where ϕ_k is given by equation (152).

In a landmark paper, Husimi [209] has considered the forced quantum mechanical oscillator and derived exact expressions for their propagators and transition probabilities in the limiting cases : for a constant angular frequency ($\omega(t) = \omega_0$), for a zero driving force ($F(t) = 0$), and more generally for $\omega(t) \neq \omega_0$ and $F(t) \neq 0$. Later, similar results has been derived differently by Popov & Perelomov [207, 208] and Meyer [210]. In the following, we summarize the principal results of these papers.

F.1 CASE OF $\omega(t) = \omega_0$

This case leads to $\rho(t) = 1$ and equation (220) simplifies to :

$$P_{n,k}(t) = \left| \int_{-\infty}^{\infty} \mathrm{d}q \; e^{im\dot{q}_c(t)/\hbar}\phi_n(q - q_c(t))\phi_k^\star(q)\right|^2 \tag{221}$$

The computation of the latter expression can be performed using the generating function of the Hermite polynomials [207, 209, 211] :

$$P_{n,k} = \frac{\mu!}{\nu!}\epsilon^{\nu-\mu}e^{-\epsilon}\left(L_{\mu}^{\nu-\mu}(\epsilon)\right)^2 \tag{222}$$

where

$$\epsilon(t) = \mathcal{W}(t)/\hbar\omega_0 = \frac{1}{2m\hbar\omega_0}\left|\int_{t_0}^{t} F(t')\xi(t')\mathrm{d}t'\right|^2 \tag{223}$$

is the classical energy transfer in unit of the quantum energy $\hbar\omega_0$ (cf. Appendix E) and $\{\nu, \mu\}$ are respectively the greater and the lesser of $\{n, k\}$; $L_{\mu}^{\nu-\mu}$ denotes the *associated* Laguerre polynomial [212].

Starting from the ground state ($k = 0$), the excitation spectrum becomes simply a Poisson distribution :

$$P_{n,0} = \epsilon^n e^{-\epsilon}/n! \tag{224}$$

which is a signature of a coherent state [210].

In some cases, one may be more interested in the moments of the energy transfer (i.e. mean and variance). For the case studied here, the average energy transfer and the variance are respectively given by [169, 210] :

$$\Delta E_F = \hbar\omega_0\epsilon \tag{225}$$

$$\Delta_F^2 = (2n+1)(\hbar\omega_0)^2\epsilon \tag{226}$$

Thus, the classical and quantum energy transfer are identical.

F.2 CASE OF $F(t) = 0$

This case leads to $q_c(t) = 0$ and only $\rho(t)$ depends on time. The calculation of the excitation spectrum yields to [208, 210] :

$$P_{n,k} = \frac{(l-p)!}{(l+p)!}\sqrt{1-\mathcal{B}}\left|\mathcal{P}_l^p\left(\sqrt{1-\mathcal{B}}\right)\right|^2 \tag{227}$$

where $l = (k+n)/2$ and $p = |k-n|/2$ and $\mathcal{P}$ denotes the *associated* Legendre polynomial [212]. The non-dimensional parameter $\mathcal{B}$ measures the strength of the quadratic perturbation [210], and its derivation as a function of ρ will be discussed later. The latter expression of $P_{n,k}$ holds only if $|n-k|$ is an even number. Indeed, transition between energy levels of different parity is not allowed because : $P_{n,k} = 0$ if $|n-k|$ is an odd number. This is related to the parity of the harmonic potential.

If the oscillator is initially in the ground state, the formula can be simplified to :

$$P_{2n,0} = \sqrt{\frac{1-\mathcal{B}}{\pi}}\frac{\Gamma(n+1/2)}{\Gamma(n+1)}\mathcal{B}^n \tag{228}$$

$$P_{2n+1,0} = 0 \tag{229}$$

where Γ is the Gamma function. Moreover, the average energy transfer and the variance can be deduced [210] :

$$\Delta E_\omega = (2n+1)\hbar\omega_0 \frac{\mathcal{B}}{1-\mathcal{B}} \tag{230}$$

$$\Delta_\omega^2 = 2(n^2+n+1)(\hbar\omega_0)^2 \frac{\mathcal{B}}{(1-\mathcal{B})^2} \tag{231}$$

On the one hand, the time-dependent energy transfer [194], can be derived differently as :

$$\begin{aligned} \Delta E_\omega(t) &= \langle\psi_n(t)|H(t)|\psi_n(t)\rangle - \langle\psi_n(0)|H(0)|\psi_n(0)\rangle \\ &= (2n+1)\hbar\omega_0 \left[\dot\rho^2 + \omega(t)^2\rho^2 + \omega_0^2/\rho^2\right]/4\omega_0 - (n+1/2)\hbar\omega_0 \\ &= (2n+1)\hbar\omega_0 \left[\dot\rho^2 + \omega(t)^2\rho^2 + \omega_0^2/\rho^2 - 2\omega_0^2\right]/4\omega_0^2 \end{aligned} \tag{232}$$

On the other hand, one can define the *adiabatic* energy-transfer, as the energy difference between the fast and adiabatic transformations :

$$\begin{aligned} \Delta E_\omega^{(\mathrm{ad})}(t) &= \langle\psi_n(t)|H(t)|\psi_n(t)\rangle - \langle\psi_n(\infty)|H(\infty)|\psi_n(\infty)\rangle \\ &= (2n+1)\hbar\omega_0 \left[\dot\rho^2 + \omega(t)^2\rho^2 + \omega_0^2/\rho^2\right]/4\omega_0 - (n+1/2)\hbar\omega_1 \\ &= (2n+1)\hbar\omega_0 \left[\dot\rho^2 + \omega(t)^2\rho^2 + \omega_0^2/\rho^2 - 2\omega_0\omega_1\right]/4\omega_0^2 \end{aligned} \tag{233}$$

Assuming that the system becomes stationary after a certain time τ (i.e. $\omega(t>\tau)=\omega_1$), $\rho(t)$ is then given by the periodic solution (208). Hence, the time average values of ρ^2, $1/\rho^2$ and $\dot\rho^2$ can be computed by performing a time-integration of these quantities over one period : $2\pi/2\omega_1$ for $t > \tau$. So, the average value of $\Delta E_\omega(t)$ noted ΔE_ω in equation (230) (or $\Delta E_\omega(t\to\infty)$), can be derived in a different manner, then the parameter $\mathcal{B}$ can be deduced explicitly.

The parameter $\mathcal{B}$ was first introduced by Popov and Perelomov [208] as a function of the classical solution $\xi(t)$ of equation (204). Indeed, if $\omega(t) \to \omega_1$ as $t \to \infty$, $\xi(t)$ has the following asymptotic form : $\xi(t) = C_1 e^{i\omega_1 t} - C_2 e^{-i\omega_1 t}$. $\mathcal{B}$ is defined as : $\mathcal{B} = |C_2/C_1|^2$, and interpreted as a reflection coefficient from a potential barrier. Yet, equation (232) gives an alternative (straightforward) way to compute the energy-transfer ΔE_ω (i.e. the parameter $\mathcal{B}$) that requires only the knowledge of $\rho(t)$ by solving (numerically) equation (168).

F.3 CASE OF $F(t) \neq 0$ AND $\omega(t) \neq \omega_0$

In the general case, the derivation of the excitation spectrum has been done in the literature [209, 210] but turns out to be lengthy and shall be omitted here. Nevertheless, the derivation of the energy transfer moments gives an overview about the spectrum and can be simply expressed, using the previous notations, as [207, 210] :

$$\Delta E = \Delta E_F + \Delta E_\omega \tag{234a}$$

$$\Delta^2 = \mathcal{D}(\mathcal{B}, \varphi_\Delta)\Delta_F^2 + \Delta_\omega^2 \tag{234b}$$

where

$$\mathcal{D}(\mathcal{B}, \varphi_\Delta) = \frac{1 - 2\sqrt{\mathcal{B}}\cos(\varphi_\Delta) + \mathcal{B}}{1 - \mathcal{B}} \tag{235}$$

with φ_Δ is defined by :

$$\varphi_\Delta = \varphi_\omega - \varphi_F \tag{236}$$
$$\varphi_\omega = \arg(C_2/C_1^\star) \tag{237}$$
$$\varphi_F = \arg(\zeta^2(t \to \infty)) \tag{238}$$

One can note that for the energy-transfer of the first moment ΔE, the roles of the perturbations $F(t)$ and $\omega(t)$ are independent and their contributions can be separated. Whereas, for the second moment Δ^2 the phase term φ_Δ that relates both perturbation plays an important role : the spectrum is largest for $\cos(\varphi_\Delta) = -1$ and smallest for $\cos(\varphi_\Delta) = 1$.

F.4 SYMMETRY OF THE TRANSITION PROBABILITY $P_{n,k}$

For the first two cases discussed previously : $F(t) = 0$ and $\omega(t) = \omega_0$, we point out the symmetry of the transition probabilities with respect to the initial and final states : $P_{n,k} = P_{k,n}$. The latter equation holds only in the case of a time-reversal Hamiltonian : $H(-t) = H(t)$ (cf. equation (218)), which is obviously the case only if : $\omega(-t) = \omega(t)$ and $F(-t) = F(t)$. The symmetry of $P_{n,k}$ is valid, more generally if $\epsilon = 0$ or $\mathcal{B} = 0$ [207, 209], that is the effect of the driving force or the harmonic perturbation vanishes (which is possible even if $F(t) \neq 0$ and $\omega(t) \neq \omega_0$). This symmetry is a specific property of an harmonic oscillator and does not arise from the principles of quantum mechanics.

In the general case, when $\epsilon \neq 0$ and $\mathcal{B} \neq 0$, the *fortuitous* symmetry of $P_{k,n}$ disappears expect in a unique case where the condition : $\mathcal{B} = \cos^2(\varphi_\Delta)$ is fulfilled. The asymmetry of $P_{n,k}$ can be easily seen from the following particular case [207] :

$$P_{1,0} = \epsilon(1 - \mathcal{B})P_{0,0} \tag{239}$$
$$P_{0,1} = \epsilon(1 - 2\sqrt{\mathcal{B}}\cos(2\varphi_\Delta) + \mathcal{B})P_{0,0} \tag{240}$$
$$P_{0,0} = \sqrt{1 - \mathcal{B}}\exp\left(-\epsilon(1 - \sqrt{\rho}\cos\varphi_\Delta)\right) \tag{241}$$

The transition probabilities and the consideration of symmetry discussed here are particularly important to design a successful beamsplitter. This design is studied in section 7.3.3, using the inverse engineering method based-on Lewis invariant I.

Part II

PUBLICATIONS & BIBLIOGRAPHY

PUBLICATIONS

Contributions to publications :

- Huet Landry, Ammar Mahdi, Morvan Erwan, Sarazin Nicolas, Pocholle Jean-Paul, Reichel Jakob, Guerlin Christine, and Schwartz Sylvain, Experimental investigation of transparent silicon carbide for atom chips, *Applied Physics Letters*, 100(12): 121114, 2012.

- Ammar Mahdi, Huet Landry, Esteve Jerome, Westbrook Chris, Bouchoule Isabelle, Pocholle Jean-Paul, Reichel Jakob, Rosenbusch Peter, Guerlin Christine, and Schwartz Sylvain, Splitting of trapped thermal atoms for atom-chip based interferometry, *Conference on Lasers and Electro-Optics Pacific Rim (CLEO-PR), 2013, Proceedings paper*

- Ammar Mahdi, Huet Landry, Esteve Jerome, Westbrook Chris, Bouchoule Isabelle, Pocholle Jean-Paul, Reichel Jakob, Guerlin Christine, and Schwartz Sylvain, Design of novel cold atom gravimeter integrated on chip and study of its theoretical performances, *The 23rd International Conference of Atomic Physics, 2012, Poster*

- Huet Landry, Ammar Mahdi, Morvan Erwan, Sarazin Nicolas, Pocholle Jean-Paul, Reichel Jakob, Guerlin Christine, and Schwartz Sylvain, Investigation of Transparent Silicon Carbide Proprieties for Atom Chips Sensors, *APS Division of Atomic, Molecular and Optical Physics Meeting Abstracts, 2012, Poster*

Experimental investigation of transparent silicon carbide for atom chips

Landry Huet,[1,2] Mahdi Ammar,[1,3] Erwan Morvan,[4] Nicolas Sarazin,[4] Jean-Paul Pocholle,[1] Jakob Reichel,[3] Christine Guerlin,[1,a)] and Sylvain Schwartz[1,b)]
[1]*Thales Research and Technology France, Campus Polytechnique, 1 av. Fresnel, 91767 Palaiseau, France*
[2]*Thales Underwater Systems, 525 route des Dolines, BP 157 Sophia-Antipolis, France*
[3]*Laboratoire Kastler-Brossel, ENS, CNRS, Université Pierre et Marie Curie – Paris 6, 24 rue Lhomond, 75005 Paris, France*
[4]*III-V Lab, Route de Nozay, 91461 Marcoussis, France*

(Received 18 August 2011; accepted 8 February 2012; published online 21 March 2012)

We investigate some properties of an atom chip made of a gold microcircuit deposited on a transparent silicon carbide substrate. A favorable thermal behavior is observed in the presence of electrical current, twice as good as a silicon counterpart. We obtain one hundred million rubidium atoms in a magneto-optical trap with several of the beams passing through the chip. We point out the importance of coating of the chip against reflection to avoid a temperature-dependent Fabry-Perot effect. We finally discuss detection through the chip, potentially granting large numerical apertures, as well as some other potential applications. © *2012 American Institute of Physics*. [http://dx.doi.org/10.1063/1.3689777]

Atom chips[1,2] are a versatile tool for the manipulation of ultracold atoms.[3,4] They have been used to create atomic waveguides, beam splitters or conveyor belts, and to achieve and handle Bose-Einstein condensates. They opened possibilities for the study of fundamental issues such as low-dimensional quantum systems, cavity quantum electrodynamics, and nanomechanical resonators. Recent results regarding on-chip radiofrequency and microwave manipulation of atoms[5–7] also hold prospects for future applications such as quantum information processing,[8,9] timekeeping,[10] or inertial sensing.[11]

One key feature of atom chips is to allow tight atomic confinement thanks to strong magnetic field gradients. To do so, electrical currents up to several amperes are typically required, and thermal management can become an issue.[12,13] Moreover, atom chips take advantage of the fact that atoms are trapped very close to the chip surface,[4] typically on the order of tens or hundreds of microns. Because the chip size is usually centimetric, this comes at the price of reducing the optical access to the atoms by almost half the full 4π solid angle.

In this paper, we propose to address these issues by using a transparent atom chip made of a gold microcircuit deposited on a single crystal silicon carbide (SiC) substrate. Single crystal SiC appears as a particularly relevant candidate substrate for atom chip applications. Its specified electrical resistivity (over 10^5 Ω cm for our high purity semi-insulating 4H SiC sample)[14] and thermal conductivity (over 390 $W\,m^{-1}\,K^{-1}$ for our sample)[14] make it well suited for supporting wires with large currents, without the need of an additional electrical insulation layer. To illustrate the latter point, we have monitored the temperature rise of our 414 μm × 15 mm × 15 mm SiC chip in the presence of electrical current and compared it to a 600 μm thick silicon chip with a 200 nm insulating silica layer, all other parameters being equal. Current was run through the central 14 mm× 100 μm × 3 μm wire of each chip. Each chip was resting along two opposite sides on copper blocks, acting as heat sinks, as shown on the inset of Fig. 1. Temperature was measured after thermalization at ambient pressure. We have used a gold wire pattern similar to the one of Ref. 15, which already has proven to achieve Bose-Einstein condensation of rubidium atoms. As can be seen on the main curve of Fig. 1, the thermal behavior of the SiC chip is more than twice as good, despite the greater thickness of the silicon chip, which is expected to favor thermal conductivity between the central wire and the heat sinks.

With a bandgap value of about 3.2 eV at room temperature,[14] another potential interest of single crystal SiC is optical transparency at all visible wavelengths. Our chip is coated, after the deposition of the wires, with a single anti-reflection (AR) layer of aluminum oxide on each side, resulting in about 2% reflection on each air/SiC interface for a 780 nm beam at a 60° incidence, as used in our magneto-optical trap (MOT) setup shown in Fig. 2. The overall substrate transmittance is about 93% when measured with a small beam propagating between wires. The difference of 3% between the overall losses and the reflection losses can mainly be attributed to absorption by the substrate, corresponding to an absorption

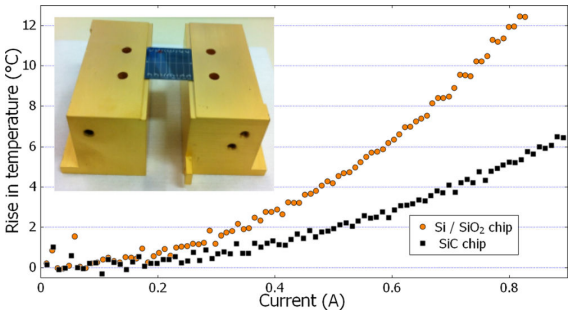

FIG. 1. (Color online) Main curve: comparison of the thermal properties of the SiC chip with that of a silicon counterpart. Inset: picture of the test setup.

a)Present address: LNE-SYRTE, Observatoire de Paris, 61 av. de l'Observatoire, 75014 Paris, France.
b)Electronic mail: sylvain.schwartz@thalesgroup.com.

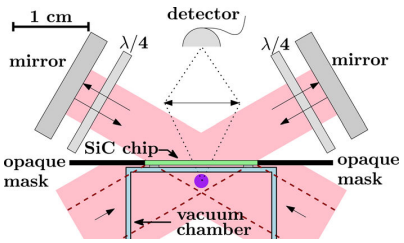

FIG. 2. (Color online) Sketch of the upper chamber part of the experimental setup. An opaque mask surrounding the chip ensures that only the fraction of the beams going through the chip (dashed lines) contributes to the MOT. An additional pair of beams perpendicular to the plane of the figure is used to complete the 6-beam MOT configuration. Atomic fluorescence is recorded through the chip.

coefficient of about $0.7\,\mathrm{cm}^{-1}$ at 780 nm. The overall transmittance of the chip drops to about 80% in the MOT setup because the beams are partially blocked by the wires. Although reflections at air/SiC interfaces are not the main source of losses, the quality of the AR coating turns out to be very important to avoid intensity and polarization fluctuations with temperature linked to a residual Fabry-Perot effect within the chip. The latter is illustrated on Fig. 3(a), where the chip transmittance is plotted against temperature. The measured period is about 11 °C, corresponding to $\partial n/\partial T \simeq 8 \times 10^{-5}/^{\circ}\mathrm{C}$ for 4H SiC at 780 nm where n is the average refractive index, which is consistent with published measurements for other SiC crystals.[16] One straightforward solution to suppress this effect would be the use of a better AR coating, for instance, based on multiple layers of dielectric materials. For example one can expect intensity fluctuations smaller than 1% if reflectivity is reduced to less than 0.25%.

In order to exploit transparency of single crystal SiC, the question of birefringence must be addressed. The substrate we use has a 4H hexagonal crystalline structure. This is one of many polytypes of SiC, of which 4H and 6H structures are increasingly used in microelectronics.[17] 4H SiC has uniaxial anisotropy with ordinary optical index $n_o = 2.617$ and extraordinary optical index $n_e = 2.666$ at 780 nm.[18] Hence, special care is required, for example, to keep the correct circular polarizations of MOT beams on the atom cloud. Assuming no polarization-dependent losses (which can be made negligible by an appropriate AR coating), the effect of the atom chip on the beam polarization can be described by a Jones matrix of

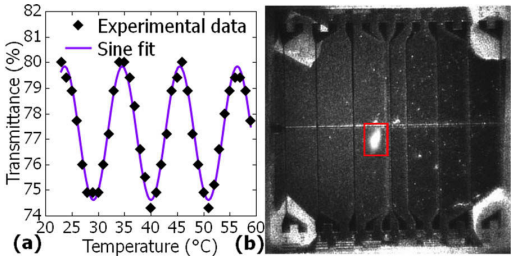

FIG. 3. (Color online) (a) Light transmittance of the SiC chip measured as a function of its surface temperature, showing a Fabry-Perot effect due to insufficient anti-reflection coating of the chip. The wavelength, angle of incidence and polarization state are the same as in the MOT setup. (b) Fluorescence imaging from the MOT atoms (in the red box) as seen through the chip.

the form $U_{\mathrm{chip}} = R_\alpha G_\gamma R_{-\alpha}$, where R_α is a rotation matrix with angle α and $G_\gamma = \begin{bmatrix} e^{i\gamma/2} & 0 \\ 0 & e^{-i\gamma/2} \end{bmatrix}$. Using computations similar to those described in Ref. 19, it can be proven that circular polarizations can be preserved in the retroreflection configuration sketched on Fig. 2 with only one single quarter-wave plate for each retro-reflected beam, provided the latter is oriented such that

$$\theta = \alpha - \pi/4, \tag{1}$$

where θ is the angle between the quarter-wave plate eigenbasis and the reference polarization basis. As can be seen in Eq. (1), the optimal value of θ depends only on the chip polarization eigenbasis and not on the phase shift γ. One can, therefore, expect robustness to variations in the refractive indices and thickness of the chip, induced for instance by temperature changes.

For the proof-of-concept experimental demonstration of a MOT with several of the beams passing through the atom chip, we have used the setup sketched on Fig. 2. The glass vacuum cell was manufactured by the company ColdQuanta, with a differential vacuum system. A ^{87}Rb MOT is formed in the ultra-high vacuum part of the cell and is loaded from a two-dimensional MOT with a push beam. The chip rests on a 1 mm-thick support on top of the glass cell. Quarter-wave plates are placed between the chip and the retro-reflection mirrors and are oriented according to Eq. (1) to ensure the same circular polarization in both beam directions inside the vacuum cell.

The possibility of imaging through the transparent chip, possibly between wires, is illustrated on Fig. 3(b). In many experiments detection occurs typically just after current has been run into the chip wires. It is therefore important that imaging is not distorted by refractive index inhomogeneities induced by a possibly time-varying temperature gradient within the chip. We have performed thermal infrared camera measurements in order to monitor the spatial dependence of temperature on the chip surface. The central wire of the chip was heated up by 50 °C, corresponding to a worst case scenario. We have observed a temperature difference on the order of 2 °C between the center and the side of the SiC chip surface (distant by 7.5 mm). Let us now consider the overall phase shift ϕ for a ray of light going through the chip. We know from our Fabry-Perot measurements that ϕ will increase by π over a temperature change of about 11 °C. Consequently, we estimate that $\phi/(2\pi)$ will change by less than 1% over an area of radius 0.8 mm on the chip surface, which may be deemed acceptable to avoid large distortions, depending on the application. For a future experiment where the chip would be part of the vacuum chamber itself, with atoms located 1 mm away from its surface, this 0.8 mm value would correspond, taking into account the $\sim 400\,\mu$m chip thickness, to a maximum numerical aperture of about 0.25. With proper thermal management, we expect that even higher numerical aperture values may be possible.

The number of atoms in a MOT can be estimated from fluorescence measurements using a photodiode. Following the analysis described in Ref. 20, we evaluate the atom number to 1×10^8 for our MOT. This is comparable to the 5×10^7 atoms

that were detected in our previous setup, which was similar to the configuration presented here but without a chip, and probably not as carefully optimized, explaining the difference in the number of atoms. Our setup also stands the comparison to the performances of other techniques of near-chip magneto-optical trapping, for example Ref. 1, while allowing unrestricted optical access to the atom cloud.

The atom number estimated above corresponds to a MOT center located 1.5 mm below the vacuum cell ceiling. By translating the quadrupole coils and realigning the optomechanical apparatus, we have measured the number of atoms as a function of the latter distance. We found that the number of atoms is reduced by 50% at about 1 mm and quickly drops to zero thereafter, which is consistent with previous observations[1] and is probably due to a reduction of the capture volume. The impossibility in our particular setup to translate the optomechanical apparatus in order to realign it optimally with the magnetic quadrupole center, together with the mask used to ensure the relevance of our proof-of-principle setup, placed drastic geometrical constraints on the trapping beams which prevented the formation of a MOT much further than 2.5 mm. Any higher distance could however be achieved in principle thanks to the transparent chip, provided the optomechanical apparatus is set up accordingly. This could in particular allow a larger capture volume than in the case of a mirror-MOT, while being much closer to the chip surface than in the case of a standard 6-beam MOT.

The possibility of trapping atoms near transparent chips could open the way to applications combining for example the simplicity of chip evaporative cooling with more complex architectures requiring full optical access such as Ramsey-Bordé interferometers[21] or Bloch oscillators.[22] It coud also be a way of combining optical trapping techniques with atom chip technology. Detection through the chip could moreover be a powerful tool to improve numerical aperture for atom optical manipulation or in-situ detection with possible applications to on-chip atomic clocks or quantum information processing. In this respect, lenses etched directly on the SiC chip[23] could combine a large numerical aperture with a particularly compact and scalable setup.

This work has been carried out within the CATS project ANR-09-NANO-039 funded by the French National Research Agency (ANR) in the frame of its 2009 program in Nanoscience, Nanotechnologies, and Nanosystems (P3N2009).

[1]J. Reichel, W. Hänsel, and T. W. Hänsch, Phys. Rev. Lett. **83**, 3398 (1999).
[2]R. Folman, P. Krüger, D. Cassettari, B. Hessmo, T. Maier, and J. Schmiedmayer, Phys. Rev. Lett. **84**, 4749 (2000).
[3]J. Fortágh, and C. Zimmermann, Rev. Mod. Phys. **79**, 235 (2007).
[4]J. Reichel and V. Vuletić, *Atom Chips* (John Wiley & Sons, Weinheim, Germany, 2011).
[5]T. Schumm, S. Hofferberth, L. Andersson, S. Wildermuth, S. Groth, I. Bar-Joseph, J. Schmiedmayer, and P. Krüger, Nat. Phys. **1**, 57 (2005).
[6]P. Böhi, M. Riedel, J. Hoffrogge, J. Reichel, T. Hänsch, and P. Treutlein, Nat. Phys. **5**, 592 (2009).
[7]C. Deutsch, F. Ramirez-Martinez, C. Lacroûte, F. Reinhard, T. Schneider, J. N. Fuchs, F. Piéchon, F. Laloë, J. Reichel, and P. Rosenbusch, Phys. Rev. Lett. **105**, 020401 (2010).
[8]T. Calarco, E. A. Hinds, D. Jaksch, J. Schmiedmayer, J. I. Cirac, and P. Zoller, Phys. Rev. A **61**, 022304 (2000).
[9]P. Treutlein, T. W. Hänsch, J. Reichel, A. Negretti, M. A. Cirone, and T. Calarco, Phys. Rev. A **74**, 022312 (2006).
[10]P. Rosenbusch, Appl. Phys. B: Lasers Opt. **95**, 227 (2009).
[11]A. Zatezalo, V. Vuletić, P. Baker, and T. Poling, in *Position, Location and Navigation Symposium, 2008 IEEE/ION*, 5-8 May 2008 (IEEE, New York, NY, 2008), pp. 940–950.
[12]J. Armijo, C. L. Garrido Alzar, and I. Bouchoule, Eur. Phys. J. D **56**, 33 (2010).
[13]S. Groth, P. Krüger, S. Wildermuth, R. Folman, T. Fernholz, J. Schmiedmayer, D. Mahalu, and I. Bar-Joseph, Appl. Phys. Lett. **85**, 2980 (2004).
[14]CREE, *Silicon Carbide Substrates and Epitaxy Product Specification* (CREE, Durham, NC, 2011).
[15]D. M. Farkas, K. M. Hudek, E. A. Salim, S. R. Segal, M. B. Squires, and D. Z. Anderson, Appl. Phys. Lett. **96**, 093102 (2010).
[16]S. Dakshinamurthy, N. Quick, and A. Kar, J. Phys. D: Appl. Phys. **40**, 353 (2007).
[17]S. Saddow and A. Agarwal, *Advances in Silicon Carbide Processing and Applications* (Artech House, Boston, MA, 2004).
[18]P. Shaffer, Appl. Opt. **10**, 1034 (1971).
[19]N. Vansteenkiste, P. Vignolo, and A. Aspect, J. Opt. Soc. Am. A **10**, 2240 (1993).
[20]H. Lewandowski, D. Harber, D. Whitaker, and E. Cornell, J. Low Temp. Phys. **132**, 309 (2003).
[21]Q. Bodart, S. Merlet, N. Malossi, F. P. D. Santos, P. Bouyer, and A. Landragin, Appl. Phys. Lett. **96**, 134101 (2010).
[22]P. Cladé, S. Guellati-Khélifa, C. Schwob, F. Nez, L. Julien, and F. Biraben, Europhys. Lett. **71**, 730 (2005).
[23]H. Lee, D. Kim, Y. Sung, and G. Yeom, Solid Films **475**, 318 (2005).

BIBLIOGRAPHY

[1] Maximilian Schlosshauer, Johannes Kofler, and Anton Zeilinger. A snapshot of foundational attitudes toward quantum mechanics. *Studies in History and Philosophy of Science Part B: Studies in History and Philosophy of Modern Physics*, 44(3):222–230, 2013.

[2] Richard P Feynman, Robert B Leighton, and Matthew Sands. Lectures on physics, vol. iii, 1965.

[3] Claude Cohen-Tannoudji. Manipulating atoms with photons. *Physica Scripta*, 1998(T76):33, 1998.

[4] Steven Chu. The manipulation of neutral particles. *Reviews of Modern Physics*, 70(3):685–706, 1998.

[5] William D Phillips. Laser cooling and trapping of neutral atoms. *Physics, 1996-2000*, 8:199, 2002.

[6] Harold J Metcalf and Peter Van der Straten. *Laser cooling and trapping*. Springer, 1999.

[7] Alain Aspect, Jean Dalibard, and Gérard Roger. Experimental test of Bell's inequalities using time-varying analyzers. *Physical review letters*, 49(25):1804, 1982.

[8] Maximilian Schlosshauer. Decoherence, the measurement problem, and interpretations of quantum mechanics. *Reviews of Modern Physics*, 76(4):1267, 2005.

[9] Daniel A Lidar, Isaac L Chuang, and K Birgitta Whaley. Decoherence-free subspaces for quantum computation. *Physical Review Letters*, 81(12):2594, 1998.

[10] Mike H Anderson, Jason R Ensher, Michael R Matthews, Carl E Wieman, and Eric A Cornell. Observation of Bose-Einstein condensation in a dilute atomic vapor. *Science*, 269(5221):198–201, 1995.

[11] KB Davis, M-O Mewes, MR van Andrews, NJ Van Druten, DS Durfee, DM Kurn, and W Ketterle. Bose-Einstein condensation in a gas of Sodium atoms. *Physical Review Letters*, 75(22): 3969, 1995.

[12] Till Rosenband, DB Hume, PO Schmidt, CW Chou, A Brusch, L Lorini, WH Oskay, RE Drullinger, TM Fortier, JE Stalnaker, et al. Frequency ratio of Al+ and Hg+ single-ion optical clocks;

metrology at the 17th decimal place. *Science*, 319(5871):1808–1812, 2008.

[13] AD Ludlow, T Zelevinsky, GK Campbell, S Blatt, MM Boyd, MHG De Miranda, MJ Martin, JW Thomsen, SM Foreman, Jun Ye, et al. Sr lattice clock at $1\times$ 10–16 fractional uncertainty by remote optical evaluation with a Ca clock. *Science*, 319(5871): 1805–1808, 2008.

[14] Christian Deutsch, Fernando Ramirez-Martinez, Clement Lacroûte, Friedemann Reinhard, Tobias Schneider, Jean-Noël Fuchs, Frédéric Piéchon, Franck Laloë, Jakob Reichel, and Peter Rosenbusch. Spin self-rephasing and very long coherence times in a trapped atomic ensemble. *Physical review letters*, 105 (2):020401, 2010.

[15] M Vengalattore, JM Higbie, SR Leslie, J Guzman, LE Sadler, and DM Stamper-Kurn. High-resolution magnetometry with a spinor Bose-Einstein condensate. *Physical review letters*, 98(20): 200801, 2007.

[16] Matthew L Terraciano, Mark Bashkansky, and Fredrik K Fatemi. A single-shot imaging magnetometer using cold atoms. *Optics express*, 16(17):13062–13069, 2008.

[17] Pascal Böhi, Max F Riedel, Theodor W Hänsch, and Philipp Treutlein. Imaging of microwave fields using ultracold atoms. *Applied Physics Letters*, 97(5):051101, 2010.

[18] L Isenhower, E Urban, XL Zhang, AT Gill, T Henage, TA Johnson, TG Walker, and M Saffman. Demonstration of a neutral atom controlled-NOT quantum gate. *Physical review letters*, 104 (1):010503, 2010.

[19] Karl D Nelson, Xiao Li, and David S Weiss. Imaging single atoms in a three-dimensional array. *Nature Physics*, 3(8):556–560, 2007.

[20] John Kitching, Svenja Knappe, and Elizabeth A Donley. Atomic sensors–a review. *Sensors Journal, IEEE*, 11(9):1749–1758, 2011.

[21] Parameswaran Hariharan. *Basics of interferometry*. Academic Press, 2010.

[22] Albert A Michelson. The relative motion of the earth and of the luminiferous ether. *American Journal of Science*, 22(128):120–129, 1881.

[23] TM Niebauer, GS Sasagawa, JE Faller, R Hilt, and Fred Klopping. A new generation of absolute gravimeters. *Metrologia*, 32 (3):159, 1995.

[24] Landry Huet. *Gravimétrie atomique sur puce et applications embarquées*. PhD thesis, Université Paris-Est, 2013.

[25] Przemyslaw Baranski, Maciej Polanczyk, and Pawel Strumillo. Fusion of data from inertial sensors, raster maps and GPS for estimation of pedestrian geographic location in urban terrain. *Metrology and Measurement Systems*, 18(1):145–158, 2011.

[26] Fabien Napolitano. Fiber-optic gyroscopes key technological advantages. *IXSEA*, pages 1–8, 2010.

[27] KTV Grattan and T Sun. Fiber optic sensor technology: an overview. *Sensors and Actuators A: Physical*, 82(1):40–61, 2000.

[28] Sylvain Schwartz. *Gyrolaser à état solide. Application des lasers à atomes à la gyrométrie.* PhD thesis, Ecole Polytechnique X, 2006.

[29] A Gauguet, Benjamin Canuel, Thomas Lévèque, Walid Chaibi, and Arnaud Landragin. Characterization and limits of a cold-atom Sagnac interferometer. *Physical Review A*, 80(6):063604, 2009.

[30] TL Gustavson, A Landragin, and MA Kasevich. Rotation sensing with a dual atom-interferometer Sagnac gyroscope. *Classical and Quantum Gravity*, 17(12):2385, 2000.

[31] Mark Kasevich and Steven Chu. Atomic interferometry using stimulated Raman transitions. *Physical Review Letters*, 67(2):181, 1991.

[32] M Kasevich and S Chu. Measurement of the gravitational acceleration of an atom with a light-pulse atom interferometer. *Applied Physics B*, 54(5):321–332, 1992.

[33] F Riehle, Th Kisters, A Witte, J Helmcke, and Ch J Bordé. Optical ramsey spectroscopy in a rotating frame: Sagnac effect in a matter-wave interferometer. *Physical review letters*, 67(2):177, 1991.

[34] Min-Kang Zhou, Bruno Pelle, Adele Hilico, and Franck Pereira dos Santos. Atomic multiwave interferometer in an optical lattice. *Physical Review A*, 88(1):013604, 2013.

[35] Pierre Cladé, Saıda Guellati-Khélifa, Catherine Schwob, François Nez, Lucile Julien, and François Biraben. A promising method for the measurement of the local acceleration of gravity using Bloch oscillations of ultracold atoms in a vertical standing wave. *EPL (Europhysics Letters)*, 71(5):730, 2005.

[36] Alex Sugarbaker, Susannah M Dickerson, Jason M Hogan, David MS Johnson, and Mark A Kasevich. Enhanced atom

interferometer readout through the application of phase shear. *Physical review letters*, 111(11):113002, 2013.

[37] Renée Charrière, Malo Cadoret, Nassim Zahzam, Yannick Bidel, and Alexandre Bresson. Local gravity measurement with the combination of atom interferometry and Bloch oscillations. *Physical Review A*, 85(1):013639, 2012.

[38] S Merlet, Q Bodart, N Malossi, A Landragin, F Pereira Dos Santos, O Gitlein, and L Timmen. Comparison between two mobile absolute gravimeters: optical versus atomic interferometers. *Metrologia*, 47(4):L9, 2010.

[39] Ch Rothleitner and Sergiy Svitlov. On the evaluation of systematic effects in atom and corner-cube absolute gravimeters. *Physics Letters A*, 376(12):1090–1095, 2012.

[40] JM McGuirk, GT Foster, JB Fixler, MJ Snadden, and MA Kasevich. Sensitive absolute-gravity gradiometry using atom interferometry. *Physical Review A*, 65(3):033608, 2002.

[41] Richard L Steiner, Edwin R Williams, David B Newell, and Ruimin Liu. Towards an electronic kilogram: an improved measurement of the Planck constant and electron mass. *Metrologia*, 42(5):431, 2005.

[42] Gérard Genevès, Pierre Gournay, A Gosset, M Lecollinet, François Villar, Patrick Pinot, P Juncar, A Clairon, A Landragin, D Holleville, et al. The BNM Watt balance project. *IEEE Transactions on instrumentation and Measurement*, 54(2):850–853, 2005.

[43] Rym Bouchendira, Pierre Cladé, Saïda Guellati-Khélifa, François Nez, and François Biraben. New determination of the fine structure constant and test of the quantum electrodynamics. *Physical Review Letters*, 106(8):080801, 2011.

[44] JB Fixler, GT Foster, JM McGuirk, and MA Kasevich. Atom interferometer measurement of the Newtonian constant of gravity. *Science*, 315(5808):74–77, 2007.

[45] G Lamporesi, A Bertoldi, L Cacciapuoti, M Prevedelli, and GM Tino. Determination of the Newtonian gravitational constant using atom interferometry. *Physical review letters*, 100(5): 050801, 2008.

[46] Savas Dimopoulos, Peter W Graham, Jason M Hogan, and Mark A Kasevich. Testing general relativity with atom interferometry. *Physical review letters*, 98(11):111102, 2007.

[47] Peter Wolf, Luc Blanchet, Christian J Bordé, Serge Reynaud, Christophe Salomon, and Claude Cohen-Tannoudji. Atom gravimeters and gravitational redshift. *Nature*, 467(7311):E1–E1, 2010.

[48] Peter Wolf, Luc Blanchet, Christian J Bordé, Serge Reynaud, Christophe Salomon, and Claude Cohen-Tannoudji. Does an atom interferometer test the gravitational redshift at the compton frequency. *Classical and Quantum Gravity*, 28(14):145017, 2011.

[49] Savas Dimopoulos, Peter W Graham, Jason M Hogan, and Mark A Kasevich. General relativistic effects in atom interferometry. *Physical Review D*, 78(4):042003, 2008.

[50] Savas Dimopoulos, Peter W Graham, Jason M Hogan, Mark A Kasevich, and Surjeet Rajendran. Atomic gravitational wave interferometric sensor. *Physical Review D*, 78(12):122002, 2008.

[51] Jason M Hogan, David MS Johnson, Susannah Dickerson, Tim Kovachy, Alex Sugarbaker, Sheng-wey Chiow, Peter W Graham, Mark A Kasevich, Babak Saif, Surjeet Rajendran, et al. An atomic gravitational wave interferometric sensor in low earth orbit (AGIS-LEO). *General Relativity and Gravitation*, 43(7):1953–2009, 2011.

[52] A Rozhnoi, M Solovieva, O Molchanov, P-F Biagi, and M Hayakawa. Observation evidences of atmospheric gravity waves induced by seismic activity from analysis of subionospheric LF signal spectra. *Natural Hazards and Earth System Science*, 7(5):625–628, 2007.

[53] KP Schwarz, O Colombo, G Hein, and ET Knickmeyer. Requirements for airborne vector gravimetry. In *From Mars to Greenland: Charting Gravity With Space and Airborne Instruments*, pages 273–283. Springer, 1992.

[54] Ken Takase. *Precision rotation rate measurements with a mobile atom interferometer*. PhD thesis, Stanford University, 2008.

[55] Xin'an Wu. *Gravity gradient survey with a mobile atom interferometer*. PhD thesis, Stanford University, 2009.

[56] Fiodor Sorrentino, Kai Bongs, Philippe Bouyer, Luigi Cacciapuoti, Marella de Angelis, Hansjoerg Dittus, Wolfgang Ertmer, Antonio Giorgini, Jonas Hartwig, Matthias Hauth, et al. A compact atom interferometer for future space missions. *Microgravity Science and Technology*, 22(4):551–561, 2010.

[57] Remi Geiger, Vincent Ménoret, Guillaume Stern, Nassim Zahzam, Patrick Cheinet, Baptiste Battelier, André Villing,

Frédéric Moron, Michel Lours, Yannick Bidel, et al. Detecting inertial effects with airborne matter-wave interferometry. *Nature communications*, 2:474, 2011.

[58] Ph Laurent, M Abgrall, Ch Jentsch, P Lemonde, G Santarelli, A Clairon, I Maksimovic, S Bize, Ch Salomon, D Blonde, et al. Design of the cold atom PHARAO space clock and initial test results. *Applied Physics B*, 84(4):683–690, 2006.

[59] M Schmidt, A Senger, M Hauth, C Freier, V Schkolnik, and A Peters. A mobile high-precision absolute gravimeter based on atom interferometry. *Gyroscopy and Navigation*, 2(3):170–177, 2011.

[60] Olivier Carraz. *Gravimètre atomique embarquable: Etude théorique et expérimentale de l'instrument*. PhD thesis, Observatoire de Paris, 2009.

[61] Jakob Reichel, W Hänsel, P Hommelhoff, and TW Hänsch. Applications of integrated magnetic microtraps. *Applied Physics B*, 72(1):81–89, 2001.

[62] Jakob Reichel. Microchip traps and Bose–Einstein condensation. *Applied Physics B*, 74(6):469–487, 2002.

[63] Ron Folman, Peter Krüger, Jörg Schmiedmayer, Johannes Denschlag, and Carsten Henkel. Microscopic atom optics: from wires to an atom chip. *Advances in Atomic Molecular and Optical Physics*, 48:263–356, 2002.

[64] József Fortágh and Claus Zimmermann. Magnetic microtraps for ultracold atoms. *Reviews of Modern Physics*, 79(1):235, 2007.

[65] Tim van Zoest, N Gaaloul, Y Singh, H Ahlers, W Herr, ST Seidel, W Ertmer, E Rasel, M Eckart, E Kajari, et al. Bose-Einstein condensation in microgravity. *Science*, 328(5985):1540–1543, 2010.

[66] Microsystems Technology Office. Chip-Scale Combinatorial Atomic Navigator. *DARPA*, pages 1–43, 2012.

[67] T Schumm, S Hofferberth, L Mauritz Andersson, S Wildermuth, S Groth, I Bar-Joseph, J Schmiedmayer, and P Krüger. Matter-wave interferometry in a double well on an atom chip. *Nature Physics*, 1(1):57–62, 2005.

[68] Y Shin, C Sanner, G-B Jo, TA Pasquini, M Saba, W Ketterle, DE Pritchard, M Vengalattore, and M Prentiss. Interference of Bose-Einstein condensates split with an atom chip. *Physical Review A*, 72(2):021604, 2005.

[69] Kenneth Maussang, G Edward Marti, Tobias Schneider, Philipp Treutlein, Yun Li, Alice Sinatra, Romain Long, Jérôme Estève, and Jakob Reichel. Enhanced and reduced atom number fluctuations in a BEC splitter. *Physical review letters*, 105(8):080403, 2010.

[70] T Berrada, S van Frank, R Bücker, T Schumm, J-F Schaff, and J Schmiedmayer. Integrated Mach-Zehnder interferometer for Bose-Einstein condensates. *Nature communications*, 4(May):2077, January 2013. ISSN 2041-1723. doi: 10.1038/ncomms3077.

[71] Pascal Böhi, Max F Riedel, Johannes Hoffrogge, Jakob Reichel, Theodor W Hänsch, and Philipp Treutlein. Coherent manipulation of Bose–Einstein condensates with state-dependent microwave potentials on an atom chip. *Nature Physics*, 5(8):592–597, 2009.

[72] Florian Baumgärtner, RJ Sewell, S Eriksson, I Llorente-Garcia, Jos Dingjan, JP Cotter, and EA Hinds. Measuring energy differences by BEC interferometry on a chip. *Physical review letters*, 105(24):243003, 2010.

[73] Julian Grond, Ulrich Hohenester, Jörg Schmiedmayer, and Augusto Smerzi. Mach-zehnder interferometry with interacting trapped Bose-Einstein condensates. *Physical Review A*, 84(2): 023619, 2011.

[74] Christian Gross, Tilman Zibold, Eike Nicklas, Jerome Esteve, and Markus K Oberthaler. Nonlinear atom interferometer surpasses classical precision limit. *Nature*, 464(7292):1165–1169, 2010.

[75] G-B Jo, J-H Choi, CA Christensen, TA Pasquini, Y-R Lee, W Ketterle, and DE Pritchard. Phase-sensitive recombination of two Bose-Einstein condensates on an atom chip. *Physical review letters*, 98(18):180401, 2007.

[76] Jakob Reichel and Vladan Vuletic. *Atom Chips*. John Wiley & Sons, 2010.

[77] VV Vladimirskii. Magnetic mirrors, channels and bottles for cold neutrons. *Zhur. Eksptl'. i Teoret Fiz.*, 39, 1960.

[78] K-J Kügler, W Paul, and U Trinks. A magnetic storage ring for neutrons. *Physics Letters B*, 72(3):422–424, 1978.

[79] Alan L Migdall, WD Phillips, JV Prodan, Thomas H Bergeman, and Harold J Metcalf. First observation of magnetically trapped neutral atoms. *Physical Review Letters*, 54:2596–2599, 1985.

[80] Tilman Esslinger, Immanuel Bloch, and Theodor W Hänsch. Bose-Einstein condensation in a quadrupole-Ioffe-configuration trap. *Physical Review A*, 58(4):R2664, 1998.

[81] M-O Mewes, MR Andrews, NJ Van Druten, DM Kurn, DS Durfee, CG Townsend, and W Ketterle. Collective excitations of a Bose-Einstein condensate in a magnetic trap. *Physical review letters*, 77(6):988, 1996.

[82] SL Cornish, NR Claussen, JL Roberts, EA Cornell, and CE Wieman. Stable 85 Rb Bose-Einstein condensates with widely tunable interactions. *Physical Review Letters*, 85(9):1795, 2000.

[83] Kevin L Moore, Thomas P Purdy, Kater W Murch, Kenneth R Brown, Keshav Dani, Subhadeep Gupta, and Dan M Stamper-Kurn. Bose–Einstein condensation in a mm-scale Ioffe–Pritchard trap. *Applied Physics B*, 82(4):533–538, 2006.

[84] Thorsten Schumm. *Bose-Einstein condensates in magnetic double well potentials*. PhD thesis, 2005.

[85] Roman Schmied, Dietrich Leibfried, Robert JC Spreeuw, and Shannon Whitlock. Optimized magnetic lattices for ultracold atomic ensembles. *New Journal of Physics*, 12(10):103029, 2010.

[86] Philipp Treutlein. *Coherent manipulation of ultracold atoms on atom chips*. PhD thesis, lmu, 2008.

[87] Daniel A Steck. Rubidium 87 d line data, 2001.

[88] William H Wing. On neutral particle trapping in quasistatic electromagnetic fields. *Progress in Quantum Electronics*, 8(3):181–199, 1984.

[89] W Ketterle, DS Durfee, and DM Stamper-Kurn. Making, probing and understanding Bose-Einstein condensates. *arXiv preprint cond-mat/9904034*, 5, 1999.

[90] DM Harber, HJ Lewandowski, JM McGuirk, and EA Cornell. Effect of cold collisions on spin coherence and resonance shifts in a magnetically trapped ultracold gas. *Physical Review A*, 66 (5):053616, 2002.

[91] Philipp Treutlein, Peter Hommelhoff, Tilo Steinmetz, Theodor W Hänsch, and Jakob Reichel. Coherence in microchip traps. *Physical review letters*, 92(20):203005, 2004.

[92] HJ Lewandowski, DM Harber, DL Whitaker, and EA Cornell. Observation of anomalous spin-state segregation in a trapped ultra-cold vapor. *arXiv preprint cond-mat/0109476*, 2001.

[93] S Gov, S Shtrikman, and H Thomas. Magnetic trapping of neutral particles: Classical and quantum-mechanical study of a Ioffe–Pritchard type trap. *Journal of Applied Physics*, 87(8):3989–3998, 2000.

[94] David E Pritchard. Cooling neutral atoms in a magnetic trap for precision spectroscopy. *Physical Review Letters*, 51(15):1336, 1983.

[95] Baolong Lu and William Arie van Wijngaarden. Bose-Einstein condensation in a QUIC trap. *Canadian journal of physics*, 82(2): 81–102, 2004.

[96] JD Weinstein and KG Libbrecht. Microscopic magnetic traps for neutral atoms. *Physical Review A*, 52(5):4004, 1995.

[97] CDJ Sinclair, EA Curtis, I Llorente Garcia, JA Retter, BV Hall, S Eriksson, BE Sauer, and EA Hinds. Bose-Einstein condensation on a permanent-magnet atom chip. *Physical Review A*, 72 (3):031603, 2005.

[98] Tetsuya Mukai, Christoph Hufnagel, A Kasper, T Meno, A Tsukada, K Semba, and F Shimizu. Persistent supercurrent atom chip. *Physical review letters*, 98(26):260407, 2007.

[99] R Gerritsma and RJC Spreeuw. Topological constraints on magnetostatic traps. *Physical Review A*, 74(4):043405, 2006.

[100] BV Hall, S Whitlock, F Scharnberg, P Hannaford, and A Sidorov. A permanent magnetic film atom chip for Bose–Einstein condensation. *Journal of Physics B: Atomic, Molecular and Optical Physics*, 39(1):27, 2006.

[101] Maciej Lewenstein, Anna Sanpera, Veronica Ahufinger, Bogdan Damski, Aditi Sen, and Ujjwal Sen. Ultracold atomic gases in optical lattices: mimicking condensed matter physics and beyond. *Advances in Physics*, 56(2):243–379, 2007.

[102] David DeMille. Quantum computation with trapped polar molecules. *Physical Review Letters*, 88(6):067901, 2002.

[103] TJ Davis. 2D magnetic traps for ultra-cold atoms: a simple theory using complex numbers. *The European Physical Journal D-Atomic, Molecular, Optical and Plasma Physics*, 18(1):27–36, 2002.

[104] Philipp Treutlein, Theodor W Hänsch, Jakob Reichel, Antonio Negretti, Markus A Cirone, and Tommaso Calarco. Microwave potentials and optimal control for robust quantum gates on an atom chip. *Physical Review A*, 74(2):022312, 2006.

[105] Thomas R Gentile, Barbara J Hughey, Daniel Kleppner, and Theodore W Ducas. Experimental study of one-and two-photon rabi oscillations. *Physical Review A*, 40(9):5103, 1989.

[106] Jean Dalibard. Collisional dynamics of ultra-cold atomic gases. In *Proceedings of the International School of Physics-Enrico Fermi*, volume 321, 1999.

[107] Wolfgang Petrich, Michael H Anderson, Jason R Ensher, and Eric A Cornell. Stable, tightly confining magnetic trap for evaporative cooling of neutral atoms. *Physical Review Letters*, 74(17): 3352, 1995.

[108] OJ Luiten, MW Reynolds, and JTM Walraven. Kinetic theory of the evaporative cooling of a trapped gas. *Physical Review A*, 53 (1):381, 1996.

[109] MÖ Oktel and LS Levitov. Collective dynamics of internal states in a Bose-Einstein gas. *Physical Review A*, 65(6):063604, 2002.

[110] Kurt Gibble. Decoherence and collisional frequency shifts of trapped bosons and fermions. *Physical review letters*, 103(11): 113202, 2009.

[111] Christian Deutsch. *Trapped Atom Clock on a Chip Identical Spin Rotation Effects in an Ultracold Trapped Atomic Clock*. PhD thesis, UPMC, PIERRE ET MARIE CURIE, 2011.

[112] P Rosenbusch. Magnetically trapped atoms for compact atomic clocks. *Applied Physics B*, 95(2):227–235, 2009.

[113] Charles C Agosta, Isaac F Silvera, Hendricus Theodorus Christiaan Stoof, and BJ Verhaar. Trapping of neutral atoms with resonant microwave radiation. *Physical review letters*, 62(20):2361, 1989.

[114] RJC Spreeuw, C Gerz, Lori S Goldner, WD Phillips, SL Rolston, CI Westbrook, MW Reynolds, and Isaac F Silvera. Demonstration of neutral atom trapping with microwaves. *Physical review letters*, 72(20):3162, 1994.

[115] Yves Colombe, Elena Knyazchyan, Olivier Morizot, Brigitte Mercier, Vincent Lorent, and Hélene Perrin. Ultracold atoms confined in rf-induced two-dimensional trapping potentials. *EPL (Europhysics Letters)*, 67(4):593, 2004.

[116] Olivier Morizot, Yves Colombe, Vincent Lorent, Hélène Perrin, and Barry M Garraway. Ring trap for ultracold atoms. *Physical Review A*, 74(2):023617, 2006.

[117] T Fernholz, R Gerritsma, P Krüger, and RJC Spreeuw. Dynamically controlled toroidal and ring-shaped magnetic traps. *Physical Review A*, 75(6):063406, 2007.

[118] Ph W Courteille, B Deh, J Fortágh, A Günther, S Kraft, C Marzok, S Slama, and C Zimmermann. Highly versatile atomic micro traps generated by multifrequency magnetic field modulation. *Journal of Physics B: Atomic, Molecular and Optical Physics*, 39(5):1055, 2006.

[119] Ch J Bordé. Atomic interferometry with internal state labelling. *Physics letters A*, 140(1):10–12, 1989.

[120] Max F Riedel, Pascal Böhi, Yun Li, Theodor W Hänsch, Alice Sinatra, and Philipp Treutlein. Atom-chip-based generation of entanglement for quantum metrology. *Nature*, 464(7292):1170–1173, 2010.

[121] Bruno Pelle, Adèle Hilico, Gunnar Tackmann, Quentin Beaufils, and F Pereira dos Santos. State-labeling Wannier-Stark atomic interferometers. *Physical Review A*, 87(2):023601, 2013.

[122] Olaf Mandel, Markus Greiner, Artur Widera, Tim Rom, Theodor W Hänsch, and Immanuel Bloch. Controlled collisions for multi-particle entanglement of optically trapped atoms. *Nature*, 425(6961):937–940, 2003.

[123] Hélène Perrin. Les houches lectures on adiabatic potentials. *Les Houches*, 2013.

[124] Claude Cohen-Tannoudji, Jacques Dupont-Roc, and Gilbert Grynberg. *Atom-photon interactions: basic processes and applications*. Wiley Online Library, 1992.

[125] J Dalibard and Claude Cohen-Tannoudji. Dressed-atom approach to atomic motion in laser light: the dipole force revisited. *JOSA B*, 2(11):1707–1720, 1985.

[126] Nikolay V Vitanov, Thomas Halfmann, Bruce W Shore, and Klaas Bergmann. Laser-induced population transfer by adiabatic passage techniques. *Annual review of physical chemistry*, 52 (1):763–809, 2001.

[127] Jean Dalibard. Des cages de lumière pour les atomes : la physique des pièges et des réseaux optiques. *Collège de France lectures*, pages 1–19, 2013.

[128] Cheng P Wen. Coplanar waveguide: A surface strip transmission line suitable for nonreciprocal gyromagnetic device applications. *Microwave Theory and Techniques, IEEE Transactions on*, 17(12):1087–1090, 1969.

[129] Kuldip C Gupta, Ramesh Garg, Inder Jit Bahl, and Prakash Bhartia. *Microstrip lines and slotlines*, volume 2. Artech house Boston, 1996.

[130] Masahiro Muraguchi, Tetsuo Hirota, Akira Minakawa, Kuniki Ohwada, and Takayuki Sugeta. Uniplanar MMICs and their applications. *Microwave Theory and Techniques, IEEE Transactions on*, 36(12):1896–1901, 1988.

[131] Brian C Wadell. *Transmission line design handbook*. Artech House Boston (Ma), 1991.

[132] W. Heinrich. Full-wave analysis of conductor losses on MMIC transmission lines. *IEEE Transactions on Microwave Theory and Techniques*, 38(10):1468–1472, 1990.

[133] T. Kitazawa and Tatsuo Itoh. Asymmetrical coplanar waveguide with finite metallization thickness containing anisotropic media. In *IEEE International Digest on Microwave Symposium*, pages 673–676. IEEE, 1990.

[134] Y. Fukuoka and T. Itoh. Analysis of slow-wave coplanar waveguide for monolithic integrated circuits. *IEEE Transactions on Microwave Theory and Techniques*, 31(7):567–573, 1983.

[135] Toshihide Kitazawa and Tatsuo Itoh. Propagation characteristics of coplanar-type transmission lines with lossy media. *Microwave Theory and Techniques, IEEE Transactions on*, 39(10):1694–1700, 1991.

[136] T. Itoh and R. Mittra. Spectral-domain approach for calculating the dispersion characteristics of microstrip lines. *IEEE Transactions on Microwave Theory and Techniques*, 21(7):496–499, July 1973. ISSN 0018-9480. doi: 10.1109/TMTT.1973.1128044.

[137] R Sorrentino, G Leuzzi, and A Silbermann. Characteristics of metal-insulator-semiconductor coplanar waveguides for monolithic microwave circuits. *Microwave Theory and Techniques, IEEE Transactions on*, 32(4):410–416, 1984.

[138] Eikichi Yamashita and Kazuhiko Atsuki. Analysis of microstrip-like transmission lines by nonuniform discretization of integral equations. *Microwave Theory and Techniques, IEEE Transactions on*, 24(4):195–200, 1976.

[139] Nihad Ibrahim Dib and Linda PB Katehi. *Theoretical characterization of coplanar waveguide transmission lines and discontinuities*. PhD thesis, University of Michigan, 1992.

[140] G.-C. Liang, Y.-W. Liu, and K.K. Mei. Full-wave analysis of coplanar waveguide and slotline using the time-domain finite-difference method. *IEEE Transactions on Microwave Theory and Techniques*, 37(12):1949–1957, 1989. ISSN 00189480. doi: 10.1109/22.44107.

[141] Robert E Collin. *Foundations for microwave engineering*. John Wiley & Sons, 2007.

[142] Wolfgang Heinrich. Quasi-TEM description of MMIC coplanar lines including conductor-loss effects. *Microwave Theory and Techniques, IEEE Transactions on*, 41(1):45–52, 1993.

[143] Philipp Treutlein. Lossy microwave transmission lines. *unpublished*, pages 1–12, 2005.

[144] Giovanni Ghione and Carlo U Naldi. Coplanar waveguides for mmic applications: Effect of upper shielding, conductor backing, finite-extent ground planes, and line-to-line coupling. *Microwave Theory and Techniques, IEEE Transactions on*, 35(3):260–267, 1987.

[145] Erik Carlsson and Spartak Gevorgian. Conformal mapping of the field and charge distributions in multilayered substrate CPWs. *IEEE Transactions on Microwave Theory and Techniques*, 47 (8):1544–1552, 1999. ISSN 00189480. doi: 10.1109/22.780407.

[146] Matthew Gillick, I.D. Robertson, and J.S. Joshi. An analytical method for direct calculation of E and H-field patterns of conductor-backed coplanar waveguides. *IEEE Transactions on Microwave Theory and Techniques*, 41(9):1606–1610, 1993. ISSN 00189480. doi: 10.1109/22.245685.

[147] Matthew Gillick, I.D. Robertson, and J.S. Joshi. Direct analytical solution for the electric field distribution at the conductor surfaces of coplanar waveguides. *IEEE Transactions on Microwave Theory and Techniques*, 41(1):129–135, 1993. ISSN 00189480. doi: 10.1109/22.210239.

[148] F Schnieder, H-M Heiliger, and W Heinrich. Coupling between neighboring CPWs in MMICs. *Microwave and Guided Wave Letters, IEEE*, 8(8):290–292, 1998.

[149] Y Shin, M Saba, TA Pasquini, W Ketterle, DE Pritchard, and AE Leanhardt. Atom interferometry with Bose-Einstein condensates in a double-well potential. *Physical review letters*, 92(5): 050405, 2004.

[150] M. Gustavsson, E. Haller, M. J. Mark, J. G. Danzl, G. Rojas-Kopeinig, and H.-C. Nägerl. Control of interaction-induced de-

phasing of Bloch oscillations. *Phys. Rev. Lett.*, 100:080404, Feb 2008.

[151] M. Fattori, C. D Errico, G. Roati, M. Zaccanti, M. Jona-Lasinio, M. Modugno, M. Inguscio, and G. Modugno. Atom interferometry with a weakly interacting Bose-Einstein condensate. *Phys. Rev. Lett.*, 100:080405, Feb 2008.

[152] James C Wyant. White light interferometry. In *AeroSense 2002*, pages 98–107. International Society for Optics and Photonics, 2002.

[153] RH Leonard and CA Sackett. Effect of trap anharmonicity on a free-oscillation atom interferometer. *Physical Review A*, 86(4): 043613, 2012.

[154] Norman Ramsey. *Molecular beams*. Oxford University Press, 1956.

[155] Friedemann Reinhard. *Design and construction of an atomic clock on an atom chip*. PhD thesis, Paris 6, 2009.

[156] Carsten Henkel, Sierk Pötting, and Martin Wilkens. Loss and heating of particles in small and noisy traps. *Applied Physics B*, 69(5-6):379–387, 1999.

[157] Martin Trinker, Sönke Groth, Stefan Haslinger, Stephanie Manz, Thomas Betz, S Schneider, I Bar-Joseph, T Schumm, and J Schmiedmayer. Multilayer atom chips for versatile atom micromanipulation. *Applied Physics Letters*, 92(25):254102–254102, 2008.

[158] Said S Bedair and Ingo Wolff. Fast, accurate and simple approximate analytic formulas for calculating the parameters of supported coplanar waveguides for (M) MIC's . *Microwave Theory and Techniques, IEEE Transactions on*, 40(1):41–48, 1992.

[159] Ying-Ju Wang, Dana Z Anderson, Victor M Bright, Eric A Cornell, Quentin Diot, Tetsuo Kishimoto, Mara Prentiss, RA Saravanan, Stephen R Segal, and Saijun Wu. Atom Michelson interferometer on a chip using a Bose-Einstein condensate. *Physical review letters*, 94(9):090405, 2005.

[160] A Günther, S Kraft, M Kemmler, D Koelle, R Kleiner, C Zimmermann, and J Fortágh. Diffraction of a Bose-Einstein condensate from a magnetic lattice on a microchip. *Physical review letters*, 95(17):170405, 2005.

[161] A Günther, S Kraft, C Zimmermann, and J Fortágh. Atom interferometer based on phase coherent splitting of Bose-Einstein condensates with an integrated magnetic grating. *Physical review letters*, 98(14):140403, 2007.

[162] Carlos L Garrido Alzar, Hélène Perrin, Barry M Garraway, and Vincent Lorent. Evaporative cooling in a radio-frequency trap. *Physical Review A*, 74(5):053413, 2006.

[163] Pascal Alexander Böhi. *Coherent manipulation of ultracold atoms with microwave near-fields*. PhD thesis, Ludwig-Maximilians-Universitat Munchen, 2010.

[164] Miteq. 2 *TO* 8 *GHz SINGLE-SIDEBAND UPCONVERTER OR I/Q MODULATOR*. SDM0208LC1CD, 2012.

[165] Philipp Treutlein. This idea has been proposed by P. Treutlein, in the "Paris-Munich Atom Chip Meeting". *Private communication*, 2010.

[166] J.B. Knorr and K. Kuchler. Analysis of Coupled Slots and Coplanar Strips on Dielectric Substrate. *IEEE Transactions on Microwave Theory and Techniques*, 23(7):541–548, July 1975. ISSN 0018-9480. doi: 10.1109/TMTT.1975.1128624.

[167] Giovanni Ghione. A CAD-oriented analytical model for the losses of general asymmetric coplanar lines in hybrid and monolithic MICs. *IEEE Transactions on Microwave Theory and Techniques*, 41(9):1499–1510, 1993. ISSN 00189480. doi: 10.1109/22.245668.

[168] AI Sidorov, BJ Dalton, SM Whitlock, and F Scharnberg. Asymmetric double-well potential for single-atom interferometry. *Physical Review A*, 74(2):023612, 2006.

[169] Rainer Reichle, D Leibfried, RB Blakestad, J Britton, JD Jost, E Knill, C Langer, R Ozeri, S Seidelin, and DJ Wineland. Transport dynamics of single ions in segmented microstructured Paul trap arrays. *Fortschritte der Physik*, 54(8-10):666–685, 2006.

[170] Andreas Walther, Frank Ziesel, Thomas Ruster, Sam T Dawkins, Konstantin Ott, Max Hettrich, Kilian Singer, Ferdinand Schmidt-Kaler, and Ulrich Poschinger. Controlling fast transport of cold trapped ions. *Physical review letters*, 109(8):080501, 2012.

[171] N Poli, F-Y Wang, MG Tarallo, A Alberti, M Prevedelli, and GM Tino. Precision measurement of gravity with cold atoms in an optical lattice and comparison with a classical gravimeter. *Physical review letters*, 106(3):038501, 2011.

[172] JA Sauer, KM Fortier, MS Chang, CD Hamley, and MS Chapman. Cavity QED with optically transported atoms. *Physical Review A*, 69(5):051804, 2004.

[173] Roger Gehr, Jürgen Volz, Guilhem Dubois, Tilo Steinmetz, Yves Colombe, Benjamin L Lev, Romain Long, Jérôme Estève, and Jakob Reichel. Cavity-based single atom preparation and high-fidelity hyperfine state readout. *Physical review letters*, 104(20): 203602, 2010.

[174] Yves Colombe, Tilo Steinmetz, Guilhem Dubois, Felix Linke, David Hunger, and Jakob Reichel. Strong atom–field coupling for Bose–Einstein condensates in an optical cavity on a chip. *Nature*, 450(7167):272–276, 2007.

[175] E Torrontegui, S Ibáñez, M Modugno, A del Campo, D Guéry-Odelin, A Ruschhaupt, Xi Chen, JG Muga, et al. Shortcuts to adiabaticity. *arXiv preprint arXiv:1212.6343*, 2012.

[176] A Couvert, T Kawalec, G Reinaudi, and David Guery-Odelin. Optimal transport of ultracold atoms in the non-adiabatic regime. *EPL (Europhysics Letters)*, 83(1):13001, 2008.

[177] Mark G Bason, Matthieu Viteau, Nicola Malossi, Paul Huillery, Ennio Arimondo, Donatella Ciampini, Rosario Fazio, Vittorio Giovannetti, Riccardo Mannella, and Oliver Morsch. High-fidelity quantum driving. *Nature Physics*, 8(2):147–152, 2011.

[178] Albert Messiah. Quantum mechanics, vol. ii. *English Edition, North Holland: Amster*, 1962.

[179] Michael V Berry. Quantal phase factors accompanying adiabatic changes. *Proceedings of the Royal Society of London. A. Mathematical and Physical Sciences*, 392(1802):45–57, 1984.

[180] Barbara Goss Levi. The geometric phase shows up in chemical reactions. *Physics Today*, 46:17, 1993.

[181] Nicola Manini and Paolo De Los Rios. The rôle of the Berry phase in dynamical Jahn-Teller systems. *Journal of Physics: Condensed Matter*, 10(38):8485, 1998.

[182] Michael Murphy, Liang Jiang, Navin Khaneja, and Tommaso Calarco. High-fidelity fast quantum transport with imperfect controls. *Physical Review A*, 79(2):020301, 2009.

[183] Claude Cohen-Tannoudji, Bernard Diu, and Frank Laloë. Quantum mechanics, 2 volume set, 2006.

[184] Satyendranath Bose. Plancks gesetz und lichtquantenhypothese. *Z. phys*, 26(3):178, 1924.

[185] Albert Einstein. *Quantentheorie des einatomigen idealen Gases*. Akademie der Wissenshaften, in Kommission bei W. de Gruyter, 1924.

[186] J-F Schaff, X-L Song, Pablo Capuzzi, Patrizia Vignolo, and Guillaume Labeyrie. Shortcut to adiabaticity for an interacting Bose-Einstein condensate. *EPL (Europhysics Letters)*, 93(2):23001, 2011.

[187] Peter Salamon, Karl Heinz Hoffmann, Yair Rezek, and Ronnie Kosloff. Maximum work in minimum time from a conservative quantum system. *Physical Chemistry Chemical Physics*, 11(7): 1027–1032, 2009.

[188] A Del Campo and MG Boshier. Shortcuts to adiabaticity in a time-dependent box. *Scientific reports*, 2, 2012.

[189] Jean-François Schaff, Pablo Capuzzi, Guillaume Labeyrie, and Patrizia Vignolo. Shortcuts to adiabaticity for trapped ultracold gases. *New Journal of Physics*, 13(11):113017, 2011.

[190] E Torrontegui, S Ibánez, Xi Chen, A Ruschhaupt, D Guéry-Odelin, and JG Muga. Fast atomic transport without vibrational heating. *Physical Review A*, 83(1):013415, 2011.

[191] H Ralph Lewis Jr and WB Riesenfeld. An exact quantum theory of the time-dependent harmonic oscillator and of a charged particle in a time-dependent electromagnetic field. *Journal of Mathematical Physics*, 10:1458, 1969.

[192] V Ermakov. Universitetskie izvestiya, 1880.

[193] AK Dhara and SV Lawande. Time-dependent invariants and the Feynman propagator. *Physical Review A*, 30(1):560, 1984.

[194] Xi Chen, A Ruschhaupt, S Schmidt, A Del Campo, D Guéry-Odelin, and JG Muga. Fast optimal frictionless atom cooling in harmonic traps: Shortcut to adiabaticity. *Physical review letters*, 104(6):063002, 2010.

[195] Yong Li, Lian-Ao Wu, and ZD Wang. Fast ground-state cooling of mechanical resonators with time-dependent optical cavities. *Physical Review A*, 83(4):043804, 2011.

[196] Matt Mackie, Ryan Kowalski, and Juha Javanainen. Bose-stimulated Raman adiabatic passage in photoassociation. *Physical review letters*, 84(17):3803, 2000.

[197] Anders S Sørensen, Ehud Altman, Michael Gullans, JV Porto, Mikhail D Lukin, and Eugene Demler. Adiabatic preparation of many-body states in optical lattices. *Physical Review A*, 81(6): 061603, 2010.

[198] Ulrich Hohenester, Per Kristian Rekdal, Alfio Borzì, and Jörg Schmiedmayer. Optimal quantum control of Bose-Einstein condensates in magnetic microtraps. *Physical Review A*, 75(2): 023602, 2007.

[199] G De Chiara, T Calarco, M Anderlini, S Montangero, PJ Lee, BL Brown, WD Phillips, and JV Porto. Optimal control of atom transport for quantum gates in optical lattices. *Physical Review A*, 77(5):052333, 2008.

[200] Michael Mundt and David J Tannor. Optimal control of interacting particles: a multi-configuration time-dependent Hartree–Fock approach. *New Journal of Physics*, 11(10):105038, 2009.

[201] Landry Huet, Mahdi Ammar, Erwan Morvan, Nicolas Sarazin, Jean-Paul Pocholle, Jakob Reichel, Christine Guerlin, and Sylvain Schwartz. Experimental investigation of transparent silicon carbide for atom chips. *Applied Physics Letters*, 100(12): 121114, 2012.

[202] D Sciti and A Bellosi. Laser-induced surface drilling of silicon carbide. *Applied surface science*, 180(1):92–101, 2001.

[203] Matthew B Squires. *High repetition rate Bose-Einstein condensate production in a compact, transportable vacuum system*. PhD thesis, Univ. Colorado, 2008.

[204] Evan Ali Salim. *Ultracold matter systems and atomtronics instrumentation.* PhD thesis, University of Colorado, 2011.

[205] Chun-lin Liao and Chun Hsiung Chen. A novel coplanar-waveguide directional coupler with finite-extent backed conductor. *IEEE Transactions on Microwave Theory and Techniques*, 51 (1):200–206, January 2003. ISSN 0018-9480. doi: 10.1109/TMTT.2002.806902.

[206] H Shigesawa, M Tsjui, and AA Oliner. Conductor-backed slot line and coplanar waveguide: Dangers and full-wave analyses. In *Microwave Symposium Digest, 1988., IEEE MTT-S International*, pages 199–202. IEEE, 1988.

[207] Askol'd Mikhailovich Perelomov and Vladimir Stepanovich Popov. Method of generating functions for a quantum oscillator. *Theoretical and Mathematical Physics*, 3(3):582–592, 1970.

[208] VS Popov and AM Perelomov. Parametric excitation of a quantum oscillator, ii. *Soviet Physics JETP*, 30(5):910–913, 1969.

[209] Kôdi Husimi. Miscellanea in elementary quantum mechanics, ii. *Progress of Theoretical Physics*, 9(4):381–402, 1953.

[210] Hans-Dieter Meyer. On the forced harmonic oscillator with time-dependent frequency. *Chemical Physics*, 61(3):365–383, 1981.

[211] Edward H Kerner. Note on the forced and damped oscillator in quantum mechanics. *Canadian Journal of Physics*, 36(3):371–377, 1958.

[212] Milton Abramowitz and Irene A Stegun. *Handbook of mathematical functions: with formulas, graphs, and mathematical tables*. Courier Dover Publications, 2012.